Modelling of crystal plasticity and grain boundary migration of 304L steel at the mesoscopic scale

Ana Laura Cruz Fabiano

▶ **To cite this version:**

Ana Laura Cruz Fabiano. Modelling of crystal plasticity and grain boundary migration of 304L steel at the mesoscopic scale. Other. Ecole Nationale Supérieure des Mines de Paris, 2013. English. NNT : 2013ENMP0088 . pastel-01069080

HAL Id: pastel-01069080

https://pastel.hal.science/pastel-01069080

Submitted on 26 Sep 2014

HAL is a multi-disciplinary open access archive for the deposit and dissemination of scientific research documents, whether they are published or not. The documents may come from teaching and research institutions in France or abroad, or from public or private research centers.

L'archive ouverte pluridisciplinaire **HAL**, est destinée au dépôt et à la diffusion de documents scientifiques de niveau recherche, publiés ou non, émanant des établissements d'enseignement et de recherche français ou étrangers, des laboratoires publics ou privés.

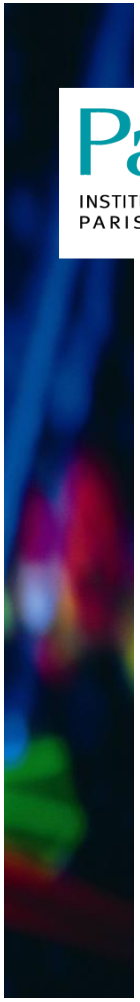

ParisTech
INSTITUT DES SCIENCES ET TECHNOLOGIES
PARIS INSTITUTE OF TECHNOLOGY

MINES ParisTech

École doctorale n° 364 : Sciences Fondamentales et Appliquées

Doctorat ParisTech

T H È S E

pour obtenir le grade de docteur délivré par

l'École nationale supérieure des mines de Paris

Spécialité " Mécanique Numérique "

présentée et soutenue publiquement par

Ana Laura CRUZ FABIANO

le 10 décembre 2013

Modelling of crystal plasticity and grain boundary motion of 304L steel at the mesoscopic scale

~~~

Modélisation de la plasticité cristalline et de la migration des joints de grains de l'acier 304L à l'échelle mésoscopique

Directeurs de thèse : **Marc BERNACKI et Roland LOGE**

Jury

Mme. Brigitte BACROIX, Directeur de recherche CNRS, LSPM, Université Paris 13	Président
M. Laurent DELANNAY, Professeur, iMMC, Université catholique de Louvain	Rapporteur
M. Frank MONTHEILLET, Directeur de recherche CNRS, SMS, ENSM-SE	Rapporteur
M. Rémy BESNARD, Ingénieur de recherche, CEA Valduc	Examinateur
M. Roland LOGE, Directeur de recherche CNRS, CEMEF, Mines ParisTech	Examinateur
M. Marc BERNACKI, Chargé de recherche, HDR, CEMEF, Mines ParisTech	Examinateur

T H È S E

MINES ParisTech
CEMEF UMR CNRS 7635
1, rue Claude Daunesse - BP207
06904 Sophia Antipolis Cedex - France
~~~

Acknowledgments

First of all, I would like to convey my deepest gratitude to my advisors Marc Bernacki and Roland Loge. I am very grateful for their help and their support. I appreciate all their contribution, ideas and remarks. Thanks to their wise advices and requirement level, my three years here in CEMEF were scientifically and personally enriching. It is important to mention Javier Signorelli and Laurent Delannay. Without their advices I would not be able to reach all the results presented in this work. Finally, I want to thank Nathalie Bozzolo for the scientific and personal conversations we had during this period.

I would also like to express my gratitude to all CEMEF staff, Goup EII and everyone from "support informatique". Special thanks go to Patrick Coels and Marie-Françoise Guenegan for their motivation and help and to the directors Yvan Chastel and Elisabeth Massoni.

I am also grateful for all my friends in CEMEF, Rebecca, Ugo, Fadi, Koffi, Andrea, Michel, Olivier, Tommy, Alexis, Karim, Ala, Christophe, Takao, Alejandro, Ke, Sira, Oscar. Life in CEMEF would not be so pleasant without them. Special thanks for Sebastian and Yuan, my two "colocs de bureau". It was a great pleasure to share with you my day by day life during these three years. At last, but not least, to Siham, a great friend that I found here. Without her support it would be more difficult to face all the challenges encountered during this thesis.

During these three years I also found good friends outside CEMEF whose support was essential during these three years. Stephanie, Fabrice, Eléonore, Mikolay, Benjamin, Nicolas, Angelo, Ashutosh, Michele, Romain, Silvia, Hue, Sara, Leo, Josette and Raymond. Special thanks for Amir and his patience to read my report. Thanks Ludo for everything. I will never forget the great moments we all spent together.

I could not fail to mention my Brazilian friends. Even though we are far from each other, I always knew that I could count on you. Silas, Vitor, Paulão, Taina, Carlinha, Diguinho, Gustavo, Bruno, Vini, Raphael, Carol, Lucas, André, David, Daniel, Steil. Thank you for your friendship!

Finally, I would like to thank my family, especially my parents for everything they have given me and all they give me every day. Thank you for your confidence, for your advices, for being there every time I needed you. Also, I want to thank my brothers and may "fake uncle" Tio Marcão.

Table of contents

General Introduction 5

1 - Constitutive Behaviour of Polycrystalline Aggregates 12
1 Introduction 13
2 Crystal Plasticity 14
2.1 Characteristics of deformed microstructure 15
2.2 Components of a single crystal model 18
2.3 Hardening 19
2.3.1 Hardening laws without size effects 20
2.3.2 Hardening laws including size effects 22
3 Single Crystal Model 31
3.1 Formulation 31
3.1.1 Elastic-Viscoplastic Formulation 31
3.1.2 Flow rule and hardening law 34
3.2 Time Integration Scheme of the constitutive law 34
4 Finite Element Formulation 36
4.1 Balance laws 36
4.2. Variational formulation 37
4.3 Time discretization 38
4.4 Spatial discretization 38
4.4.1 The MINI-element 39
4.4.2 The discrete problem 40
5 Resolution 42
5.1 Non-linear system of equation to be solved 42
5.2 Resolution of the non-linear system 43
5.3 General solution procedure and numerical implementation 44
6 Conclusion 45

2 - Statistical generation of polycrystals in a finite element context and a level-set framework – Method and results 47
1 Introduction 48
2 Voronoï and Laguerre Voronoï tessellations 49
3 Microstructure immersion in FE Mesh 52
4 Microstructure Generation - Results 55
4.1 Obeying a grain size distribution in 2D microstructures 56
4.1.1 Voronoï Tessellation Method 56
4.1.2 Laguerre-Voronoï Tessellation Method 59
4.2 Obeying a grain size distribution in 3D microstructures 63
4.2.1 Voronoï Tessellation Method 64
4.2.2 Laguerre-Voronoï Tessellation Method 65
4.3 Topological study of 2D Laguerre-Voronoï microstructures 67
4.4 Morphological study of Laguerre-Voronoï microstructures 71
5 Conclusion 76

3- Deformation behaviour of 304L steel polycrystal and tantalum olygocrystal 78
1 Introduction 79
2 304L Steel Case 79

2.1 304L stainless steel 79
2.1.1 Chemical composition 79
2.1.2 Mechanical behaviour 80
2.1.3 Microstructural characterization - initial state 82
2.2 Planar compression test (Channel Die test) 84
2.2.1 Description of the test 84
2.2.2 Material parameters - 304L 85
2.3 Effects of mesh type in highly resolved polycrystalline simulations 89
2.3.1 Considering only SSDs 89
2.3.2 Considering both SSDs and GNDs 90
2.4 Results 92
2.4.1 Stress - Strain analysis 92
2.4.2 Dislocations density and energy distribution analysis 93
2.4.3 Strain distribution analysis 99
2.4.4 Grain size effects 101
3 Tantalum Case 102
3.1 Tantalum 102
3.2 Compression test 103
3.2.1 Test description 103
3.2.2 Digital oligocrystal 103
3.2.3 Material parameters 104
3.3 Results 105
3.3.1 Sample shape 105
3.3.2 Dislocations density distribution 106
3.3.3 Deformation distribution 111
3.3.4 Texture analysis 115
4 Conclusion 118

4- Grain Boundary Migration - Grain Growth Modelling 120
1 Introduction 121
2 Context and Equations 121
2.1 Full Field modelling of grain growth assuming isotropic grain boundary energy and mobility 121
2.2 The equations 123
2.2.1 Mobility 123
2.2.2 The grain boundary energy 124
3 Finite element model in a level set framework 127
3.1 Velocity field expression 127
3.2 Numerical treatment for multi-junctions 128
3.3 Container level set functions 129
3.4 Grain growth algorithm 130
4 Results 130
4.1 Academic Test - Circular grain case 130
4.2 Academic test - 3 grains case 132
4.3 Von Neumann-Mullins cases 133
4.4 304L - 2D polycrystal grain growth 136
4.5 Influence of the microstructure generation method on grain growth prediction 139
5 Assessment of simplified 2D grain growth models from numerical experiments based on a level set framework 141
5.1 Grain size distributions 142

5.2 Burke and Turnbull study 147
5.3 Hillert/Abbruzzese model study 150
6 Conclusion 154

5- Grain Boundary Migration - Static Recrystallization 157
1 Introduction 158
1.1 Static recrystallization 158
1.1.1 Nucleation mechanisms 159
1.1.2 Nuclei growth 162
1.3 The Johnson-Mahl-Avrami-Kolmogorov (JMAK) model 163
1.4 304L steel static recrystallization 164
1.4.1 Strain level effect 164
1.4.2 Temperature and strain rate effects 164
1.5 Recrystallization simulations using a full field formulation 166
2 Finite element model and level set framework 167
2.1 Velocity field expression 167
2.2 Recrystallization algorithm 168
3 Results 169
3.1 Academic Test - Circular grain case 169
3.2 Academic Test – 2 grains case 171
3.3 Polycrystalline 2D simulation 173
3.3.1 Random nucleation sites 173
3.3.2 Necklace-type nucleation sites 177
4 Coupling crystal plasticity and static recrystallization 182
4.1 Critical dislocation density and nucleus radius 182
4.2 Number of nucleation sites 183
4.3 Coupling with crystal plasticity results 184
4.4 3D recrystallization kinetics results in site saturated nucleation conditions 187
5 Conclusion 191

Conclusions and future work 193

References 197

Appendix 207

General Introduction

Aims

Metallic materials exhibit a crystalline structure and are in essence heterogeneous materials. They are in fact polycrystals, each crystal presenting a continuous lattice orientation. All mechanical and functional properties of metals are strongly related to their microstructures, which are themselves inherited from thermal and mechanical processing. In a general view, the physical phenomenon induced by the thermo-mechanical processes generates complex microstructure changes and these microstructure evolutions modify the material properties. Thus, the understanding and modelling of these microstructure evolutions during thermo-mechanical processes are of prime importance concerning the prediction and the control of the material mechanical properties. In this work, the addressed relevant physical phenomena are recovery, recrystallization and grain growth. Microstructural transformations such as phase transformation or particles precipitation will not be discussed.

The term recovery refers to changes in a deformed material which occur prior to recrystallization and which partially restore the material properties to their values before deformation. It is known that recovery is primarily due to modifications in the dislocations structure of the material. A part of the existing dislocations will be annihilated while the others are reorganised. Normally, the dislocations reorganize themselves into cells. Dislocation recovery corresponds to a series of events which are schematically illustrated in figure I.1.

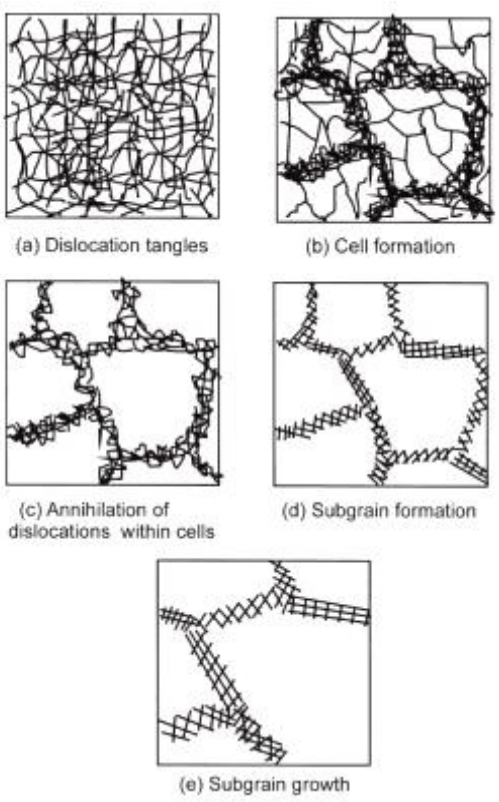

Figure I.1: *Various stages in the recovery of a plastically deformed material [Humphreys, 2004].*

Whether any or all of these stages occur during the annealing of a particular specimen will depend on a important number of parameters, including the material purity, strain, deformation and annealing temperature. A review of the intensive work done concerning the recovery of deformed metals can be found in [Beck, 1954], [Bever, 1957], [Titchener, 1958] and [Nes, 1995].

The recrystallization process involves the formation of new strain-free grains in certain parts of the material and the subsequent growth of these to consume the deformed microstructure. The location where these new grains will be formed depends on the material microstructure before plastic deformation. It is convenient to divide the recrystallization process into two regimes: nucleation which corresponds to the first appearance of new grains in the microstructure, and growth during which the new grains replace the deformed material.

The progress of recrystallization with time is commonly represented by a plot of the volume fraction of material recrystallized (X) as a function of time. This plot usually has a characteristic sigmoidal form. Figure I.2 illustrates static recrystallization steps.

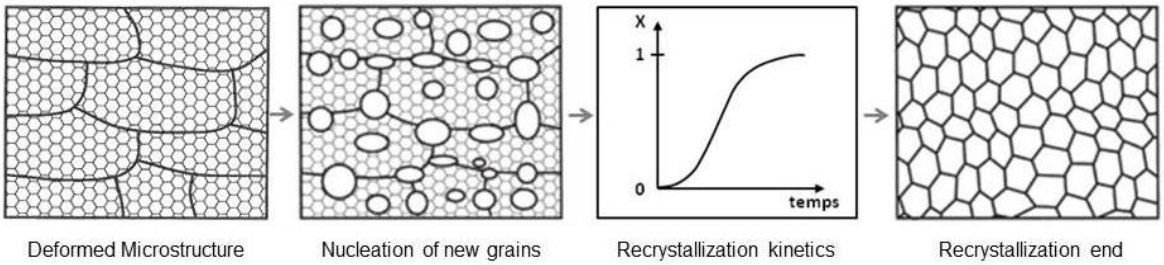

Figure I.2: *Static recrystallization scheme [images from Humphreys, 2004].*

The grain boundary motion driving forces are the internal energy difference stored during plastic deformation (in the form of crystallographic defects, especially dislocations) between two adjoint areas (recrystallization phenomenon) and the reduction in the energy which is stored in the form of grain boundaries (grain growth phenomenon). In [Doherty, 1997] and [Rios, 2005], the authors present a complete review of the recrystallization process.

Recovery, recrystallization and grain growth processes can occur statically (after plastic deformation), or dynamically (during plastic deformation). The way these phenomena will occur is based on the material properties and the processing conditions (temperature and strain rate).

Grain growth is a phenomenon occurring during and after a polycrystal full recrystallization and has the effect of increasing the average grain size at the expense of smaller ones that will tend to disappear. The grain growth kinetics is slower than the recrystallization kinetics. The grain growth driving force is the reduction in the material energy stored in the form of grain boundaries. Figure I.3 illustrates the grain growth phenomenon.

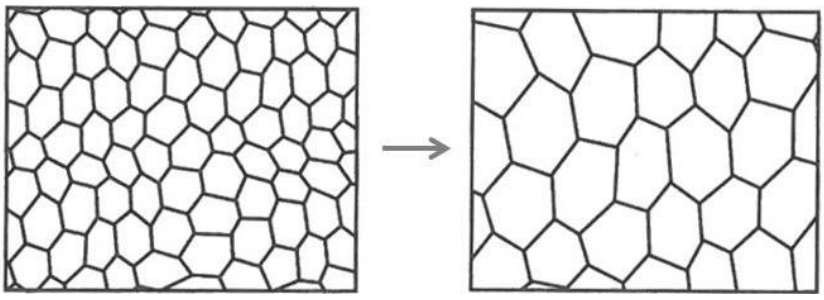

Figure I.3: *Grain growth scheme [images from Humphreys, 2004].*

Although recrystallization often precedes grain growth, it is of course not a necessary precursor. The theoretical basis for understanding grain growth was laid in [Smith, 1948], [Smith, 1952], [Burke, 1952], [Hillert, 1965].

It is interesting to highlight that materials processing, including recrystallization and grain growth, is affected by the grain boundary properties. A grain boundary separates two

regions of the same crystal structure but of different orientation. The grain boundary is made of many crystal lattice defects (like dislocations and vacancies) with a thickness of a few atomic layers (figure I.4).

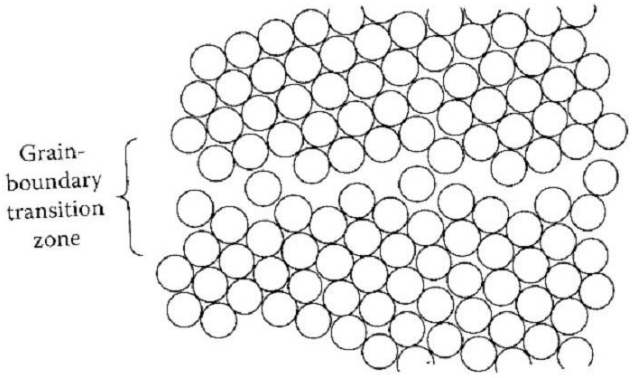

Figure I.4: *Scheme of a disordered grain boundary structure [Porter, 2008].*

The nature of any given boundary depends on the misorientation of the two adjoining grains and of the orientation of the boundary plane relative to them. The lattices of two grains can be made to coincide by rotating one of them through a suitable angle about a single axis. In general the axis of rotation will not be simply oriented with respect to either grain or the grain boundary plane. However, there are two special types of boundary that are relatively simple: pure tilt and pure twist (figure I.5). The difference between these two simple boundaries is related to the rotation axis direction relative to the grain boundary. The first grain boundary type, the tilt boundary, occurs when the axis of rotation is parallel to the grain boundary plane while a twist boundary is formed when the rotation axis is perpendicular to the grain boundary.

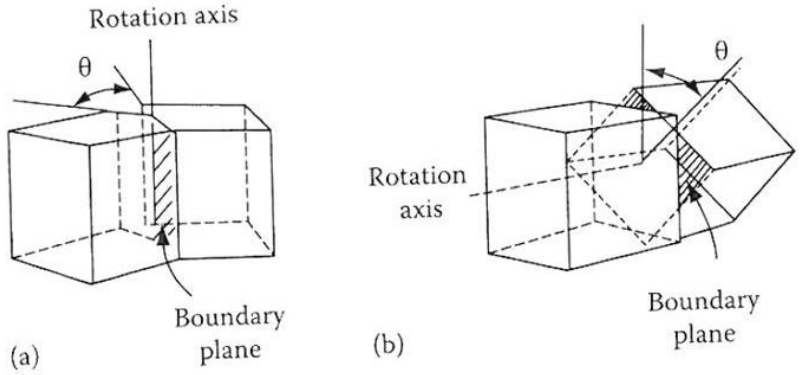

Figure I.5: *The relative orientation of the crystals and the boundary forming (a) a tilt boundary and (b) a twist boundary [Porter, 2008].*

Another convenient classification of grain boundaries is related to their misorientation. The first group corresponds to the grain boundaries whose misorientation is greater than a certain critical angle - high angle grain boundaries, and the second corresponds to those whose misorientation is smaller than this critical angle - low angle grain boundaries. The critical angle at which the transition from low to high angle boundaries occurs is typically taken between 10° and 15° for cubic materials. The difference in structure between low angle and high angle grains boundaries is illustrated by the bubble-raft model in figure I.6.

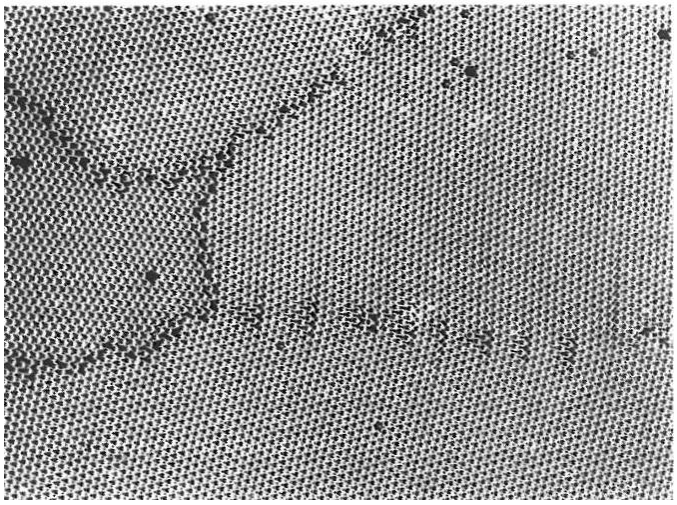

Figure I.6: *Raft of soap bubbles showing several grains varying misorientation. Note that the boundary with the smallest misorientation is made up of a row of dislocations, whereas the high angle boundaries have a disordered structure in which individual dislocations cannot be identified [Shewmon, 1969].*

High angle boundaries contain large areas of poor fit and have a relatively open structure. The bonds between the atoms are broken or highly distorted. In low angle boundaries most of the atoms fit very well into both lattices. Normally this boundary is formed by a few aligned dislocations. As a consequence, the lattice presents a very little free volume and the interatomic bonds are lightly distorted.

Thus, a precise prediction of grain boundary motion remains also dependent of a precise description of the grain boundary physical properties according to its nature and to the thermal state.

Finally, as already underlined, during a deformation, the microstructure of a metal changes in several ways, but, the most important change for grain boundary motion is the accumulation of dislocations. The stored dislocations are the main defects responsible for the internal energy increasing during plastic deformation. The sum of the energy of all dislocations represents the deformation stored energy. Knowing that every stage of the annealing process involves loss of some of the stored energy, the correct prediction of the stored energy after deformation is essential to correctly predict the microstructure evolution during annealing treatments.

The objective of this Ph.D. thesis is the development of a numerical model able to predict microstructure evolution, including the material hardening, recrystallization and grain growth at the mesoscopic scale. The motivation behind the modelling of polycrystalline metallic material evolutions during thermo-mechanical treatments at this scale are:

- from a technological point of view, assist the design of thermomechanical processes by taking into consideration microstructural features, such as crystallographic orientations, in order to account for macroscopic anisotropic behaviour,
- the use of full field models, as the one presented in this work, allows the verification and the improvement of models which were developed based on theoretical assumptions which are not easily verified experimentally (mean field models),
- from a more fundamental point of view, increase our understanding of the mechanisms operating at the microstructural scale.

Framework and layout of this thesis

Even if the scope of the present work seems rather fundamental, the development of more accurate numerical models for the grain size predictions in metals during thermomechanical treatments is nowadays of prime importance in order to conform to increasingly tighter standards without excessive development costs, mainly in the nuclear and aeronautic domains. This observation seems perfectly illustrated by the fact that the present work, dedicated to models of polycristalline structures, was supported by an industrial consortium involving five partners. Indeed, this PhD thesis was conducted as a part of the MicroPro project which gathers the following partners:

- ArcelorMittal/Industeel (www.industeel.info): hot rolled metallic plates producer.
- Areva/Sfarsteel (www.areva.com): world-leading company in nuclear energy.
- Ascometal (www.ascometal.fr): special steels pieces producer.
- Aubert et Duval (www.aubertduval.fr): special steels pieces producer.
- CEA (www.cea.fr): nuclear power applications developer.

The manuscript is organized as follows: the first chapter presents a review of crystal plasticity and work hardening models existing in the literature. Also, a detailed description of the crystal plasticity model used during this Ph.D. thesis is presented. Two different hardening laws are presented and discussed. The first one does not take into account the size effects, contrary to the second one. The finite element implementation associated to the model with an implicit integration is exposed. After presenting the crystal plasticity models, the digital microstructure statistical generation together with the grain boundary description method are presented in chapter 2. Two different digital microstructure generation methods are discussed and tested in order to statistically obey the features of the considered microstructures: the Voronoï, and the Laguerre-Voronoï methods. The grain boundary description is performed with an implicit method capturing the grain interfaces and immerging them in a finite element mesh [Bernacki, 2009]. This method is based on a level-set approach allowing to define the different interfaces and to perform meshing adaptation. In chapter 3, crystal plasticity numerical results are presented and discussed. Two different test cases are used in order to validate the hardening laws implemented in the crystal plasticity model. The first one corresponds to a planar compression test (channel die test) on a 304L steel polycrystal. The second one corresponds to a simple compression test on a tantalum olygocrystal composed of six different grains. After presenting the crystal plasticity simulations results, an extension of the model developed in [Bernacki, 2008], [Bernacki, 2009] and [Logé, 2008] concerning the modelling of grain boundary migration in a full field context is proposed. In chapter 4, the addition of the grain growth phenomenon by capillarity to the full field model is detailed. A few academic tests are presented in order to validate the proposed grain growth algorithm, and this is followed by a 2D study of polycrystalline grain growth. Full field predictions are compared to those of different grain growth mean field models, and conclusions are drawn on the applicability of the latter. Finally, in chapter 5, static recrystallization is investigated. A first study analysing the influence of the capillarity effects during the recrystallization process is presented and, in a second part, the static recrystallization model is coupled to the crystal plasticity model detailed in the first chapter. Comparisons between experimental results on

304L steel and the numerical predictions obtained with the proposed new formalism are discussed.

All the developments and calculations of this PhD thesis were performed with CimLib, a C++ finite element library developed at CEMEF [Digonnet, 2007].

The work involved in this PhD thesis has contributed to the following written communications:

- A.L. Cruz-Fabiano, R. Logé and M. Bernacki, *Assessment of simplified 2D grain growth models from numerical experiments based on a level set framework*, submitted to Modeling and Simulation in Materials Science and Engineering in 2013.

and to the following oral communications:

- M. Bernacki, K. Hitti, A.L. Cruz-Fabiano, A. Agnoli, R. Logé, *Génération statistique de VERs et modélisation EF d'évolutions microstructurales*, Journées thématiques MECAMAT, 10-11 Mai 2011, CEMEF, Sophia-Antipolis.
- A.L. Cruz-Fabiano, R. Logé, M. Bernacki, *Modelling of static and dynamic recrystallization processes at the mesoscopic scale in 304L stainless steel*, Journées thématiques MECAMAT, 10-11 Mai 2011, CEMEF, Sophia-Antipolis.
- A.L. Cruz-Fabiano, R. Logé, M. Bernacki, *Comparison between different simplified grain growth models using "full field" modelling method results*, ECCOMAS 2012, Vienna, Austria, September 10-14, 2012
- A.L. Cruz-Fabiano, R. Logé, M. Bernacki, I. Poitrault, M. Teaca, A. Gingell, F. Perdriset, E. Guyot, *Modèles de recristallisation et de croissance de grains de l'acier inoxydable 304L et applications industrielles*, Journée "Aciers inoxydables et Industrie Nucléaire, dernières avancées", SF2M, 16 Mai 2013, Saint Etienne.
- M. Bernacki, N. Bozzolo, R. Logé, Y. Jin, A. Agnoli, A.L. Cruz-Fabiano, A.D. Rollett, G.S. Rohrer, J.-M. Franchet, J. Laigo, *Full field modelling of recrystallization in superalloys thanks to level-set method*, EUROSUPERALLOY 2014, Giens, France, May 13-16, 2014.

Résumé français

Ce chapitre constitue l'introduction de cette thèse. Les objectifs de ce travail de thèse ainsi que les concepts généraux de joints de grains, restauration, recristallisation et croissance des grains y sont présentés. Finalement, l'organisation de ce manuscrit de thèse est détaillée et les contributions liées à ces travaux de thèse sont énumérées.

Chapter 1

Constitutive Behaviour of Polycrystalline Aggregates

Contents

1 Introduction 13
2 Crystal Plasticity 14
2.1 Characteristics of deformed microstructure 15
2.2 Components of a single crystal model 18
2.3 Hardening 19
2.3.1 Hardening laws without size effects 20
2.3.2 Hardening laws including size effects 22
3 Single Crystal Model 31
3.1 Formulation 31
3.1.1 Elastic-Viscoplastic Formulation 31
3.1.2 Flow rule and hardening law 34
3.2 Time Integration Scheme of the constitutive law 34
4 Finite Element Formulation 36
4.1 Balance laws 36
4.2 Variational formulation 37
4.3 Time discretization 38
4.4 Spatial discretization 38
4.4.1 The MINI-element 39
4.4.2 The discrete problem 40
5 Resolution 42
5.1 Non linear system of equation to be solved 42
5.2 Resolution of the non linear system 43
5.3 General solution procedure and numerical implementation 44
6 Conclusion 45

1 Introduction

As it was discussed in the General Introduction, the main objective of this Ph.D. thesis is the development of a numerical model able to predict microstructure evolution, including the material hardening, recrystallization and grain growth at the mesoscopic scale. These microstructural evolutions are not independent from each other. In a simple way, one can say that recrystallization processes depend on the nature of the deformed state, especially the dislocation density distribution and the crystallographic misorientations. The material state after plastic deformation depends itself on the deformation process (rolling, wire drawing, extrusion, compression, tension, torsion, shear, etc.) and on the type of material. Both aspects play an important role in the recrystallization kinetics taking place during or after plastic deformation. At the same time, grain growth kinetics is linked to the grain size distribution after total recrystallization. Since these phenomena are linked to each other, a first step of an accurate modelling of recrystallization and grain growth involves the correct prediction of the microstructural heterogeneities developed during plastic deformation. So, in this work, some of the phenomena involved in plastic deformation of metals are considered, in order to predict important features of a final deformed state.

The simulation of the microstructure transformation during plastic deformation is not a simple problem. Numerous models have been developed to describe the microstructure evolution taking into account the material texture and the influence of the neighbouring grains (crystal plasticity models). In [Resk, 2010], the author presents an interesting review of several models. Here, only the main approaches are described.

One of the first models proposed to take the texture into account was proposed by Taylor [Taylor, 1938]. This model, also known as full-constrained model, is still used in order to study the constitutive response of polycrystalline materials due to its low numerical cost. However, since this model assumes that all grains deform in the exact same manner as the polycrystal, violating the stress equilibrium, the interaction between neighbouring grains are not taken into account and, as a result, this model is not able to describe the features of the deformed state. Anyhow, in large scale applications, texture-induced anisotropy is fairly well predicted [Marin, 1998a], especially for materials presenting a high degree of crystal symmetry (like cubic crystals) and subjected to strains well beyond the elastic limit.

To improve the prediction of polycrystalline deformation behaviour, other models such as relaxed-constraint [Honeff, 1981], [Kocks, 1982] and multi-grains-relaxed-constraint models [Van Houtte, 2002], [Van Houtte, 2005] have been developed. Relaxed-constraint models satisfy selected compatibility relations and ignore some intergranular equilibrium components. In other words, these models are based on the idea of freeing some degrees of freedom of each grain in order to improve textures predictions. One of the main conceptual faults of these relaxed-constraint models is the fact that the volume average of the velocity gradients over the whole polycrystal might not be equal to the macroscopic one.

As opposed to the Taylor model, the self-consistent models satisfy both compatibility and equilibrium between grains in an average sense [Eshelby, 1957]. In [Eshelby, 1957] the authors considered the problem of determining the stress and strain in an elastic ellipsoidal inclusion surrounded by an unbounded elastic medium. The particle and the medium present the same properties. When dealing with polycrystalline materials, each grain is considered as an inclusion embedded in a polycrystalline medium composed of all other grains. The medium behaviour is determined by considering different representative grains. These grains represent all other grains having the same crystallographic orientation. Finally, the overall behaviour is computed as the average response of the representative grains. Later on, the model was extended to elastic-plastic behaviour [Berveiller, 1979], [Hill, 1965], and to viscoplastic behaviour [Hutchinson, 1976], [Lebensohn, 1993], [Molinari, 1987].

Both Taylor type and self-consistent models assume that individual grains deform homogeneously. As a consequence, it is not possible to predict the exact positions of nucleation sites during recrystallization. In order to capture the intragranular heterogeneities developed during plastic deformation, two methods can be used.

The first one is the finite element method. With this method, both intra and intergranular heterogeneities can be computed. The constitutive response of each finite element integration point is determined using the single crystal constitutive model. The main advantage of finite element models compared to the other polycrystal plasticity models is that morphological effects (grain size, shape and topology) can be taken into account.

The second one is the fast Fourier transform (FFT). This method has been used to describe the mechanical behaviour of polycrystalline aggregates with periodic boundary conditions for elastic deformations [Brenner, 2009] and for rigid-viscoplastic conditions [Lebensohn, 2001], [Lebensohn, 2008], [Lee, 2011]. In [Lebensohn, 2001], the authors showed that the FFT method is numerically less expensive than the finite element method for problems of the same size. However, the need of periodic boundary conditions and of regular grids that cannot be adapted during the simulation represent the model principal limits.

Concerning the crystal plasticity simulations, the work presented in this report is a continuation of the work developed by H. Resk [Resk, 2010] during her Ph.D. thesis at CEMEF. The main objective of her Ph.D. project was the development of a crystal plasticity finite element model (CPFEM) and its implementation within the CimLib library. The hardening model considered during her Ph.D. thesis was a Voce type saturation law, a model where the dislocation density is implicitly represented. During the present Ph.D. thesis, due to the interest in modelling recrystallization processes based on crystal plasticity simulation results, the explicit computation of dislocation densities was adopted, i.e. dislocation densities were internal variables of hardening laws. Two kinds of hardening models are studied: the first one does not consider grain size effects, while the second one does. When size effects are considered, two kinds of dislocation density are taken into account: the statistically stored dislocations (SSDs) and the geometrically necessary dislocations (GNDs).

In this chapter, a bibliographic review of the crystal plasticity theory is presented. Different hardening laws that can be found in the literature are highlighted, and the differences between the two dislocation types (SSDs and GNDs) are discussed. In a second part, the single crystal plasticity model implemented in the CimLib library is presented and finally, the finite element implementation of the above constitutive laws is detailed, in the context of an implicit integration.

2 Crystal Plasticity

In crystal plasticity theory, the material plastic deformation is modelled using the slip system activity concept. Dislocations are assumed to move across the crystal lattice along specific slip systems, which are characterized by specific crystallographic planes and directions. When the material is subjected to loading, the applied stress resolved along the slip direction on the slip plane initiates and controls the extent of dislocation glide. This latter has the effect of shearing the material whereas the material volume remains unchanged and the crystal lattice remains constant. Moreover, the crystal lattice can deform elastically. However, elastic strains are small compared to plastic strains and are sometimes neglected in crystal plasticity models. Finally, the crystal lattice can also rotate to accommodate the applied loading. This lattice rotation (or spin), is responsible for texture development. The concept of lattice rotation in crystal plasticity is not, at first hand, easy to grasp, especially compared to material rotation (or rigid body rotation). In [Peeters, 2001], the authors illustrate well this fundamental difference with Figure 1.1.

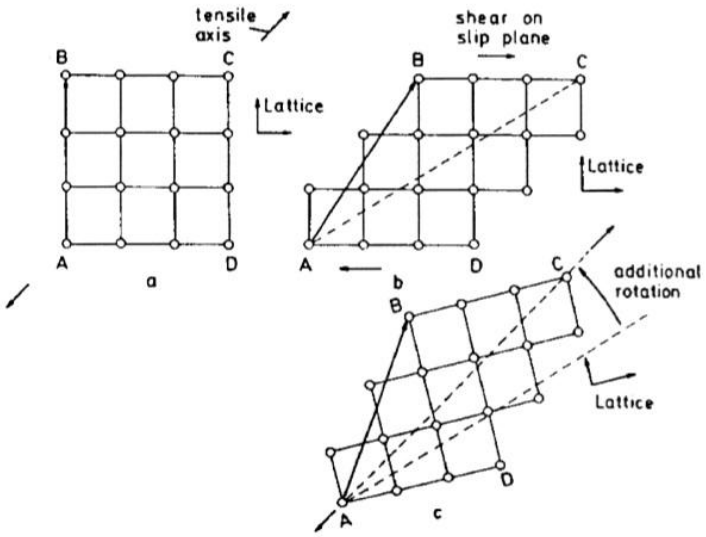

Figure 1.1: *"(a) and (b) A shear γ on a slip plane does not cause the lattice to rotate, although a material vector may rotate; (b) and (c) An additional rotation - which also causes the crystal lattice to rotate - will bring the crystal in a position corresponding to the strain forced upon it: e.g. pure elongation in the direction AC" [Peeters, 2001].*

Normally, dislocation slip takes place on most densely packed planes and directions. In the case of FCC metals (like the 304L austenitic steels), slip occurs in {111} planes and <110> directions. Therefore, crystallographic slip is assumed to occur on the 12 octahedral {111}<110> slip systems. These considerations form the basis of classical crystal plasticity theory. Other modes of deformation in polycrystals, like twinning or grain boundary sliding, are neglected in this discussion.

2.1 Characteristics of deformed microstructure

As it was discussed in the General Introduction, the material microstructure after plastic deformation plays an important role in recovery, recrystallization and grain growth phenomena. In this paragraph, a brief review of the microstructure changes suffered by the material during thermo-mechanical process is presented.

When polycrystalline materials, with an assumed random crystallographic texture, plastically deform, deformation is essentially heterogeneous even under simplified condition. This is a consequence of the interaction between neighbouring grains leading to the formation of complex microstructures. During the material deformation, its microstructure changes in diverse ways. First, the grains shape changes and, often, an increase in the total grain boundary area takes place. The new grain boundary areas are created during deformation by the incorporation of some of the dislocations that are continuously created. The rate of increase of grain boundary area per unit volume depends on the mode of deformation. Figure 1.2 illustrates the calculated increase in the grain boundary area as a function of strain for several deformation modes.

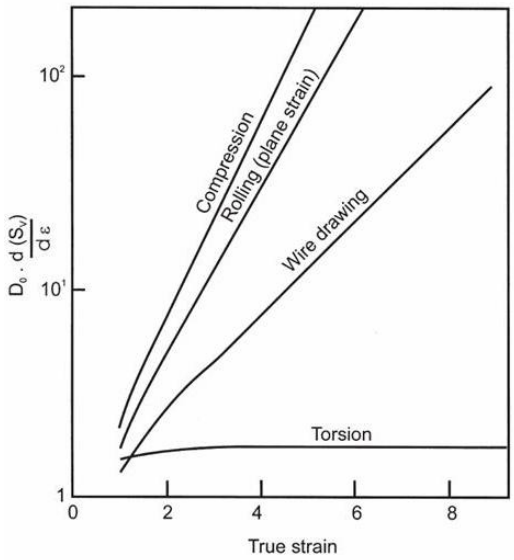

Figure 1.2: *Rate of growth of grain boundary area per unit volume (S_v) for different modes of deformation assuming an initial cubic grain size D_0, [Humphreys, 2004].*

Nucleation of new grains normally occurs on the areas near the grain boundaries. As a consequence, the increase in the grain boundary surface may impact the nucleation of new grains during recrystallization.

A second main microstructural change is the appearance of an internal structure within the grains. Once again, this material change is a result of the accumulation of dislocations during plastic deformation. Figure 1.3 summarises the main features of the deformed state according to their length scale.

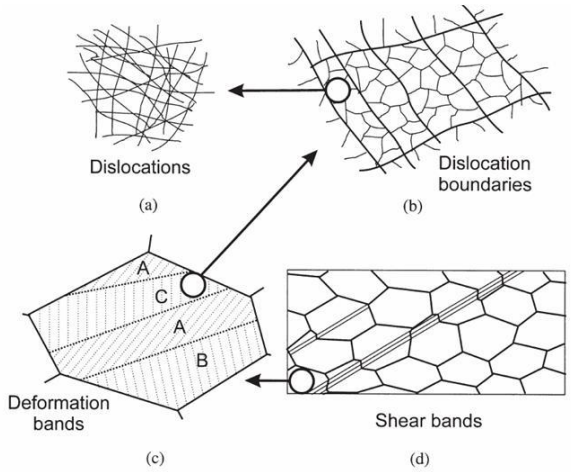

Figure 1.3: *The hierarchy of microstructure in polycrystalline metal deforming by slip. The various features are shown at increasing scales: (a) dislocations, (b) dislocation boundaries, (c) deformation and transition bands within a grain, (d) specimen and grain scale shear bands. [Humphreys, 2004].*

Shear bands (Figure 1.4a) are non-crystallographic in nature and may pass through several grains. They are a result of plastic instability and it can be compared to the 'necking' occurring in a tensile test. Deformation or transition bands (Figure 1.4b) are the consequence of subdivision within grains into regions of different orientations. This is a consequence of either heterogeneous stress transmitted by neighbouring grains or the intrinsic instability of the grains during plastic deformation. At lower scale, the deformed polycrystalline aggregate is made of cells or sub-grains (Figure 1.4c and 1.5b). These cells are essentially low angle

grain boundaries which subdivide the grain, producing heterogeneities inside the different grains. This is a consequence of having non homogeneous dislocations distributions. Each cell boundary contains a rich density of entangled dislocations and the cells bulk areas are almost dislocation free. Finally, dislocations can also exist in random structures (Figure 1.5a and 1.5c), especially after low strains. In metals which do not form cells, such diffuse arrangements of dislocations are found even after large strains.

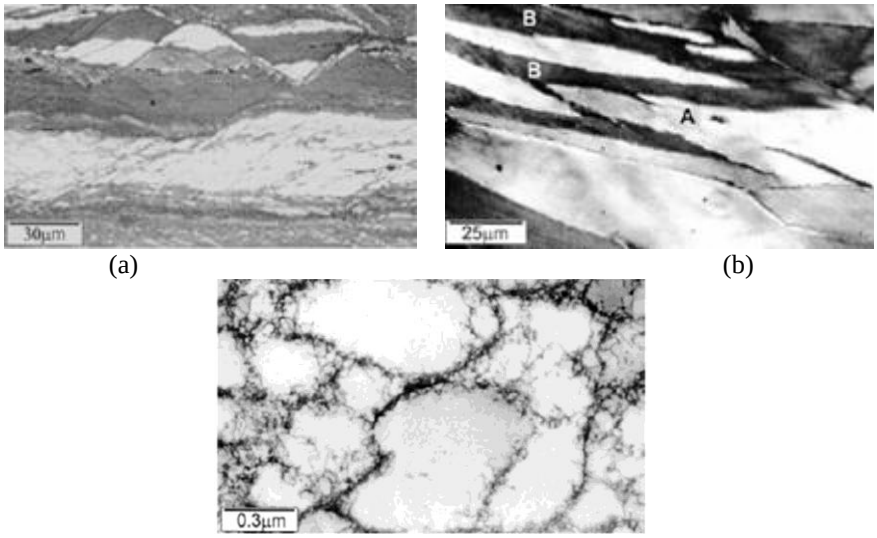

(a) (b)

(c)

Figure 1.4: *(a) Shear bands in Al–Zn–Mg alloy cold rolled 90%, (b) deformation bands (B) in a grain (A) in Al-1%Mg, (c) cell structure in 25% cold rolled copper. [Humphreys, 2004].*

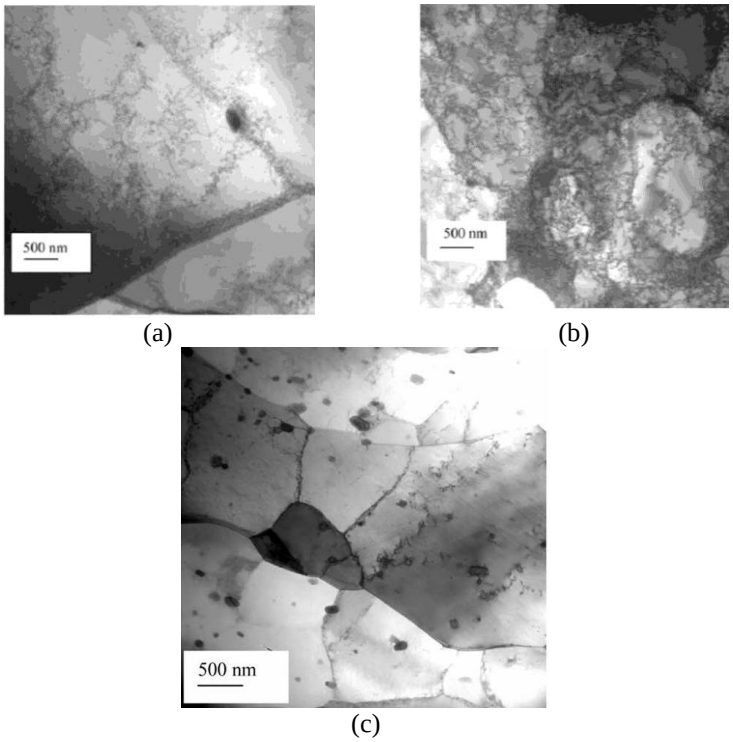

(a) (b)

(c)

Figure 1.5: *TEM bright field images of an Al alloy (5005) deformed at (a) 2% and (b) 10% and of another Al alloy (3003) deformed at 2%.(c) [Trivedi, 2004].*

Finally, during deformation the crystallographic orientations change relative to the direction(s) of the applied stress(es). These changes are not random and involve rotations which are related to the crystallography of the deformation (as discussed in the introduction of

section 2). As a consequence the grains acquire a preferred orientation (texture), which becomes stronger as deformation proceeds.

Since annealing processes (recovery, recrystallization and grain growth) involve the loss of some of the energy stored in the material during plastic deformation, first of all, the material microstructure induced by plastic deformation must be correctly characterized and/or modelled.

2.2 Components of a single crystal model

In order to account for the mechanics of grain structure heterogeneous deformation, crystal plasticity models are based on microstructural variables such as crystallographic orientations and dislocation densities. Polycrystal models are based on single crystal models as illustrated in Figure 1.6.

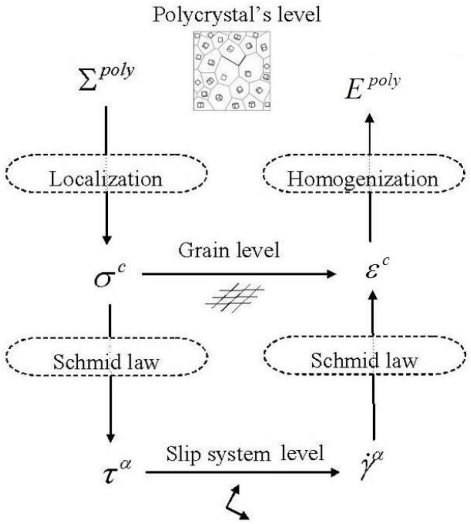

Figure 1.6: *From polycrystal level to slip system level [Resk, 2010].*

In Figure 1.6, Σ^{poly} corresponds to the macroscopic stress applied on the material. Using continuum mechanics, we are able to compute the local stress σ^c and, using crystal plasticity theory, we compute the critical resolved shear stress (CRSS) τ^α for slip system α. Once the CRSS value is known, the dislocation slip rate $\dot{\gamma}^\alpha$ is computed and, based on the dislocation slip rate, we are able to compute the local strain (ε^c). Finally, based on the computed ε^c, the macroscopic strain is calculated (E^{poly}).

Three components are needed in order to describe the mechanical behaviour of a single crystal. The first one is a kinematic framework describing the motion of the single crystal. Generally, the kinematic decomposition used in crystal plasticity is the multiplicative decomposition (originally developed by [Bilby, 1957], [Kröner, 1971], [Lee, 1967] and [Lee, 1969]) as opposed to an additive decomposition [Shabana, 2008] which is normally used for small deformations. In classical plasticity theory, if elastic behaviour is considered, the decomposition is composed of a plastic and an elastic term.

Secondly, an elastic relation describing the elastic behaviour depending on the crystal structure of the material is needed. Elastic strains are small compared to plastic ones but are sometimes important to consider if the aim of the simulations is to compute residual stress [Marin, 1988a]. The assumption of small elastic strains enables nevertheless simplifications in the governing equations [Marin, 1988b]. In others applications where elasticity is not of concern, the elastic behaviour is neglected [Beaudoin, 1995].

Finally, the evolution rules for the intragranular variables of the model, flow rule and hardening rule, need to be established. Different forms of these equations can be found in the literature. In the following, we will concentrate on viscoplastic flow rules.

In its simplest form, the viscoplastic behaviour is described by a power law, as first introduced by [Hutchinson, 1977]:

$$\dot{\gamma}_\alpha = \dot{\gamma}_0 \left| \frac{\tau_\alpha}{\tau_c^\alpha} \right|^{\frac{1}{m}} sign(\tau_\alpha) \tag{1.1}$$

where $\tau^\alpha = T : M^\alpha$ is the resolved shear stress, $\dot{\gamma}_0$ is a reference slip rate, *m* the sensitivity exponent and τ_c the CRSS for slip system α [Delannay, 2006], [Erieau, 2004], [Marin, 1988b]. A rate sensitive formulation is used here in order to avoid the non-uniqueness problem associated with the identification of the active slip systems in rate independent formulations.

2.3 Hardening

The hardening rule represents the strain-induced evolution of the material resistance to plastic deformation. This strain-induced evolution is a consequence of the increased number of dislocations present in the material during plastic deformation. Although the hardening depends on the dislocation density existing in the material, this quantity is not always used explicitly in the calculation. In [Resk, 2009], [Resk, 2010], [Logé, 2008] the authors use the Voce type saturation law in order to compute the material hardening:

$$\dot{\tau}_c = H_0 \left(\frac{\tau_{sat} - \tau_c}{\tau_{sat} - \tau_0} \right) \sum_\alpha |\dot{\gamma}_\alpha|, \tag{1.2}$$

where τ_0 and τ_{sat} are, respectively, the initial and saturation values of CRSS, H_0 is a hardening coefficient. In [Iadicola, 2012] the authors use another example of implicit hardening law. In this case, the increase of the CRSS form primary work-hardening is given by an extended Voce hardening law:

$$\tau_c = \tau_0 + (\tau_1 + \theta_1 \gamma) \left(1 - \exp\left(-\gamma \left| \frac{\theta_0}{\tau_0} \right| \right) \right), \tag{1.3}$$

where γ, $(\tau_1 + \tau_0)$, θ_0 and θ_1 are the accumulated slip (shear), the back-extrapolated CRSS, the initial hardening rate and the asymptotic hardening rate on each slip system, respectively. In this paper the authors incorporate latent hardening of multiple slip planes allowing the model to explain the decrease in flow stress when changing from equal-biaxial to uniaxial deformation.

Hardening models can be more physically-based if expressed in terms of dislocation densities and if the basic mechanisms of dislocation generation and annihilation are considered. Moreover, strain gradient concepts, which lead to size-dependent effects, can be introduced directly at the level of the hardening model. In both cases, the CRSS is often given by:

$$\tau_c = \tau_0 + \alpha\mu b\sqrt{\rho_T}\,, \tag{1.4}$$

where α is a constant, μ is the elastic shear modulus, b the Burgers vector amplitude, and ρ_T the "total" dislocation density (i.e. considering all types of dislocations). Differences arise mainly from the way of computing the evolution of one or more dislocation densities.

2.3.1 Hardening laws without size effects

In this paragraph the size effects are not taken into account, meaning that the deformation gradient in the material is no considered when calculating the dislocation densities. In other words, only the statistically stored dislocations (SSDs) are considered.

A common way of writing the dislocation evolution equation is to consider two terms, one due to hardening (+), and the other due to annealing (-):

$$\dot{\rho} = \dot{\rho}^{(+)} - \dot{\rho}^{(-)}. \tag{1.5}$$

The hardening term usually relates to Frank-Read sources of dislocations, while the annealing term is connected to the annihilation of parallel dislocations of opposite signs. An exception for this kind of presentation is the power law [Montheillet, 2009]:

$$\frac{\partial\rho}{\partial\varepsilon} = \frac{K_1}{\rho^{\nu}}\,, \tag{1.6}$$

with $\nu \geq 0$, since it leads to closed–form expressions. In this case, K_1 is a material parameter related to the material hardening. The dislocation density rate decreases with strain, even though the model does not present a specific term for the recovery.

The second hardening law is the Yoshie-Laasraoui-Jonas equation [Laasraoui, 1991]:

$$\frac{\partial\rho}{\partial\varepsilon} = K_1 - K_2\rho\,, \tag{1.7}$$

where K_1 and K_2 are two material parameters, related to the production and the annealing of dislocations, respectively. K_1 is a positive parameter so as the dislocation density increases with the increase of the plastic deformation by slip over all the slip systems. However, the increase of the number of dislocations favours on the other hand the annealing mechanism as the more dislocations, the higher the probability they come in contact to one another. This explains the $-K_2\rho$ term, with K_2 a positive parameter. In this case, stress saturation is reached when $\rho = \frac{K_1}{K_2}$.

A third widely used model is the Kocks-Mecking equation [Kocks, 1976]:

$$\frac{\partial\rho}{\partial\varepsilon} = K_1\sqrt{\rho} - K_2\rho\,. \tag{1.8}$$

Here, once again, K_1 and K_2 are two material parameters representing respectively the production and the annealing of dislocations. In this case we consider that the dislocation production also increases with the increase in dislocation density. The increase of the number of dislocations favours not only the annealing mechanism but also the creation of new

dislocations by a Frank-Read source mechanism. In this case, stress saturation is reached when $\rho = (K_1/K_2)^2$.

Finally, a more general differential equation for the material hardening can be computed [Montheillet, 2009]:

$$\frac{\partial \rho}{\partial \varepsilon} = K_1 \rho^{\xi} - K_2 \rho \,. \tag{1.9}$$

The hardening law represented by Equation 1.9, is able to represent both Yoshie-Laasraoui-Jonas ($\xi = 0$ - Equation 1.7) and Kocks-Mecking ($\xi = 1/2$ - Equation 1.8) relations. However, it is valuable to observe that any other expression can be used.

In [Estrin, 1998a], static recovery is taken into account by including an extra term to the above Kocks-Mecking equation:

$$\frac{\partial \rho}{\partial \varepsilon} = K_1 \sqrt{\rho} - K_2 \rho - \frac{r}{\dot{\varepsilon}}, \tag{1.10}$$

where

$$r = r_0 \exp\left(-\frac{U_0}{k_B T}\right) \sinh\left(\frac{\beta \sqrt{\rho}}{k_B T}\right), \tag{1.11}$$

with U_0 being the activation energy, β and r_0 constants and k_B the Boltzmann constant.

Finally, more sophisticated formulations to calculate the dislocation evolution during plastic deformation can be found in the literature. As an example, in [Roters, 2000], Roters et al. propose a model based on three different kinds of dislocations: ρ_w represents the immobile dislocations that we find in the material cell walls; ρ_i represents the immobile dislocations inside the cells, and ρ_m the mobile dislocations inside the cells. Figure 1.7 illustrates these different types of dislocations.

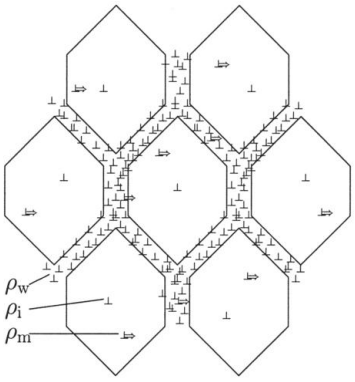

Figure 1.7: *Schematic drawing of the arrangement of the three dislocation classes considered in the three-internal variables model: mobile dislocations (ρ_m), immobile dislocations in the cell interiors (ρ_i) and immobile dislocations in the cell walls (ρ_w) [Roters, 2000].*

For each dislocation type an evolutionary equation is proposed. These equations are based on physical phenomena of generation and annihilation of dislocations. The mobile dislocations carry the plastic strain and it is assumed that the mobile dislocations density can

evolve according to three mechanisms: the formation of dislocation dipoles, the formation of dislocation locks, and annihilation. It is interesting to note that dislocation dipoles can still move, but since their motion does not contribute to the net strain, they are no longer considered in the class of mobile dislocations. Consequently, the evolution Equation 1.5 applied to mobile dislocations becomes:

$$\dot{\rho}_m = \dot{\rho}_m^+ - \dot{\rho}_m^-(\text{annihilation}) - \dot{\rho}_m^-(\text{lock}) - \dot{\rho}_m^-(\text{dipole}). \quad (1.12)$$

Considering the immobile dislocations (ρ_i), the rate of increase of the dislocation density inside the cells is equal to the decrease of the mobile dislocation due to the formation of locks ($\dot{\rho}_m^-(\text{lock})$). Since locks cannot glide, the only process to decrease the immobile dislocation density is annihilation by dislocation climb. Based on these considerations, the evolutionary equation for the immobile dislocations becomes:

$$\dot{\rho}_i = \dot{\rho}_i^+ - \dot{\rho}_i^-(\text{climb}) = \dot{\rho}_m^-(\text{lock}) - \dot{\rho}_i^-(\text{climb}). \quad (1.13)$$

The third type of dislocations concerns the immobile dislocations in the cell walls ρ_w. These dislocations undergo the same processes as those in the cell interiors, but there is one additional process, which contributes to the increase of this particular dislocation density. It can be assumed that all dislocation dipoles finally end up and accumulate in the cell walls. As dipoles are created in the whole volume, but stored only in the walls, they represent the main mechanism of ρ_w generation. As a consequence, the evolutionary equation for these dislocations is:

$$\dot{\rho}_w = \dot{\rho}_{wi}^+ - \dot{\rho}_w^-(\text{climb}) = \frac{1}{f_w}\dot{\rho}_m^-(\text{dipole}) - \dot{\rho}_w^-(\text{climb}). \quad (1.14)$$

where f_w is the volume fraction of cell walls. All terms of these different evolutionary equations are detailed with various expressions in [Roters, 2000]. In [Estrin, 1998b] Estrin proposes a similar model but considering only two dislocation types: immobile dislocations in cells walls (ρ_w) and dislocations inside the cells (ρ_c).

The difficulty when dealing with several dislocation types is related to the introduction of several material parameters which are often difficult to identify. This largely explains the success of simpler equations like those of Yoshie-Laasraoui-Jonas [Laasraoui, 1991] or Kocks-Mecking [Kocks, 1976], discussed earlier.

2.3.2 Hardening laws including size effects

When a polycrystalline material is subjected to a stress, the dislocation slip systems are activated and the material is plastically deformed. Determining which slip systems will be activated in each grain of the polycrystal depends on the grain crystallographic orientation and on the crystallographic texture of the material [Sarma, 1996], [Van Houtte, 2005]. In addition, differences in the crystallographic orientation between neighbouring grains induce a heterogeneous plastic deformation. As we can see in Figure 1.8, if each grain is caused to undergo its uniform strain, the result is the formation of overlaps in some places and voids in others. For this reason, a certain amount of dislocations must be introduced into the material in order to ensure the crystal lattice continuity.

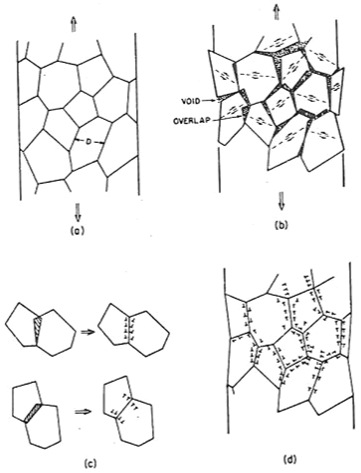

Figure 1.8: *If each grain of a polycrystal, shown at (a), deforms in a uniform manner, overlap and voids appear (b). These can be corrected by introducing geometrically necessary dislocations, as shown at (c) and (d) [Ashby, 1970].*

Several examples found in the literature illustrate the importance of these geometrically necessary dislocations in the mechanical behaviour of the material [Gerken, 2008a], [Gerken, 2008b], [Petch, 1953], [Hall, 1951], [Chen, 1998], [Papadopoulos, 1996]:

- The Hall-Patch relation [Petch, 1953], [Hall, 1951], which connects the yield strength with the grain size. The increase in the yield strength with the decrease of the grain size is explained by the presence of grain boundaries, which represent obstacles to dislocation slip. The presence of dislocations due to plastic deformation gradient has an important role explaining this phenomenon.
- the initiation and propagation of cracks across grains are highly dependent on deformation gradient effects. Chen [Chen, 1998] showed a maximum shear stress up to three times greater than that estimated with the conventional elastic-plastic fracture mechanics.
- Papadopoulos and Panoskaltsis [Papadopoulos, 1996] discussed the importance of these plastic deformation gradients for the fatigue resistance of metals.

The total density of dislocations which can be found in a slip system α is expressed as:

$$\rho_T^\alpha = \rho_S^\alpha + \rho_G^\alpha . \tag{1.15}$$

In this expression, ρ_S^α corresponds to the statistically stored dislocation density (SSD) and ρ_G^α corresponds to the geometrically necessary dislocations (GND) introduced in the model to ensure the crystal lattice continuity.

GNDs and SSDs

The concept of GNDs was first proposed by Nye [Nye, 1953] and Ashby [Ashby, 1970]. The GNDs appear in areas of strain gradient, thus ensuring the crystal lattice continuity. These regions of deformation gradients are a consequence of the existence of the geometric constraints of the crystal lattice, that is to say, inconsistencies in the crystal lattice due to the presence of non-uniform plastic deformations, [Arsenlis, 1999], [Evers, 2002], [Ma, 2006].

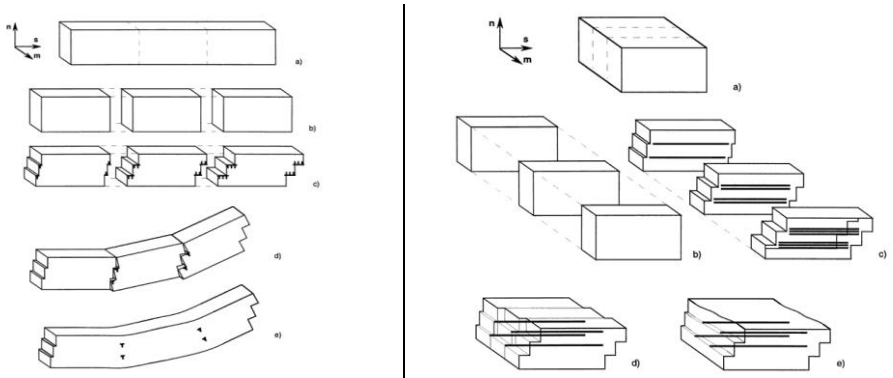

(a) (b)

Figure1.9*: Diagram of the accumulation process of geometrically necessary dislocations (GNDs) edge type (a) and screw type (b) [Arsenlis, 1999].*

Figure 1.9 illustrates the GNDs formation process. A crystal divided in several blocks is submitted to a shearing stress. Each block of the crystal will suffer a different plastic deformation which is not necessarily the same as the neighbouring blocks. The dislocations of the same type but with different sign will annihilate. The dislocation excess resulting from this annihilation step is proportional to the gradient strain in the direction of the dislocation slip [Abrivard, 2009]. In other words, we can say that this dislocation excess is proportional to the plastic strain gradient.

During plastic deformation, grain boundaries areas are more susceptible to plastic deformation gradients. As a consequence, the formation of GNDs near the grain boundary areas is favoured. The GNDs formed in this area can be identified by transmission microscope images as dislocations rooted in the grain boundaries areas. In [Yu, 2005], Yu performed this kind of analysis using aluminium samples formed by ultrafine grains initially free of dislocations. The presence of GNDs results in an increase of the strain energy near the grain boundaries due to the relative rotation between the grains. In other words, the presence of the GNDs around the grain boundaries affects the material hardening.

The GNDs are immobile dislocations. They remain in the areas of strain deformation to ensure the continuity of the material. Since the GNDs are immobile dislocations, they do not have a significant influence on plastic deformation. However, due to their static nature, these dislocations work as obstacles for the slip of other dislocations. As a consequence, the GNDs have an important role in the material hardening.

The SSDs are the dislocations accumulated in the material during homogeneous plastic deformation. These dislocations can be divided in two different groups. The first one is the mobile SSDs, which are able to glide over activated slip systems. The second one corresponds to the immobile SSDs. In this case the dislocations are immobile either because they belong to an inactive slip system, or because they are anchored dislocations.

Physically there is no difference between GNDs and SSDs. They cannot be distinguished by image analysis methods. The difference between these two different types of dislocations is the role they play during plastic deformation. A second difference is the distribution of their sign in space. The SSDs, as a result of their statistical nature, present a random distribution across the grains. Some of these dislocations cancel the influence of the others and, as a consequence, the SSDs do not contribute to the plastic deformation heterogeneity. Unlike the SSDs, the GNDs sign is strongly dependent on the geometry. Therefore, the GNDs present a high periodicity since these dislocations exist to ensure the material continuity in areas of deformation gradient, for example at the grain boundaries. The scheme of Figure 1.10 illustrates the difference between these two types of dislocations.

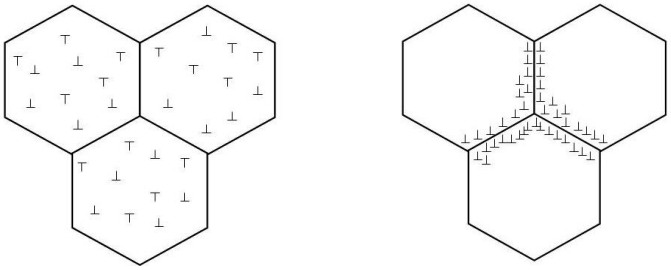

(a) *(b)*

***Figure 1.10**: Schematic illustration of dislocation sign distribution for (a) SSDs and (b) GNDs.*

To sum up we can say that the SSD density is a characteristic of the material, that is, of the crystal structure, shear modulus, stacking fault energy, etc. On the other hand, the GND density is a characteristic of the microstructure, that is, the geometric arrangement and size of grains and phases.

Crystal plasticity models based on plastic deformation gradient

Efforts to incorporate inhomogeneities of plastic deformation in the standard models of continuum mechanics are multiple, but the proposed theories can be classified into two groups:

1 - High-order or top down: the material behaviour is considered to be a function of the material deformation and/or the stress state. In this case, the determination of the stress and deformation states is considered crucial for determining the mechanical behaviour and the evolution of the state of the material. From a more practical point of view, this type of model introduces significant changes in the finite element formulation of the classical crystal plasticity model. Ohno and Okumura [Ohno, 2007], Gerken and Dawson [Gerken, 2008a], [Gerken, 2008b], Gurtin [Gurtin, 2008], [Gurtin, 2002], [Gurtin, 2000] proposed this kind of approach.

2 - Low-order or bottom up: the material behaviour is considered as dependent on the action of dislocations, and the definition of this dependence through time defines the behaviour and material state. This kind of approach is often easier to implement, as compared to the higher order models, since the classical crystal plasticity formulation remains unchanged. In order to take into account the GNDs effects, the equation of dislocation density evolution in time is modified. Evers [Evers, 2004], Bassani [Bassani, 2001], Beaudoin [Beaudoin, 2000], Voyiadjis [Abu Al-Rub, 2006], Busso [Busso, 2000], Acharya [Acharya, 2001], [Acharya, 2004], Ma [Ma, 2006], Acharya and Bassani [Acharya, 2000] proposed this kind of model.

High-order/topdown models

The model proposed by Gurtin [Gurtin, 2008], [Gurtin, 2002], [Gurtin, 2000] can be summarized by the following:

1 – Multiplicative decomposition of deformation gradient tensor (F) in elastic (F^e) and plastic (F^p) portions;

2 – The mechanical model is linked to the work done by each active slip system. Energy principles account for the work associated with each activated slip system. A system of microforces also associated to dissipated work accompanies that introduced by dislocation

slip. The microforces system consists of a stress vector, ξ^α, and a scalar value representing the internal forces π^α with a microforce balance that is supplemental to the classical Newtonian balances of momentum. Denoting τ^α the stress projected to the slip plane α, the microforces equilibrium equation is given by:

$$Div\xi^\alpha + \tau^\alpha - \pi^\alpha = 0; \tag{1.16}$$

3 – A mechanical version of the second thermodynamic law is proposed. In this case, the idea that the internal increase in the material internal energy is not greater than the work performed by each slip system is considered. Thus, an energy inequality is established:

$$J^{-1}\dot{\Psi} - CL^e - \sum_{\alpha=1}^{A}\left(\xi^\alpha.grad\dot{\gamma}^\alpha + \pi^\alpha\dot{\gamma}^\alpha\right) \le 0, \tag{1.17}$$

with Ψ the material internal energy, C the Cauchy stress tensor, $L^e = \dot{F}^e F^{e-1}$ the elastic deformation rate tensor, $J = \det F^e$ and $\det F^p = 1$ (plastic deformation with volume conservation). From the inequality 1.17, constitutive equations for ξ^α and π^α are established:

$$\pi^\alpha = H(\dot{\gamma}^\alpha)\sigma^\alpha + J^{-1}\left(S^{\alpha t}T + TS^\alpha\right)G, \tag{1.18}$$

$$\xi^\alpha = J^{-1}F^e(m^\alpha \times Ts^\alpha), \tag{1.19}$$

where α = 1, 2, …, A labels the individual slip systems and A is the total number of slip systems existing in the material.

Substituting Equations 1.18 and 1.19 into the balance Equation 1.16, the equation used to compute the resolved shear stress on a slip system α is obtained:

$$\tau^\alpha = H(\dot{\gamma}^\alpha)\sigma^\alpha + J^{-1}\left(S^{\alpha t}T + TS^\alpha\right)G - div\left[J^{-1}F^e(m^\alpha \times Ts^\alpha)\right], \tag{1.20}$$

where $H(\dot{\gamma}^\alpha)\sigma^\alpha$ characterizes the stress dependency on the dislocations slip rate, G is the geometrically necessary dislocations (GNDs) density, and $T = \dfrac{\partial\Psi(G)}{\partial G}$ represents the GNDs energetic contribution to the material hardness. T is a function of partial derivatives that do not exist in the classical crystal plasticity model. Moreover, when determining the constitutive equations of the model, the internal energy of the material (Ψ) is expressed as the sum of the elastic energy of the material added to an energy value due to the presence of a small amount of crystalline defects. The model is therefore only valid for small plastic deformation.

The tensor G is written as a function of an edge dislocation density (ρ_E) and a screw dislocation density (ρ_S), as follows:

$$G = \sum_\alpha\left(\rho_S^\alpha s^\alpha \otimes s^\alpha + \rho_E^\alpha l^\alpha \otimes s^\alpha\right), \tag{1.21}$$

where s^α is a vector parallel to the Burgers vector (b^α), $l^\alpha = m^\alpha \times s^\alpha$, with m^α the normal to the slip plane. $s^\alpha \otimes s^\alpha$ and $l^\alpha \otimes s^\alpha$ are canonical dislocation dyads. If $l^\alpha \otimes b^\alpha$ is a

dislocation dyad, for an edge dislocation $l^\alpha \perp b^\alpha$ and for a screw dislocation $l^\alpha = b^\alpha$. ρ_S and ρ_E are calculated using equations proposed by [Arsenlis, 1999]:

$$\rho_E^\alpha = -s^\alpha . grad\gamma^\alpha \text{ and } \rho_S^\alpha = l^\alpha . grad\gamma^\alpha . \tag{1.22}$$

Finally, the addition of a microforces tensor requires the need for supplementary boundary conditions beyond the classical macroscopic boundary conditions used. These extra boundary conditions are used in order to solve the partial differential equations (PDEs) that represent the non-local yield conditions while the standard boundary conditions are used to solve the PDEs that represent the standard force balance. Two extra boundary conditions are needed: first, if a grain boundary is considered to be "rigid", i.e. it does not allow the dislocation passage, the boundary condition is assumed to be $\dot{\gamma}^\alpha = 0$. However, if the grain boundary does allow the dislocation passage, only shear stress is assumed to operate at the boundary, and the condition is $\xi^\alpha . n = 0$.

Ohno and Okumura [Ohno, 2007] proposed a model that takes into account the GNDs energy to analyze the grain size impact on the material initial yield strength. The energy value is used to construct a high order stress tensor. Both the GNDs energy and the high stress tensor are incorporated in Gurtin's [Gurtin, 2008], [Gurtin, 2002], [Gurtin, 2000] theory of plastic deformation gradient. The model has been applied to the determination of the yield strength dependence on the grain size of 2D and 3D single crystals. The model is however not suited for the modeling of large plastic deformation of polycrystalline materials.

In [Gerken, 2008a], [Gerken, 2008b], Gerken and Dawson proposed another high-order model example. This model is based on the multiplicative decomposition of the gradient deformation tensor into three parts. Proposing this multiplicative decomposition, their idea is to develop a more accurate representation of the mechanism responsible for deformation. In the classical crystal plasticity model, the gradient deformation tensor is usually decomposed into two parts: one related to the reversible or elastic part of the deformation, and the second one to the permanent or plastic part. In the new model, the third term of the gradient deformation tensor corresponds to the "long range" strain that is a deformation of the lattice due to dislocations remaining in the lattice (the GNDs). This long range deformation is related to slip gradient which results in a differential equation relating the total deformation to the three deformation mechanisms represented by the three factors of the multiplicative decomposition. Figure 1.11 illustrates the multiplicative decomposition of the gradient deformation tensor used in this model.

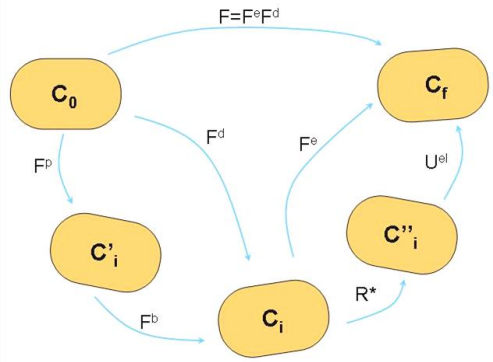

Figure 1.11: *Multiplicative decomposition of the deformation gradient including terms for crystallographic slip, long range strain, rotation and elastic strain.*

In Figure 1.11, F^e represents the elastic part of the deformation which can be decomposed into two parts: U^{el}, corresponding to the stretching of the crystal lattice, and R^*, representing the lattice rigid rotation. F^d represents the deformation induced by dislocations, which can also be divided into two parts. The first one, F^p, represents the permanent deformation due to dislocation slip. The second one, F^b, represents a long range deformation due to the GNDs distribution in the crystalline structure.

Based in this assumption, the shear rate along each active slip system is given by:

$$\dot{\gamma}^{\alpha} = \dot{\gamma}_0 \left(\frac{\tau^{\alpha}}{g^{\alpha}} \right)^{\frac{1}{m}} \operatorname{sgn}\left(\tau^{\alpha}\right), \tag{1.23}$$

where m the strain rate sensitivity, τ^{α} the shear stress projected to the slip system, and g^{α} the hardness of the slip system. g^{α} depends on the SSDs and GNDs densities and is given by:

$$g^{\alpha} = G_1(\gamma) + G_2\left(\frac{\partial \gamma}{\partial x_i} \right), \text{ with,} \tag{1.24}$$

$$\frac{\partial G_1(\gamma)}{\partial t} = h_0 \left(\frac{g_S - g^{\alpha}}{g_S - g_0} \right) \dot{\gamma}, \tag{1.25}$$

$$G_2\left(\frac{\partial \gamma}{\partial x_i} \right) = \beta \mu \sqrt{\rho_{GND}} = \beta \mu \sqrt{\sum_{\alpha} \left| \frac{\partial \gamma^{\alpha}}{\partial d^{\alpha}} \right|}. \tag{1.26}$$

The functions $G_1(\gamma)$ and $G_2\left(\frac{\partial \gamma}{\partial x_i} \right)$ represent the hardness due to the presence of SSDs, and GNDs, respectively. In Equation 1.26 d^{α} represents the dislocation slip direction.

Unlike the model proposed by Gurtin [Gurtin, 2008], [Gurtin, 2002], [Gurtin, 2000], this model proposed by Gerken and Dawson [Gerken, 2008a], [Gerken, 2008b] allows the modeling of GNDs effects for large plastic deformation, which makes its use more interesting in the context of recrystallization phenomena. Furthermore, the model evaluates the GNDs effects not only on the material stress state (Equation 1.24), but also on the material deformation (F^b). The F^b tensor allows the estimation of the crystal lattice rotation due to the presence of GNDs.

Low-order/bottom up models

All low order methods rely on an internal state variable approach to determine the macroscopic response of the material whereby strain gradient effects are introduced directly into the evolutionary laws of the state variables. The strain gradient effects are incorporated by determining the GND density and distribution based on the Nye's tensor. The Nye's tensor gives a measure of the plastic deformation incompatibility. In a physical way, Nye's tensor can be interpreted as a measure for the closure failure of Burger's circuit enclosing an infinitesimal surface. The inner product of Nye's tensor Λ with the unit normal vector n of surface S is integrated over the surface.

$$G = \int_S \Lambda.ndS\,, \tag{1.27}$$

with G being the cumulative Burger's vector. This vector represents the GNDs density enclosing the surface *S*. Finally, the Nye's tensor is given by

$$\Lambda = curl\left\{F^p\right\} = \nabla \times F^p\,, \tag{1.28}$$

where F^p is the plastic deformation gradient.

Bassani [Bassani, 2001] and Acharya [Acharya, 2000] propose a model that takes into account the influence of GNDs and SSDs implicitly. The CRSS is calculated being proportional to the Nye's tensor. However, dislocation density values are not explicitly calculated. When modeling recrystallization phenomena, the dislocation density value is usually essential information. Implicit models are therefore not of great interest for applications related to recrystallization phenomena.

Al-Rub [Al-Rub, 2006] has proposed a model that represents, explicitly, the GNDs and SSDs contribution to the material hardening. In this case, the CRSS is given by:

$$\tau = \tau_0 + \alpha\mu b\sqrt{\rho_S + \rho_G}\,. \tag{1.29}$$

An evolution equation is proposed for each type of dislocation. As indicated above, the GNDs density is linked to the incompatibility of the plastic deformation and the crystal lattice rotation. As a consequence, GNDs are not created or annihilated like the SSDs; either they are transported from/to other regions where there is a deformation gradient, or they are the result of geometrical reactions between other existing GNDs.

The GNDs accumulate in proportion to the plastic deformation gradient [Ashby, 1970], [Nix, 1998], [Arsenlis, 1999], according to Equation 1.22. The evolution of SSDs density is calculated using the equation proposed by Beaudoin [Beaudoin, 2000], based on the Kocks-Mecking equation (Equation 1.8):

$$\dot{\rho}_S = \left(K_0\rho_G + \frac{K_1}{b}\sqrt{\rho_S} - K_2\rho_S\right)\dot{\gamma}^P\,, \tag{1.30}$$

where $K_0\rho_G$ represents the immobile dislocations increase due to the tangle of mobile dislocations with the GNDs.

Busso [Busso, 2000] has also proposed a hardening law that explicitly represents the GNDs and SSDs contributions. The description of the flow characteristics in a generic slip system (α) under a given temperature, microstructural state and resolved shear stress (τ^α) is based on the dislocation mechanics and stress-activation concepts introduced by Busso [Busso, 1996]. The particular form of the flow rule exhibits an explicit dependence of the activation energy on a driving stress (τ_l^α) which accounts for lattice friction effects and thermally activated obstacles:

$$\tau_l^\alpha = \left|\tau^\alpha\right| - S^\alpha\,\frac{\mu}{\mu_0}\,, \tag{1.31}$$

where S^α represents the athermal component of the flow stress over slip resistance and μ/μ_0 the ratio of the shear modulus at the temperature of interest to that at 0 K. Both SSDs and GNDs contribute to the total slip resistance S^α as follows:

$$S^\alpha = \mu_0 b^\alpha \sqrt{\lambda_S^2 \sum_\beta \rho_S^\beta + \lambda_G^2 \sum_\beta \delta_G^{\alpha\beta} \rho_G^\beta}\,, \tag{1.32}$$

where λ_S and λ_G are statistical coefficients accounting for the deviation from regular spatial arrangements of SSDs and GNDs and $\delta_G^{\alpha\beta}$ is a function representing the interaction between different GNDs populations existing in the material.

SSDs are decomposed into pure edge ($\rho_{S_e}^\alpha$) and screw ($\rho_{S_{sw}}^\alpha$) components in order to account for their different mobilities, hardening and recovery process. Dislocations generation is assumed to be related to Frank-Read sources and the annihilation is assumed to occur due to sign differences between the same type of parallel dislocations. The evolutionary laws are written as balance laws between dislocation generation and annihilation:

$$\begin{cases} \dot{\rho}_{S_e}^\alpha = \dfrac{C_e}{b^\alpha}\left[K_e \sqrt{\sum_\beta \rho_T^\beta} - 2d_e \rho_{S_e}^\alpha \right] \left| \dot{\gamma}^\alpha \right|, \\ \dot{\rho}_{S_{sw}}^\alpha = \dfrac{C_{sw}}{b^\alpha}\left[K_{sw} \sqrt{\sum_\beta \rho_T^\beta} - \rho_{S_{sw}}^\alpha \left\{ K_{sw} \pi d_{sw}^2 \sqrt{\sum_\beta \rho_T^\beta} + 2d_{sw} \right\} \right] \left| \dot{\gamma}^\alpha \right|. \end{cases} \tag{1.33}$$

In this expression, d_e and d_{sw} are critical distances for spontaneous annihilation of opposite sign edge and screw dislocations respectively. C_e and C_{sw} represent the relative contributions of edge and screw dislocations to the slip produced by SSDs while K_e and K_{sw} are related to their respective mean free path.

For describing the evolution of GNDs, a vector field $\dot{\rho}_G^\alpha$ related to the GND density is introduced for every slip system. This dislocation line vector can be further discretised into its edge and screw components by solving along axes of the coordinate system defined in terms of the slip direction m^α, the slip plane normal n^α and a third orthogonal direction $t^\alpha = m^\alpha \times n^\alpha$:

$$\dot{\rho}_G^\alpha = \dot{\rho}_{G_{sm}}^\alpha m^\alpha + \dot{\rho}_{G_{et}}^\alpha t^\alpha + \dot{\rho}_{G_{en}}^\alpha n^\alpha\,. \tag{1.34}$$

Here, $\dot{\rho}_{G_{sm}}^\alpha$ refers to its screw component parallel to m^α while $\dot{\rho}_{G_{et}}^\alpha$ and $\dot{\rho}_{G_{en}}^\alpha$ are the edge components parallel to t^α and n^α, respectively (Figure 1.12).

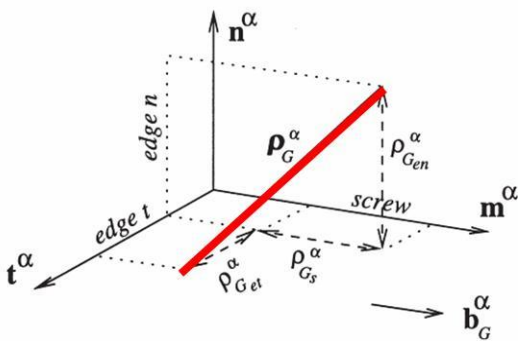

Figure 1.12: *Local orthogonal coordinate system of reference for a generic geometrically necessary dislocation line in an arbitrary slip system α.*

Nye's dislocation tensor (Equation 1.28) is used to define a tensorial measure of the GND density which can be related to the resultant Burger's vector (Equation 1.27) of all GNDs. The evolution of GNDs is obtained by differentiating Equation 1.27 with respect to time. As a result of this mathematical treatment, the GNDs density is calculated as:

$$b^{\alpha}\left(\dot{\rho}^{\alpha}_{G_{sm}} m^{\alpha} + \dot{\rho}^{\alpha}_{G_{et}} t^{\alpha} + \dot{\rho}^{\alpha}_{G_{en}} n^{\alpha}\right) = curl\left(\gamma^{\alpha} n^{\alpha} F^{p}\right), \tag{1.35}$$

where F^p is the plastic deformation gradient (Figure 1.13). The determination of Equation 1.35 is presented in details in [Busso, 2000], [Abrivard, 2009]. The *curl* term translates the dependency of the GND density evolution on the spatial gradient of the slip rate, hence the non-local terminology which is sometimes used to describe strain-gradient plasticity concepts. Finally, the total GND density value is given by:

$$\dot{\rho}^{\alpha}_{G} = \dot{\rho}^{\alpha}_{G_{sm}} + \dot{\rho}^{\alpha}_{G_{et}} + \dot{\rho}^{\alpha}_{G_{en}} . \tag{1.36}$$

3 Single Crystal Model

Following the previous considerations, it is chosen here to adopt a constitutive behaviour at the single crystal level which is based on an elastic-viscoplastic crystal plasticity formulation, enriched by the introduction of both SSDs and GNDs, according to the principles of low order / bottom up models.

3.1 Formulation

3.1.1 Elastic-Viscoplastic Formulation

The single crystal model described here relies on an elastic-viscoplastic formulation. The main concepts are highlighted in this section and more details can be found elsewhere [Delannay et al., 2006]. In this model, plastic deformation is achieved by dislocation slip. For instance, in the case of an FCC crystal, the dislocation slip happens along the {111} <110> crystallographic systems while for a BCC crystal, the dislocation slip takes place especially along the {110} <111>. The kinematics of the single crystal is a combination of dislocation slip, lattice rotation and elastic stretch. Figure 1.13 illustrates the multiplicative decomposition, which corresponds to that given in Figure 1.11 but without the concept of long range strain.

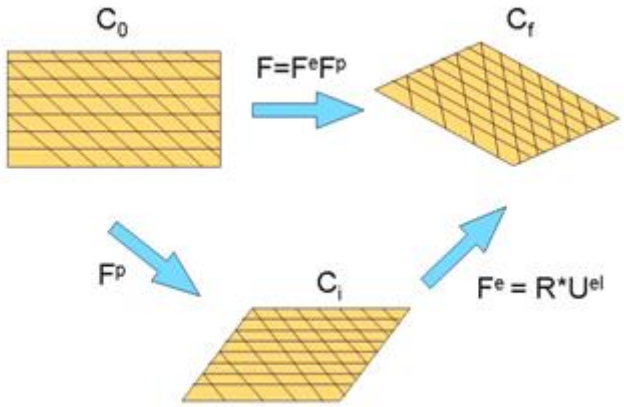

Figure 1.13: *Crystal kinematics: initial (C_0), intermediate (C_i) and final configuration (C_f)*

The deformation gradient tensor F, typically considered in finite strain kinematics, is decomposed as follows:

$$F = F^{el} F^{p} = R^{*} U^{el} F^{p} \tag{1.37}$$

where R^* is the lattice rotation and U^{el} the elastic stretch. The intermediate configuration C_i corresponds to a stress-free configuration or "relaxed" configuration obtained by elastically unloading the crystal in the final configuration C_f and rotating it. In other words, this intermediate configuration represents the plastic deformation without taking into account the elastic deformation. An additional fictitious configuration could be introduced between C_i and C_f as in [Marin and Dawson, 1998d] where it is obtained by elastically unloading C_f to a relaxed state but without rotation. The crystal constitutive equations could be written in any of these configurations and this choice conditions the procedure and scheme used to integrate them. Here, the equations are written in the intermediate configuration C_i. In this case, the velocity gradient tensor L is given by:

$$L = \dot{F} F^{-1} = \dot{R}^{*} R^{*T} + R^{*} \left(\dot{U}^{el} U^{el\,-1} \right) R^{*T} + R^{*} U^{el} \left(\dot{F}^{p} F^{p\,-1} \right) U^{el\,-1} R^{*T} . \tag{1.38}$$

The plastic velocity gradient L^p, accounting for the dislocation slip, is then written as follows:

$$L^{p} = \dot{F}^{p} F^{p\,-1} = \sum_{\alpha} M^{\alpha} \dot{\gamma}^{\alpha} . \tag{1.39}$$

In this expression, M^{α} is the Schmid tensor of slip system α. The Schmid tensor has the same expression in the initial and intermediate configuration as crystallographic slip does not distort the lattice.

The elastic strain tensor E is calculated with respect to the intermediate configuration and is therefore given by:

$$E = \frac{1}{2} \left(F^{el\,T} F^{el} - 1 \right) = \frac{1}{2} \left(U^{el\,T} U^{el} - 1 \right) \tag{1.40}$$

The work-conjugate measure of stress is the second Piola-Kirchhoff stress T. This latter is related to the Cauchy stress σ through:

$$T = \det\left(F^{el}\right) F^{el^{-1}} \sigma F^{el^{T}} = \det\left(U^{el}\right) U^{el^{-1}} R^{*T} \sigma R^{*} U^{el^{-1}} . \tag{1.41}$$

The fourth order anisotropic elasticity operator C sets the proportionality of T with regards to E via the relation:

$$T = CE . \tag{1.42}$$

In a crystal with cubic symmetry (such as FCC or BCC), with the cartesian axes oriented along the cube edges, the nonzero elements of C are the same ones as for the isotropic solid, but the three values C_{11}, C_{12} and C_{44} are independent. So, for FCC crystals the elasticity matrix takes the following form:

$$\begin{pmatrix} C_{11} & C_{12} & C_{12} & 0 & 0 & 0 \\ C_{12} & C_{11} & C_{12} & 0 & 0 & 0 \\ C_{12} & C_{12} & C_{11} & 0 & 0 & 0 \\ 0 & 0 & 0 & C_{44} & 0 & 0 \\ 0 & 0 & 0 & 0 & C_{44} & 0 \\ 0 & 0 & 0 & 0 & 0 & C_{44} \end{pmatrix}. \tag{1.43}$$

This form of the anisotropic elastic tensor allows for the separation of the deviatoric and spherical components of T, which has consequences in terms of finite element implementation.

For materials subjected to important plastic strains, the elastic strains are small compared to the plastic one. Typically, in metal forming operations, they never exceed 1%. It is then assumed that they are small compared to unity. This assumption yields:

$$U^{el} = I + \varepsilon^{el} , \tag{1.44}$$

where I is the identity tensor, ε^{el} is a symmetric tensor with $\left\|\varepsilon^{el}\right\| << 1$. Neglecting higher order terms in ε^{el} leads to:

$$\begin{aligned} U^{e^{-1}} &= \left(I + \varepsilon^{el}\right)^{-1} \approx \left(I - \varepsilon^{el}\right) \\ \det\left(U^{el}\right) &= \det\left(I + \varepsilon^{el}\right) = 1 + tr\left(\varepsilon^{el}\right) \end{aligned}, \tag{1.45}$$

For the same sake of simplification, for any tensor $\mathbf{X}$, $\varepsilon^{el} : \mathbf{X}$ is neglected compared to $\mathbf{X}$. Bearing these assumptions in mind the velocity gradient tensor can be rewritten as:

$$L = \dot{R}^{*} R^{*T} + R^{*}\left(\varepsilon^{el} + \sum_{\alpha} M^{\alpha} \dot{\gamma}^{\alpha}\right) R^{*T} . \tag{1.46}$$

and Equations 1.40, 1.41 and 1.42 simplify to:

$$T = C\varepsilon^{el} = R^{*^{T}} \sigma R^{*} \tag{1.47}$$

3.1.2 Flow rule and hardening law

In order to complete the single crystal model, the viscoplastic power law is used as a flow rule (Equation 1.1). Regarding the hardening, it is assumed that all slip systems have the same τ_c and that they all harden according to Equation 1.4.

Hardening law - SSDs

Considering only the SSDs, the Yoshie-Laasraoui-Jonas equation (Equation 1.7) can be implemented within the crystal plasticity model. To transform this equation, used at the macroscopic scale, to the dislocation slip scale (mesoscale), the strain term is replaced by the total dislocation slip, and K_1 and K_2 values are divided by the polycrystal Taylor factor (M). At the mesoscale (the transformation from macro to mesoscale is discussed in chapter 3), the Yoshie-Laasraoui-Jonas equation becomes:

$$\dot{\rho} = \left(K_1^{'} - K_2^{'}\rho\right)\sum_{\alpha}\left|\dot{\gamma}^{\alpha}\right| \tag{1.48}$$

where $K_1^{'} = \frac{K_1}{M}$ and $K_2^{'} = \frac{K_2}{M}$.

Hardening law - GNDs

Considering the GNDs, the Busso [Busso, 2000] model (Equation 1.35) may be implemented in a standard crystal plasticity model. The gradient terms require a non-local computation, which can for example be done using a finite element formulation.

It is important to highlight that only the GND evolutionary equation proposed by Busso is implemented here. The equations considering the SSD density evolution proposed by Busso can be replaced by Equation 1.48.

3.2 Time Integration Scheme of the constitutive law

To summarize, the equations describing the elastic-viscoplastic model can be listed as follows:

Kinematics: $$L_{sym} \rightarrow D = R^{*}\left(\varepsilon^{el} + \sum_{\alpha}\frac{1}{2}\left(M^{\alpha} + M^{\alpha^T}\right)\dot{\gamma}^{\alpha}\right)R^{*T}, \tag{1.49a}$$

Kinematics: $$L_{ant} \rightarrow W = \dot{R}^{*}R^{*T} + R^{*}\left(\varepsilon^{el} + \sum_{\alpha}\frac{1}{2}\left(M^{\alpha} - M^{\alpha^T}\right)\dot{\gamma}^{\alpha}\right)R^{*T}, \tag{1.49b}$$

Elasticity: $$T = C\varepsilon^{el}, \tag{1.49c}$$

Schmid Law: $$\tau^{\alpha} = T : M^{\alpha} \tag{1.49d}$$

Flow: $$\dot{\gamma}^{\alpha} = \dot{\gamma}_0\left|\frac{\tau^{\alpha}}{\tau_c}\right|^{\frac{1}{m}} sign\left(\tau^{\alpha}\right), \tag{1. 49e}$$

Hardening: $$\tau_c = \tau_c + \alpha\mu b\sqrt{\rho_T} \tag{1. 49f}$$

SSDs evolution: $$\dot{\rho}_S = \left(K_1^{'} - K_2^{'}\rho\right)\sum_{\alpha}\left|\dot{\gamma}^{\alpha}\right| \tag{1. 49g}$$

GNDs evolution:
$$\dot{\rho}_G^{\alpha} = \frac{1}{b^{\alpha}} curl\left(\gamma^{\alpha} n^{\alpha} F^{p}\right) = \frac{1}{b^{\alpha}} curl(A). \quad (1.\ 49h)$$

The objective of the integration of the constitutive model is to compute the model-dependent variables at time $t + \Delta t$, given that their values are known at time t and that the applied deformation is known for every crystal (L or equivalently D and W). In the previous system, the unknown independent variables are: the crystal stress $T\big|_{t+\Delta t}$ (or equivalently the elastic deformation $\varepsilon^{el}\big|_{t+\Delta t}$), the slip resistance $\tau_c\big|_{t+\Delta t}$ and the lattice orientations $R^*\big|_{t+\Delta t}$. These constitute the state variables of the problem. In order to simplify the time integration procedure, one can choose to eliminate the lattice rotation from this system (and hence the evolutionary Equation 1.49b) which is approximated by $\tilde{R}^*$ as follows:

$$R^*\big|_{t+\Delta t} \approx \tilde{R}^* = W\Delta t R^*\big|_t . \quad (1.50)$$

As mentioned in [Delannay 2006], the impact of such an approximation in negligible in metal forming simulations such as those performed in this work. The update of the lattice orientation is performed later, after the integration of the rest of the equations, as it is explained below.

Equations 1.49a, 1.49c and 1.49d are combined in order to find the crystal stresses $T\big|_{t+\Delta t}$. A fully implicit time integration scheme yields the following discretized equations:

$$T\big|_{t+\Delta t} = T\big|_t + C\left[\tilde{R}^{*T}\,\Delta D\tilde{R}^* - \frac{1}{2}\left(M^{\alpha} + M^{\alpha^T}\right)\Delta\gamma^{\alpha}\right], \quad (1.51)$$

$$\text{where } \Delta\gamma^{\alpha} = \dot{\gamma}^{\alpha}\big|_{t+\Delta t}\Delta t = \dot{\gamma}_0\left(\frac{M^{\alpha} : T\big|_{t+\Delta t}}{\tau_c\big|_{t+\Delta t}}\right)^{1/m} sign\left(M^{\alpha} : T\big|_{t+\Delta t}\right)\Delta t, \quad (1.52)$$

$$\text{and } \tau_c\big|_{t+\Delta t} = \tau_c\big|_t + \frac{\alpha\mu b}{2}\frac{1}{\sqrt{\rho\big|_{t+\Delta t}}}\Delta\rho . \quad (1.53)$$

Concerning the evolution of dislocation density, the SSDs density is calculated implicitly, transforming equation 1.48 into:

$$\Delta\rho = \left(K'_1 - K'_2\,\rho\big|_{t+\Delta t}\right)\sum_{\alpha}\left|\Delta\gamma^{\alpha}\right|. \quad (1.54)$$

In order to determine the evolution of the GNDs, the quantity *curl*(*A*) (Equation 1.49h) has to be calculated. Given that the spatial variation of the quantity (*A*) is necessary to estimate its *curl*, spatial information must be known, for example by using a finite element mesh (see section 4). *A* is then calculated at each Gauss point and linearly interpolated to the mesh elements nodes using the shape functions of the element. Subsequently, the *curl* of (*A*) is calculated. As described in equation 1.36 and recalled here, the three components of the dislocation density vector field are added, leading to the total GNDs density, for each slip system α:

$$\dot{\rho}_G^{\alpha} = \dot{\rho}_{G_{sw}}^{\alpha} + \dot{\rho}_{G_{et}}^{\alpha} + \dot{\rho}_{G_{en}}^{\alpha} . \tag{1.55}$$

Then the GNDs densities of each slip system are added in order to calculate the total GNDs density:

$$\dot{\rho}_G = \sum_{\alpha} \dot{\rho}_G^{\alpha} . \tag{1.56}$$

An explicit update is performed using a forward Euler scheme,

$$\rho_{G,t+\Delta t} = \rho_{G,t} + \Delta t \dot{\rho}_{G,t+\Delta t} . \tag{1.57}$$

Since the GNDs are explicitly updated, the accuracy of the solution is ensured only if a sufficiently small time step is used.

A two level iterative scheme is used to solve the above system. A first Newton-Raphson procedure solves Equation 1.51, while a second one computes the slip increments $\Delta\gamma^{\alpha}$ (1.52) based on the stress estimate. Slip resistance is computed subsequently using Equation 1.53 and these three operations are performed until convergence. Finally, regarding lattice reorientation, Equation 1.49b is integrated using an exponential map [Simo, 1998]. In practice, all these equations are expressed in the crystal reference frame, so that M^{α} is identical in crystals belonging to the same phase. At the beginning of the simulation, the orientation of each crystal is recorded and used to shift from the sample coordinate system to the crystal coordinate system ($R_0 R^{*T}$).

4 Finite Element Formulation

The finite element model is composed of a representation and meshing of the microstructure and of a finite element formulation used to solve the mechanical problem. Representation and meshing of the microstructure are discussed in details in chapter 2. In this part, the solution of the mechanical model in a finite element formulation is presented.

Finite element simulations in solid mechanics are dominated either by displacement/velocity based formulations or by mixed formulations such as displacement/pressure or velocity/pressure formulations.

In this work, a mixed velocity/pressure finite element formulation is used with appropriate combination of interpolation functions. More specifically, the mini-element (P1+/P1) with linear continuous pressure and linear velocity with a bubble function added at its centre for this latter, is used. Specific details of the formulation are found below.

4.1 Balance laws

The resolution of the mechanical problem is based on momentum and mass conservation coupled with the appropriate boundary conditions and constitutive equations. In local form, the conservation of momentum and mass is written as:

$$div\sigma + \rho g = \rho \frac{dv}{dt}, \tag{1.58}$$

$$\frac{d\rho}{dt} + \nabla.(\rho v) = 0. \tag{1.59}$$

where v is the velocity vector, σ is the Cauchy stress tensor, ρ the density and g the gravity.

Appropriate surface traction and velocity boundary conditions are given by:

$$v = v_{app} \text{ on } \Gamma_v, \tag{1.60}$$

for the velocity vector v, and:

$$\sigma_n = t = t_{app} \text{ on } \Gamma_t, \tag{1.61}$$

for the traction vector t where $\Gamma = \Gamma_v \cup \Gamma_t$ is the boundary of the domain Ω.

In the present work, we restrict our attention to isothermal, quasi-static deformation of polycrystalline aggregates. Also neglecting body forces, Equation 1.58 is reduced to:

$$div\sigma = 0. \tag{1.62}$$

The Cauchy stress tensor σ can be decomposed into its deviatoric and spherical (pressure) components. However, such decomposition is only meaningful if the constitutive law, that is to be solved in concert with this equation, can give the evolution of the deviatoric and pressure components separately. Besides, for constitutive models that account for the elastic behaviour, Equation 1.59 is replaced by the volumetric response of the elasticity relations, as the density can be directly determined once the motion of the body is obtained. Bearing these hypotheses in mind, the final system of equations to be solved may be written as:

$$\begin{cases} divS - \nabla p = 0, \\ tr\dot{\varepsilon} + \dfrac{\dot{p}}{\chi} = 0, \end{cases} \tag{1.63}$$

where S and p are respectively the deviatoric and pressure components of σ, χ the bulk (elastic) modulus and $\dot{\varepsilon}$ the strain rate tensor defined as:

$$\dot{\varepsilon} = \frac{1}{2}\left(\nabla v + \nabla v^T\right) \tag{1.64}$$

4.2 Variational formulation

The formulation of the finite element problem is based on the weak integral form of the system presented in 1.63. The procedure for obtaining the weak form consists of first multiplying the equations by test functions $v^* \in V$ and $p^* \in P$ where V and P are appropriate functional spaces given by:

$$\begin{cases} V = \left\{ v, v \in H^1(\Omega)^d \mid v = v_{app} \text{ on } \Gamma_v \right\}, \\ V_0 = \left\{ v, v \in H^1(\Omega)^d \mid v = 0 \text{ on } \Gamma_v \right\}, \\ P = \left\{ p, p \in L^2(\Omega) \right\}, \end{cases} \tag{1.65}$$

with *d* the space dimension, *V* the space of kinematically admissible velocity fields and V_0 the space of kinematically admissible velocity fields to zero.

Integrating over the volume of the domain Ω and using the Green formula yields the following variational problem:

$$find\,(v, p) \in (V, P)\, such\ that\ \forall (v^*, p^*) \in (V_0, P):$$

$$\begin{cases} \int_\Omega S(v) : \dot{\varepsilon}(v^*) d\Omega - \int_\Omega p . \nabla v^* \, d\Omega - \int_{\Gamma_t} t_{app} . v^* \, d\Gamma = 0, \\ \int_\Omega \left(tr\, \dot{\varepsilon} + \frac{\dot{p}}{\chi} \right) p^* \, d\Omega = 0. \end{cases} \tag{1.66}$$

4.3 Time discretization

The large deformation of the microstructure is modelled using an updated Lagrangian framework. In this incremental approach, the total simulation time t_{tot} is discretized into *N* increments such that $t_{tot} = \bigcup_{i=0}^{N-1} [t_i, t_i + \Delta t_i]$. At time *t* the configuration of the body Ω^t is known and the solution (v^t, p^t) satisfying the balance laws at that time, can be determined based on stresses calculated at time $t + \Delta t$. The new configuration is the updated one, using a finite difference scheme, namely an Euler explicit scheme:

$$x^{t+\Delta t} = x^t + v^t \Delta t \tag{1.67}$$

with *x* the node coordinates vector and v^t the velocity vector solution of the mechanical problem on the current configuration.

4.4 Spatial discretization

In order to compute the solution of the variational problem given by Equation 1.66 using the finite element method, the domain Ω is discretized such that:

$$\Omega_h = \bigcup_{K \in \Im_h(\Omega)} K, \tag{1.68}$$

where Ω_h is a spatial discretization of the domain Ω, $\Im_k(\Omega)$ a finite element mesh of the domain Ω, *K* a simplex and *h* a parameter denoting the mesh size.

We introduce the functional vector spaces of finite dimensions V^h and P^h close to the continuous spaces *V* and *P* of infinite dimension, such that the discrete solution $(v_k, p_k) \in (V_k, P_k)$ is close to the "real" one $(v, p) \in (V, P)$. The spaces V^h and P^h have to be chosen in such a way that the existence and uniqueness of the solution is guaranteed. For this

purpose, these spaces cannot be chosen independently. They have to satisfy the Brezzi Babuska stability conditions [Brezzi, 1991]. In this respect, the MINI-element $P1^+/P1$ is a convenient and an appropriate choice.

4.4.1 The MINI-element

The MINI-element is an isoparametric triangle in 2D and tetrahedron in 3D with a linear interpolation for the pressure field. On the other hand, the velocity field interpolation has a linear component and a nonlinear one, the so-called bubble function, which is added at the centre of the element as shown in Figure 1.14 for the 3D case.

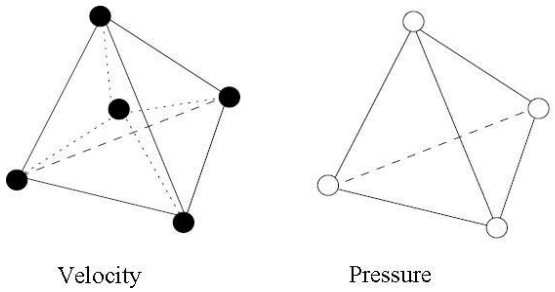

Figure 1.14: *MINI-Element $P1^+/P1$.*

For such an element, the finite element spaces can be written as:

$$\begin{cases} W_h = V_h \oplus B_h, \\ W_{h0} = V_{h0} \oplus B_h, \\ V_{h0} = \left\{ v_h \in (\varepsilon^0(\Omega_h))^d : v_h \mid_K \in P_1(K), v_h \mid_{\Gamma_{K_{vh}}} = 0 \right\}, \\ V_h = \left\{ v_h \in C^0(\Omega_h)^d : v_h \mid_K \in P_1(K), v_h|_{\Gamma_{K_{vh}}} = v_{app} \right\}, \\ B_h = \left\{ b_h \in C^0(\Omega_h)^d : b_h|_K \in P_1(K_i) \text{ and } b_h|_{\Gamma_K} = 0 \right\}, \\ P_h = \left\{ p_h \in C^0(\Omega_h)^d : p_h|_K \in P_1(K) \right\}, \end{cases} \tag{1.69}$$

where d is the space dimension, K_i, $i = 1 \ldots d + 1$ are the $d + 1$ sub-simplexes composing K.

Denoting N^l and N^b the linear and bubble shape functions respectively, the discretized velocity and pressure fields can be written as:

$$w_h = v_h + b_h = \sum_{i=1}^{Nbnode} N_i^l(x) v_i + \sum_{j=1}^{Nbelt} N_j^b(x) b_i, \tag{1.70}$$

$$p_h = \sum_{i=1}^{Nbnode} N_i^l(x)\, p_i, \tag{1.71}$$

where *Nbnode* and *Nbelt* are the total number of nodes and elements in the mesh respectively. On the local level, for each element, the velocity and pressure unknowns are written as:

$$w_h = v_h + b_h = \sum_{i=1}^{d+1} N^l(x) V_i + N^b(x) b_j, \tag{1.72}$$

$$p_h = \sum_{i=1}^{d+1} N^l(x) P_i, \tag{1.73}$$

where N^b is a linear function defined on each of the $d + 1$ sub-elements.

For each element K, the bubble function has the following fundamental properties:

1 - $\int_K \mathbf{A} : \nabla b_h d\Omega_K = 0$ for any constant tensor $\mathbf{A}$, therefore $\int_K \nabla v_h : \nabla b_h d\Omega_K = 0$,

2 - $\int_K v_h . \nabla b_h d\Omega_K = -\int_K \nabla v_h . b_h d\Omega_K$,

3 - $b_h = 0$ on Γ_K.

4.4.2 The discrete problem

The discrete problem is formulated as follows:

find $\forall (w_h = v_h + b_h, p_h) \in (W_h, P_h)$ *such that* $\forall (w_h^* = v_h^* + b_h^*, p_h^*) \in (W_{h0}, P_h)$*:*

$$\begin{cases} \int_{\Omega_h} S(w_h) : \dot{\varepsilon}(w_h^*) d\Omega - \int_{\Omega_h} p_h . \nabla w_h^* d\Omega - \int_{\Gamma_t} t_{app} . w_h^* d\Gamma = 0, \\ \int_{\Omega_h} \left(tr\, \dot{\varepsilon}(w_h) + \dfrac{\dot{p}}{\chi} \right) p_h^* d\Omega = 0. \end{cases} \tag{1.74}$$

Taking into consideration the decomposition $w_h = v_h + b_h$ and $w_h^* = v_h^* + b_h^*$ the previous system can be rewritten as:

$$\begin{cases} \int_{\Omega_h} S(v_h + b_h) : \dot{\varepsilon}(v_h^*) d\Omega - \int_{\Omega_h} p_h . \nabla v_h^* d\Omega - \int_{\Gamma_t} t_{app} . v_h^* d\Gamma = 0, \\ \int_{\Omega_h} S(v_h + b_h) : \dot{\varepsilon}(b_h^*) d\Omega - \int_{\Omega_h} p_h . \nabla b_h^* d\Omega - \int_{\Gamma_t} t_{app} . b_h^* d\Gamma = 0, \\ \int_{\Omega_h} \left(tr\, \dot{\varepsilon}(v_h + b_h) + \dfrac{\dot{p}_h}{\chi} \right) p_h^* d\Omega = 0. \end{cases} \tag{1.75}$$

It has been shown [Jaouen, 1998] that in the case of an elastic-viscoplastic constitutive law, the deviatoric component S can be decomposed into a linear $S(v_h)$ and a bubble part $S(b_h)$. This yields to:

$$\begin{cases} \int_{\Omega_h} S(v_h) : \dot{\varepsilon}(v_h^*) d\Omega + \int_{\Omega_h} S(b_h) : \dot{\varepsilon}(v_h^*) d\Omega - \int_{\Omega_h} p_h . \nabla v_h^* d\Omega - \int_{\Gamma_t} t_{app} . v_h^* d\Gamma = 0, \\ \int_{\Omega_h} S(v_h) : \dot{\varepsilon}(b_h^*) d\Omega + \int_{\Omega_h} S(b_h) : \dot{\varepsilon}(b_h^*) d\Omega - \int_{\Omega_h} p_h . \nabla b_h^* d\Omega - \int_{\Gamma_t} t_{app} . b_h^* d\Gamma = 0, \\ \int_{\Omega_h} \left(tr \dot{\varepsilon}(v_h + b_h) + \frac{\dot{p}_h}{\chi} \right) p_h^* d\Omega = 0. \end{cases} \quad (1.76)$$

In practice, the system 1.76 is equivalent to the following system:

$$\begin{cases} \sum_{K \in \Im_h(\Omega)} \left[\int_K S(v_h) : \dot{\varepsilon}(v_h^*) d\Omega_K + \int_K S(b_h) : \dot{\varepsilon}(v_h^*) d\Omega_K - \int_K p_h . \nabla v_h^* d\Omega_K - \int_{\Gamma_K} t_{app} . v_h^* d\Gamma_K \right] = 0, \\ \sum_{K \in \Im_h(\Omega)} \left[\int_K S(v_h) : \dot{\varepsilon}(b_h^*) d\Omega_K + \int_K S(b_h) : \dot{\varepsilon}(b_h^*) d\Omega_K - \int_K p_h . \nabla b_h^* d\Omega_K - \int_{\Gamma_K} t_{app} . b_h^* d\Gamma_K \right] = 0, \\ \sum_{K \in \Im_h(\Omega)} \left[\int_K \left(tr \dot{\varepsilon}(v_h + b_h) + \frac{\dot{p}_h}{\chi} \right) p_h^* d\Omega_K \right] = 0. \end{cases} \quad (1.77)$$

Thanks to the bubble function properties, we have:

$$\int_{\Omega_K} S(v_h) : \dot{\varepsilon}(b_h^*) d\Omega_K = \int_{\Omega_K} S(b_h^*) : \dot{\varepsilon}(v_h) d\Omega_K = 0; \quad (1.78)$$

$$\int_{\Gamma_K} t_{app} . b_h^* d\Gamma_K = 0. \quad (1.79)$$

Considering these properties and removing the subscribe *h* for more clarity, the system 1.77 becomes:

$$\begin{cases} \sum_{K \in \Im_h(\Omega)} \left[\int_{\Omega_K} S(v) : \dot{\varepsilon}(v^*) d\Omega_K - \int_{\Omega_K} p . \nabla v^* d\Omega_K - \int_{\Gamma_K} t_{app} . v^* d\Gamma_K \right] = 0, \\ \sum_{K \in \Im_h(\Omega)} \left[\int_{\Omega_K} S(b) : \dot{\varepsilon}(b^*) d\Omega_K - \int_{\Omega_K} p . \nabla b^* d\Omega_K \right] = 0, \\ \sum_{K \in \Im_h(\Omega)} \left[\int_{\Omega_K} \left(tr \dot{\varepsilon}(v + b) + \frac{\dot{p}}{\chi} \right) p^* d\Omega_K \right] = 0. \end{cases} \quad (1.80)$$

The elastic viscoplastic constitutive behavior is used in the crystal plasticity simulations, which is a non-linear constitutive behavior. As a consequence, system 1.80 is also non-linear. The non-linearity related to the material behavior does not require fundamental reformulation of the problem, as opposed to geometric non-linearities. However, the constitutive law and the system of equations are written in incremental form. Small step increments are needed to

correctly account for path dependence and obtain physically sound solution. In incremental form, the problem can be re-written as follows:

Given S_n, p_n, t_n *and* Ω_n *such that equilibrium is satisfied at time t,* $\forall(v^*+b^*, p^*)\in(W_0, P)$*:*

$$\begin{cases} \sum_{K\in\Im_h(\Omega_n)}\left[\int_{\Omega_K} S_n(v):\dot{\varepsilon}(v^*)d\Omega_K - \int_{\Omega_K} p_n.\nabla v^* d\Omega_K - \int_{\Gamma_K} t_{app_n}.v^* d\Gamma_K\right]=0, \\ \sum_{K\in\Im_h(\Omega_n)}\left[\int_{\Omega_K} S_n(b):\dot{\varepsilon}(b^*)d\Omega_K - \int_{\Omega_K} p_n.\nabla b^* d\Omega_K\right]=0, \\ \sum_{K\in\Im_h(\Omega_n)}\left[\int_{\Omega_K}\left(tr\dot{\varepsilon}_n(v+b)+\frac{\dot{p}_n}{\chi}\right)p^* d\Omega_K\right]=0. \end{cases} \quad (1.81)$$

Find v_{n+1} *kinematically admissible,* S_{n+1}, p_{n+1}, t_{n+1} *and* Ω_{n+1} *that satisfy the equilibrium at time* $t+\Delta t$, $\forall(v^*+b^*, p^*)\in(W_0, P)$*:*

$$\begin{cases} \sum_{K\in\Im_h(\Omega_{n+1})}\left[\int_{\Omega_K} S_{n+1}(v):\dot{\varepsilon}(v^*)d\Omega_K - \int_{\Omega_K} p_{n+1}.\nabla v^* d\Omega_K - \int_{\Gamma_K} t_{app_{n+1}}.v^* d\Gamma_K\right]=0, \\ \sum_{K\in\Im_h(\Omega_{n+1})}\left[\int_{\Omega_K} S_{n+1}(b):\dot{\varepsilon}(b^*)d\Omega_K - \int_{\Omega_K} p_{n+1}.\nabla b^* d\Omega_K\right]=0, \\ \sum_{K\in\Im_h(\Omega_{n+1})}\left[\int_{\Omega_K}\left(tr\dot{\varepsilon}_{n+1}(v+b)+\frac{\dot{p}_{n+1}}{\chi}\right)p^* d\Omega_K\right]=0. \end{cases} \quad (1.82)$$

In practice, if the time step is taken sufficiently small so as to enable small strain increments, Ω_{n+1} is taken equal to Ω_n. The configuration of the body is then updated via Equation 1.67.

5 Resolution

5.1 Non-linear system of equation to be solved

The nonlinear algebraic system of Equations 1.77 can be written as global residuals as follows:

$$R=\begin{cases} R^v(v_h,b_h,p_h)=R^{vv}+R^{vb}+R^{vp}+F^v=0 \\ R^b(v_h,b_h,p_h)=R^{bv}+R^{bb}+R^{bp}+F^b=0 \\ R^p(v_h,b_h,p_h)=R^{pv}+R^{pb}+R^{pp}=0 \end{cases} \quad (1.83)$$

Taking into consideration the various simplifications, the actual discrete problem 1.80 yields the following system, decoupled in terms of v_h and b_h:

$$R=\begin{cases} R^{v}(v_h,p_h)=R^{vv}+0+R^{vp}+F^{v}=0 \\ R^{b}(b_h,p_h)=0+R^{bb}+R^{bp}+0=0 \\ R^{p}(v_h,b_h,p_h)=R^{pv}+R^{pb}+R^{pp}=0 \end{cases} \tag{1.84}$$

In a more general form, if α stands for a vector containing the discretization parameters (pressure and velocity), the incremental problem consists of solving $R(\alpha_{n+1}) = 0$ starting from a (pseudo) equilibrium solution at $R(\alpha_n) = 0$ such that $\alpha_{n+1} = \alpha_n + \Delta\alpha_n$.

5.2 Resolution of the non-linear system

A Newton-Raphson method is used to solve the non-linear system 1.84. The Newton-Raphson converges quite rapidly, providing that the initial guess is close to the actual zone containing the solution. If this is the case, the convergence is quadratic. Otherwise, it may diverge.

The method consists in linearizing the residual $R(\alpha_{n+1})$ with respect to the discretization parameter α. This yields to:

$$R\left(\alpha_{n+1}^{i+1}\right)\cong R\left(\alpha_{n+1}^{i}\right)+\left(\frac{\partial R}{\partial \alpha}\right)_{n+1}^{i}\delta\alpha_{n}^{i}=0, \tag{1.85}$$

where *i* stands for the iteration counter. The iterative correction is then given by:

$$\left(\frac{\partial R}{\partial \alpha}\right)_{n+1}^{i}\delta\alpha_{n}^{i}=-R\left(\alpha_{n+1}^{i}\right). \tag{1.86}$$

Once convergence is achieved, the variables are updated as follows:

$$\alpha_{n+1}^{i+1}=\alpha_{n+1}^{i}+\delta\alpha_{n}^{i}=\alpha_{n}+\Delta\alpha_{n}^{i}. \tag{1.87}$$

Applying this procedure to the system 1.84 yields, in each element, the following algebraic system:

$$\begin{pmatrix} K^{vv} & 0 & K^{vp} \\ 0 & K^{bb} & K^{bp} \\ K^{pv} & K^{pb} & K^{pp} \end{pmatrix}_{n+1}^{i}\begin{pmatrix} \delta_v \\ \delta_b \\ \delta_p \end{pmatrix}_{n}^{i}=-\begin{pmatrix} R^{v} \\ R^{b} \\ R^{p} \end{pmatrix}_{n+1}^{i}, \tag{1.88}$$

where K^{xy} are the local stiffness matrix components. These are given by:

$$K^{xy}=\frac{\partial R^{xy}}{\partial x}, \tag{1.89}$$

with $(x,y)\in\{v,b,p\}$.

A condensation of the bubble is used at the local level in order to eliminate the extra degree of freedom δ_b associated with the bubble [Jaouen, 1998]:

$$\delta_b = -\left(K^{bb}\right)-1\left(R^b + K^{bp}\delta_p\right). \tag{1.90}$$

This yields to the following local system, where the unknowns are the pressure and the three components of the velocity field:

$$\begin{pmatrix} K^{vv} & K^{vp} \\ K^{pv} & K^{pp} - K^{bp^{-1}}(K^{bb})^{-1}K^{bp} \end{pmatrix}_{n+1}^{i} \begin{pmatrix} \delta_v \\ \delta_p \end{pmatrix}_n^i = -\begin{pmatrix} R^v \\ R^p - K^{bb^t}(K^{bb})^{-1}R^b \end{pmatrix}_{n+1}^{i}. \tag{1.91}$$

In effect, the use of the bubble function in the mini-element is equivalent to adding stabilizing terms to the local (and so to global) stiffness matrix of the problem. These stabilizing terms are responsible for the versatility of the mini-element, which can be used in all contexts (compressible or nearly incompressible materials).

The Newton-Raphson (NR) method is the most widely used method to solve the equilibrium equations in crystal plasticity models. However, different methods to solve this equilibrium problem can be found in the literature. In [Hoon Kim, 2013], Hoon Kim proposes a Nelder-Mead (NM) simplex algorithm. With this technique it is possible to solve the equilibrium equations without the first order derivatives of the constitutive equations. Hoon Kim compared the results obtained with both techniques and similar results were obtained. In [Chockalingam, 2013], Chockalingam proposes a Jacobian-Free Newton Krylov (JFNK) method. In this case the Jacobian can be approximated with finite differences, thereby avoiding the calculation of the first order derivatives. In his paper Chockakingam shows that, when using a temperature dependent flow rule, the calculation using the JFNK method can be seven times faster than the calculation performed using the NR technique. However, when using the simpler power flow rule, it was found that the JFNK method was 67% slower than NR.

5.3 General solution procedure and numerical implementation

In order to solve the mechanical problem, the constitutive law has to be coupled to the finite element scheme. It is important to note that, given the type of element used in this work, there is only one Gauss point per element for integration of the constitutive equations. The solution procedure at a given time step can be summarized as follows:

CP1 → calculate the initial estimate of the velocity vector (solution of the previous increment),

CP2 → compute the element velocity gradient used as input to the constitutive model,

CP3 → iterate at the constitutive law level in order to compute the table variables at time $t + \Delta t$ and the tangent modulus,

CP4 → solve the global system of equations for the velocity and pressure fields at time $t + \Delta t$ using a Newton-Raphson algorithm and go back to point 2 until convergence is achieved,

CP5 → if convergence occurs, update the velocity and pressure fields and the configuration of the body and move on to the next increment.

To ensure that the strain increment remains small so as to ensure optimum convergence of the procedure, an automatic time step adaptation algorithm is used. The automatic adaptation of time step depends on the strain imposed in this given time step. If the strain increment in a given time increment is higher than a critical value, the time step will automatically decrease. On the other hand, if the strain increment is smaller than a limit value, the time step will increase. Moreover, an automatic subincrementation algorithm is adopted in order to ensure accurate integration of the constitutive equations. This subincrementation is performed inside the crystal plasticity code when the calculation does not converge. In this case, the time step is divided in a few subincrements and the simulation is repeated for all subincrements.

6 Conclusion

As it was discussed in this chapter introduction, the correct simulation of the material microstructure evolution during thermo-mechanical process is of prime importance in order to simulate recrystallization and grain growth phenomena. In this chapter the process of plastic deformation of FCC metals is briefly reviewed so as to underline the resulting intergranular and intragranular heterogeneities. The mechanical behaviour of a single crystal is analysed, with emphasis on a finite element implementation. The slip system concept represents a homogenized way of taking into consideration the motion of individual dislocations gliding under the effect of the critical resolved shear stress. The flow rule reflects the non-linear relationship between strain rate and stress. Considering the hardening, physically-based models were emphasized, focusing on the use of one or several dislocation densities as primary variables. The account of size effects was discussed, distinguishing between statistically stored dislocations (SSDs), and geometrically necessary dislocations (GNDs). A simple model (Yoshie-Laasraoui-Jonas) is adopted to estimate the SSD density evolution with plastic deformation, while the Busso model is chosen to calculate the contribution of the GND density. Finally, the link between the crystal plasticity model and the finite element formulation is presented as well. The crystal plasticity simulation results are presented and discussed in chapter 3.

Résumé en Français

Lorsqu'un matériau polycristallin est soumis à une transformation thermomécanique, ses propriétés mécaniques évoluent de manière corrélée à sa microstructure. De plus, ces changements microstructuraux sont également de première importance vis-à-vis des cinétiques de restauration, recristallisation et croissance de grains pendant les traitements de recuit. Ainsi, afin de bien modéliser les phénomènes de recristallisation et de croissance de grains, la prédiction de l'état microstructural d'un matériau polycristallin après déformation plastique doit être correctement réalisée. Dans ce chapitre, la déformation plastique des matériaux métalliques présentant une structure de type C.F.C. est brièvement présentée. De plus, un état de l'art des différents modèles de simulation de la plasticité cristalline existant dans la littérature est présenté : l'accent est mis sur les modèles d'écrouissage. Deux types de modèle d'écrouissage sont présentés : un premier modèle qui considère uniquement les densités de dislocations totales, et un deuxième modèle qui différencie les dislocations statistiquement stockées (SSDs), des dislocations géométriquement nécessaires (GNDs). Dans le premier cas, le modèle de Yoshie-Laasraoui-Jonas est implémenté et, dans le deuxième, le modèle de Busso. Finalement le couplage entre le modèle de plasticité cristalline retenu et une

formulation éléments finis est présenté. Les résultats des simulations de plasticité cristalline sont présentés et discutés dans le chapitre 3.

Chapter 2

Statistical generation of polycrystals in a finite element context and a level-set framework – Method and results

Contents

1 Introduction 48
2 Voronoï and Laguerre Voronoï tessellations 49
3 Microstructure immersion in FE Mesh 52
4 Microstructure Generation - Results 55
4.1 Obeying a grain size distribution in 2D microstructures 56
4.1.1 Voronoï Tessellation Method 56
4.1.2 Laguerre-Voronoï Tessellation Method 59
4.2 Obeying a grain size distribution in 3D microstructures 63
4.2.1 Voronoï Tessellation Method 64
4.2.2 Laguerre-Voronoï Tessellation Method 65
4.3 Topological study of 2D Laguerre-Voronoï microstructures 67
4.4 Morphological study of Laguerre-Voronoï microstructures 71
5 Conclusion 76

1 Introduction

Metallurgical phenomena occurring in metallic materials during thermo-mechanical processing (plastic deformation, recovery, recrystallization, grain growth, phase transformations, etc.) are closely related to the material microstructural condition. The grain size distribution, the presence or not of precipitates together with their shape and distribution, the dislocation density distribution after plastic deformation, all these factors can completely change the metallurgical phenomena kinetics. As a consequence, the material thermo-mechanical behaviour will also change. Therefore, in order to accurately model the metallurgical phenomena occurring during thermo-mechanical processing, it has become more and more frequent to build the so called “digital microstructures”, which are numerical representations (and idealizations) of real ones.

If one looks at the dislocation density distribution induced by plastic deformation, different models can be identified in the literature. Such models can be used to compute the dislocation density evolution during plastic deformation, and some of them have been presented and discussed in chapter 1. In chapter 3, a comparison between crystal plasticity simulation results, based on two different hardening laws, are discussed. Finally, the influence of the dislocation density distribution on the recrystallization kinetics is analysed in chapter 5.

In this work, idealized metallic microstructures will be considered, in particular ignoring the potential presence of precipitates. An example of digital microstructure generated considering the presence of precipitates can be found in [Agnoli, 2012]. In this chapter we will focus on the generation of digital microstructures obeying a given experimental grain size distribution, and on the construction of the associated finite element meshes.

The creation of representative digital microstructures based on experimental data is not a simple problem and is not related only to the creation of polycrystalline materials. When modelling particle suspensions, porous media or powders, the correct representation of the experimental data is of prime importance. In [Hitti, 2011], [Hitti, 2012] the authors presented and discussed all the challenges that must be overcome in order to correctly generate a representative microstructure based on experimental data. In the work presented here, we use the model developed by [Hitti, 2011] and implemented in the CimLib library to generate our digital microstructures.

In [Hitti, 2011] two different techniques to generate representative digital microstructures are implemented. The first one is the Voronoï tessellation method, a geometric method that partitions a space into convex polyhedral cells. Owing to its resemblance to many cellular structures appearing in the nature, Voronoï tessellations are used in a wide range of fields, including biology [Finney, 1978] and zoology [Mallory, 1983]. However, the Voronoï tessellation presents some limitation towards grain size distributions despite its widely use and easy numerical implementation. In fact, with this method, the location of the Voronoï cell nuclei is the only way to define the Voronoï tessellations without control on the cell characteristics. The second technique is the Laguerre-Voronoï tessellation method [Aurenhammer, 1987], [Imai, 1985]. A Laguerre-Voronoï diagram corresponds to a Voronoï diagram where the location of the cells faces is constrained by a given non-intersecting spherical packing.

Once the digital microstructure is generated, it must be connected to finite element simulations. Once again, several techniques are available in the literature. The most widely used method consists in generating a surface mesh for each grain, and then generating a volume mesh based on these surface meshes [Rollet, 2004]. In this work, we use instead an implicit method to capture the grain interfaces. This implicit method is based on a level-set approach to define the different interfaces. The use of level-set functions in modelling equiaxed polycrystals made of Voronoï cells was introduced by Bernacki [Bernacki, 2009].

This approach was applied successfully for the generation of 2D or 3D polycrystals but for a moderate number of grains. Indeed, one difficulty of this method is the numerical cost, which depends on the number of grains, as well as on the finite element mesh used to describe the polycrystal.

In this chapter both models implemented by [Hitti, 2011], Voronoï and Laguerre-Voronoï tessellations, are presented. The method used to immerse these digital microstructures in a finite element mesh using a level-set approach is discussed. Moreover, the methodology used to generate adapted anisotropic finite element mesh is also described. Finally, the capabilities of the proposed numerical framework are illustrated. More precisely, the characteristics of the generated digital microstructures are discussed in terms of grain size distribution (in 2D and 3D) and morphological/topological attributes (in 2D).

It must be underlined that all the distributions or mean values discussed in this chapter concerning grain features (grain size, number of sides...) were evaluated as number-weighted (otherwise, it will be indicated in the text).

2 Voronoï and Laguerre Voronoï tessellations

The Voronoï tessellation is the most widely used method for generating digital polycrystalline microstructures [Rollett, 2004]. In [Logé, 2008], [Bernacki, 2009], [Resk, 2009] and [Quey, 2011] the authors use the Voronoï method associated with a level set framework and a finite element formulation to model crystal plasticity and static recrystallization. Another example can be found in [Elsey, 2009] where the authors also generate their digital microstructures using the Voronoï method. They then simulate the grain growth phenomenon using a level set framework associated with a finite difference formulation. Such attractiveness of Voronoï tessellation can be explained by its simplicity of implementation. Indeed the Voronoï tessellation or diagram is fully described by a set of N seeds or Voronoï nuclei $(S_i)_{i=1,\dots,N}$. Each nucleus S_i defines a Voronoï cell V_i, which consists of all points closer to S_i than to any other nucleus (see Figure 2.1):

$$V_i = \left\{ x \in R^d \,/\, d(x, S_i) = \min_{1 \le j \le N} d(x, S_j) \right\} \tag{2.1}$$

where d is the space dimension and $d(.,.)$ is the usual Euclidian distance.

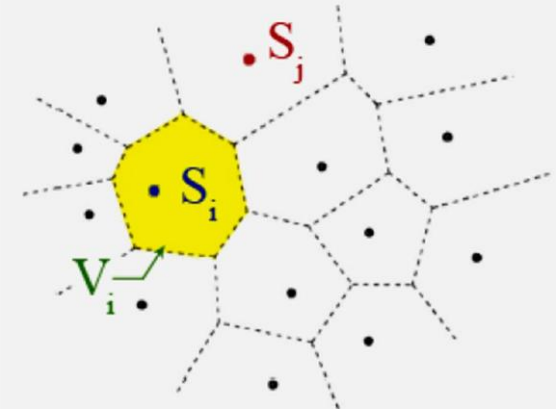

Figure 2.1: *A Voronoï diagram in 2D.*

The Voronoï diagrams can be generated using two different techniques. The first one is a direct method, which consists in constructing the perpendicular bisectors of the adjacent sites and their intersections will form the diagram. The second is based on the construction of

Delaunay's triangulation (Voronoï's dual) and then drawing the perpendicular bisectors of its edges. Figure 2.2 illustrates the Voronoï nuclei (left side) used to generate a 3D Voronoï diagram made of 100 cells.

Despite its widespread use, the classical Voronoï method does not allow to obey a given grain size distribution. In fact, only the mean grain size is set. Even though, in general, this limit is not discussed; in [Xu, 2009], Xu highlighted divergences between statistical properties classically observed in equiaxed polycrystals and the results obtained using Voronoï method.

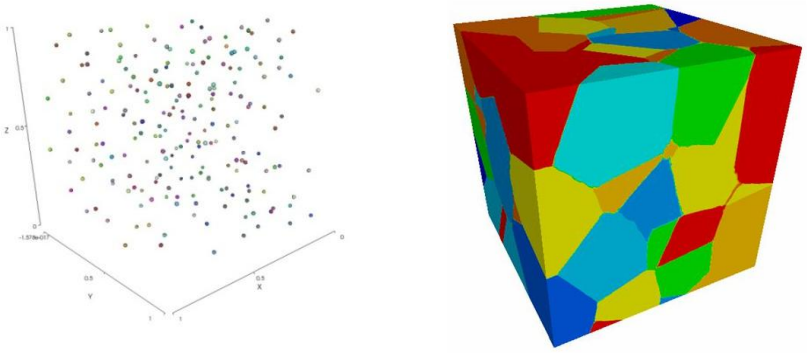

(a) (b)

Figure 2.2: (a) *100 sites of Voronoï in a unit cube and (b) the resulting 3D Voronoï structure.*

Hence, obeying a specific grain size distribution while generating a statistical digital microstructure is not easy. To obtain such microstructures, the Laguerre-Voronoï tessellation Method can be used [Aurenhammer, 1987], [Imai, 1985]. This method consists in using a distribution of non-intersected spherical particles that serves as a basis for constructing the microstructure. In this case, the Laguerre-Voronoï tessellation is described by a set of N seeds and weights $(S_i, r_i)_{i=1,\ldots,N}$. Each nucleus and weight (S_i, r_i) defines a Laguerre-Voronoï cell L_i, which consists of all points closer to S_i, via the power distance (defined below), than to any other nucleus:

$$L_i = \left\{ x \in R^d \,/\, \Pi(x, S_i) = \min_{1 \le j \le N} \Pi(x, S_j) \right\}, \tag{2.2}$$

where $\prod(x, S_i) = d(x, S_i)^2 - r_i^2$ is the power distance of S_i to x. Figure 2.3 illustrates a set of spherical particles used as a base to generate the corresponding Laguerre-Voronoï cells.

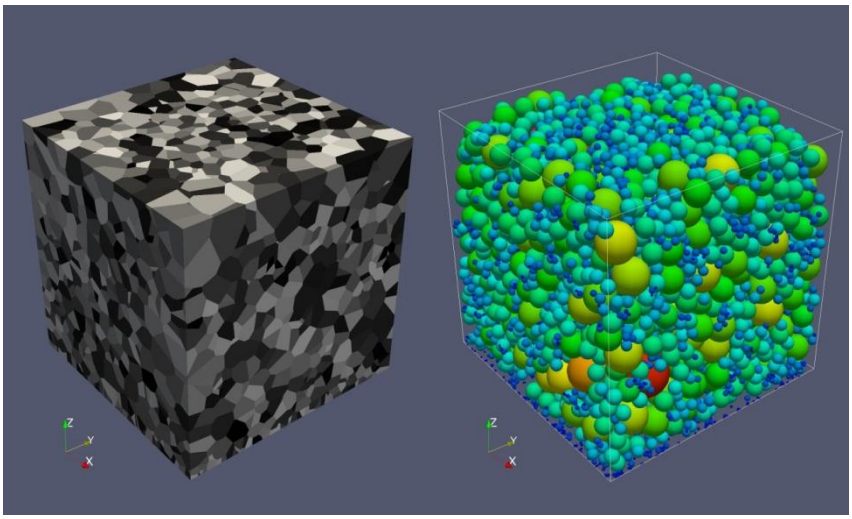

Figure 2.3: *A 3D Laguerre-Voronoï tessellation and the dense sphere packing used to generate it.*

This method was successfully used to model polycrystalline structures [Fan, 2004], [Hitti, 2011], [Hitti, 2012] and nanostructured materials [Benabbou, 2010]. In [Lavergne, 2013], using the Laguerre-Voronoï method, the authors generate not only microstructures with equiaxed grains but also more complex microstructures with elongated or flat grains. It is important to underline that the simplicity of Laguerre-Voronoï methodology is only apparent. Indeed, in order to obey statistically a given grain size distribution, the principal difficulty of the Laguerre-Voronoï methodology is in the generation of the dense sphere packing which must obey the size distribution with the highest possible density. Once the microstructure is generated, the digital microstructure must be linked to the finite elements mesh. In the context of unstructured meshes, as used in this work, different methods can be found in the literature. The most widely used method consists in generating a surface mesh for each cell (coincident with the neighboring grain) and then generating a volume mesh based on these surface meshes (Figure 2.4) [Rollet, 2004].

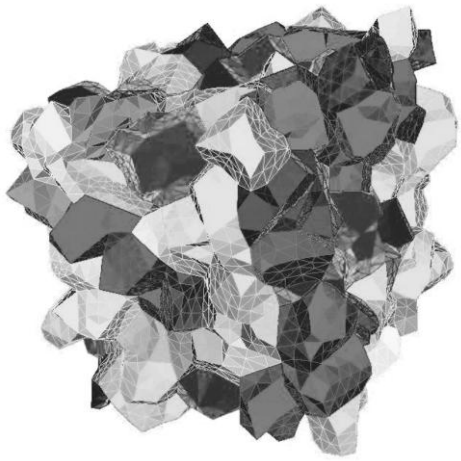

Figure 2.4: *Three-dimensional mesh of an equiaxed single-phase microstructure containing 134 grains (Voronoï cells) generated using a surface mesh [Rollet, 2004].*

This method is appropriate in the case of polycrystals deformation simulation. However, when modeling recrystallization and grain growth, the grain boundaries move with nucleation and disappearance of certain grains. In these situations, the remeshing operations needed to take into account these topological events are extremely complex. So, the use of this method is not straightforward in those conditions. That is the reason why finite element methods emphasizing an explicit description of grains boundaries (for example: Vertex methods [Barrales, 2008]) are confronted to problems of mesh management which are mainly inextricable in 3D, and this explains also the current craze for methods favoring an implicit grain boundaries description such as the phase field [Suwa, 2008], [Takaki, 2010] or level set methods.

Since 2005, CEMEF works on the development of a formalism to generate polycrystals immerged into finite element mesh. This formalism, described in the following, is based on an optimized level set functions calculation from Voronoï or Laguerre-Voronoï sites, and a mesh adaptation in the context of a large number of level set functions forming a partition of the study area [Loge, 2008], [Hitti, 2012], [Bernacki, 2009], [Resk, 2009].

3 Microstructure immersion in FE Mesh

In our methodology, the locations of the grain boundaries are defined implicitly using a level-set framework. A level-set function ϕ, defined over a domain Ω, is called distance function of an interface Γ of a sub-domain Ω_S if, at any point x of Ω, it corresponds to the distance from Γ. In turn, the interface Γ is given by the zero isovalue of the function ϕ:

$$\begin{cases} \phi(x) = \chi_{\Omega_S}(x)d(x,\Gamma) - \chi_{\overline{\Omega_S}}(x)d(x,\Gamma), x \in \Omega \\ \Gamma = \{x \in \Omega, \phi(x) = 0\}. \end{cases} \quad (2.3)$$

with χ_{Ω_S} the characteristic function of Ω_S equal to 1 in Ω_S and 0 elsewhere. With the previous proposed equation: $\phi(x) \geq 0$ inside the domain defined by the interface Γ and $\phi(x) \leq 0$ outside this domain. Assuming that the domain is a polycrystal, for each existing grain in the domain, a level-set function is created. So, if domain Ω is formed by N grains, we will have N level set functions $\{\phi_i, 1 \leq i \leq N\}$. In this case, a global unsigned level-set function can be defined as:

$$\forall x \in \Omega,\ \phi_{glob}(x) = \max_{1 \leq i \leq N}(\phi_i(x)). \quad (2.4)$$

This function is positive everywhere and tends to zero on the grain boundaries network. Figures 2.5 a, b, c illustrates three level set functions for three different grains forming a triple junction in 2D (grain boundaries correspond to the black lines) and Figure 2.5d illustrates the global level set function (Equation 2.4) for these three same grains.

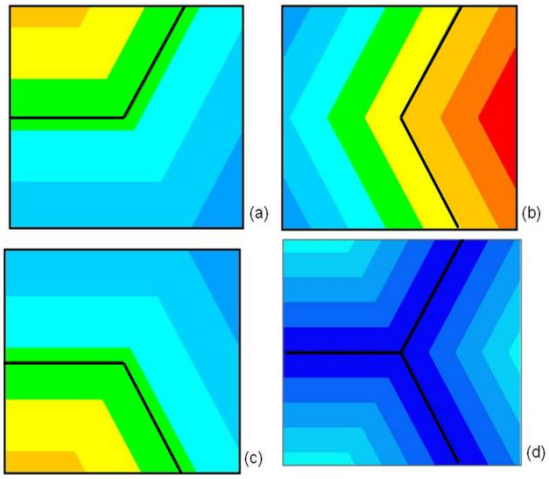

Figure 2.5: *(a), (b) and (c) Three level-set functions defining three grains and (d) the global level-set function.*

In the following, we explain how the level-set functions of the considered cells (in Voronoï or Laguerre-Voronoï formalisms) can be defined in an unstructured FE mesh.

Concerning Voronoï cells, the idea is to consider for each FE mesh integration point X of coordinates x and two Voronoï nuclei s_i and s_j, the function:

$$\alpha_{ij}(x) = \frac{1}{2}\left\| \vec{s_i s_j} \right\| - \frac{\vec{s_i s_j} \cdot \vec{s_i x}}{\left\| \vec{s_i s_j} \right\|}, 1 \le i, j \le N,\ j \ne i, \tag{2.5}$$

which corresponds to the signed distance of X to the perpendicular bisector of $[s_i s_j]$. The level-set function $\phi_i(x)$, defining the Voronoï cell of the nucleus s_i, is then given by:

$$\phi_i(x) = \min_{\substack{1 \le j \le N \\ j \ne i}} \left(\alpha_{ij}(x)\right),\ 1 \le i \le N. \tag{2.6}$$

Moreover, for the above level-set calculation, the Delaunay triangulation [Frey, 1999], [Hitti, 2012] can be helpful. The Delaunay triangulation gives the graph of each nucleus s_i, which is the set of the nuclei $\{s_j, s \ne i\}$ that share an edge of the Delaunay triangulation with s_i. As a consequence, the graph of each nucleus s_i, which corresponds to the set of its neighbours in the Delaunay triangulation, is sufficient to determine the level-set functions and Equation 2.6 can be rewritten:

$$\phi_i(x) = \min_{j \in Graph(s_i)} \left(\alpha_{ij}(x)\right),\ 1 \le i \le N. \tag{2.7}$$

Figure 2.6 illustrates how useful the Delaunay triangulation is for calculating level-set functions. Without it, to calculate the level-set defining the Voronoï cell of nucleus S_i, all the nuclei S_j ($j \ne i$) must be taken into consideration in the algorithm. Thanks to the Delaunay triangulation, only the points S_j belonging to the graph (S_i) are considered. The computation time decrease depends on the number of grains and the number of nodes existing in the domain. In [Hitti, 2011] the computation time decrease for different meshes and number of grains is presented.

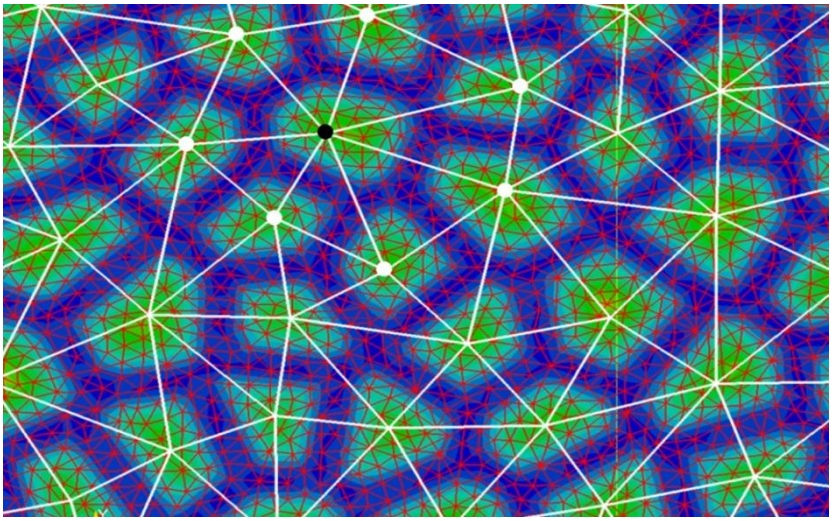

Figure 2.6: *FE Mesh (red), Delaunay triangulation (white), s_i site (black), its graph (white dots) and the global level-set function [Hitti, 2011].*

Concerning Laguerre-Voronoï cells, the level-set functions are also given by Equation 2.7 (with graph*(s_i)* given by the weighted Delaunay triangulation [Hitti, 2011], [Hitti, 2012]) but the α_{ij} functions (Equation 2.5) are modified as follows:

$$\alpha_{ij}(x) = \frac{1}{2}\left(\left\| \vec{s_i s_j} \right\| + \frac{r_i^2 - r_j^2}{\left\| \vec{s_i s_j} \right\|} \right) - \frac{\vec{s_i s_j} \cdot \vec{s_i x}}{\left\| \vec{s_i s_j} \right\|}, 1 \le i, j \le N, j \ne i, \quad (2.8)$$

where r_i and r_j are, respectively, the radii of s_i and s_j.

Until now, only the microstructure generation and its immersion into a finite element mesh have been discussed without dealing with the problem of the mesh refinement required for a good accuracy of the calculations. The use of a monolithic approach in association with a level set description of the digital microstructure leads to the need of using a fine mesh or a high interpolation degree at the interfaces to ensure the correct description of the microstructure. It is important to highlight that the grain boundary velocity during grain growth and recrystallization depends on the grain morphology (grain boundary curvature – see chapter 4). So, the correct description of the microstructure is of prime importance in order to ensure the correct simulation of grain boundary motion. Moreover, an accurate description of the grain boundaries is also needed when dealing with possible physical properties discontinuities appearing at interfaces or multiple junctions. In our numerical strategy, meshing adaption with a P1 interpolation order was preferred. If a global isotropic remeshing of the mesh can be used to reach the desired accuracy in the interface description, this strategy leads to a significant increase in computational resources. Therefore, an adaptive anisotropic remeshing technique is favored. It is valuable to underline that the use of anisotropic mesh elements generates no damage to recrystallization or grain growth simulations since grain boundary velocity is always perpendicular to the grain boundary, i.e. in the direction of the mesh refinement. Different ways to generate an adapted anisotropic mesh are found in the literature. In this Ph.D. work, two methods have been used to build anisotropic mesh metrics, from which anisotropic meshes were built using the MTC topological mesher-remesher developed by Coupez et al. [Coupez, 2000].

The first method, called *a priori*, consists in refining the mesh in a small thickness zone around the interfaces. The refinement operates only in the direction perpendicular to the interface, leading to an anisotropic mesh. In order to create an anisotropic mesh, in a first step, the thickness (e) of the re-meshing zone is defined. Next, the mesh size in the direction perpendicular to the interface (h_f) inside the re-meshed zone is imposed. Finally, a coarser mesh size (h) is imposed far from the interface. The h value is also generally used as the mesh size in the direction tangential to the interface, inside the re-meshed zone.

When dealing with polycrystalline aggregates and multiple interfaces, the above strategy is repeated for each grain. Combining all information, the number of refinement directions is then evaluated at each mesh node. For the nodes outside the remeshed zone, there is no refinement direction and, as a consequence, the mesh size is isotropic with a mesh size equal to h. As the number of refinement directions increases, the mesh size is reduced in one or several directions. This happens when the node is placed on the remeshing zone of two different level-set functions. As a consequence, at the triple or multiple junctions, the refinement may become isotropic with a mesh size equal to h_f [Resk, 2009], [Bernacki, 2009].

When using this method, the number of elements existing in the final mesh cannot be easily controlled, which can lead to a dramatically increase of the computation time, especially in 3D.

The second method, called *a posteriori* method, consists in using an error analysis in order to obtain an optimal mesh for a given physical field and number of elements [Almeida, 2000], [Mesri, 2008]. In our particular case, as we seek to adapt our mesh in the grain boundary areas extending perpendicularly to the interfaces, we use a function based on the global level set function of our microstructure to generate the adapted mesh. This anisotropic

(re-)meshing method leads to a very high accuracy near the interfaces without increasing dramatically the computation resources [Coupez, 2000] since the number of elements is imposed. [Almeida, 2000], [Mesri, 2008]. Figure 2.7 illustrates meshes obtained with the two methods, a priori and a posteriori.

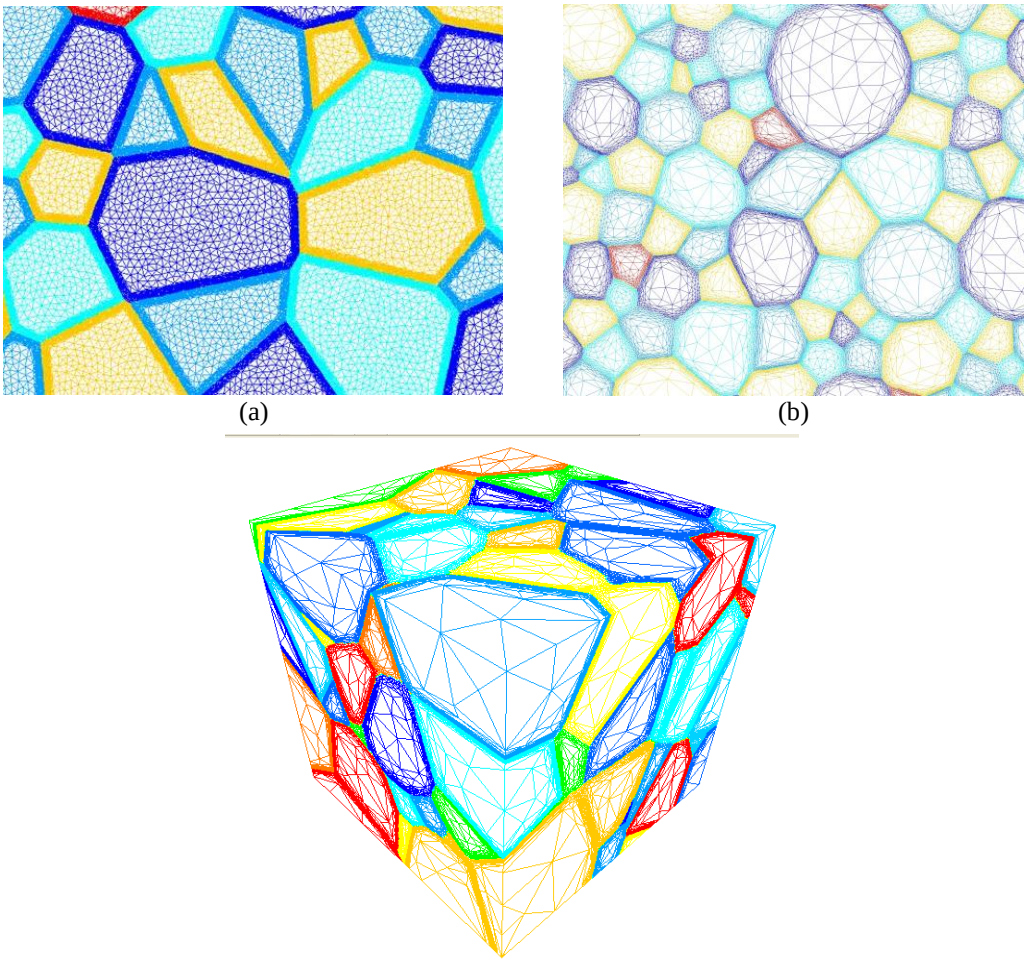

(a) (b)

(c)

Figure 2.7: *(a) Zoom of a 2D microstructure immerged in a finite element mesh adapted using an a priori method. The mesh is formed by 148 802 elements. (b) Zoom of a 2D microstructure immerged in a finite element mesh adapted using an a posteriori method. This mesh is formed by 102 135 elements. (c) 3D polycrystal immerged in a finite element mesh adapted using an a posteriori technique. This mesh is composed of 984 884 elements.*

4. Microstructure Generation - Results

In the above topics of this chapter, all the numerical tools needed to generate the digital microstructures used in all simulations performed during this project have been presented. Once the basic concepts are well understood, we are now interested in study the capabilities and the limitations of the digital microstructure generation methods.

In the following topics, we will discuss the relevance of choosing the Laguerre-Voronoï method instead of the Voronoï method, based on the ability of obeying a given grain size distribution (2D and 3D). Finally, a topological and morphological analysis of 2D digital microstructures generated using the Laguerre-Voronoï method is presented.

4.1 Obeying a grain size distribution in 2D microstructures

A 2D 304L experimental grain size distribution was obtained using optical microscope image analysis (Fig. 2.8). Surface preparation included a standard metallographic method consisting in successive wet grinding from 600 grit paper to 4000 grit. The sample was then polished using a 1 µm diamond paste. A final procedure using colloidal silica (OPS) was used to obtain a good finish of the surface. The polished samples were etched with a chemical solution composed of a 50 ml hydrochloric acid (HCl) solution (100 ml of HCl for 1 litre of water) and 15 drops of H_2O_2 (~5ml). To obtain a representative result, 21 images have been combined. Figure 2.8 shows a part of the total image. Grain boundaries were identified and are drawn with white lines. The thin and elongated twin boundaries were not taken into account when determining the number-weighted grain size distributions.

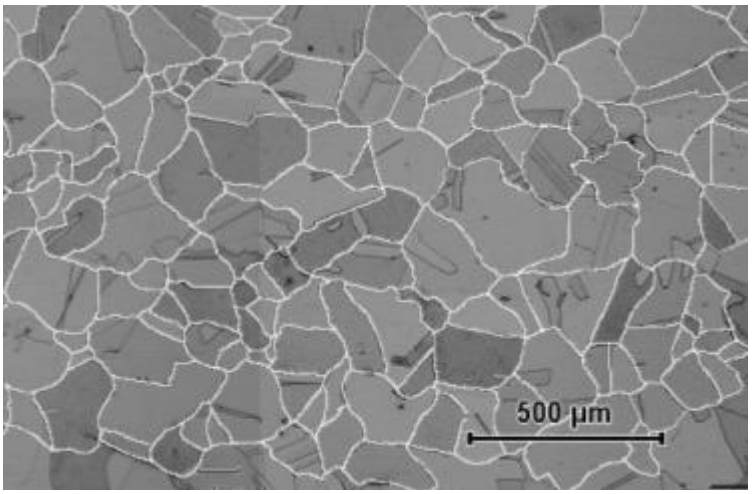

Figure 2.8: *Optical microscope image of 304L stainless steel with grain boundaries drawn in white lines.*

Image analysis of the surface was done with the Visilog 6.3 software, and involved the calculation of individual grain areas. Equivalent circles with the same areas were used to build the statistical distributions. Only the grains with a radius larger than 30µm were considered, for the following reasons:

- The total volume fraction of small grains is limited (volume fraction = 0.025) and therefore does not influence very much the macroscopic mechanical behaviour;
- in grain growth regime, the smallest grains disappear fast, within a first initial transient;
- from a mesh adaptation point of view, it is preferable to limit the grain size difference between smaller and larger grains.

4.1.1 Voronoï Tessellation Method

Thanks to the previously described experimental work, the mean grain radius of 304L steel samples was estimated at 67.4 µm. In order to study the Voronoï method, two digital microstructures obeying this mean grain size have been randomly generated (ten times). The first one is composed of 280 grains, in a 2 mm x 2 mm square domain, and the second one exhibits 10080 grains, in a 12 mm x 12 mm square domain (see Figure 2.9). The average of

the numerical grain size distributions obtained was then compared to the experimental 304L grain size distribution as illustrated in Figure 2.10. We can observe that the generated distributions are really different from the experimental one. While the experimental distribution shows a log-normal behavior, both numerical microstructures are closer to a Gaussian number-weighted grain size distribution, independently of the number of grains in the aggregate.

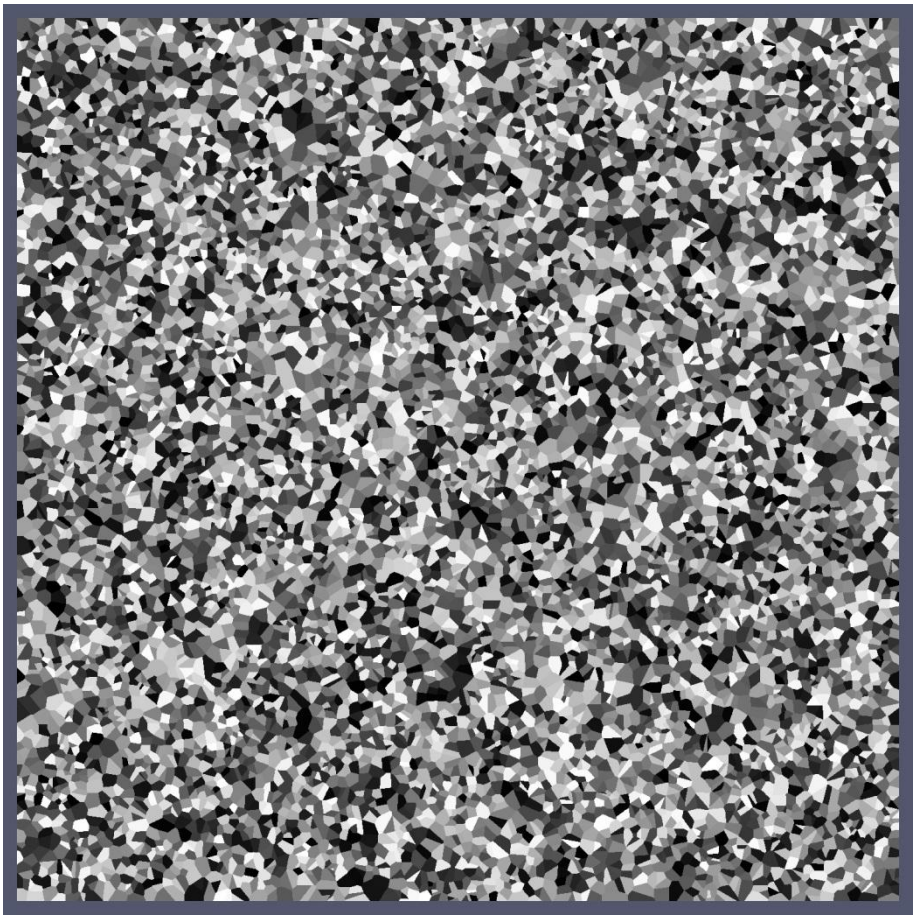

(a)

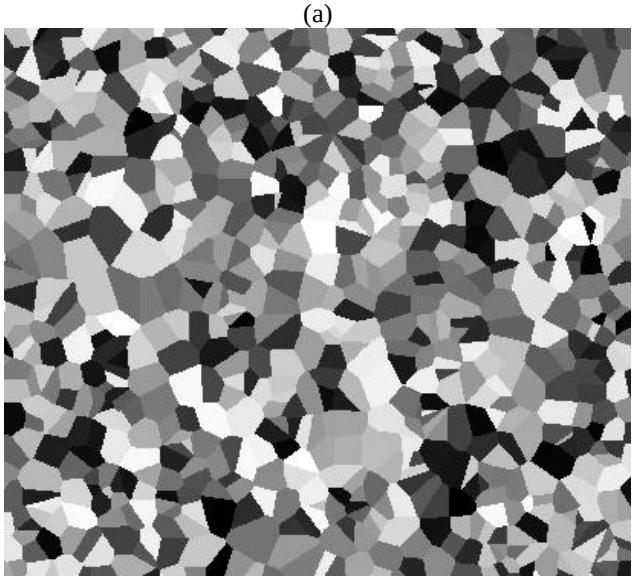

(b)

Figure 2.9: *Virtual generation of a 304L polycrystal using the Voronoï method (10080 grains in a 12 mm x 12 mm square domain): (a) complete image of the digital microstructure, (b) zoom of the same microstructure.*

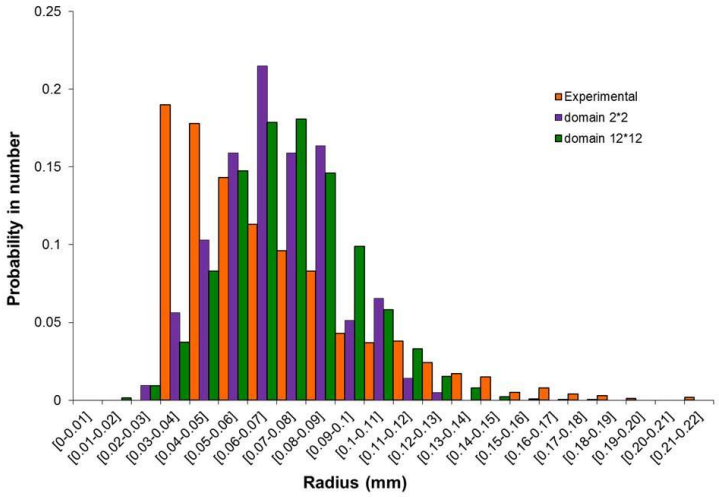

(a)

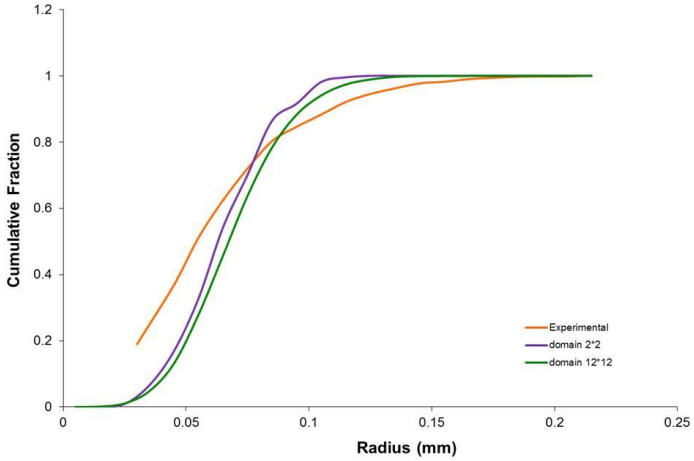

(b)

Figure 2.10: *Comparison between experimental 304L data and digital microstructures generated (average of ten generations) using a Voronoï method in a 2 mm x 2 mm domain and in a 12 mm x 12 mm domain: (a) grain size distribution and (b) cumulative fraction.*

The L2 errors (Equation 2.9 - with f_{ex} the discrete experimental fractions and f_{num} the discrete numerical ones) were evaluated for the two Voronoï tessellations in terms of both grain size distribution and cumulative fraction distribution. The results are summarized in Table 2.1.

$$EL2(\%) = \sqrt{\frac{\sum (f_{ex} - f_{num})^2}{\sum f_{ex}^{\ 2}}}.100, \tag{2.9}$$

Table 2.1 *Probability in number and cumulative fraction L2 error for Voronoï microstructures (average of ten generations).*

Voronoi $\overline{R} = 67.4\mu m$	Histogram L2 Error (%)	Cumulative fraction L2 Error (%)	Number of grains
2 mm x 2 mm	78.6	11.8	280
12 mm x 12 mm	63	11.2	10080

These results illustrate that the Voronoï method is not appropriated to generate a log normal grain size distribution and that, more precisely, its use should be restricted to Gaussian grain size distributions. Considering that log normal grain size distributions are extremely common, the Voronoï method is not, in general, the appropriate tool to generate a numerical aggregate obeying an experimental grain size distribution. Xu, in [Xu, 2009], highlighted similar divergences between statistical properties classically observed in equiaxed polycrystals, and the results obtained using the Voronoï method.

4.1.2 Laguerre-Voronoï Tessellation Method

Regarding the Laguerre-Voronoï method, first results concern the experimental 304L steel grain size distribution: 8 different digital microstructures are generated using 8 different domain sizes: x mm x x mm, $x \in \{1, 2, \ldots, 6, 8, 12\}$. Figure 2.11 illustrates the average results obtained for ten generations of microstructures in the domains 4 mm x 4 mm, 8 mm x 8 mm and 12 mm x 12 mm. The L2 error between the experimental data and the numerical results for the considered microstructures are presented in Figure 2.12.

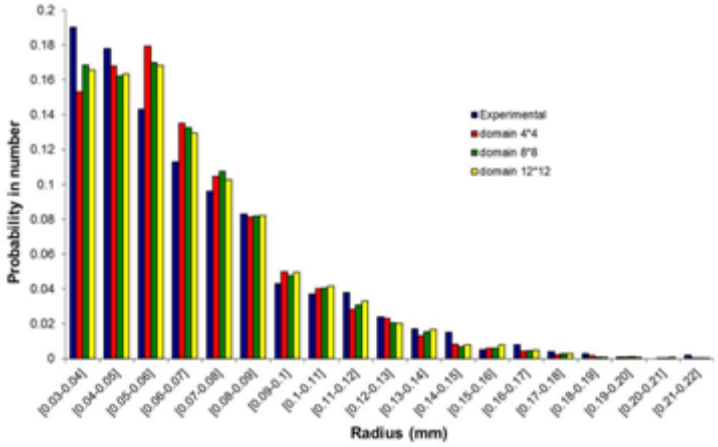

(a)

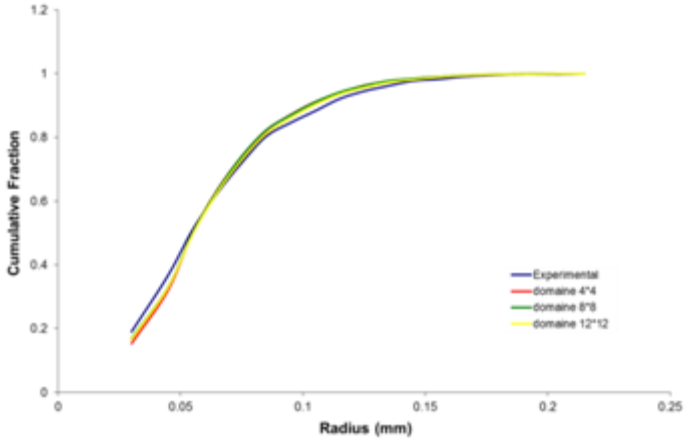

(b)

Figure 2.11: *(a) Comparison between numerical grain size histograms obtained using a Laguerre-Voronoï method (average of ten generations in domains 4 mm x 4mm, 8 mm x 8 mm and 12 mm x 12 mm) and the experimental one (for 304L steel) and (b) comparison between the cumulative fraction distributions for the same cases.*

Analysing Figure 2.12, we observe that the L2 error decreases with the increase of the domain size. This behaviour is expected since increasing the domain size implies generating a larger number of grains and hence a better representation of the microstructure. For domains larger than 4 mm x 4 mm, the error stabilises around 12 %. In the histogram of Figure 2.11, the grain size distribution error is concentrated in the small grain size families. This is due to a slight mismatch between the size of the Laguerre-Voronoï sphere and the grain size obtained after the creation of the Laguerre-Voronoï cells. Thereby, a few grains that should be placed in the range [30, 40] are placed in the [40, 50] range. Considering the cumulative fraction curve of Figure 2.11, the error is smaller than 3.5% for all investigated cases. Nevertheless, when compared to the results obtained for Voronoï tessellations (Table 2.1), and to the state of art [Hitti, 2012], the errors obtained here correspond to very good descriptions of the experimental distribution. There is however a need to continue improving the algorithm of digital microstructure generation, especially for the small grain size range.

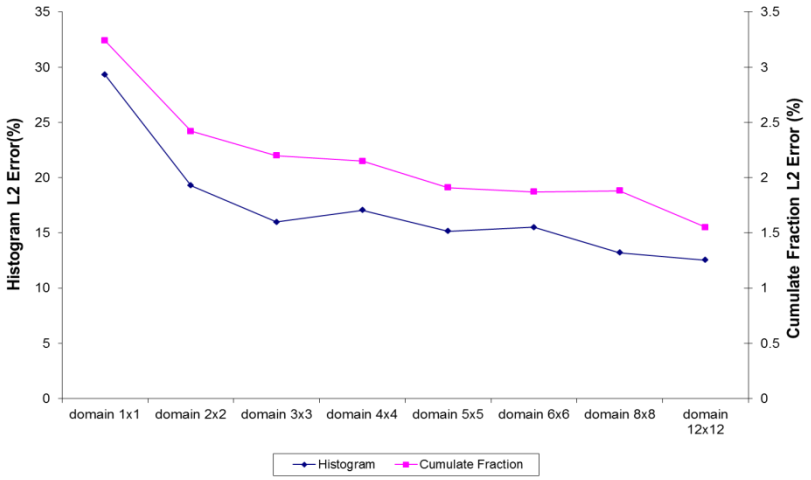

Figure 2.12: *Error L2 between experimental data and numerical results (average of ten generations) of digital microstructures obtained using a Laguerre-Voronoï method - Histogram error (blue line) and cumulative fraction error (pink line).*

Figure 2.13 illustrates one of the digital microstructures generated using the Laguerre-Voronoï method in the 12 mm x 12 mm domain.

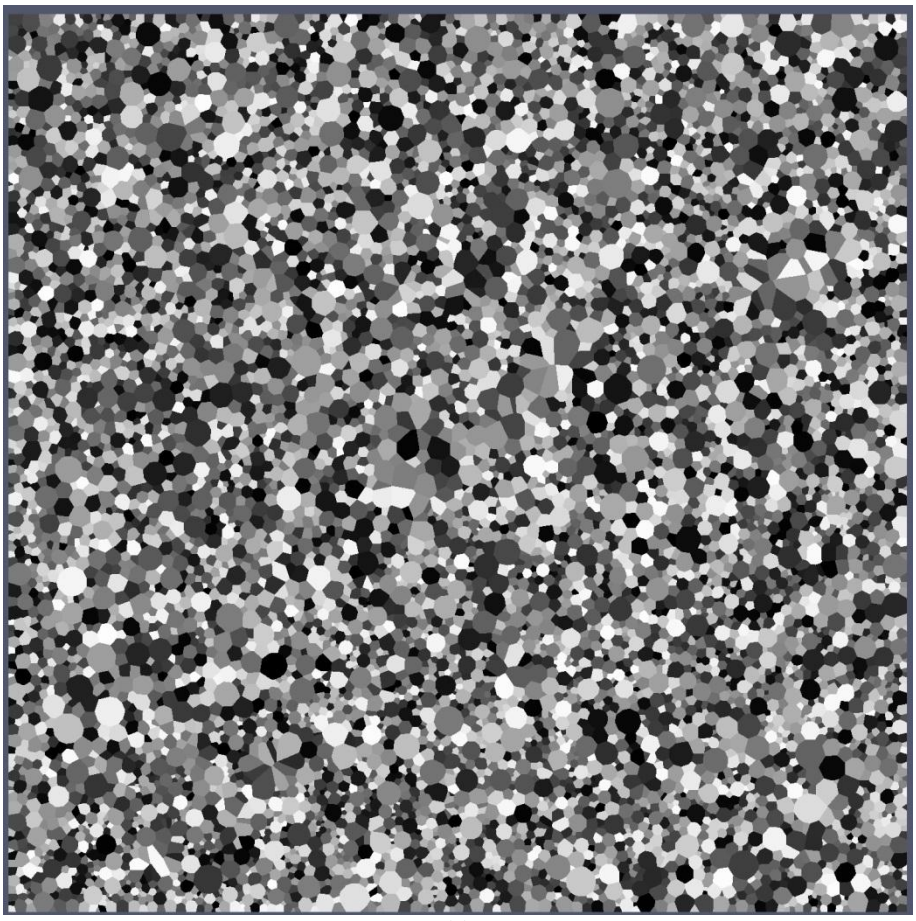

(a)

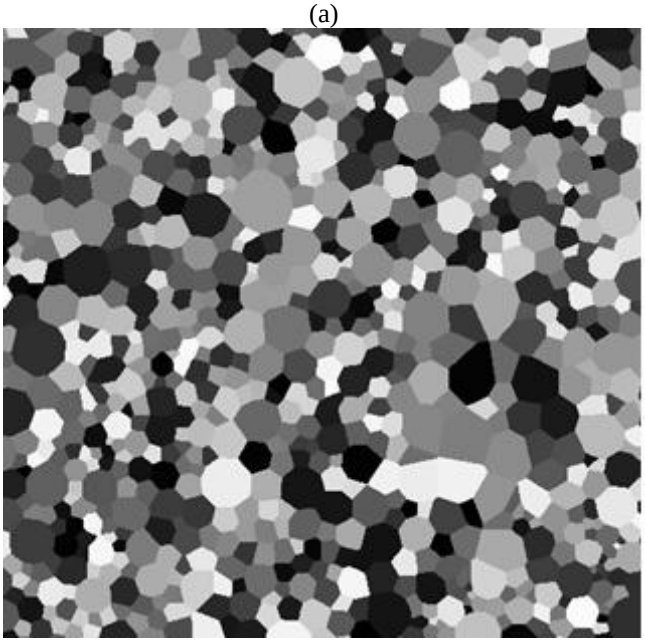

(b)

Figure 2.13: *A 2D digital microstructure made of 8294 grains obtained using a Laguerre-Voronoï method, based on a 304L steel experimental grain size distribution (domain size: 12 mm x 12 mm): (a) complete image of the digital microstructure, (b)zoom of the same microstructure.*

After analysing the possibility of generating a digital microstructure with a grain size distribution close to that of the experimental 304L steel, a more general study can be done about the capacity to generate various grain size distributions. Six different 2D digital microstructures are studied, whose features are presented in Table 2.2.

Table 2.2: *Features of 6 grain size distributions.*

	Mean Radius - μ (µm)	Standard Deviation - σ (µm)	σ/μ	Initial number of grains	Domain Size (mm)
Log1	61.7	7.2	0.12	9728	11 x 11
Log2	63.7	14.1	0.22	10517	12 x 12
Log3	67.4	23.5	0.35	10464	13 x 13
Log4	71.4	31.6	0.44	9999	14 x 14
Log5	75.3	38.4	0.51	8583	14 x 14
Bimodal	62.8	24.3	0.37	9933	12 x 12

The first five distributions are "synthetic" log normal, meaning that they are not based on real experimental data. In these cases, the mean grain size is more or less the same, with a standard deviation ranging between 7µm and 40µm. The last distribution corresponds to a "synthetic" bimodal distribution. The number of grains is around 10,000 for all microstructures, ensuring good microstructure representativity. Figure 2.14 describes comparisons between imposed distributions and the obtained numerical results, and between the theoretical and numerical cumulative fractions. Distributions and cumulative fractions are given as a function of the normalized equivalent radius $(R/< R >)$, where $<R>$ corresponds to the mean grain size. Table 2.3 gives the L2 errors between the theoretical and the numerical distributions and cumulative fractions.

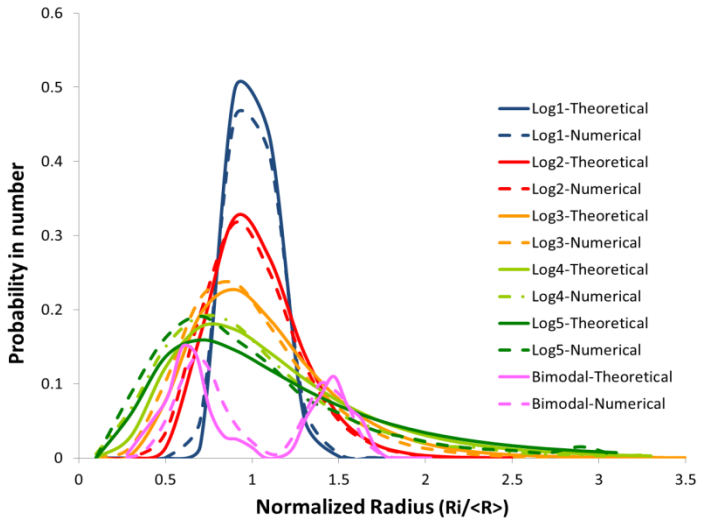

(a)

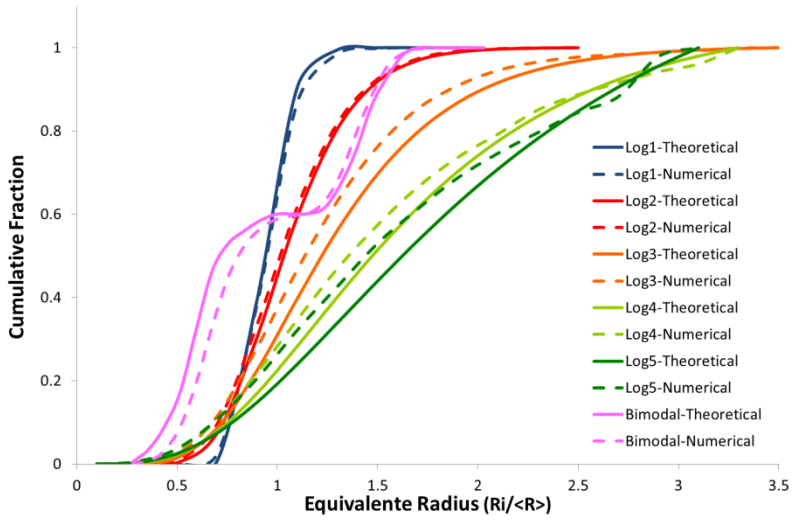

(b)

Figure 2.14: *Grain size distributions histograms (a) Log1, Log2, Log3, Log4, Log5 and Bimodal and cumulative fraction (b) Log1, Log2, Log3, Log4, Log5 and Bimodal.*

Table 2.3 *Distribution and cumulative fraction L2 errors for the 6 microstructures of Table 2.2.*

	Histogram L2 Error (%)	Cumulative fraction L2 Error (%)	Number of grains
Bimodal	34.7	8.3	9933
Log1	9.0	2.9	9728
Log2	9.2	7.1	10517
Log3	11.4	2.0	10464
Log4	16.8	1.8	9999
Log5	18.9	4.9	8583

Errors are higher for more complex distributions, like the Bimodal distribution. However, as mentioned earlier, when compared to the state of art in this domain [Hitti, 2012], the errors obtained here correspond to very good descriptions of all distributions.

4.2 Obeying a grain size distribution in 3D microstructures

In order to generate a 3D digital microstructure close to that of 304L, the 3D experimental grain size distribution was estimated using the Saltykov method [Underwood, 1970]. This method allows converting a 2D grain size distribution (bar-plots), for an equiaxed microstructure, to a 3D discrete grain size distribution. This method is based on the idea that all grains are spheres and the 3D distributions prediction is based on the probability of a sphere being intersected by a plane section. In [Tucker, 2012] the authors have shown, for a Ni-Based superalloy, that the Saltykov method corrects the disparity between the 2D and 3D grain size distribution mainly for the mean and the upper grain size ranges. The method is explained in details in Appendix 1. Figure 2.15 describes the 3D extrapolated discrete grain size distribution of the 304L steel.

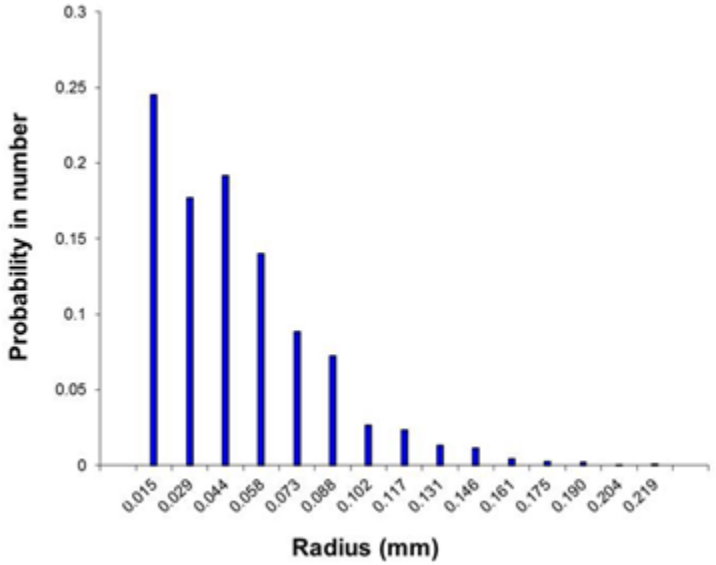

Figure 2.15: *3D extrapolated grain size distribution obtained using the Saltykov method, for the 304L steel.*

The predicted distribution exhibits a large number of small grains. The mean grain radius is equal to 48.8 µm in 3D (in 2D, mean grain radius is equal to 67.4µm).

4.2.1 Voronoï Tessellation Method

Figure 2.16 illustrates one of the digital microstructures obtained using the Voronoï method, considering 16636 grains randomly generated in a 2 mm x 2 mm x 2 mm RVE (i.e. obeying the prescribed 3D mean grain size of 48.8 µm for 304L). As for the 2D discussions, ten distinct digital microstructures have been generated and Figure 2.17 gives a comparison between the average of those numerical distributions, and the experimental one.

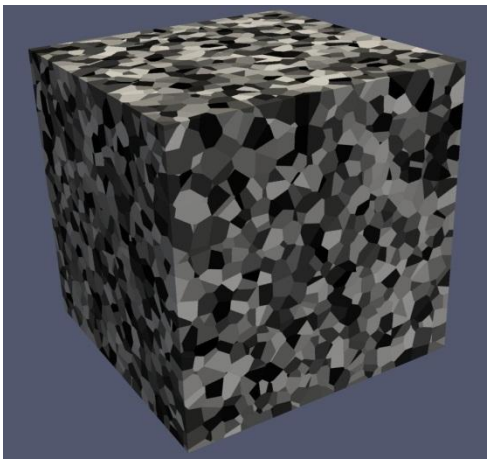

Figure 2.16: *A 3D microstructure of 16636 grains generated using a Voronoï method in the domain 2 mm x 2 mm x 2mm for the 304L steel.*

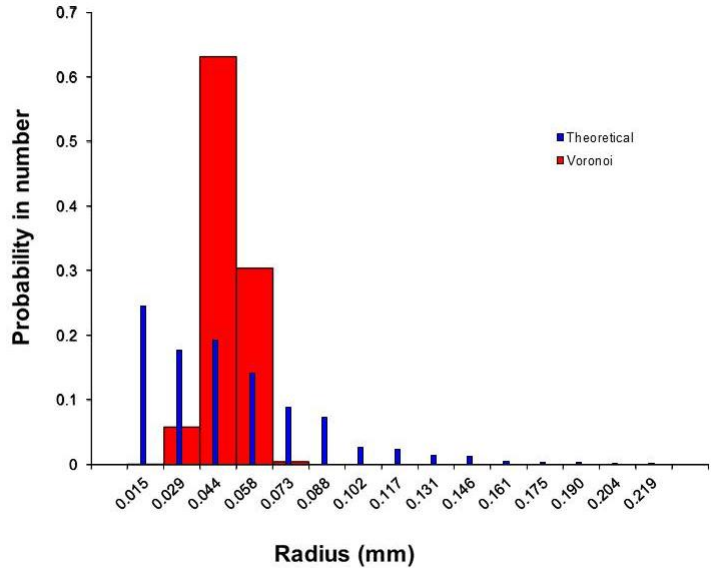

Figure 2.17: *Comparison between the numerical 3D grain size distribution (average of ten calculations – bar-plots) obtained using a Voronoï method and the 3D extrapolated 304L one ("theoretical" discrete distribution).*

The L2 error between the experimental and numerical distributions is equal to 137.8% (each set of the numerical distributions being replaced by its mean value for this calculation); showing that the digital microstructure obtained using the Voronoï method is completely inadequate.

4.2.2 Laguerre-Voronoï Tessellation Method

Regarding the Laguerre-Voronoï method, ten digital microstructures were also generated based on the extrapolated 304L steel 3D grain size distribution obtained with the Saltykov method. Figure 2.18 illustrates a comparison between the experimental distribution and the average of the numerical grain size distributions.

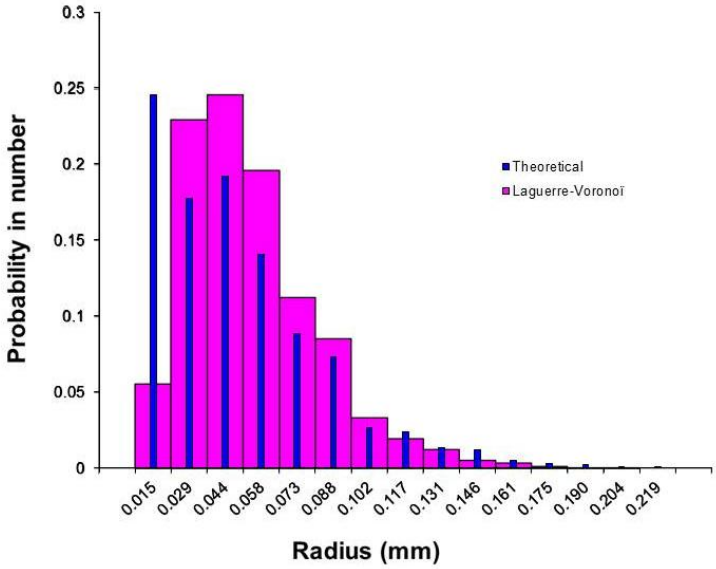

Figure 2.18: *Comparison between the 3D numerical grain size distribution (average of ten calculations – bar-plots) obtained using a Laguerre-Voronoï method and the extrapolated 304L one ("theoretical" discrete distribution).*

The average of the number of grains generated in a 2 mm x 2 mm x 2 mm domain is equal to 6407. The L2 error between the experimental distribution and the average of the numerical ones (each bin of the numerical distributions being replaced by its mean value) is equal to 53%. In Figure 2.18, once again, the error is concentrated in families of smaller radii. Knowing that the smallest grains are the first to disappear during grain growth modelling and also that the reduced volume fraction of smaller grains (volume fraction = 0.02) leads to a minor influence on the global mechanical behaviour of the RVE, one can decide to compare the experimental and numerical volume-weighted grain size distributions (Figure 2.19). In this case, the L2 error is reduced to 36.3%. The results become acceptable, although some improvements could be done in the future. The same analysis was performed for the microstructure generated using the Voronoï method, and the error for the volume-weighted distribution, 212.2%, is even larger than the error for the number-weighted distribution (137.8%).

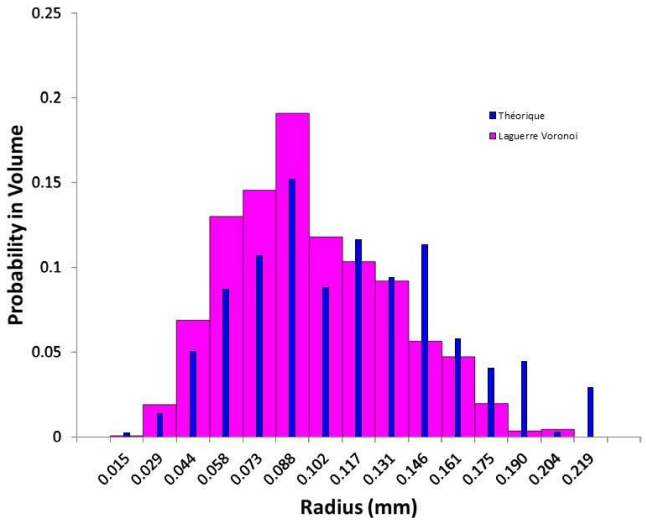

Figure 2.19: *Comparison between the 3D numerical volume weighted grain size distribution (average of ten calculations – bar-plots) obtained using a Laguerre-Voronoï method and the extrapolated 304L one ("theoretical" discrete distribution).*

Figure 2.20 illustrates one of the 3D digital microstructures obtained using the Laguerre-Voronoï method.

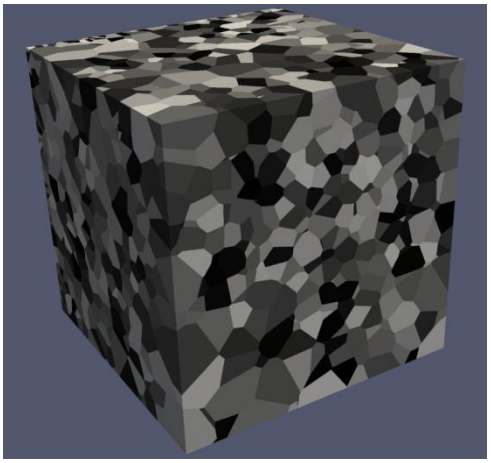

Figure 2.20: *A 3D microstructure made of 6400 grains generated using a Laguerre-Voronoï method in the domain 2 mm x 2 mm x 2mm for the 304L steel.*

4.3 Topological study of 2D Laguerre-Voronoï microstructures

In this work, all digital microstructures will be used in order to simulate plastic deformation with crystal plasticity (chapter 3), static recrystallization (chapter 5) and grain growth (chapter 4) phenomena. Previous discussions in this chapter have illustrated the capability of the proposed numerical strategy to generate polycrystals in a FE context, which obey grain size distributions in 2D and in 3D. However, all the above cited phenomena are also dependent on the material structure and on the microstructural topology. For example, in chapter 5, a discussion about the topological distribution of new (recrystallized) grains and its influence on the recrystallization kinetics is presented. In the case of grain growth, the associated kinetics depends on the microstructure topology, especially the number of sides of each grain, as discussed in [Hillert, 1965], [Abbruzzese, 1992a], [Abbruzzese, 1992b]. In addition, in [Abbruzzese, 1992a], [Abbruzzese, 1992b] the authors show that their grain growth equations, commonly used in grain growth mean field models [Bernard, 2011], are valid only if the microstructure obeys a "Special Linear Relationship" (SLR) between the grain number of sides, and the radius size. In this subsection, the topological characteristics of seven 2D different grain size distributions (the six distributions presented in Table 2.2 plus the 304L distribution) are presented. In fact, a similar topological study as the one presented in [Abbruzzese, 1992a] is performed and the SLR is studied in order to verify if the Abbruzzese grain growth model hypothesis is valid for the initial microstructures generated using our Laguerre-Voronoï algorithm. Considering the 3D microstructures, despite our capability to generate them numerically, it is currently estimated that the accuracy of the grain size distribution still needs improvements, in order to generate realistic results, from which topological and morphological studies could be performed.

Table 2.4 shows that all seven digital microstructures present a mean number of sides around 6. However, from Figure 2.21 it is observed that distributions of sides number (n) vary significantly from one case to another. For example, the Log1 distribution is narrower than the others, while the Bimodal distribution has two peaks.

Table 2.4 *Average number of sides for the seven microstructures generated numerically.*

	Initial number of grains	Mean number of sides (n)	Domain Size (mm)
Log1	9728	5.99	11 x 11
Log2	10517	5.98	12 x 12
Log3	10464	5.88	13 x 13
Log4	9999	5.95	14 x 14
Log5	8583	6.00	14 x 14
Bimodal	9933	5.90	12 x 12
304L	9211	5.88	13 x 13

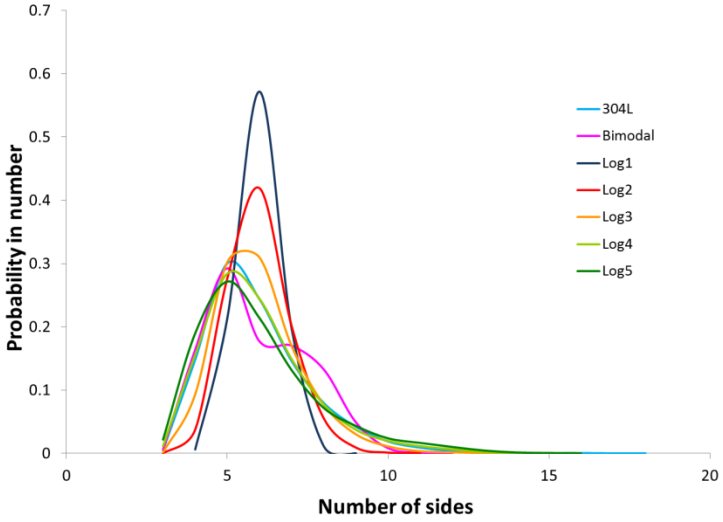

Figure 2.21: *Number of sides distributions for all seven 2D digital microstructures: 304L, Bimodal, Log1, Log2, Log3, Log4 and Log5.*

One can notice also a correlation between the number of sides distribution and the grain size distribution. For the same microstructure, both curves present more or less the same shape. Based on this idea, one can imagine a correlation between the sides number and the grain radius. This intuition is confirmed in Figure 2.22, where radius values are normalized according to:

$$r = \left(R / < R >\right). \tag{2.10}$$

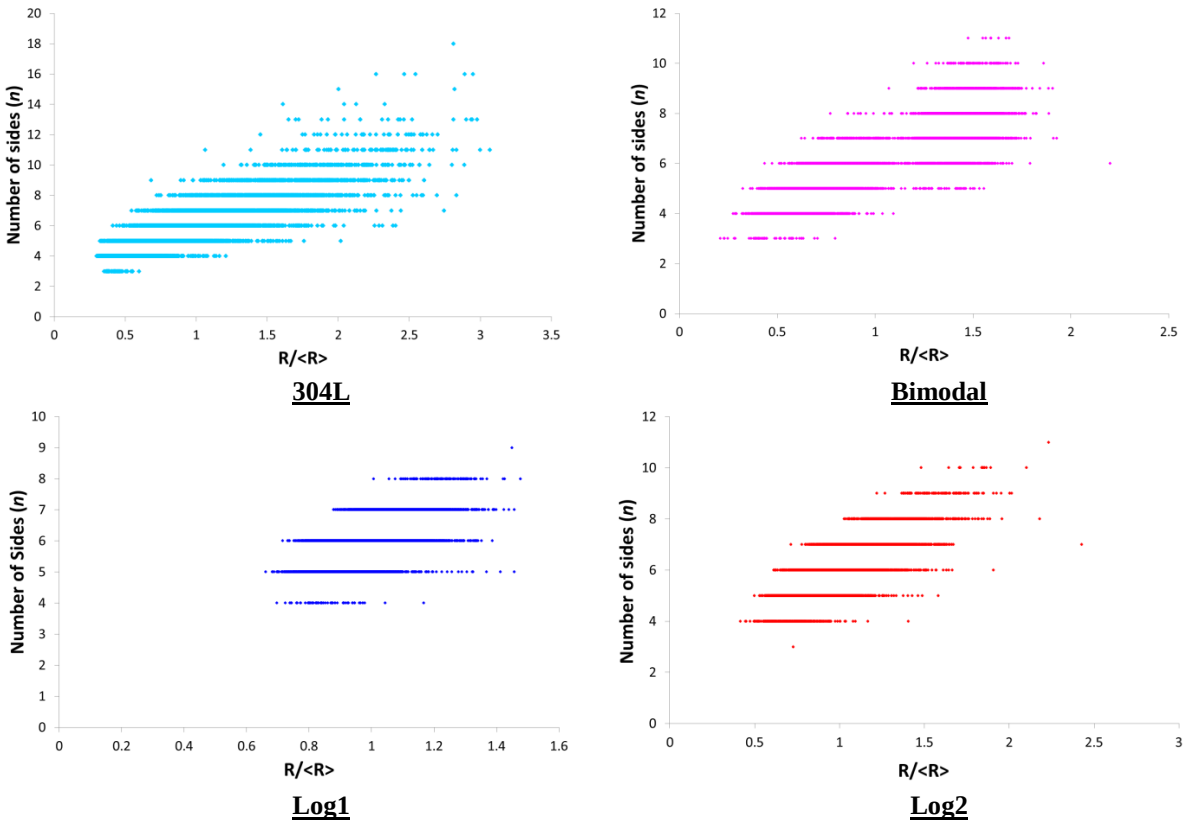

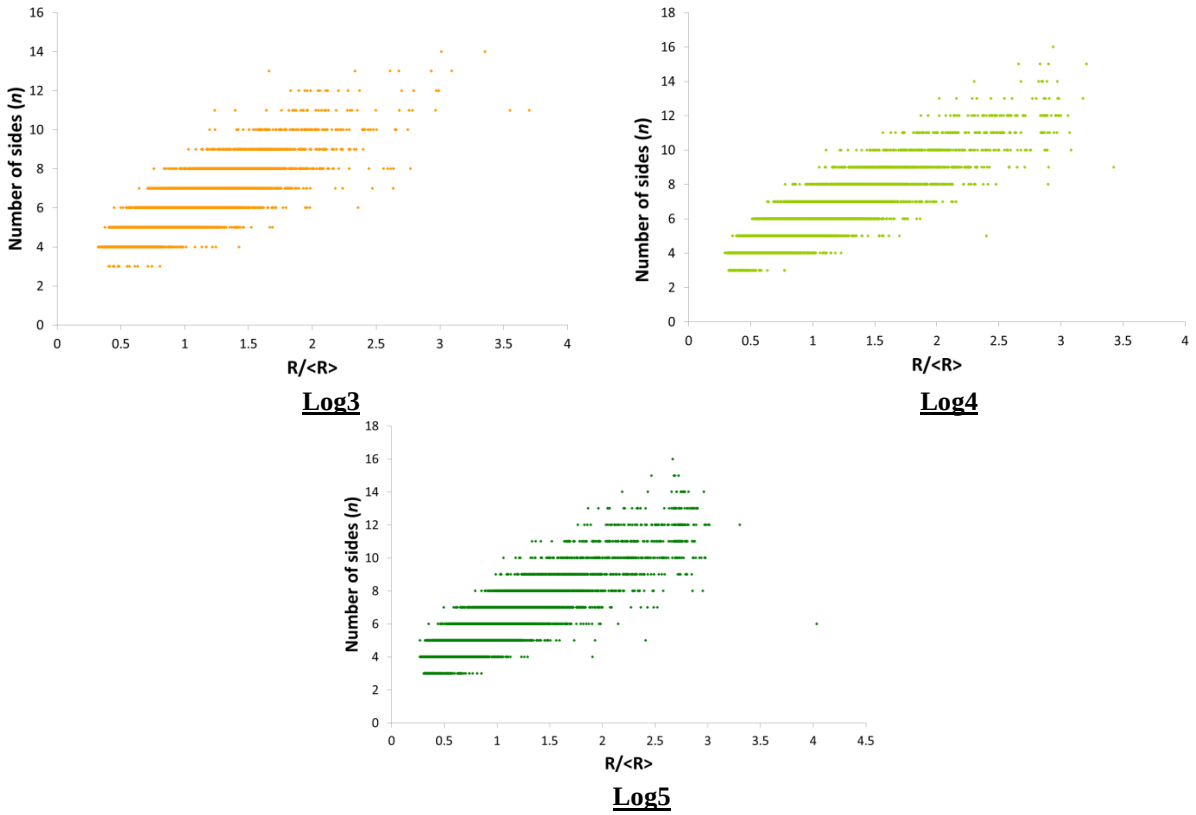

Figure 2.22: *Normalized radius vs. number of sides for all considered digital microstructures.*

Since, in general, the larger grains have a larger number of sides, the two parameters r (normalized radius) and n (number of sides) of the distribution are not independent of each other. But a unique mathematical relationship between the values r and n which would be valid for individual grains cannot exist, i.e. grains with the same equivalent radius may have different number of sides. Only statistical relationships considering grain families (each family being labeled with a subscript i) can be expressed. In [Abbruzzese, 1992a], Abbruzzese proposes the following two linear relationships between r_i (grain radius of grain family i) and n_i (number of sides of grain family i).

$$< n_i >= a_0 + a r_i \,, \tag{2.11}$$

$$n_i = b_0 + b < r_i > \,, \tag{2.12}$$

with a_0, a, b_0 and b being constants. The curve $< n_i >= f(r_i)$ is obtained by averaging over the n at a given r_i while the curve $n_i = f(< r_i >)$ is calculated by averaging over the r_i at a given n. Also, in [Abbruzzese, 1992a], it is shown that:

$$a_0 + a = b_o + b = 6 \,. \tag{2.13}$$

Verifications of these relations have been performed on the seven digital microstructures generated with the Laguerre-Voronoï tessellations.

Figure 2.23 illustrates the relationships $n_i = f(< r_i >)$ and Table 2.3 gives the corresponding b and b_0 values obtained by linear regression.

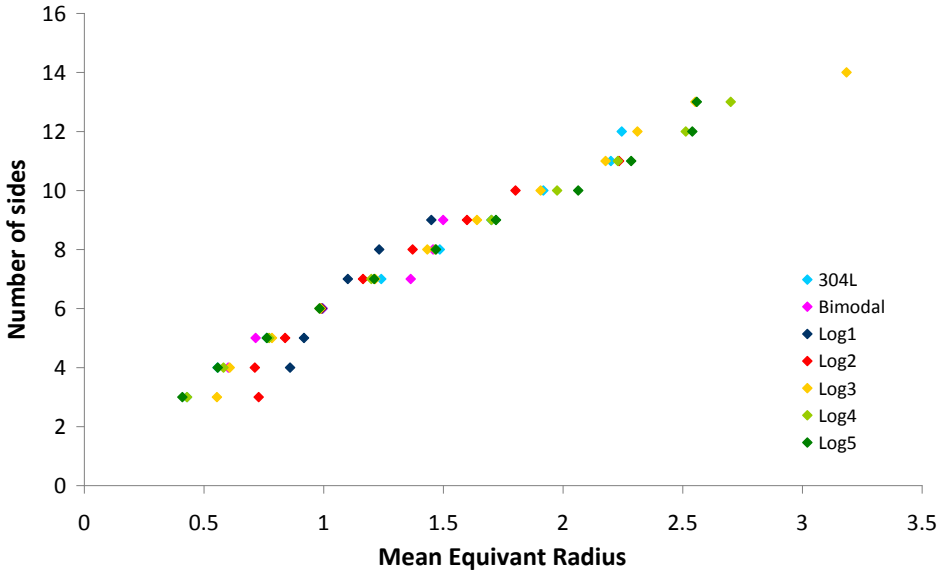

Figure 2.23: $n_i = f(< r_i >)$ *relationship for all seven digital microstructures.*

Table 2.5: *Values of b_0 and b (Equation 2.13) obtained by linear regression.*

	b	b_0	b_0+b
304L	4.56	1.33	5.98
Bimodal	4.64	1.37	6.01
Log1	8.26	-2.52	5.74
Log2	4.36	1.76	6.12
Log3	4.52	1.44	5.96
Log4	4.22	1.65	5.87
Log5	4.21	1.67	5.88

In [Abbruzzese, 1992a], it was found b = 4.14 and b_0 = 1.83. Except for the Log1 distribution, the b and b_0 values measured in the digital microstructures are similar. Interestingly, the study performed by Abbruzzese is based on an experimental distribution of an Al-3%Mg alloy with a log normal grain size distribution. Log1 distribution is close to a sharp normal distribution which may be the reason for the different behaviour presented by this distribution. However, the summations of $b_0 + b$ for all digital microstructures are around 6, which agrees well with 2.13.

Now, considering relationship 2.12, Figure 2.24 illustrates the relationship between $< n_i >= f(r_i)$ obtained for the seven digital microstructures, and Table 2.4 gives a and a_0 values obtained by linear regression.

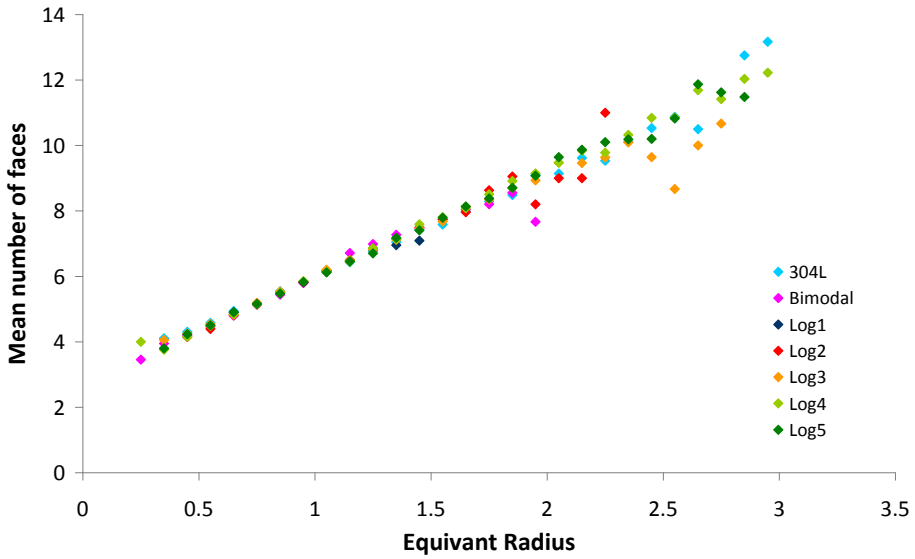

Figure 2.24: $< n_i >= f(r_i)$ *relationship for all seven digital microstructures studied.*

Table 2.6: *Values of* a_0 *and a (Equation 2.12) obtained by linear regression.*

	a_0	a	a_0+a
304L	3.01	2.99	6.00
Bimodal	3.22	2.77	5.99
Log1	3.10	2.88	5.98
Log2	3.02	2.9	5.92
Log3	2.99	3.02	6.01
Log4	3.22	2.8	6.02
Log5	3.20	2.78	5.98

In [Abbruzzese, 1992a], it was found a = 2.99 and a_0 = 2.98, with therefore a good agreement with Table 2.6. The summations of a_0 + a are all very close to 6, which again validates relation 2.13. Relation 2.12 is the "Special Linear Relationship" proposed by Abbruzzese and used to determine the Abbruzzese mean field grain growth model presented in [Abbruzzese, 1992b]. Hence, the results obtained here illustrate that topological characteristics of the 2D Laguerre-Voronoï tessellations are in agreement with the topological assumptions of the famous Hillert and Abbruzzese grain growth model. More global analysis concerning grain growth modelling of the considered microstructures in the full field FE/level set context will be detailed in chapter 4.

4.4 Morphological study of Laguerre-Voronoï microstructures

The Laguerre-Voronoï method is generally used to generate microstructures composed of equiaxed grains. Since the Laguerre-Voronoï method consists in using a distribution of non-intersected spherical (in 3D, circular in 2D) particles that serve as a basis for constructing the microstructure, one can indeed expect to generate equiaxed grains when using this method. However, if these spherical (in 3D, circular in 2D) particles compaction is not as dense as possible, the generated digital microstructure may present non-equiaxed grains. In other words, the generation of equiaxed digital grains is ensured by a good dense sphere packing algorithm in the Laguerre-Voronoï tessellation. In this subsection, the digital morphology of the seven 2D different grain structures numerically generated is analyzed. The objective is to verify the absence of a morphological texture in the digital microstructures.

One way to verify in 2D if a grain is equiaxed is to compare its equivalent radius whose calculation is based on the grain surface (R), with the equivalent radius calculated using the grain perimeter (R_{eqS} – Equation 2.14, where L is the grain perimeter).

$$R_{eqS} = \frac{L}{2\pi}. \tag{2.14}$$

The smallest the difference between R and R_{eqS}, the closest to a circular shape the grain is and consequently the more equiaxed. In Figure 2.25, this analysis was performed for all grains of the considered digital Laguerre-Voronoï microstructures (one of the ten generations). It can be recognized that, roughly, $R_{eqS} \approx R$ for all microstructures.

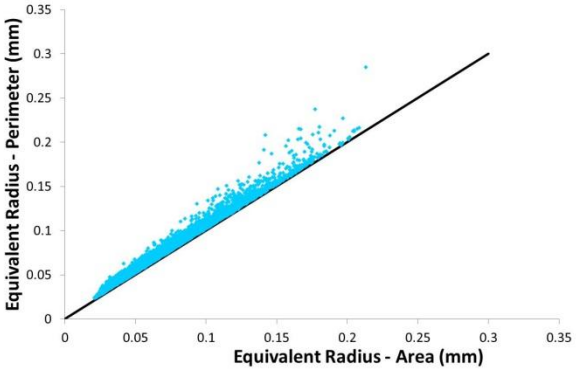

304L

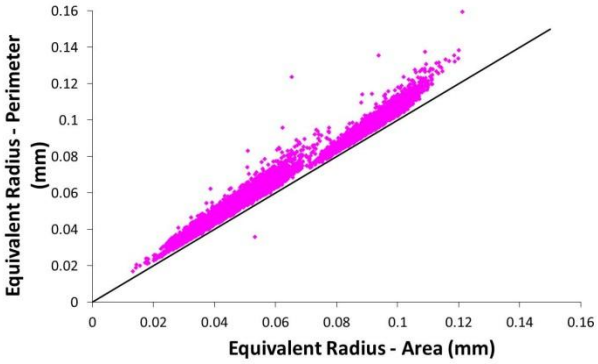

Bimodal

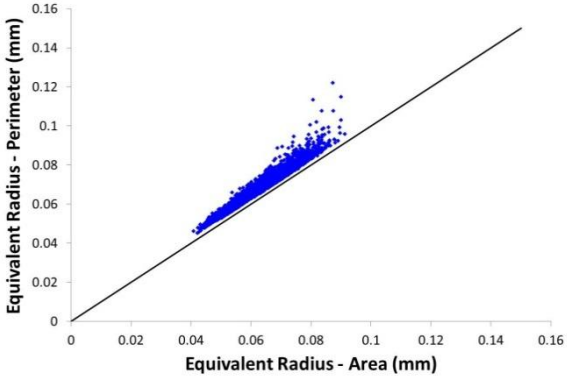

Log1

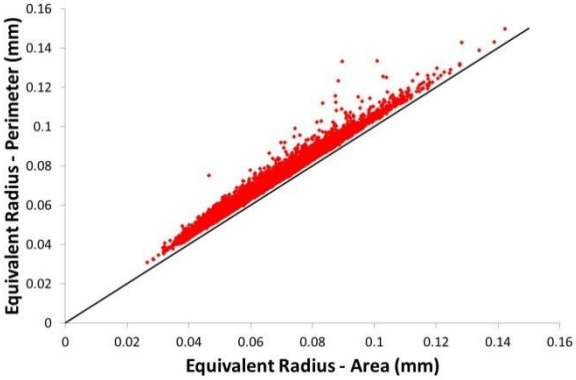

Log2

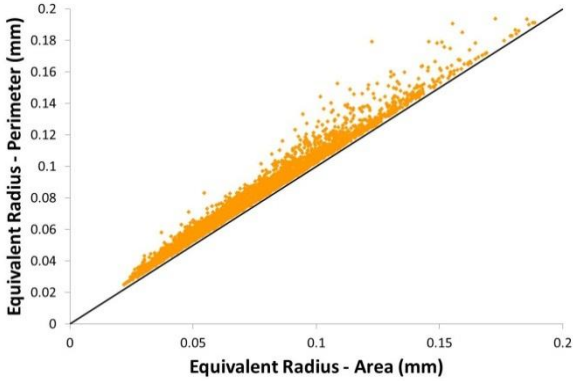

Log3

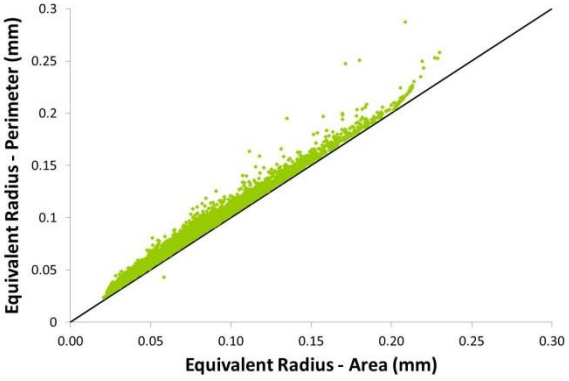

Log4

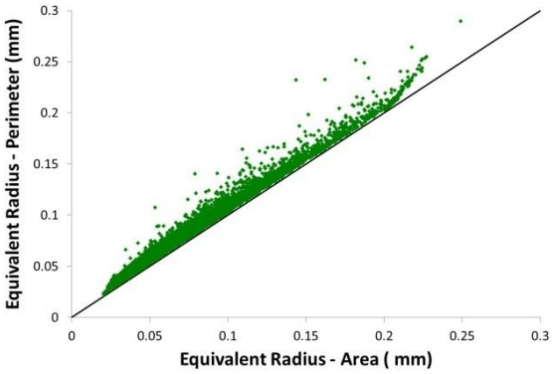

Log5

Figure 2.25: *R_{eqS} vs. R for all seven digital microstructures: 304L, Bimodal, Log1, Log2, Log3, Log4 and Log5*

For nearly equiaxed grains, the difference between R and R_{eqS} is rather small, amounting to mean value smaller than 12% [Abbruzzese, 1992a]. From Table 2.7 we observe that all digital microstructures exhibit a mean error between R and R_{eqS} which is smaller than 12%. However, analysing the graphs from Figure 2.26, it can be concluded that this difference is concentrated on grains with smaller equivalent radii. Statistically speaking, the smaller grains are less equiaxed than the largest ones. This means that with the Laguerre-Voronoï method, compaction problems occur mainly on small circles areas.

Table 2.7: *Mean error between R_{eqS} and R for all digital microstructures.*

	Mean error between R_{eqS} and R (%)
304L	8.8
Bimodal	9.8
Log1	7.5
Log2	8.1
Log3	8.3
Log4	9.9
Log5	10.8

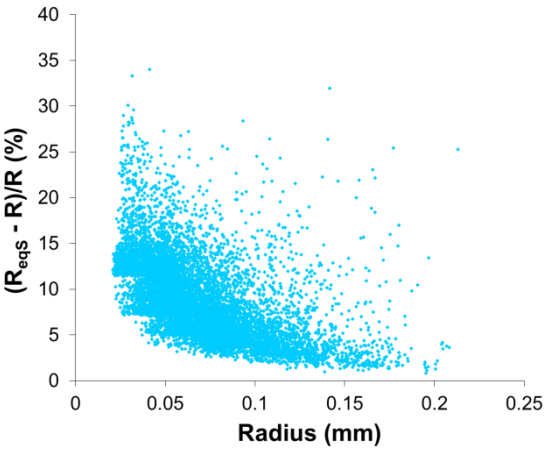

304L

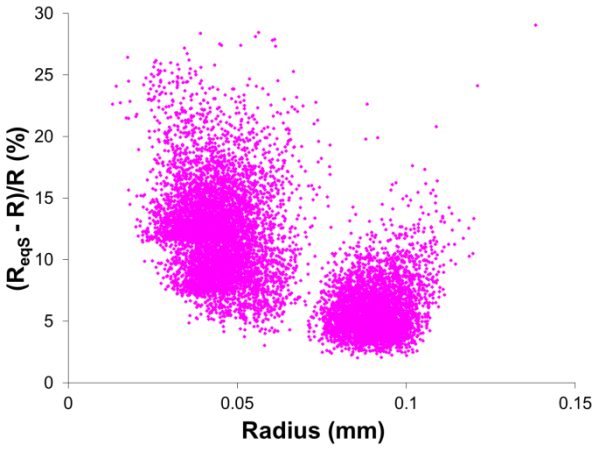

Bimodal

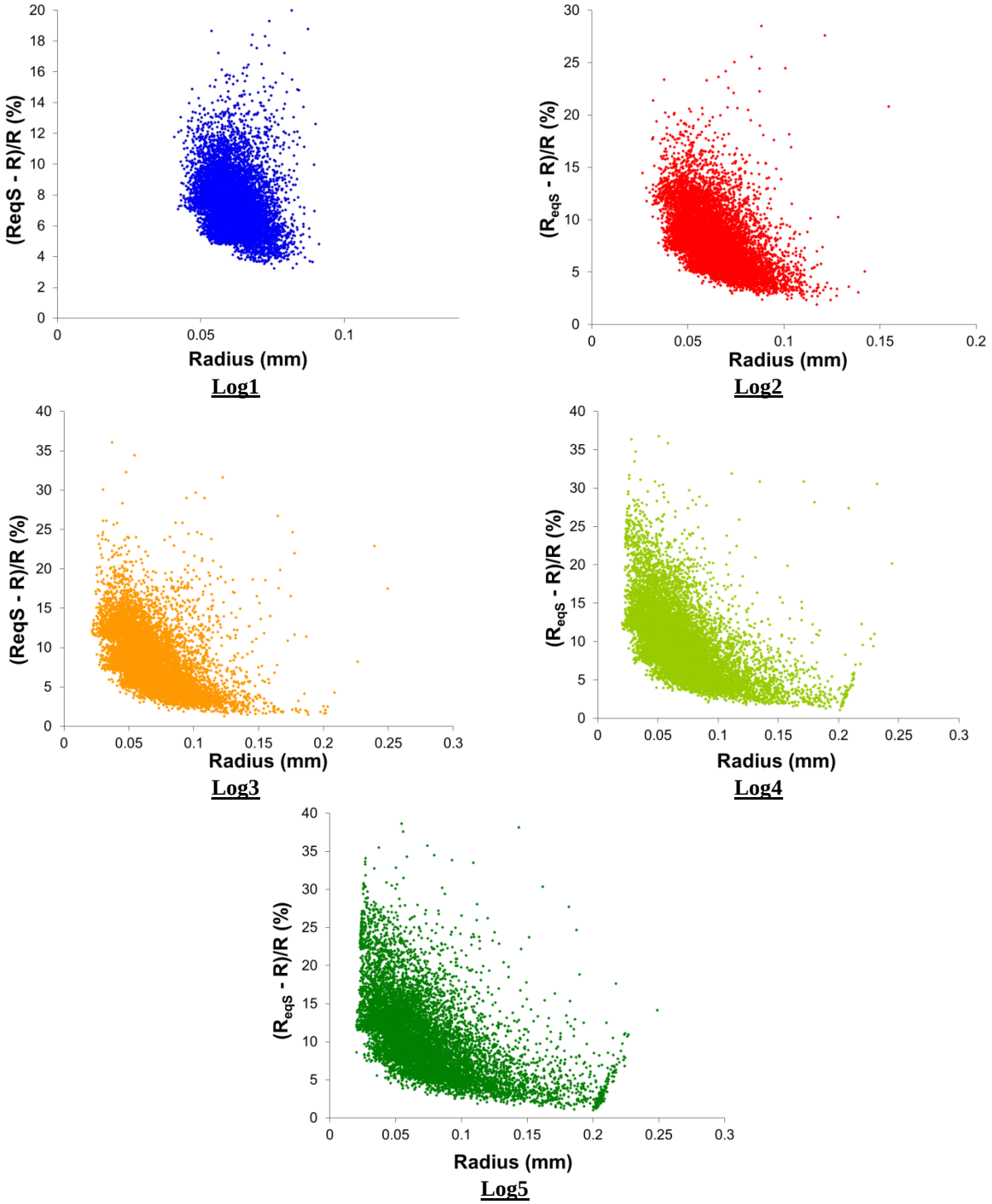

Figure 2.26: *Difference between R_{eqS} and R vs. radius dispersion for all seven digital microstructures studied.*

Finally, the relationship between the grain perimeter S and the grain area A is studied. Analyzing graphs from Figure 2.27, an approximate equation $S = f(A)$ was obtained for all the considered microstructures, which are summarized in Table 2.8. Behaviours are very similar.

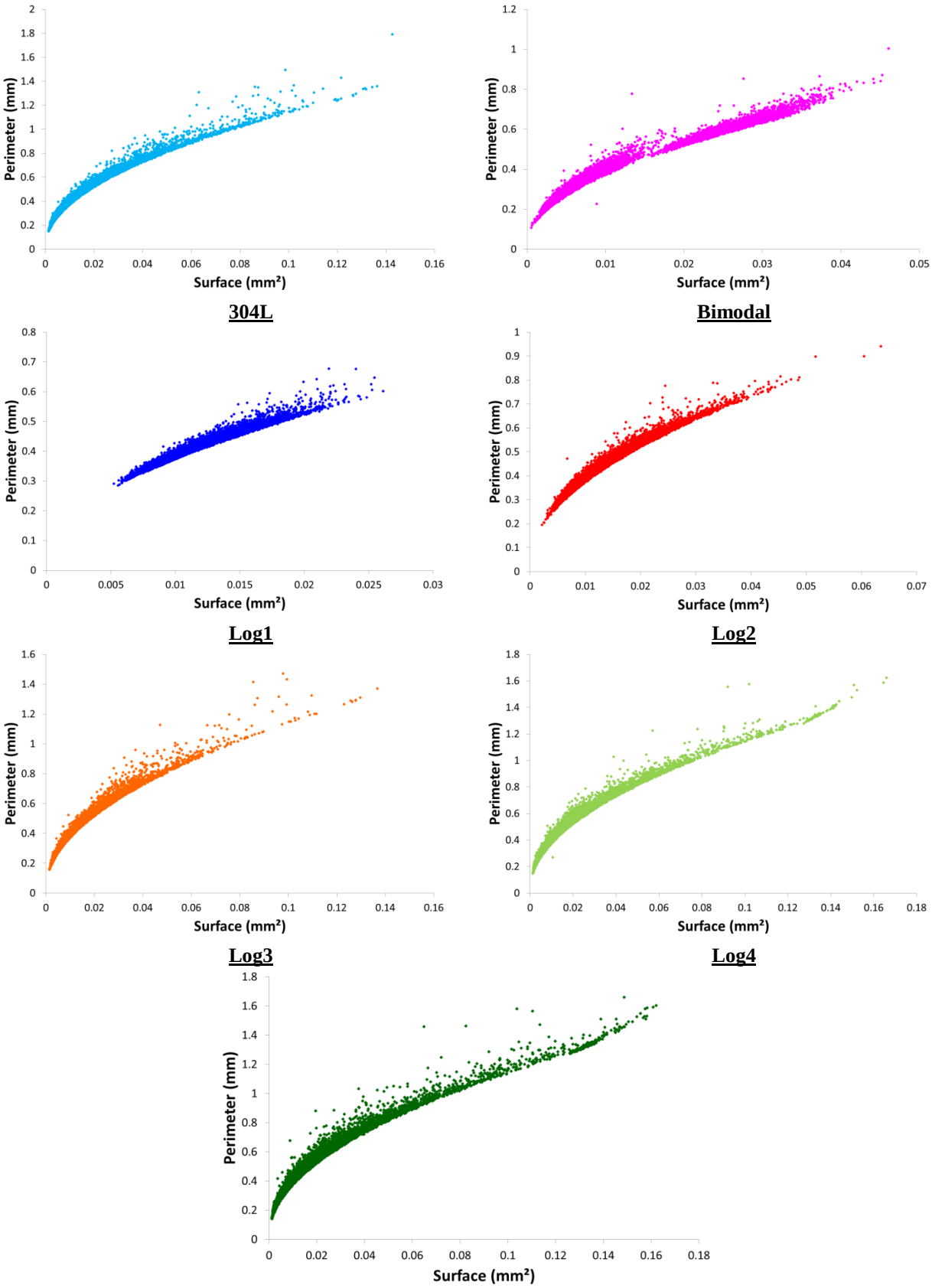

Figure 2.27: *Grain perimeter as a function of grain area dispersion for all digital microstructures: 304L, Bimodal, Log1, Log2, Log3, Log4, and Log5.*

Table 2.8: $S = f(A)$ *equations for all digital microstructures: 304L, Bimodal, Log1, Log2, Log3, Log4 and Log5. S is the mean perimeter and A the mean area of grains.*

	$S = f(A)$
304L	$S = 3.81A^{0.5}$
Bimodal	$S = 3.85A^{0.5}$
Log1	$S = 3.83A^{0.5}$
Log2	$S = 3.84A^{0.5}$
Log3	$S = 3.82A^{0.5}$
Log4	$S = 3.85A^{0.5}$
Log5	$S = 3.86A^{0.5}$

Based on an average of the equations from Table 2.8, a statistical equation for the relationship between the grain perimeter and the grain surface for a 2D microstructure generated using the Laguerre-Voronoï method can be proposed:

$$S = 3.84A^{0.5}. \tag{2.15}$$

Comparing Equation 2.15 with the one expected for a perfect circular shape $\left(S = 3.5A^{0.5}\right)$, it is concluded that the Laguerre-Voronoï method not only generates microstructures obeying a given grain size distributions, but also leads to equiaxed microstructures.

5 Conclusion

This chapter presents the main mathematical tools used to generate and to immerge digital microstructures into a finite element mesh. Initially, with respect to the microstructure generation, the Voronoï and the Laguerre-Voronoï methods were presented. The conclusions are:

- For 2D digital microstructures, the use of a Laguerre-Voronoï method allows the generation of a microstructure obeying an experimental grain size distribution with a very low L2 error, and this does not require a very high number of grains in the digital microstructure.
- The use of the Voronoï method in 2D does not allow obeying a given grain size distribution. Even though the mean grain size can be set properly, the error between the numerical and the experimental grain size distributions can be very high, even when generating a large number of grains.
- The above results were also verified for 3D digital microstructures.

In a second part, a topological study of seven different 2D digital microstructures was presented. In all microstructures, the mean number of grain sides was around six, but the distribution of the number of sides differed from one microstructure to another. Two statistical linear relationships between the grain size and the number of sides, proposed by [Abbruzzese, 1992a], were critically analysed. For all investigated 2D digital microstructures, these linear relationships were verified.

Finally, a morphological study of the same seven 2D digital microstructures was presented. The objective of this study was to verify if the digital microstructures generated using the Laguerre-Voronoï algorithm are equiaxed. Based on the results discussed in this chapter, one can conclude that, even though the smallest grains are less equiaxed than the

larger ones, the digital microstructures generated with our Laguerre-Voronoï algorithm can be considered, overall, as very close to perfectly equiaxed microstructures.

Concerning the last two topics, recommended future work would be to perform the same study in 3D.

Résumé en français

Dans ce chapitre, les principaux outils numériques utilisés dans la génération statistique et l'immersion des microstructures digitales dans un maillage éléments finis sont présentés. Concernant la génération statistique des microstructures digitales, deux méthodes sont discutées : l'approche de type Voronoï et l'approche de type Laguerre-Voronoï. Il est tout particulièrement illustré que la méthode de Laguerre-Voronoï permet de respecter une distribution expérimentale de taille de grains contrairement à l'approche de type Voronoï.

Dans une deuxième partie, une étude topologique de sept microstructures digitales 2D générées par l'approche de type Laguerre-Voronoï retenue est présentée. Il est mis en lumière que les relations de type SLR proposées par Abbruzzese [Abbruzzese, 1992a] sont vérifiées pour l'ensemble des microstructures.

Finalement, une étude morphologique des mêmes microstructures digitales en 2D est présentée afin de vérifier le caractère equiaxe ou non des microstructures générées par cette approche.

Chapter 3

Deformation behaviour of 304L steel polycrystal and tantalum oligocrystal

Contents

1 Introduction 79
2 304L Steel Case 79
2.1 304L stainless steel 79
2.1.1 Chemical composition 79
2.1.2 Mechanical behaviour 80
2.1.3 Microstructural characterization - initial state 82
2.2 Planar compression test (Channel Die test) 84
2.2.1 Description of the test 84
2.2.2 Material parameters - 304L 85
2.3 Effects of mesh type in highly resolved polycrystalline simulations 89
2.3.1 Considering only SSDs 89
2.3.2 Considering both SSDs and GNDs 90
2.4 Results 92
2.4.1 Stress - Strain analysis 92
2.4.2 Dislocations density and energy distribution analysis 93
2.4.3 Strain distribution analysis 99
2.4.4 Grain size effects 101
3 Tantalum Case 102
3.1 Tantalum 102
3.2 Compression test 103
3.2.1 Test description 103
3.2.2 Digital oligocrystal 103
3.2.3 Material parameters 104
3.3 Results 105
3.3.1 Sample shape 105
3.3.2 Dislocations density distribution 106
3.3.3 Deformation distribution 111
3.3.4 Texture analysis 115
4 Conclusion 118

1 Introduction

Recrystallization processes depend on the nature of the deformed state. In order to accurately model recrystallization, microstructural heterogeneities, and the associated distribution of defects, must be understood, and even predicted. This explains the close connection between recrystallization and plasticity phenomena.

In this chapter, a crystal plasticity model, based on the concept of dislocation slip (presented in details in chapter 1) is tested and calibrated using two different test cases. The first one corresponds to a planar compression test (channel die test) on a 304L steel polycrystal, taking place at high temperature. The second one corresponds to a simple compression test on a tantalum oligocrystal composed of six different grains. In both materials, emphasis is given on the use of statistically stored dislocations (SSD), and geometrically necessary dislocations (GND). The latter introduce grain size effects in plasticity, and reorganize the spatial distribution of dislocation densities, which is shown to influence the potential location of recrystallization nuclei.

2 304L Steel Case

2.1 304L stainless steel

2.1.1 Chemical composition

304L steel is an F.C.C. (face centred cubic) stainless steel. The major feature of a stainless steel is its resistance to corrosion. This property is reached by adding more than 10.5% of chromium to the alloy. Except for chromium, the principal added element is nickel, which helps stabilizing austenite at low temperatures. Austenitic stainless steels do not undergo phase transformation upon cooling or heating. They are therefore good candidates for the investigation of recrystallization and grain growth processes. The chemical composition of 304L steel is presented in Table 3.1.

Table 3.1: 304L stainless steel chemical composition [Roucoules, 1994].

Component	C	Mn	Si	P	S	Cr	Ni	N
Weight percentage	<0.03	<2.00	<0.75	<0.045	<0.03	12.0~18.0	8.0~12.0	<0.10

Sometimes, residual ferrite is found in 304L steel (as shown in Figure 3.1), but it usually represents less than 1% of the total volume. The presence of residual ferrite may be a consequence of heterogeneous nickel distribution, and/or solidification conditions.

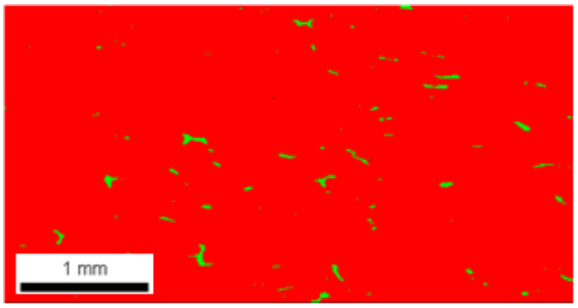

Figure 3.1: *EBSD analysis showing residual ferrite in a 304L austenitic stainless steel. The red zones correspond to the austenitic phase while the green zones correspond to the ferrite phase.*

Since the residual ferrite represents a small amount of the material, it will not be considered in the modelling work, i.e. 100% austenite will be assumed.

The 304L alloy is widely used in equipment and utensils for food processing and handling, beverages and dairy products. It is also found in heat exchangers, piping, tanks and other equipment which are in contact with fresh water.

2.1.2 Mechanical behaviour

The mechanical properties and behaviour of metallic materials depend mostly on the dislocation content and structure, the grain size and the texture. The dislocation density of a typical annealed state is ~10^{11} m^{-2} (although this may significantly vary from one material to another), which may increase to as much as ~10^{16} m^{-2} when the material is heavily deformed. The increase of material dislocation density is responsible for the material work hardening. In 1934, Taylor [Taylor, 1934] put forward the idea of hardening: some dislocations become 'stuck' inside the crystal and act as sources of internal stress, which oppose the motion of other gliding dislocations [Ashby, 2009]. Also, dislocations multiplication and annihilation depend on the temperature and strain rate. It is therefore expected that the material mechanical behaviour will depend on temperature and strain rate. It is interesting to highlight that when deformation at sufficiently high temperature exceeds a critical strain, dynamic recrystallization is initiated and increases with further deformation until a steady state where the microstructure is stable due to a dynamic equilibrium between softening by dynamic nucleation and work-hardening. The onset of dynamic recrystallization is identified as a peak on the stress-strain curve followed by a material softening. 304L steel recrystallizes dynamically under the analysed conditions so, its stress-strain curves will present the typical dynamic recrystallization behaviour. All experiments presented in this topic were performed by Ke HUANG during his PhD Thesis [Huang, 2011].

Temperature influence

In order to study the temperature influence on the 304L steel mechanical behaviour, torsion tests (Appendix 3) at 900°C, 1000°C, 1100°C and 1150°C were conducted with a constant strain rate of 0.01 s^{-1}. The smoothed stress-strain curves are presented in Figure 3.2.

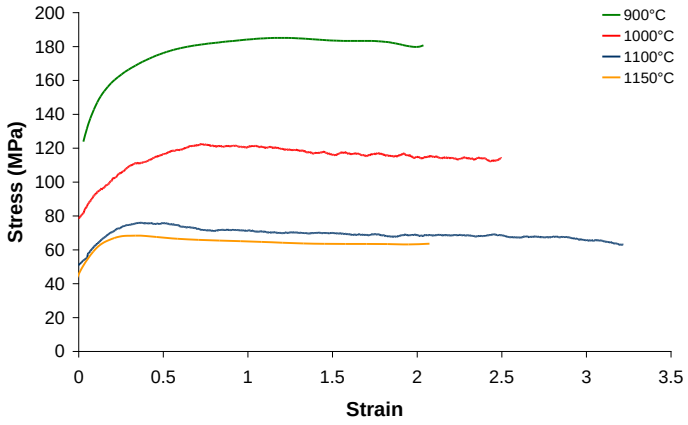

Figure 3.2: *Stress - strain curves for 304L steel torsion test for different temperatures: 900°C, 1000°C, 1100°C and 1150°C -* $\dot{\varepsilon}$ *=0.01* s^{-1} *[Huang, 2011].*

At a deformation temperature of 900°C, the flow stress increases gradually and no apparent stress peak is found before fracture. The dynamic recrystallization of 304L steel in these conditions is very slow, which may explain the difficulty in identifying a peak.

At a moderate temperature of 1000°C, some changes of stress-strain curves are observed. The stress shows more softening compared to the curve at 900°C. Considering the microstructure evolution, the flat grain boundaries become irregular after a small deformation of 0.3 (Figure 3.3.a), and start to serrate at a deformation level equal to 0.5 (Figure 3.3.b). Some small nuclei (new recrystallized grains) can be found among the original grain boundaries while other initial grain boundaries remain undecorated at $\varepsilon = 1.0$ (Figure 3.3.c). One can conclude that dynamic recrystallization starts at a strain between 0.5 and 1.0 at this temperature. With further deformation (Figures 3.3.d, 3.3.e and 3.3.f), the dynamically recrystallized grains volume fraction increases gradually and a large fraction of the initial microstructure is replaced by smaller grains.

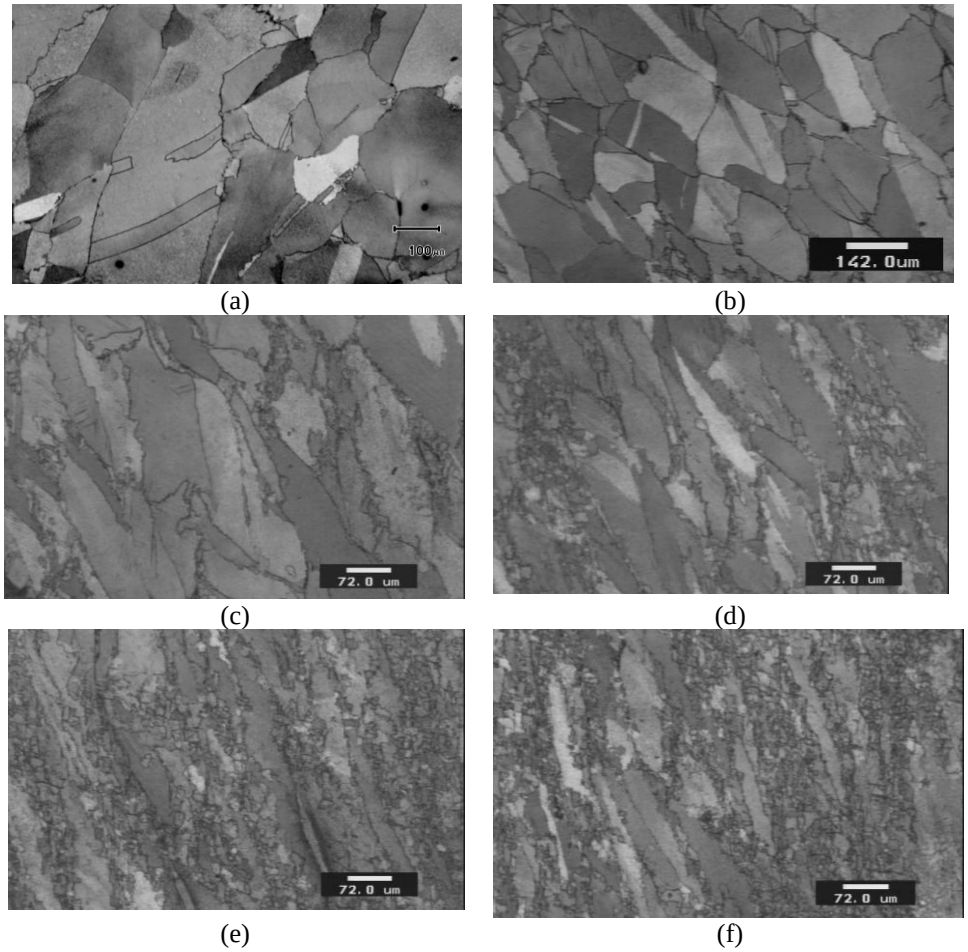

(a) (b) (c) (d) (e) (f)

Figure 3.3: *Microstructure of samples deformed a 1000°C, $\dot{\varepsilon}$ =0.01 s^{-1} for (a) $\varepsilon = 0.3$, (b) $\varepsilon = 0.5$, (c) $\varepsilon = 1.0$, (d) $\varepsilon = 1.5$, (e) $\varepsilon = 2.0$ and (f) $\varepsilon = 2.5$ [Huang, 2011].*

The stress-strain curves at higher temperature (1100°C and 1150°C) exhibit typical dynamic recrystallization behaviour, with a distinct stress peak followed by a mechanical steady state, which continues until fracture of the sample.

Comparing all stress-strain curves, the usual trend is confirmed, i.e. (i) the flow stress decreases with increasing temperature, and (ii) the peak stress appears at lower strain with increasing temperature.

Strain rate influence

In order to study the strain rate influence on the 304L steel mechanical behaviour, tests with $\dot{\varepsilon}$ = 0.01 s^{-1}, $\dot{\varepsilon}$ = 0.1 s^{-1} and $\dot{\varepsilon}$ = 1 s^{-1} were conducted at a constant temperature of 1000°C. The smoothed stress-strain curves are presented in Figure 3.4.

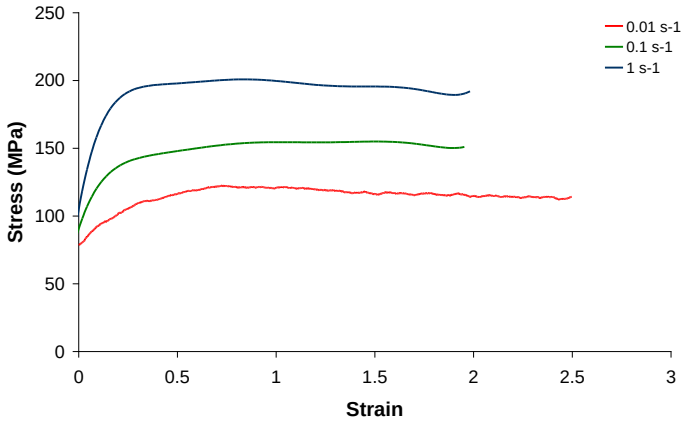

Figure 3.4: *Stress - strain curves for 304L steel torsion test for different strain rates; 0.01 s^{-1}, 0.1 s^{-1} and 1 s^{-1} at 1000°C.*

Analysing Figure 3.4 the expected trend of a stress increase with increasing strain rate is found. For example, increasing the strain rate from $\dot{\varepsilon}$ = 0.01 s^{-1} to $\dot{\varepsilon}$ = 1 s^{-1} leads to an increase of flow stress of about 80 MPa. At lower strain rate ($\dot{\varepsilon}$ = 0.01 s^{-1}) the typical flow stress curve induced by dynamic recrystallization is obtained (as already mentioned in paragraph A.1.2.1). As strain rate increases to $\dot{\varepsilon}$ = 0.1 s^{-1} and $\dot{\varepsilon}$ = 1 s^{-1}, the flow curves show a broader peak followed by softening. This is likely due to deformation heating, as documented in the literature [Mataya, 1990]. In [McQueen, 1995], [Mirzadeh, 2013], [El-Wahabi, 2003], [Dehghan-Manshadi, 2008] the authors present 304L steel experimental results for different test conditions. All results show similar tendencies to the ones presented here.

In this chapter, only plastic deformation is studied, and therefore only the first part of the stress-strain curves, before the stress peak, is considered in the comparisons between the numerical and experimental results. Even though it is possible to simulate large simulations, as Resk describes in [Resk, 2009], [Resk, 2010], in the case of 304L steel, the numerical results have no physical meaning for strain values higher than the strain peak, due to the occurrence of dynamic recrystallization transforming the microstructure. In the case of a deformation at 1000°C and 0.01 s^{-1}, stress-strain curves are analysed for strain values smaller than 0.6.

2.1.3 Microstructural characterization - initial state

The initial state of 304L steel samples is characterized using EBSD maps. From Figure 3.5, we observe that the initial sample present a completely recrystallized microstructure. Also, we identify a large number of twin boundaries: 48% of all grain boundaries are, in fact, annealing twins.

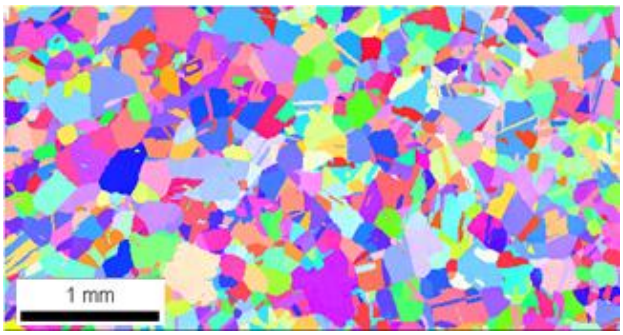

Figure 3.5: *304L steel EBSD map*

As discussed in chapter 2, in the initial state, the material presents a log-normal grain size distribution (chapter 2, paragraph 4). From the pole figure given in Figure 3.6 and the orientation distribution functions (ODF) in Figure 3.7, it is concluded that the material has a quasi-random crystallographic texture.

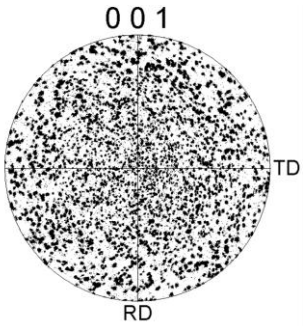

Figure 3.6: *304L steel pole Figure - initial state.*

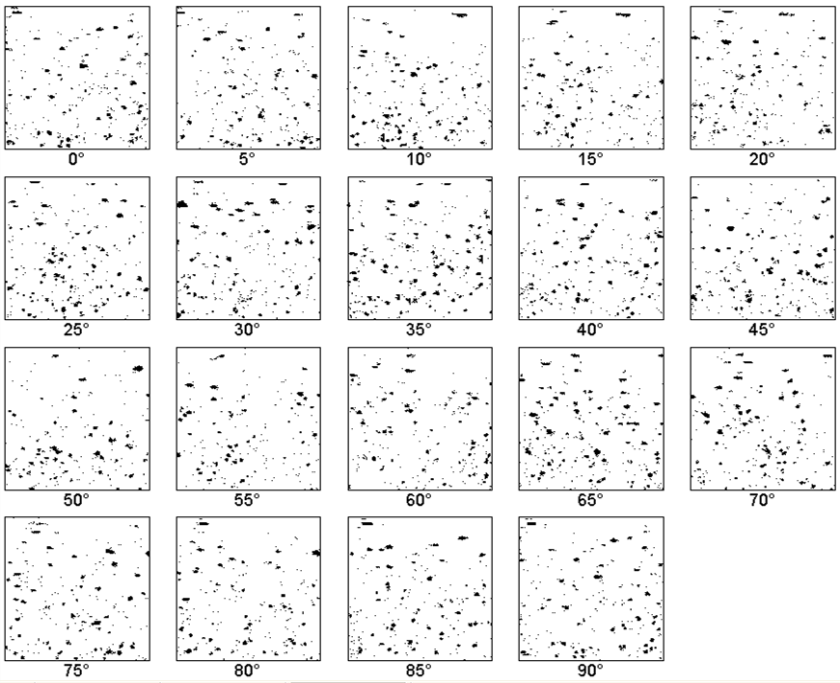

Figure 3.7: *Orientation distribution function of 304L steel at the initial state.*

In the description of the initial microstructure of the investigated 304L steel, and in particular for the crystal plasticity calculations, the discrete set of grains crystallographic orientations is therefore selected in a random way. The corresponding Euler angles are given in Appendix 2.

2.2 Planar compression test (Channel Die test)

2.2.1 Description of the test

The planar compression test is a compression test where deformation proceeds along two directions, as the case in the rolling process. In the simulations, a normal force is applied in the $-z_0$-direction and the material thinning results in extension along the x_0-direction, as illustrated in Figure 3.8.a.

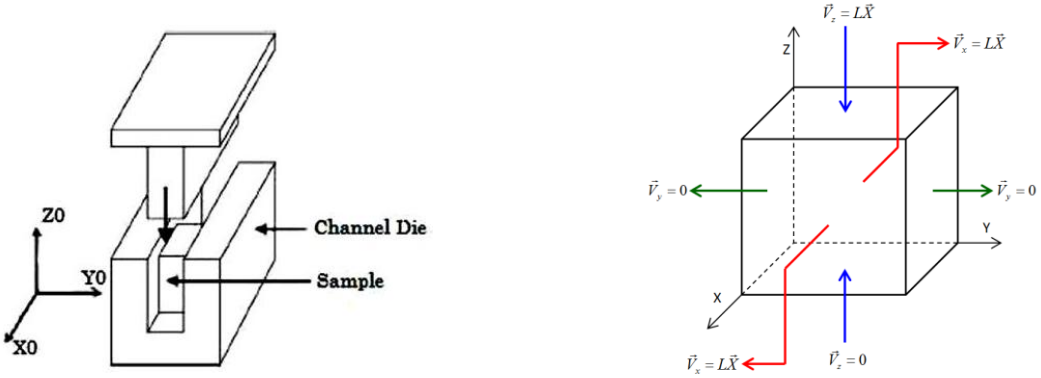

(a) (b)

Figure3.8: *(a) Channel die test description. (b) Homogeneous strain rate boundary conditions for a channel die test.*

Homogeneous strain rate boundary conditions are applied: at every node belonging to the boundary of the domain $\partial\Omega$, the three components of the velocity v are prescribed according to the following equation:

$$v = L\vec{X} \text{ on } \partial\Omega, \tag{3.1}$$

where L represents the velocity gradient tensor and $\vec{X}$ the position vector in the current configuration. For the channel die example, L is given by:

$$L = \begin{pmatrix} \beta & 0 & 0 \\ 0 & 0 & 0 \\ 0 & 0 & -\beta \end{pmatrix} \tag{3.2}$$

with β being a constant. Figure 3.8.b illustrates the boundary conditions for the channel die test.

2.2.2 Material parameters - 304L

As discussed in chapter 1, the material hardening is computed according to the following rule:

$$\sigma_c = \sigma_0 + M\alpha\mu b\sqrt{\rho_T}\,, \tag{3.3}$$

where σ_0 is the "dislocation free" yield stress, M the Taylor factor, α a constant, μ the shear modulus, b the magnitude of the burgers vector, and ρ_T the total dislocation density which is often expressed as $\rho_T = \rho_S + \rho_G$. In this case ρ_S is the statistically stored dislocation (SSD) density and ρ_G the geometrically necessary dislocation (GND) density.

Considering only the SSDs, the Yoshie-Laasraoui-Jonas [Laasraoui, 1991] equation was implemented in our crystal plasticity model:

$$\dot{\rho}_S = \left(K_1 - K_2\rho_T\right)\dot{\varepsilon}\,, \tag{3.4}$$

where K_1 and K_2 are material parameters. Since these parameters are identified from macroscopic mechanical tests, Equation 3.4 needs to be adjusted to the context of crystal plasticity, describing mesoscopic scale phenomena. This adjustment is explained in details in the following topics.

Considering the GNDs, the Busso [Busso, 2000] model was implemented in the crystal plasticity model (chapter 1, paragraph 2).

$$b^\alpha\left(\dot{\rho}^\alpha_{G_{sm}} b^\alpha + \dot{\rho}^\alpha_{G_{et}} t^\alpha + \dot{\rho}^\alpha_{G_{en}} n^\alpha\right) = curl\left(\dot{\gamma}^\alpha n^\alpha F^p\right). \tag{3.5}$$

Six parameters involved in Equations 3.3 to 3.5 can be found in the literature: the shear modulus μ; the constant α; the magnitude of the burgers vector b; the components of the anisotropic elastic tensor modulus C_{11}, C_{12} and C_{44}. On the other hand, K_1, K_2 and σ_0 must be identified from mechanical testing at different temperatures and strain rates.

Shear modulus μ

Following the method proposed by Frost and Ashby [Frost, 1982], Gavard [Gavard, 2001] analysed the 304L steel shear modulus evolution with temperature using experimental data presented in Table 3.2

Table 3.2: *Shear modulus of 304L [ASM, 1982].*

T(°C)	24	149	260	371	482	593	704	816
μ (GPa)	79/77	73/72	70/68	66/64	55/61	59/58	55/55	50/52

Linear dependence with temperature was found between 24 and 816°C, as shown in Figure 3.9.

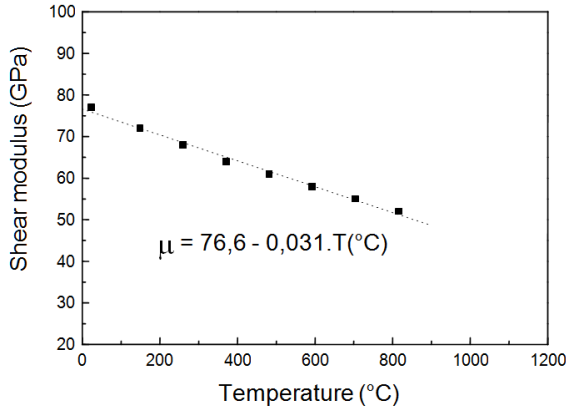

Figure 3.9: *Shear modulus evolution of 304L steel with temperature [Gavard, 2001]*

The curve of Figure 3.9 is then extrapolated until 1200°C, which leads to shear modulus values presented in Table 3.3.

Table 3.3: Shear modulus from room temperature to 1200°C for 304L steel [ASM, 1982]

T(°C)	25	850	950	1000	1050	1100	1200
μ (GPa)	75.8	50.2	47.0	45.5	43.9	42.4	39.3

K'$_1$, K'$_2$ and τ_0

At the macroscopic scale, the material hardening is computed using Equations 3.3 and 3.4. The K_1 and K_2 identification procedure at this scale is explained in details in [Jonas, 2009]. To compute the hardening at the mesoscopic scale, Equations 3.3 and 3.4 are modified according to Equations 3.6 and 3.7 by considering the meaning of the Taylor factor (*M*). The Taylor Factor is a geometric factor which describes the propensity of a crystal to slip (or not slip) based on the orientation of the crystal relative to the sample reference frame.

Macroscopic		Mesoscopic
$\sigma_c = \sigma_0 + M\alpha\mu b\sqrt{\rho}$	$\longrightarrow$	$\tau_c = \tau_0 + \alpha\mu b\sqrt{\rho}$ (3.6)
$\dot{\rho} = (K_1 - K_2\rho)\dot{\varepsilon}$	$\longrightarrow$	$\dot{\rho} = (K'_1 - K'_2\rho)\sum_\alpha \dot{\gamma}$ (3.7)

Equation 3.3 is divided by *M*, i.e. $\tau_0 = \frac{\sigma_0}{M}$. In Equation 3.4, $K_1^{'} = \frac{K_1}{M}$, $K_2^{'} = \frac{K_2}{M}$ due to the fact that $M\dot{\varepsilon} = \sum_\alpha \dot{\gamma}$. The Taylor factor value depends on the mechanical solicitation and on the grain orientation [Humphreys, 2004]. As a consequence, parameters K_1, K_2 and σ_0 are, at the grain scale, also dependent on the Taylor factor. On the contrary, K'_1, K'_2 and τ_0 are independent of the Taylor factor value; they are intrinsic to the material, at a given temperature and strain rate. As a consequence, once K'_1, K'_2 and τ_0 are correctly identified, the crystal plasticity model can be used to model any mechanical condition, and should account for the loading path influence. The identification procedure of these parameters is detailed below.

First of all, K_1, K_2 and σ_0 are identified using experimental curves of 304L steel torsion tests. Figure 3.10 illustrates a comparison between the experimental (1000°C and $\dot{\varepsilon} = 0.01$)

results (green line) and the theoretical curve (red line) obtained with K_1 = 10.1 10^{14} m^{-2}, K_2 = 3.3 and $\sigma_0 = 53MPa$ (red line).

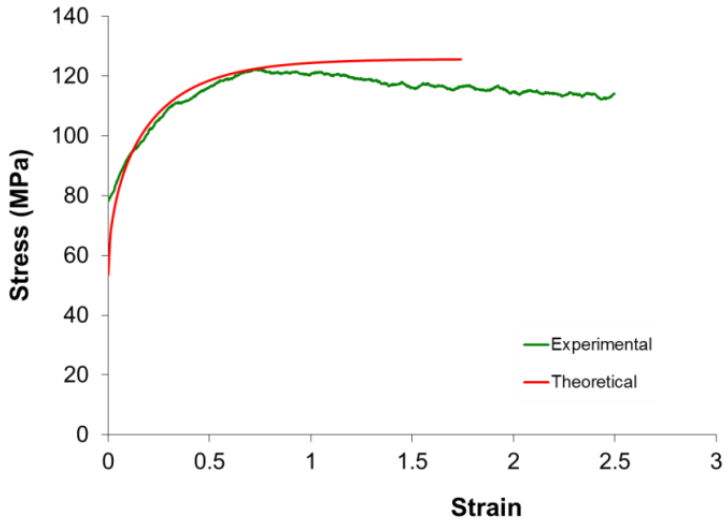

Figure 3.10: *Comparison between experimental results and theoretical stress - strain curves for 304L steel at 1000°C and deformation rate equal to 0.01 s^{-1}.*

Secondly, the 304L steel mean Taylor factor during a torsion test is identified using EBSD analysis. As shown in paragraph 2.1.3, the 304L steel exhibits a quasi-random texture. To further verify the material isotropy, the mean Taylor factor of a torsion test is calculated for 3 different solicitation directions, using the TSL OIM Analysis software. According to Table 3.4, the mean M is 3.3. In order to obtain K'_1, K'_2 and τ_0 values, we therefore need to divide K_1, K_2 and σ_0 by this value. For a planar compression test, the mean Taylor factor is in average 3.33, but no experimental data is available for this test.

As the Taylor factor depends on the grains crystallographic orientations, the particular set of representative grains used in simulations may influence the mean Taylor factor value and, as a result, influence the polycrystal mechanical behaviour. In this work we perform simulations with 50-grain domains and 100-grain domains. The corresponding mean Taylor factor values for our 50-grain and 100-grain polycrystal are given for torsion and planar compression tests in Table 3.4. The crystallographic orientations of all grains are given in Appendix 2.

Table 3.4: *304L steel mean Taylor factor for planar compression and torsion solicitations for a 50-grain, 100-grain polycrystal, and for the total domain measured experimentally.*

Planar compression test			
Velocity gradient tensor (L)	Taylor factor		Mean
$\begin{pmatrix} 1 & 0 & 0 \\ 0 & 0 & 0 \\ 0 & 0 & -1 \end{pmatrix}$	50 grains	3.39	50 grains = 3.36
	100 grains	3.34	
	Total domain	3.36	100 grains = 3.33
$\begin{pmatrix} 1 & 0 & 0 \\ 0 & -1 & 0 \\ 0 & 0 & 0 \end{pmatrix}$	50 grains	3.38	
	100 grains	3.36	
	Total domain	3.33	Total domain = 3.33

Torsion test			
Velocity gradient tensor (L)	Taylor factor		Mean
$\begin{pmatrix} 0 & 1 & 0 \\ 1 & 0 & 0 \\ 0 & 0 & 0 \end{pmatrix}$	50 grains	3.27	50 grains = 3.27
	100 grains	3.31	
	Total domain	3.31	100 grains = 3.30
$\begin{pmatrix} 0 & 0 & 1 \\ 0 & 0 & 0 \\ 1 & 0 & 0 \end{pmatrix}$	50 grains	3.25	
	100 grains	3.28	
	Total domain	3.28	Total domain = 3.30

$\begin{pmatrix} 0 & 0 & 0 \\ 0 & 1 & 0 \\ 0 & 0 & -1 \end{pmatrix}$	50 grains	3.29	
	100 grains	3.28	
	Total domain	3.31	

$\begin{pmatrix} 0 & 0 & 0 \\ 0 & 0 & 1 \\ 0 & 1 & 0 \end{pmatrix}$	50 grains	3.29	
	100 grains	3.30	
	Total domain	3.30	

Based on Table 3.4, we conclude that, in all cases, the Taylor factor value is higher for a planar compression solicitation than for a torsion solicitation. Also, for both cases, the 100-grain domain shows the same mean Taylor factor value as that of the total measured domain. In the case of planar compression solicitation, we observe that the mean Taylor factor value for a 50-grain domain is larger than the one for a 100-grain domain. For the torsion solicitation, the inverse is observed. Knowing the K'_1, K'_2 and τ_0 intrinsic parameters of 304L, and the mean Taylor factor values of 304L for different mechanical solicitations and domain size, theoretical stress-strain curves can be predicted from numerical simulations. This reasoning is however valid when considering only SSDs.

When considering both SSDs and GNDs, an extra amount of dislocation is added to the material. As a consequence K'_1, K'_2 and τ_0 values must be re-adjusted to keep a good match with experimental results.

304L steel parameters

Table 3.5 presents the material parameters used in simulations considering only SSDs and simulations considering both SSDs and GNDs. Due to confidentiality, these parameters are represented using capital letters. These parameters are valid for deformations at 1000°C and with a strain rate of 0.01 s^{-1}. For different conditions, new parameters need to be identified, using the same procedure as that explained in the above paragraphs.

Table 3.5: *304L steel parameters used in the crystal plasticity model.*

	SSDs	SSDs + GNDs
K'_1 (m^{-2})	A	A
K'_2	B	2.9B
τ_0 (MPa)	C	C
C_{11} (GPa)	202	202
C_{12} (GPa)	86.6	86.6
C_{44} (GPa)	57.7	57.7

	SSDs	SSDs + GNDs
$\dot{\gamma}_0$ (s^{-1})	0.001	0.001
α	D	D
μ (GPa)	E	E
b (m)	$0.254\ 10^{-9}$	$0.254\ 10^{-9}$
m	F	F

The only different parameter between the SSDs and the SSDs+GNDs case is the K'_2 value. As discussed in chapter 1, when the GNDs are taken into account, an extra amount of dislocations is introduced. As a consequence, in order to match the macroscopic mechanical behaviour, dislocation recovery is chosen to increase, leading to a higher value of K'_2.

It is important to note that other combinations of parameter values for the SSDs+GNDs case would probably allow to correctly predict the experimental stress-strain curve. It is chosen here to keep the same K'_1 value, and to adapt the K'_2 value, but additional tests with variable initial grain sizes would potentially provide other solutions. We also keep in mind that the presence of GNDs introduces strong intragranular gradients of dislocation densities. Those are not easily captured by such a simple model, which ignores, for example, dislocation transport [Arsenlis, 2004].

2.3 Effects of mesh type in highly resolved polycrystalline simulations

The study of mesh size effect on the material mechanical behaviour or on the texture predictions is a subject discussed by several authors. In fact, meshes can be structured ("regular") or unstructured ("free"), with various degrees of mesh refinement.

In order to study the mesh influence on the mechanical behaviour of 304L steel, when considering only SSDs, a 50-grain polycrystal is generated in a 0.4 mm x 0.4 mm x 0.4 mm domain. The crystallographic orientations of all grains are based on experimental EBSD measurements, and given in Appendix 2.

Four different meshes are studied: 2 of them are isotropic without local mesh adaptation, and the other 2 meshes are also isotropic but with mesh adaptation around the grain boundaries. Table 3.6 sums up all meshes features and Figure 3.11 gives a graphical illustration. A planar compression test is simulated using material parameters from Table 3.5. In Table 3.6, the mesh size is normalized by the mean grain radius.

Table 3.6: *Mesh features - considering only SSDs.*

		Normalized mesh size inside the grain	Normalized mesh size on the grain boundary	Number of mesh elements
Mesh 1	Non adapted	0.297	0.297	80,000
Mesh 2	Non adapted	0.178	0.178	400,000
Mesh 3	Adapted	0.297	0.119	745,000
Mesh 4	Adapted	0.237	0.119	780,000

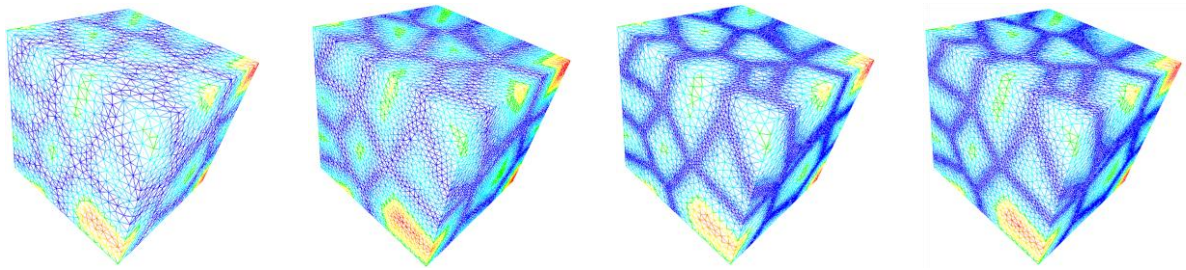

Mesh 1 Mesh 2 Mesh 3 Mesh 4

Figure 3.11: *The four meshes used to test the mesh influence on crystal plasticity numerical results, considering only SSDs – colour scale represents the distance function.*

2.3.1 Considering only SSDs

In [Sarma, 1996] the authors show that the use of a coarse discretization, in conjunction with regular meshes and with only one element per grain (but with more than one integration point), is relatively adequate for texture evolution predictions. Other authors have shown that increasing mesh refinement has very little impact on the global stress-strain response of the polycrystal when using conventional crystal plasticity [Barbe, 2001a], [Barbe, 2001b], [Buchheit, 2005], [Diard, 2005], [Resk, 2009]. However, all agree that finely discretized meshes are needed to capture local details of microstructure evolution and local gradients, regardless of the mesh type.

In this case, the mesh influence on the stress-strain curve is studied. The macroscopic stress is computed based on the equivalent Von-Mises stress (at each mesh element) as follows:

$$\sigma_{macro} = \frac{1}{V}\int_{\Omega} \sigma_{eq} d\Omega \ \ and \ \ \sigma_{eq} = \sqrt{\frac{3}{2} tr(S^2)}\,, \tag{3.8}$$

where V is the total volume of the representative volume element (RVE). Similarly, the macroscopic strain is computed based on the equivalent strain as:

$$\varepsilon_{macro} = \frac{1}{V}\int_{\Omega} \varepsilon_{eq} d\Omega \text{ and } \varepsilon_{eq} = \int_{t} \dot{\varepsilon}_{eq} dt = \int_{t} \left(\sqrt{\frac{2}{3} \dot{\varepsilon} : \dot{\varepsilon}} \right) dt\,. \tag{3.9}$$

The obtained stress-strain curves for meshes 1, 2, 3 and 4 are then compared to the theoretical curve calculated using parameters from Table 3.5 and the Taylor factor value for a 50-grain domain under a planar compression solicitation (M = 3.36, Table 3.4). Figure 3.12 presents the obtained results.

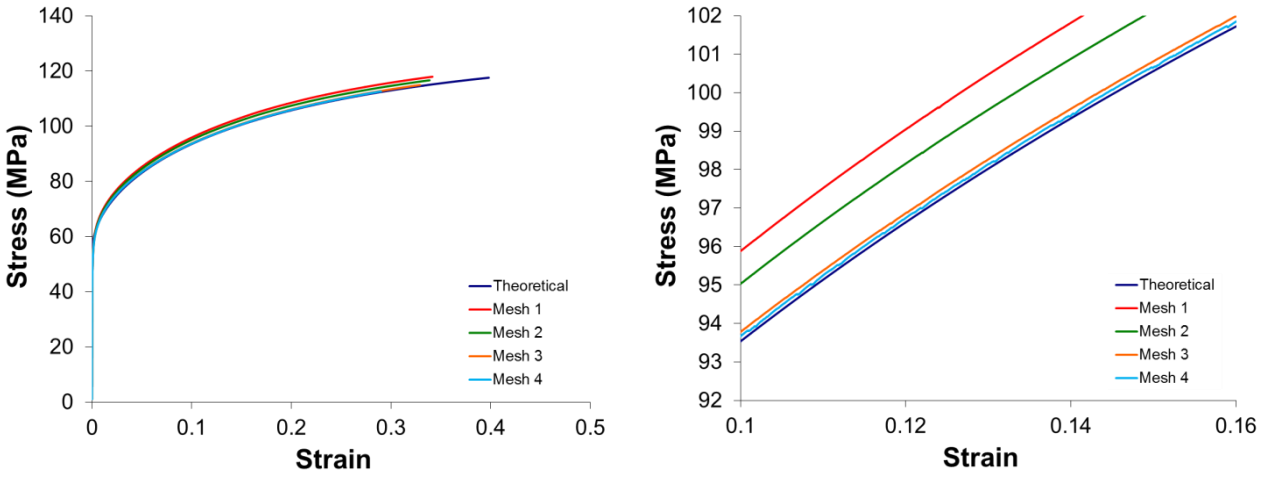

Figure3.12: *Stress - strain curves comparison between the theoretical result and the numerical result obtained with four different finite element meshes: (a) complete curve; (b) zoom for strains from 0.1 to 0.18.*

Comparing mesh 1 (red line) and mesh 2 (green line) curves (both meshes are isotropic and non-adapted), it is concluded that accuracy is improved when decreasing the mesh size.

Comparing mesh 3 (orange line) and mesh 4 (light blue line) - both meshes are isotropic and adapted with the same mesh size near the grain boundaries – leads to the influence of the intragranular mesh size, which is small. In other words, the mesh size near the grain boundaries matters more than the intragranular one, even though we only deal here with SSDs. This is further confirmed by comparing mesh 1 (red) to mesh 3 (orange): the sole refinement of mesh size near the grain boundaries is enough to significantly improve the results.

2.3.2 Considering both SSDs and GNDs

Once again, the stress-strain curves are plotted using Equations 3.8 and 3.9 in order to study the mesh influence. Figure 3.13.a presents the stress-strain curves for all four meshes compared to the theoretical curve (which considers only SSDs).

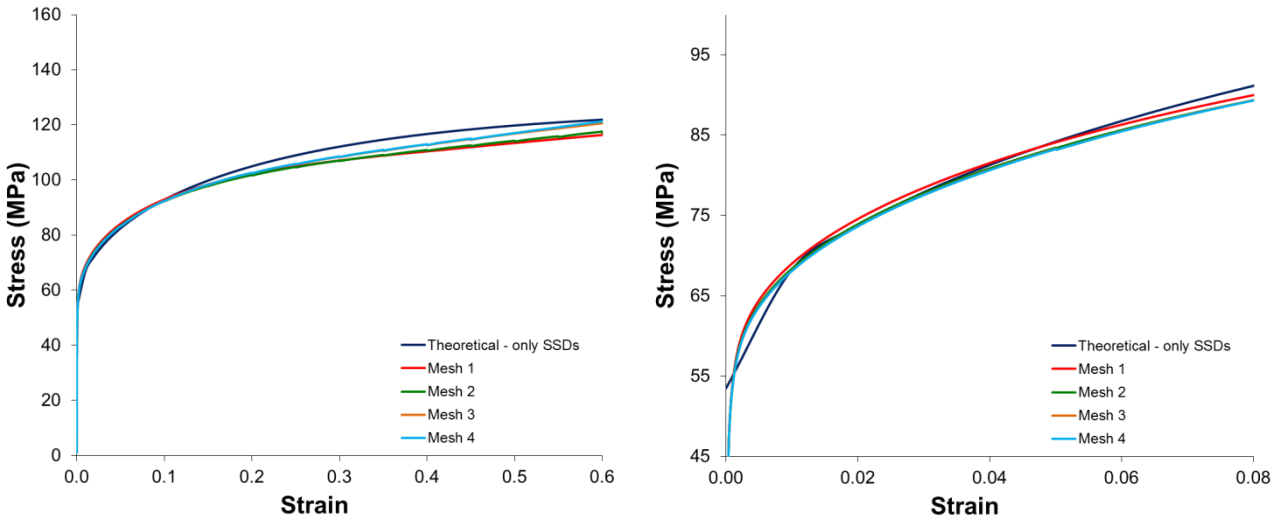

Figure 3.13: *Stress - strain curves comparison between the numerical results obtained with four different finite element meshes and the theoretical curve calculated when considering only SSDs: (a) complete curve; (b) zoom for strains from 0 to 0.08.*

From Figure 3.13.b representing the stress-strain curves for low strain levels, it is seen that all meshes present a similar behaviour as the one obtained previously with only SSDs. However, for strains larger than 0.1, we observe that simulations using mesh 3 (orange line) and mesh 4 (light blue line) predict a more important hardening. It is interesting to highlight that this mesh influence takes place only after the GND density reaches a critical value. For small deformations, dislocation density is mostly controlled by SSD density, and the extra hardening behaviour is not observed. As GNDs build-ups are associated with slip gradients developing at the grain boundaries, in this case, the mesh sensitive response is linked to a significant increase in the number of GNDs relative to the SSD population. Thus mesh sensitivity increases as the element size around the boundaries decreases. Figure 3.14 illustrates the increased GND density in mesh 3 and 4 along grain boundaries, as compared to mesh 1 and mesh 2. The dislocation density distribution will be discussed in more details in paragraph 2.4.2.

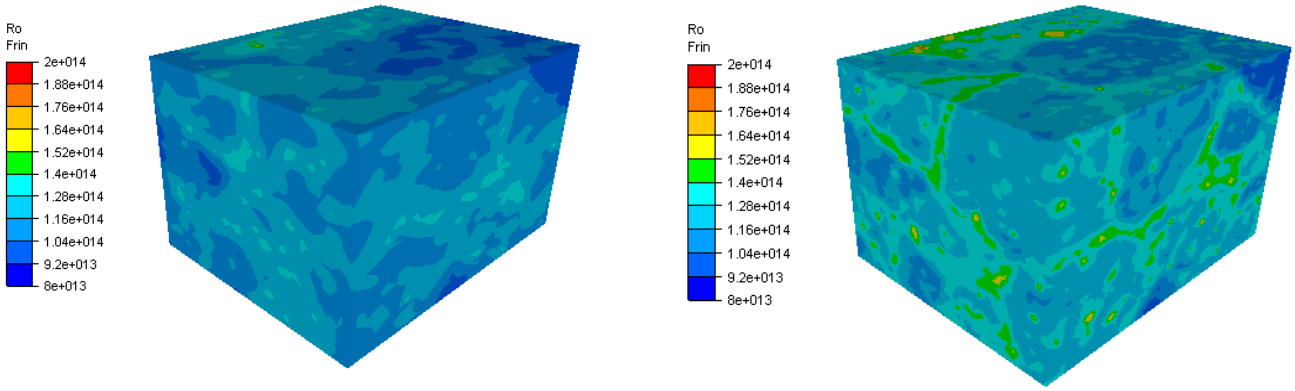

Mesh 1 Mesh 2

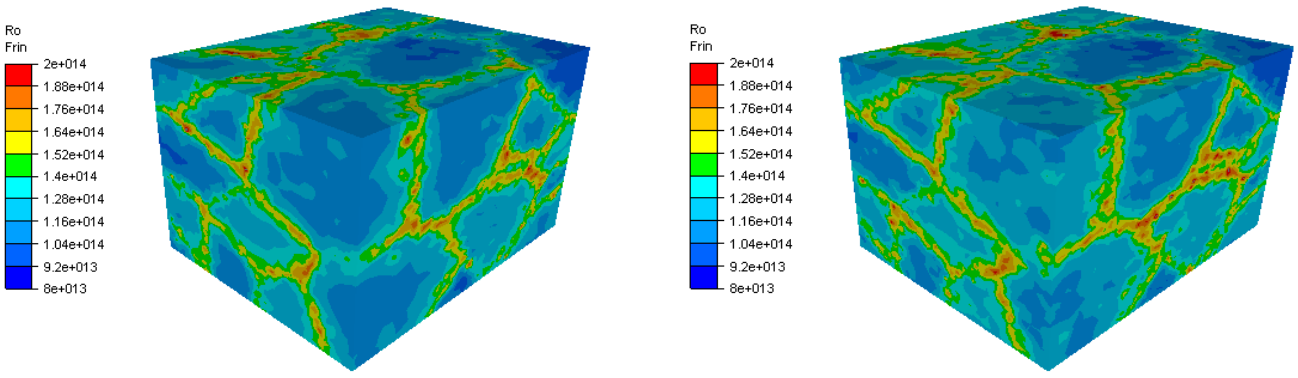

Mesh 3 Mesh 4

Figure 3.14: *GND density distribution for four different meshes for ε = 0.3.*

In [Abrivard, 2009] the authors also show the effect of the mesh refinement on the stress-strain curves of a 2D 20-grain Al polycrystal. Their model presents mesh sensitivity as soon as plastic deformation occurs. Also, this effect has been underlined by Cheong in [Cheong, 2005] for Cu polycrystal from grains smaller than 30 µm during tensile loadings. In order to avoid this mesh sensitivity, [Abrivard, 2009] proposes that the strain gradient should be calculated not for all Gauss points presented in the mesh, but only for Gauss points with a critical distance from each other. The critical distance would be linked to the GNDs spread at the grain boundary [Liang, 2009]. In the present study, since the stress difference between the different meshes is small (around 10 MPa), the method was not implemented. It may be done in future work however.

2.4 Results

The planar compression test presented earlier is used to simulate 304L steel rolling. A 0.5 mm x 0.5 mm x 0.5 mm cubic 100-grain RVE is generated.

2.4.1 Stress - Strain analysis

The macroscopic stress-strain numerical curve is plotted considering the equivalent Von-Mises stress (at each mesh element) using Equation 3.8, and the equivalent strain using Equation 3.9. Figure 3.15 illustrates a comparison between the numerical results, the theoretical result and the experimental torsion-test result.

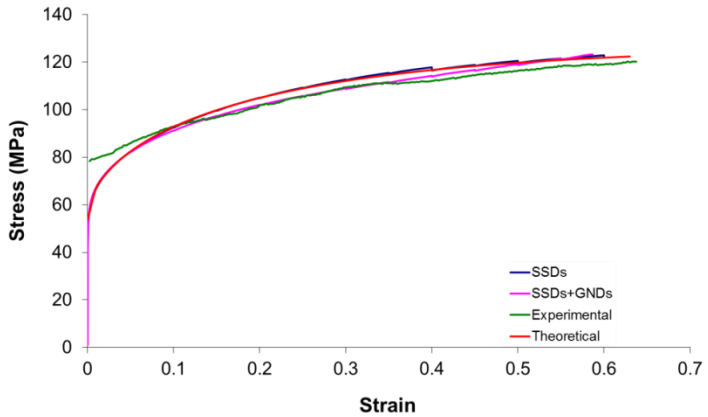

Figure 3.15: *Stress - strain curves: comparison between numerical, theoretical and experimental results.*

Both SSDs and SSDs+GNDs models predict well the experimental mechanical behaviour, even though the simulation is in plane strain compression, while the experimental curve comes from a torsion test. This is due to the fact that mean Taylor factors are close to each other, as shown previously in Table 3.4. This can be visualized by comparing the "theoretical curve", which takes into account the correct mean Taylor factor, and the experimental curve: they are very close to each other.

Looking at the stress distribution throughout the RVE (Figure 3.16), it is seen that in taking into account SSDs + GNDs, the stress concentration near the grain boundaries becomes more evident. Consequently, even though the macroscopic stress-strain behaviour is similar for both hardening models, the stress distribution in the microstructure is different.

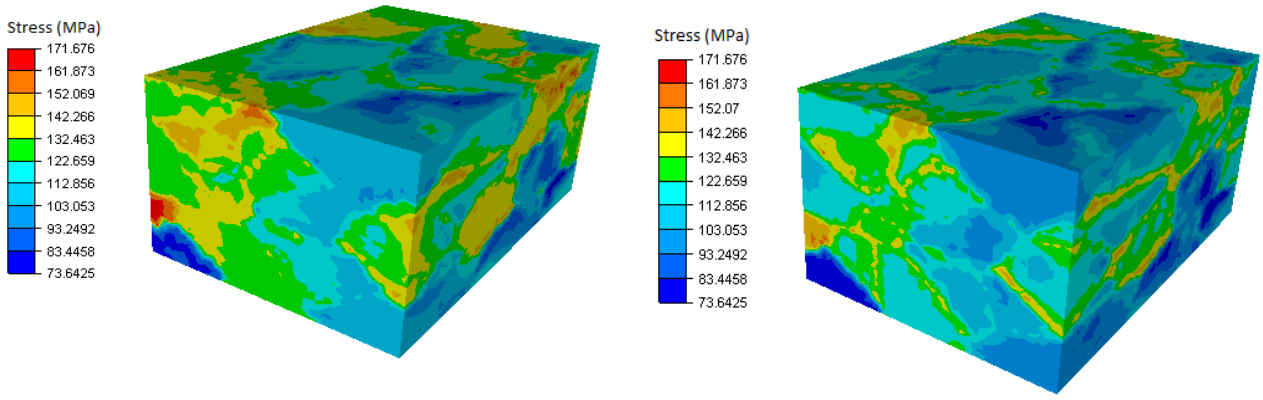

SSD SSD+GND

Figure 3.16: *304L steel stress distribution for ε = 0.5, for strain rate equal to 0.01 s^{-1} and T = 1000°C.*

A possible outcome of these crystal plasticity simulations is the possibility to predict nucleation events in recrystallization regime. This motivates further a detailed study of dislocation densities and strain distribution inherited from plastic deformation.

2.4.2 Dislocations density and energy distribution analysis

Figure 3.17 shows the dislocation density distribution considering the two hardening models, for ε = 0.5.

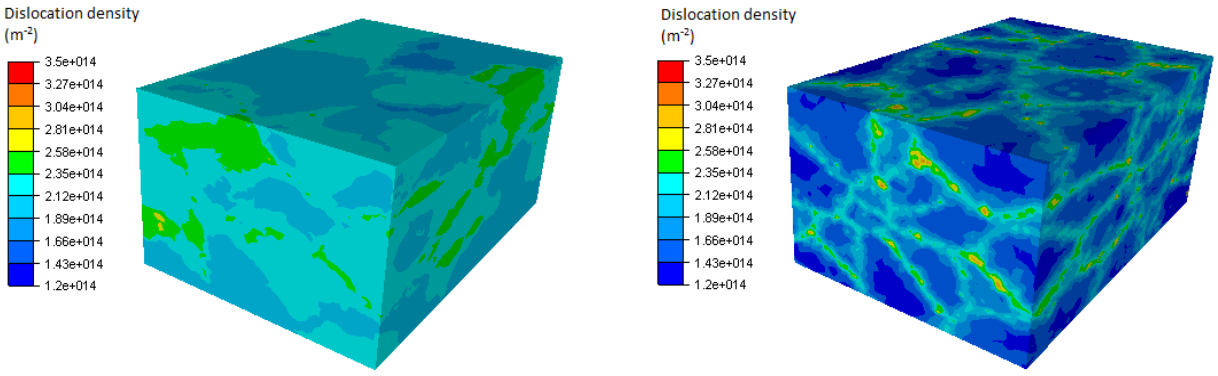

SSD SSD+GND

Figure 3.17: *Dislocation density distribution for ε = 0.5, for strain rate equal to 0.01 s^{-1} and T = 1000°C.*

Analysing Figure 3.17, we observe that the model taking into account both SSDs and GNDs presents a dislocation density concentration near the grain boundaries while the model considering only the SSDs densities present a more homogeneous dislocation density distribution.

The average dislocation density over the whole RVE is computed as:

$$\rho_{moy} = \frac{1}{V}\int_{\Omega} \rho d\Omega , \tag{3.10}$$

where ρ is the dislocation density in a given mesh element.

Figure 3.18 shows that dislocation density is an increasing and non-linear function of the plastic deformation. For simulations considering only SSDs, saturation of hardening leads to a maximum dislocation density given by $\frac{K'_1}{K'_2} = 3.0610^{14}$ m^{-2}.

For the model considering SSD + GND, for strain levels between 0 and 0.4, the dislocation variation behaviour is similar to previous case. However, for strain levels higher than 0.4, an extra increase of the dislocation variation is observed. At this stage, the material hardening near grain boundaries becomes high, and continued hardening in these zones might be overestimated.

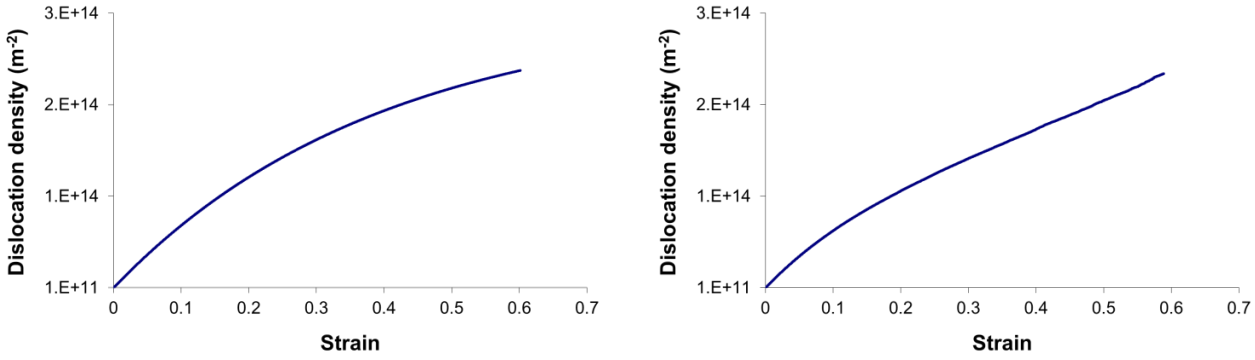

SSD SSD+GND

Figure 3.18: *Global dislocation density evolution with macroscopic strain.*

The dislocation energy is computed using the dislocation density from:

$$E_{disloc} = \frac{\mu b^2}{2}\rho , \tag{3.11}$$

where μ is the shear modulus. The global dislocation energy evolution therefore follows the same trend as that of the global dislocation density given in Fig. 3.18.

Instead of looking at the global dislocation density evolution (RVE scale), it is interesting to focus on the dislocation density evolution at the grain scale. To do so, ten randomly chosen grains are analysed. We compute their dislocation density evolution using:

$$\rho_{grain} = \frac{1}{V_{grain}}\int_{\Omega_{grain}} \rho d\Omega . \tag{3.12}$$

Figure 3.19 illustrates the calculated evolutions for both hardening models.

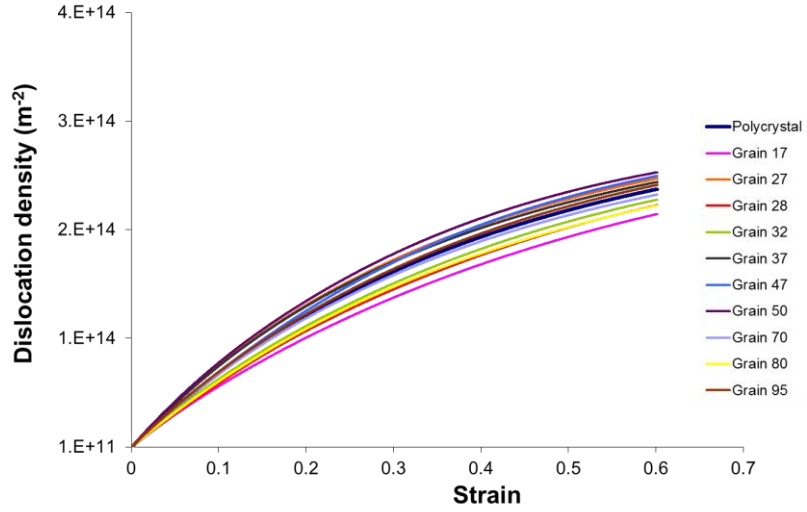

SSD

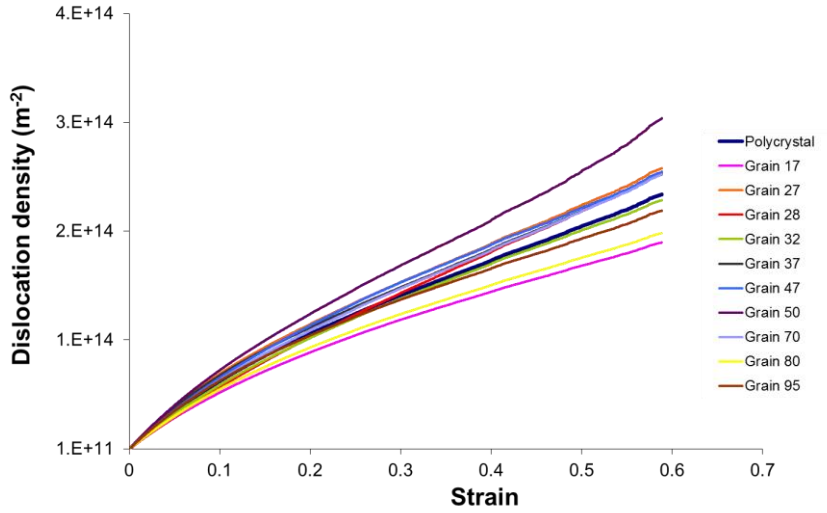

SSD+GND

Figure3.19: *Dislocation density evolution for ten randomly chosen grains.*

The mechanical response of the selected grains is different from each other, with dislocation densities spreading around the RVE (global) value. A first reason comes from the grain crystallographic orientations: the distribution of slip rates along the different slip systems results in dissimilar dislocation density evolutions. A second reason comes from the location of the grains, whether they interact with neighbours, with the fixed walls of the channel die, or with the zone of free boundaries.

It is also noticed that the grain behaviour may change during deformation. For example, when considering only SSDs, grain 80 initially hardens faster than grain 28, but after a while, this trend is inversed. This is of course the consequence of crystal lattice rotation, keeping in mind that this rotation is non homogeneous. Another example can be found in comparing grains 27 and 47.

Comparing the two hardening models, similar trends are observed for small strain levels, since hardening is then mostly controlled by SSDs multiplication. For higher strain levels, the introduction of GNDs does make a difference, as discussed already when analysing the global RVE behaviour. For example, at a strain level of 0.5, the highest dislocation density is not reached for the same grains with the two hardening models (see grain 28). This can be connected to the saturation behaviour, which automatically leads to dislocation

densities of $K_1^{'}/K_2^{'}$ for all grains in the SSDs model, whereas no saturation is reached when introducing GNDs.

At the intra-granular scale, the dislocation density distribution can be analysed as a function of the distance to the grain boundary. All mesh elements are then taken into account and the mean dislocation density (taken over the entire polycrystal) is computed only as a function of the distance to the closest grain boundary. Figure 3.20 shows the results for different deformation levels. The distance to the closest grain boundary is normalized by the polycrystal mean grain size.

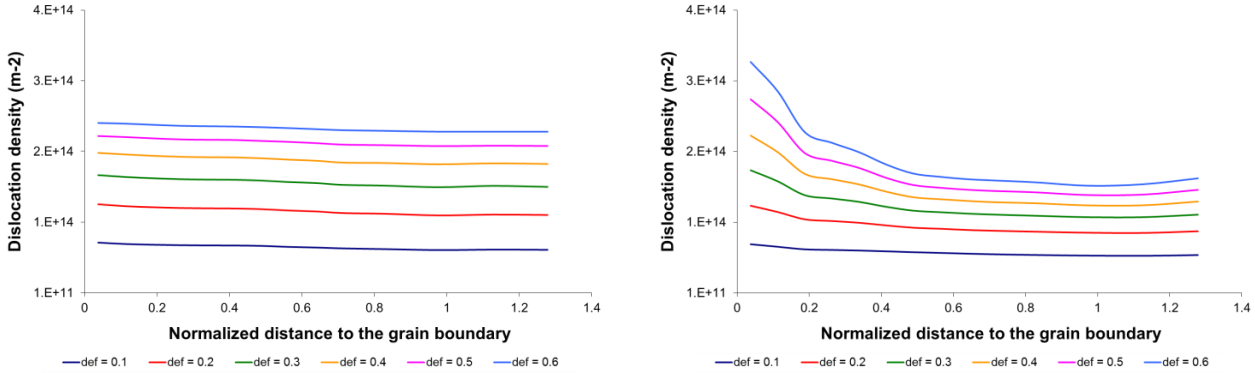

SSD SSD+GND

Figure 3.20: *Dislocation density distribution as a function of the normalized distance to the closest grain boundary for ε=0.1, ε=0.2, ε=0.3, ε=0.4, ε=0.5 and ε=0.6.*

In the SSD hardening model, the dislocation density is, in average, slightly higher near the grain boundaries. However the difference between the grain boundaries zone and the grain bulk is small. SSDs have a statistical nature, and only the local increase of the amount of strain near the boundaries can explain this result. In average, the dislocation distribution throughout the grain is quasi uniform.

On the other hand, when considering the SSD + GND hardening model a clear increase of the dislocation density is noticed near the grain boundaries, as expected. Since the nucleation of new grains is often considered to predominantly take place in zones of highest dislocation densities, it is concluded here that the choice of hardening model will have a strong impact on the predicted location of recrystallization nuclei.

One way of normalizing the above results is to write:

$$\rho\left(\phi(x)/<R>,\varepsilon\right)=\beta\left(\phi(x)/<R>,\varepsilon\right)<\rho>(\varepsilon), \tag{3.13}$$

where $\rho\left(\phi(x)/<R>,\varepsilon\right)$ is the mean dislocation density at position $\phi(x)$, $<\rho>(\varepsilon)$ is the RVE mean dislocation density, $\beta\left(\phi(x)/<R>,\varepsilon\right)$ is the proportionality coefficient and $<R>$ is the mean grain size. Figure 3.21 illustrates the $\beta\left(\phi(x)/<R>,\varepsilon\right)$ values evolution obtained for both hardening models.

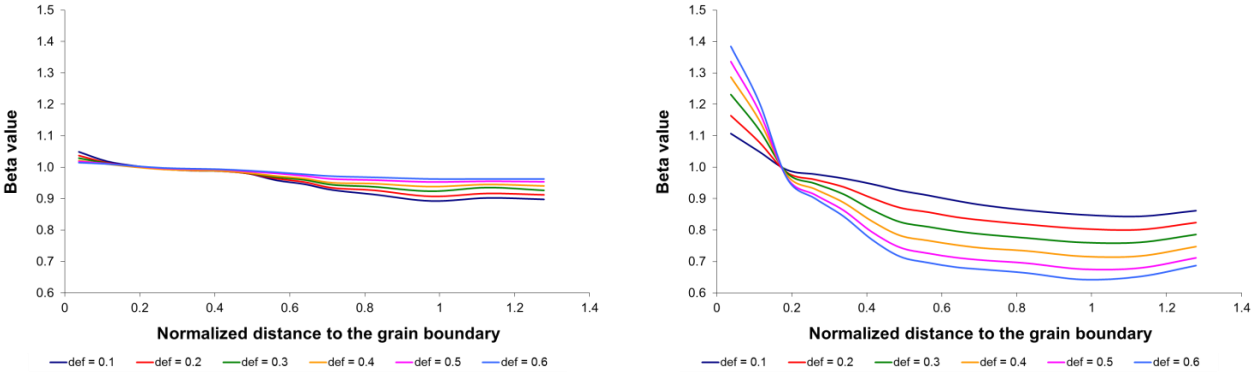

SSD SSD+GND

Figure 3.21: *Beta value as a function of the normalized distance to the closest grain boundary for ε=0.1, ε=0.2, ε=0.3, ε=0.4, ε=0.5 and ε=0.6.*

In the SSD model, the dislocation density is shown to be more and more uniform when the strain level increases. The opposite holds for the SSD + GND model.

Instead of looking at mean values, one can also detail the spread of dislocation densities as a function to the normalized distance to the closest grain boundary (Figure 3.22), and for a given strain level.

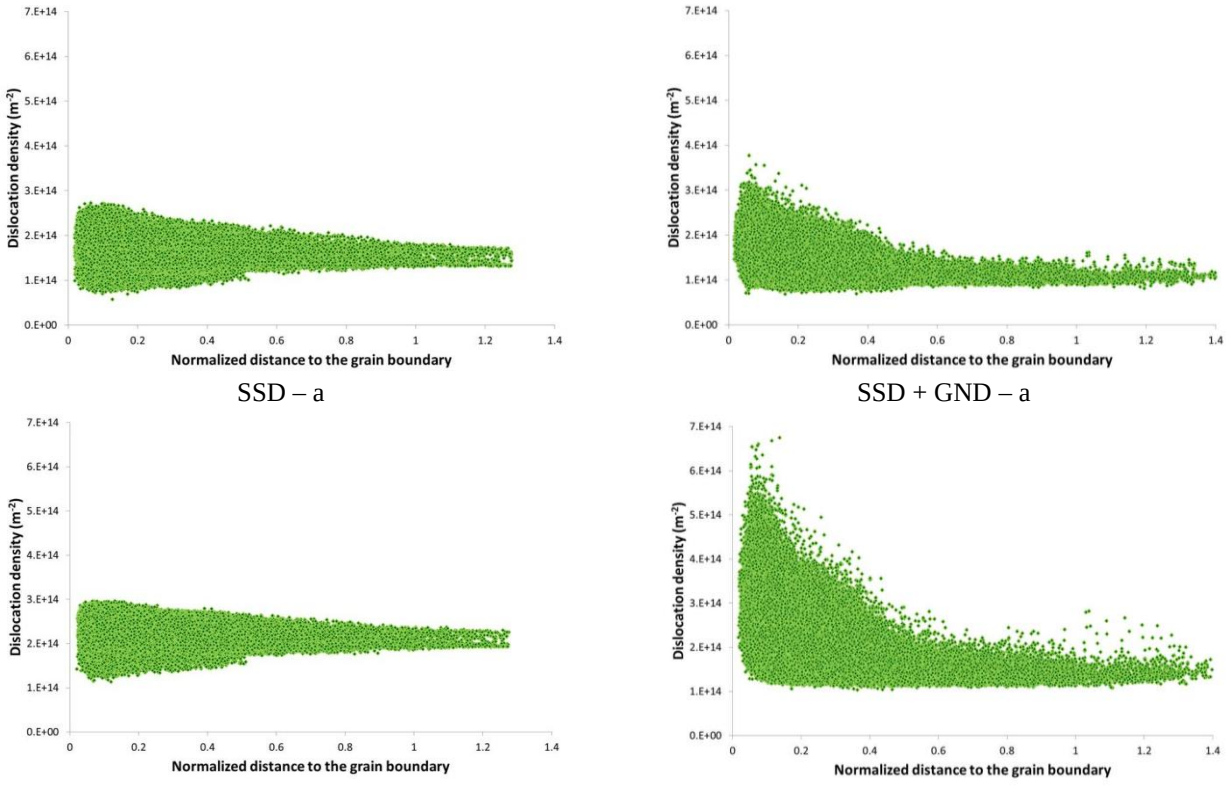

SSD – a SSD + GND – a

SSD – b SSD + GND – b

Figure3.22: *Dislocation density spread for (a) ε=0.3 and (b) ε=0.5.*

Even with the SSD hardening model, the spread of dislocation densities is highest near the grain boundaries. As a consequence, dislocation energy gradients are also expected to be the highest near the grain boundaries, and this is confirmed by Figure 3.23. This, again, promotes a preferential positioning of recrystallization nuclei near the grain boundaries. However, in the SSD model, Figure 3.24 shows that not all the grain boundaries would be potential nucleation sites.

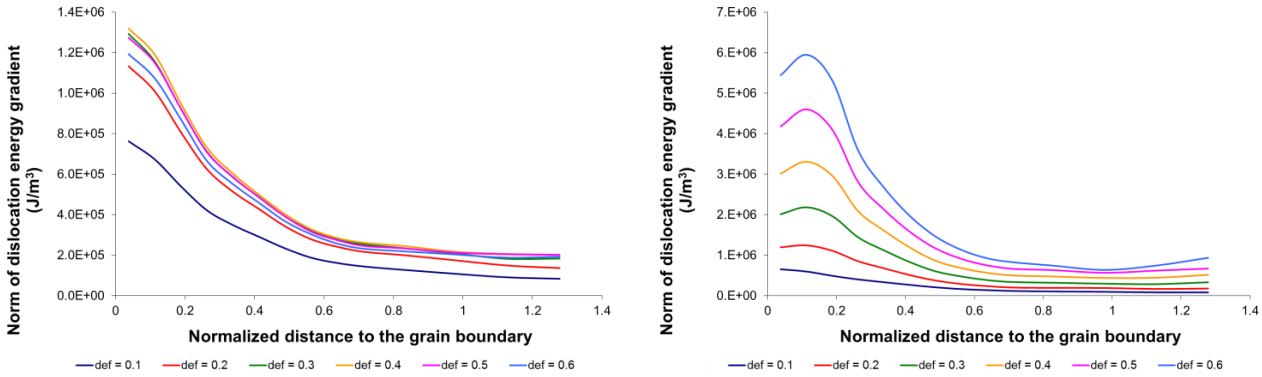

SSD SSD+GND

Figure 3.23: *Norm of dislocation energy gradient as a function of the normalized distance to the closest grain boundary for ε=0.1, ε=0.2, ε=0.3, ε=0.4, ε=0.5dand ε=0.6.*

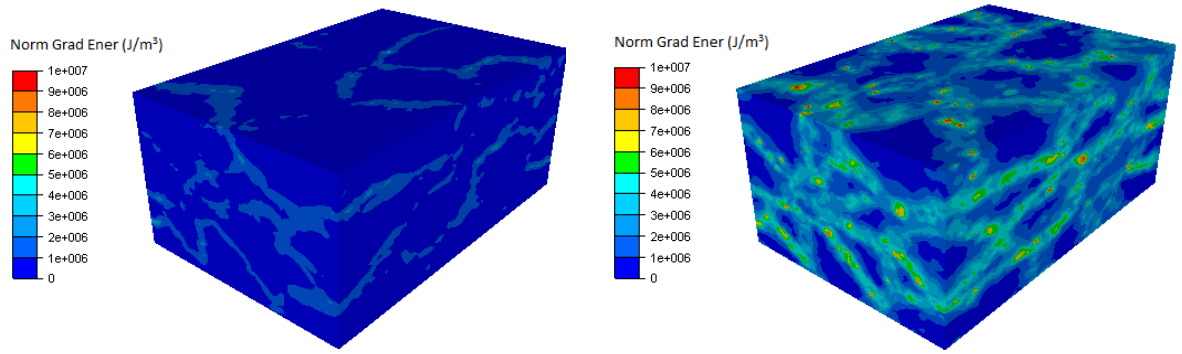

SSD SSD + GND

Figure 3.24: *Norm of dislocation energy gradient distribution for ε = 0.5, for strain rate equals to 0.01 s^{-1} and T = 1000°C.*

Coming back to Figure 3.22, with the SSD+GND hardening model, it is observed that not only the mean dislocation density is higher near the grain boundaries, but also the deviation from the mean. This dislocation density spread increases with increasing strain levels. This leads, as in the SSD case, to an increase of dislocation energy gradient near the grain boundaries, but with higher amplitude (Figure 3.23). The norm of dislocation energy gradient globally increases near the grain boundaries as illustrated in Figure 3.23. The slight decrease observed in Figure 3.23.SSD+GND very close to the grain boundaries is due to a mesh size effect. Indeed, this is a purely interpolation effect and it should not be considered in the physical analysis. Also, the increase is more systematic (i.e. it holds for all grain boundaries), as can be seen in Figure 3.24.

Figure 3.25 describes the dislocation density distribution for five different normalized distances to the grain boundary (d = 0.037, d = 0.113, d = 0.414, d = 0.827 and d = 1.128) and for two different deformation levels (ε = 0.3, ε = 0.5).

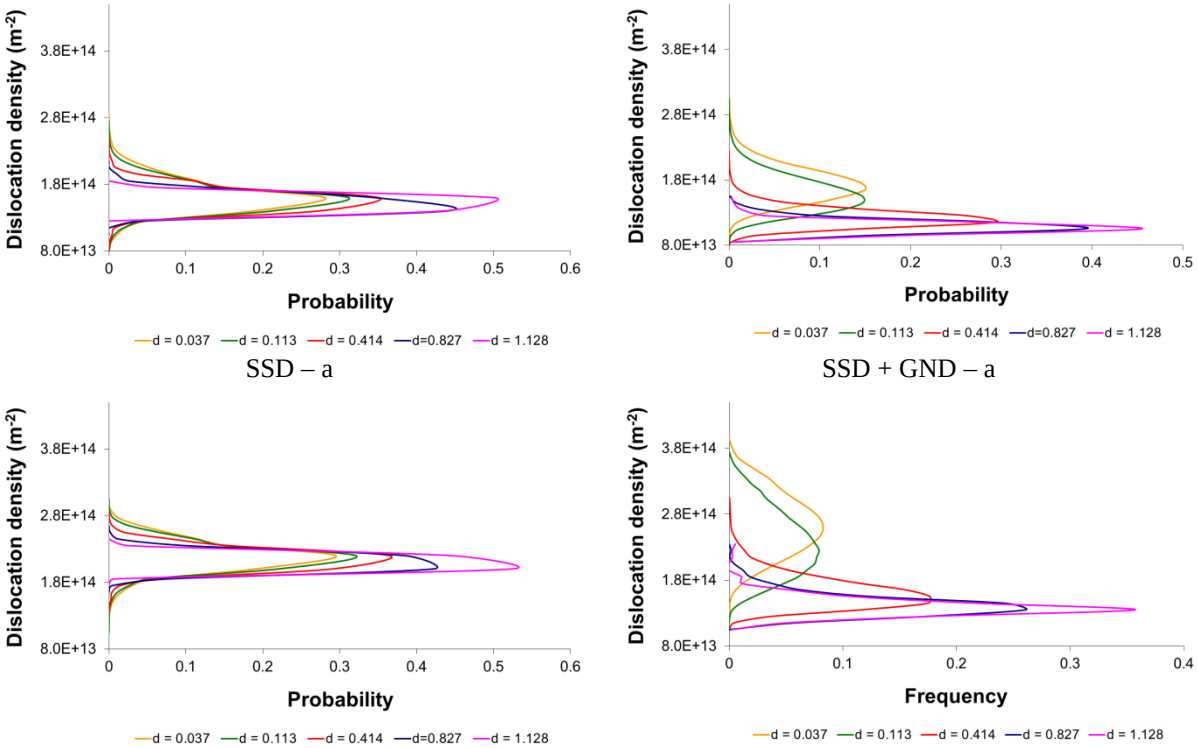

Figure 3.25: *Dislocation density distribution for five different normalized distances to the grain boundaries: d = 0.037, d = 0.113, d = 0.414, d = 0.827 and d = 1.128. Results for two strain levels (a) ε=0.3 and (b) ε=0.5 are presented.*

The distributions depend on the distance to the grain boundary. In the SSD model, the distribution is wider when approaching the grain boundary. Reversely, it becomes narrower with increased deformation levels. The highest dislocation densities always remain close to the grain boundary, although the mean value is almost uniform (as noticed earlier).

In the SSD+GND model, one can summarize that (i) both the distribution width and the mean dislocation density are increased when approaching the grain boundaries, and (ii) with increasing strain levels, distributions become wider and spatially more heterogeneous.

Based on the above results, one can conclude that nucleation processes during recrystallization will be predicted to take place mostly near the grain boundaries, in both hardening models, since in this area we find the highest levels of dislocation density and dislocation gradient values. A striking difference between the SSD and the SSD+GND hardening models, is that the former predicts homogenization of hardening with increased levels of strain, whereas the latter predicts more and more heterogeneity.

2.4.3 Strain distribution analysis

From Figure 3.26, the introduction of GNDs does not have a significant influence on strain distribution. A few areas of higher strain levels can be identified, but the difference with the SSD model is minor.

At the intra granular scale, Figure 3.27 describes the mean strain as a function of the distance to the closest grain boundary, following the idea used already for dislocation densities. Here again, distances are normalized by the mean grain size of the polycrystal, and results are given for different macroscopic deformation levels.

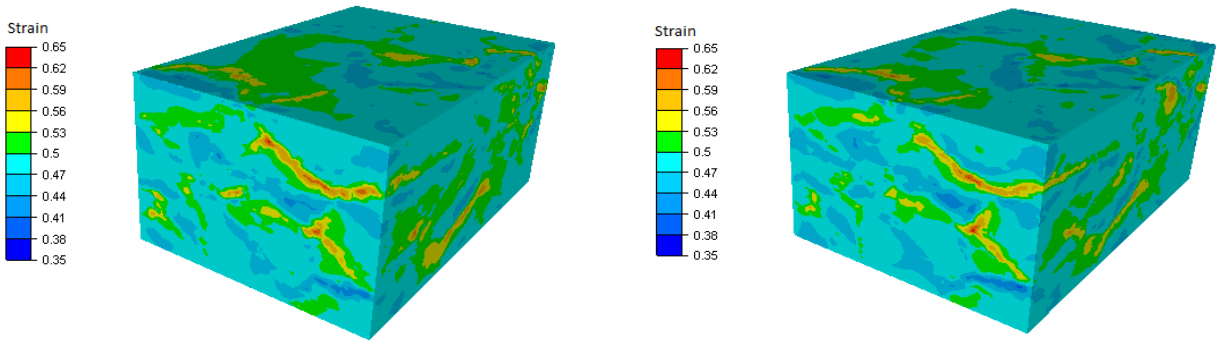

SSD SSD+GND

Figure 3.26: *Strain distribution for ε = 0.5, for strain rate equals to 0.01 and T = 1000°C.*

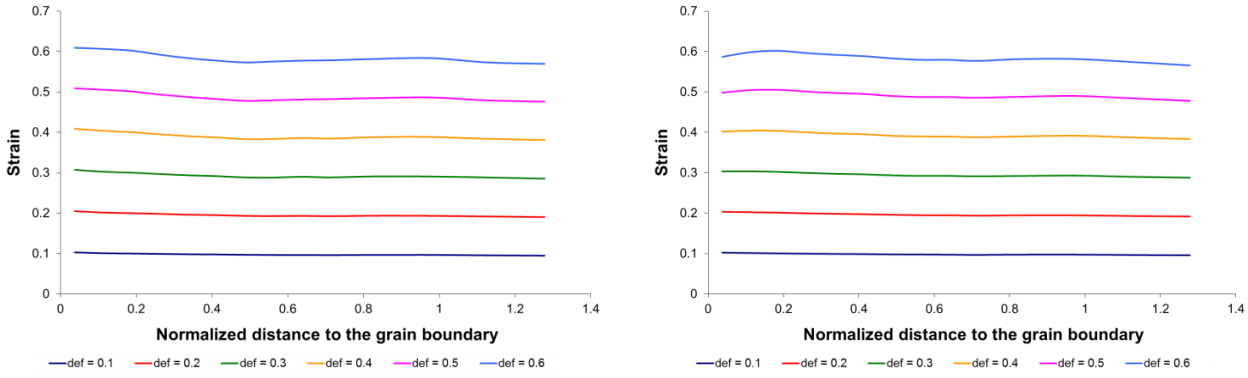

SSD SSD+GND

Figure 3.27: *Strain distribution in function of the normalized distance to the grain boundary for ε=0.1, ε=0.2, ε=0.3, ε=0.4, ε=0.5 and ε=0.6.*

The strain distributions show slightly higher values near the grain boundaries, for both hardening models. In Figure 3.28, the spread of these values is, like for dislocation densities, increased near the grain boundaries.

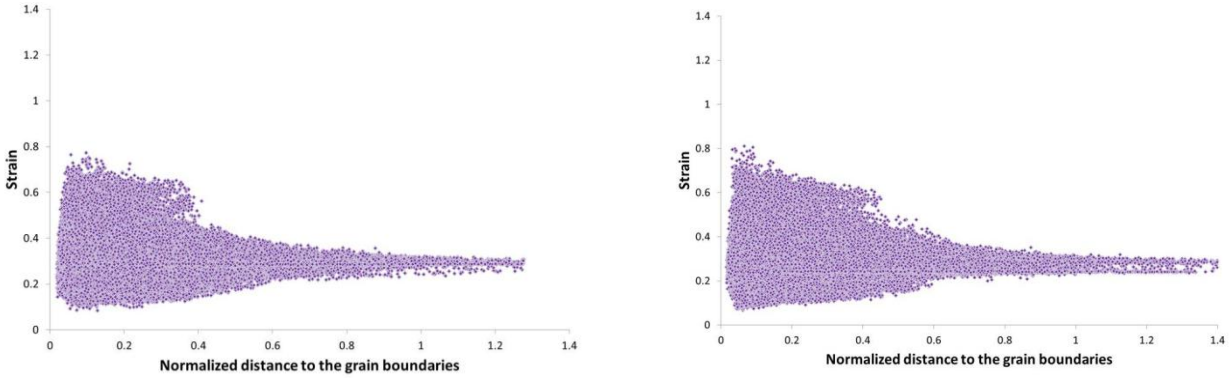

SSD – a SSD + GND – a

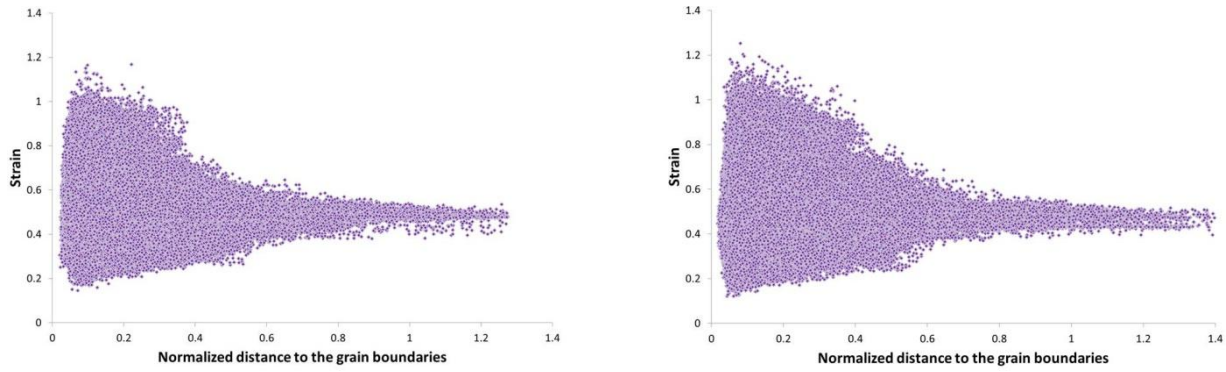

SSD – b SSD + GND – b

Figure 3.28: *Strain dispersion for (a) ε=0.3 and (b) ε=0.5.*

The deviation of strain values with respect to the mean increases with an increase of the macroscopic strain, for both hardening models. The spread in the SSD+GND model is a little higher.

2.4.4 Grain size effects

The grain size effect on the 304L steel mechanical behaviour has been investigated at T = 1000°C. The simulated strain rate is 0.01 s^{-1}. The simulations predictions for three grain sizes (0.2< R >,< R > and 3.2 < R >, with < R > being the experimental mean grain size) are presented in Figure 3.29.a. It is observed that an initial grain size reduction results in the polycrystal strengthening. For each grain size, the build-up of strain gradients leads to the accumulation of GNDs during deformation, affecting significantly the hardening behaviour of polycrystalline aggregates.

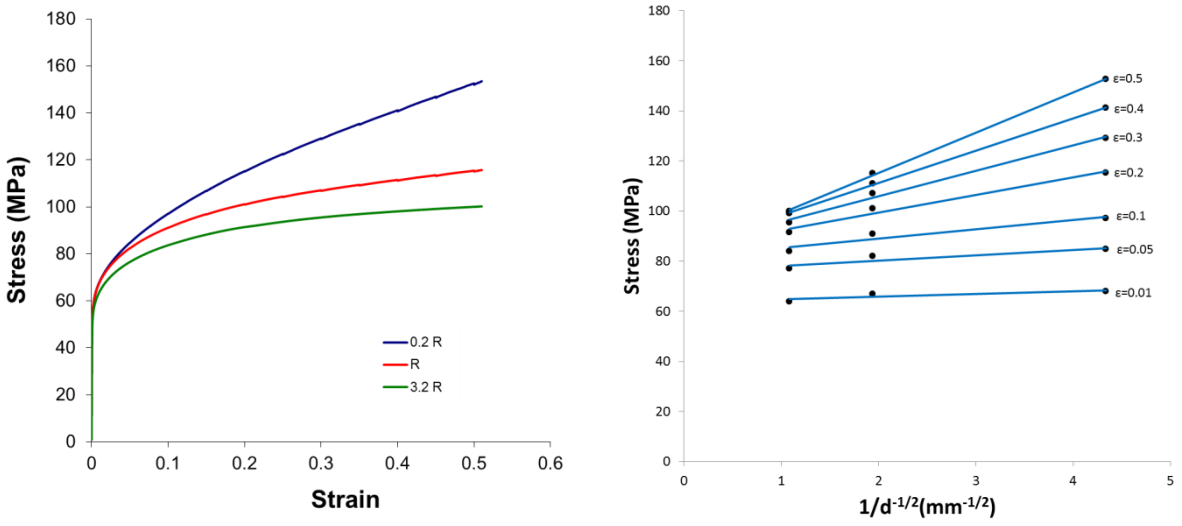

(a) (b)

Figure 3.29: *(a) Stress-strain numerical curves for three different initial grain sizes: 0.2< R >, < R > and 3.2 < R > with < R > being the mean grain size measured on 304L samples. (b) Flow stress dependency on grain size at various strain levels (black dots) with the fitted Hall-Petch relation (blue lines).*

It was found that the grain size dependence of the flow stress, σ, follows a modified Hall-Petch equation of the type:

$$\sigma = \sigma_0(\varepsilon) + k(\varepsilon) d^{-\frac{1}{2}}, \tag{3.14}$$

where $\sigma_0(\varepsilon)$ and *k(ε)* are parameters varying with the strain level. In Figure 3.29.b, the linear interpolation of the numerical results for different grain sizes is done in a Hall-Petch graph. The stress variation with the grain size follows well relation (3.14), for all investigated macroscopic deformation levels.

In [Mirzadeh, 2013], the effect of 304L steel grain size influence on the stress-strain curve is studied, and a similar behaviour is observed. Also, it is important to highlight that, for smaller grain sizes, the dynamic recrystallization onset is at smaller strain levels. As a consequence, for a polycrystal with 0.2<R>, results for strain levels larger than 0.3 may not have a physical meaning.

Predicted stresses probably overestimate the experimental results, as was already noticed by [Abrivard, 2009] in the small grain sizes range. This is probably a consequence of the GND evolution model, which does not account well for dislocation transport and/or the annihilation of dislocations. Dislocation annihilation is computed only by the SSD evolution equation.

The SSD+GND model however predicts physical results in terms of grain size effects. In order to improve this study, complementary experimental tests, with samples presenting different initial mean grain sizes, should be done. Also, an improvement in the GND evolution equation formalism is needed.

3 Tantalum Case

This second study relates to uniaxial compression tests of tantalum olygocrystals. Olygocrystals are macroscopic samples containing only a few grains, i.e. the grains have mm to cm sizes. The experimental compression tests were performed by Christophe Kerisit during his Ph.D. [Kerisit, 2012]. Tantalum was chosen here for two main reasons: (i) the technical possibility of producing olygocrystals, with columnar structures and (ii) its high ductility at room temperature.

With such samples, it is possible to perform a numerical study on:

- the evolution of the macroscopic shape of the samples, which is a consequence of the plastic anisotropy of single crystals;
- the local distributions of dislocation densities and strain (as was done for 304L steel);
- global and local texture evolutions.

Some of these quantities can be measured experimentally, and can serve as validations of the crystal plasticity models. In future work, heat treatments of the deformed samples can then be used to identify the spatial positioning of recrystallization nuclei, and attempt the development of appropriate nucleation criteria.

3.1 Tantalum

Tantalum is a rare material presenting a B.C.C. (body-centred cubic) crystalline structure, with a lattice parameter equal to 3.3 x 10^{-10} m. This material has a high fusion temperature (2996 °C) and also a high density (16650 kg.m^{-3}). The 3 active slip systems

families accommodating plastic deformation are {110} <111>, {112} <111> and {123} <111>, leading, in total, to 48 different slip systems.

Pure tantalum is known to be very ductile at room temperature, but when temperature increases, hydrogen (for T > 200°C), oxygen (for T > 300°C), nitrogen (for T > 1100°C) and carbon (for T > 1200°C) diffuse into the material. The introduction of these elements results in a strength increase, and a ductility decrease. As a consequence, all tantalum heat treatments should be performed under good vacuum conditions. The mechanical behaviour of tantalum is identified and studied in details in [Kerisit, 2012]. The hardening model used to describe tantalum hardening is the equivalent to the Laasraoui-Jonas implemented in the crystal plasticity code.

3.2 Compression test

3.2.1 Test description

Figure 3.30 illustrates the principle of uniaxial compression tests performed on the Ta samples.

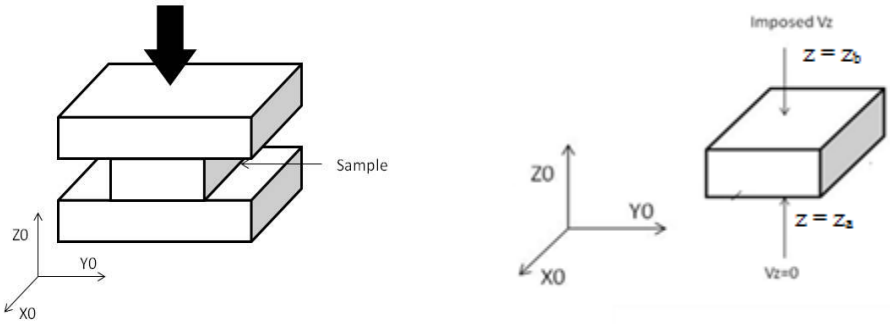

(a) (b)

Figure 3.30: *Simple compression test sketch: (a) test description, (b) imposed boundary conditions.*

The mean digital microstructure deformation (over the volume Ω) is controlled by imposing the velocity on the $z = z_a$ and $z = z_b$ planes (Fig. 3.30.b). In this case, $\dot{\varepsilon} = 0.01\ s^{-1}$.

3.2.2 Digital oligocrystal

The studied oligocrystal is a 28.2 mm x 5.9 mm x 5 mm parallelepiped composed of 6 grains which are assumed to be quasi columnar. The oligocrystal is digitally generated and immerged into a finite element mesh. In this case, neither the Voronoï nor Laguerre-Voronoï methods are used. Each grain is generated individually and then, the six different grain meshes are immerged in a unique mesh. Each grain is represented using a different level set function (chapter 2). Figure 3.31 illustrates the real and the digital olygocrystals.

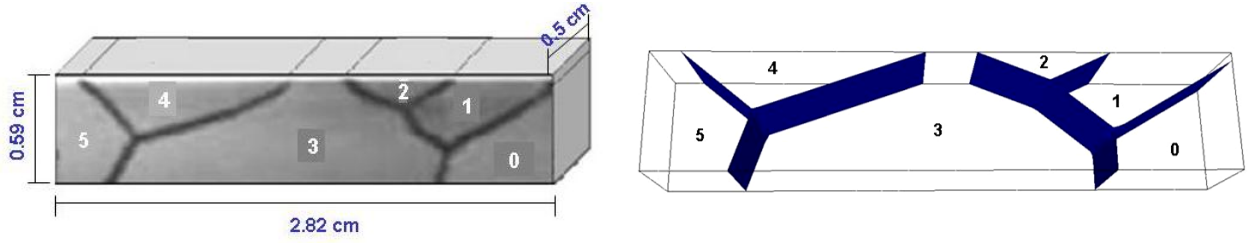

(a) (b)

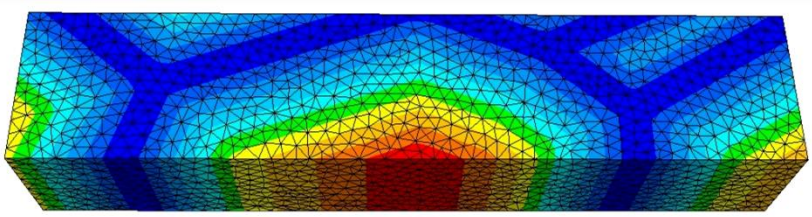

(c)

Figure 3.31: *(a) Real tantalum oligocrystal, (b) digital oligocrystal and (c) the same digital olygocrystal immerged into a finite element mesh.*

3.2.3 Material parameters

Tantalum material parameters used in the simulations are presented in Table 3.8.

Table 3.8: *Tantalum parameters at room temperature [Frénois, 2001].*

C_{11}(GPa)	C_{12}(GPa)	C_{44}(GPa)	$\dot{\gamma}_0$ (s^{-1})	μ (GPa)	b (m)	m
266	161	82	0,001	72	$0{,}286\ 10^{-9}$	20

$\dot{\gamma}_0$ is a reference slip rate and m the sensitivity exponent. K'_1, K'_2, τ_0 and α parameters have been identified as well, but, for confidentiality reasons, the numerical values are not given. The same material parameters are used for both SSD and SSD + GND hardening models, because the GND influence on the macroscopic mechanical behaviour is negligible when dealing with very large grain sizes, as it is observed in figure 3.32.

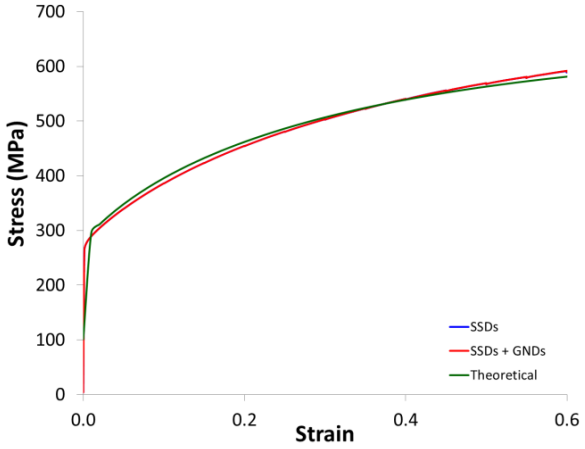

Figure 3.32: *Stress-strain numerical curves compared to the theoretical curve.*

The Euler crystallographic orientation angles and Taylor factors are given for each of the 6 grains in Table 3.9.

Table 3.9: *Crystallographic orientation (Euler angles) and Taylor factor of all six oligocrystal grains.*

	Φ_1	Φ	φ_2	Taylor Factor for a simple compression test
Grain 0	76,6°	43,3°	304,2°	3.351
Grain 1	8,0°	4,2°	343,8°	2.431
Grain 2	276,0°	36,0°	92,0°	3.493
Grain 3	227,5°	51,8°	138,9°	3.644
Grain 4	18,1°	40,3°	354,4°	3.605
Grain 5	300,5°	35,0°	49,2°	3.058

Although the BCC structure exhibits 48 different slip systems, it was chosen here to restrict the description to 24 slip systems ({110} <111>, {112} <111>).

3.3 Results

3.3.1 Sample shape

The first thing to be examined is the oligocrystal shape after deformation. Figure 3.33 compares the experimental and the two numerical oligocrystals obtained after a deformation of $\varepsilon_{ZZ} = 0.5$. The two numerical simulations correspond to the two usual hardening models (SSDs, SSDs + GNDs).

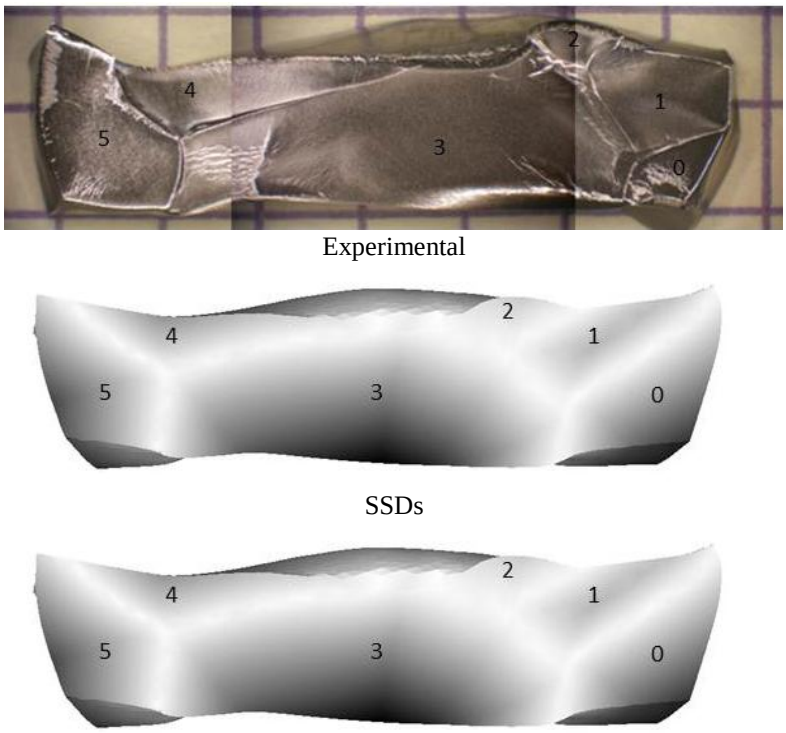

Figure 3.33: *Comparison between experimental and numerical (both SSDs and GNDs+SSDs simulations) oligocrystal shapes after a deformation of 0.5 (ε_{ZZ} = 0.5).*

A first observation is that the hardening model does not influence the predicted final shape.

Comparing with experiments, it is noticed that grains 2, 3, 4 and 5 have a final shape which is well predicted. Grain 3 in particular: the material shear – a consequence of the anisotropy – goes in the good direction, with appropriate curvatures of the external boundaries. Similar comments apply to grains 2 and 4.

However, numerical results of grains 0 and 1 do not agree well with the experimental results. Experimentally, these two grains bend downwards, while the prediction goes upwards. The shearing of grain 0 seems to follow a good trend, but there is clearly an experimental change which cannot be captured by the model. One possible explanation would be the existence of another grain underneath the surface, before deformation, which then came

onto the surface during deformation (which would mean that the initial microstructure was not, as assumed, columnar in this region).

Despite some differences between the experimental and numerical results one can conclude that the numerical model has a good ability in predicting final shapes induced by plastic deformation.

3.3.2 Dislocations density distribution

Figure 3.34 gives the spatial distributions of dislocation densities for both hardening models (only SSD and SSD+GND), in the final deformed configuration.

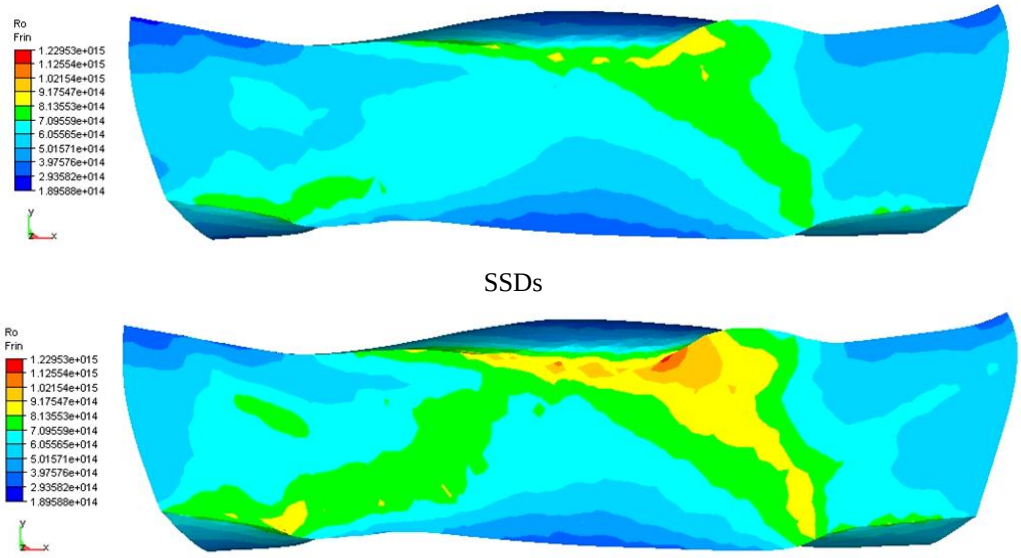

Figure 3.34: *Dislocation density distribution for ε_{ZZ} = 0.5, for two numerical olygocrystals: considering only SSD and considering both SSD + GND.*

As usual, the introduction of GNDs increases the dislocation density near the grain boundaries.

Once again, the average dislocation density over the whole sample is computed using Equation 3.10, and the evolution with the macroscopic strain is presented in Figure 3.35.

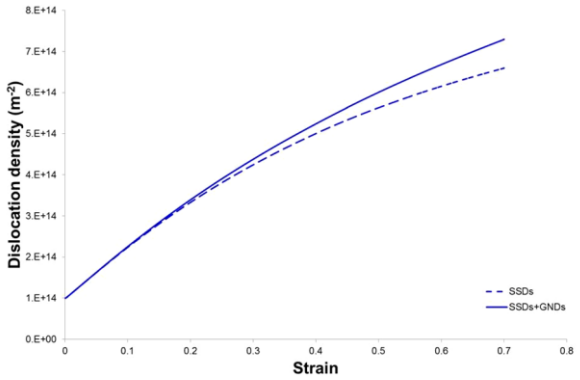

Figure 3.35: *Sample average dislocation density evolution for hardening models considering only SSDs and both SSD + GND.*

Differences between the two hardening models start appearing around a deformation of 0.2. However, even after a deformation of 0.5, the predicted average dislocation densities remain very close (and hence lead to a similar macroscopic mechanical behaviour), due to the very large grain sizes in the sample.

A grain-by-grain analysis is done in Figure 3.36.

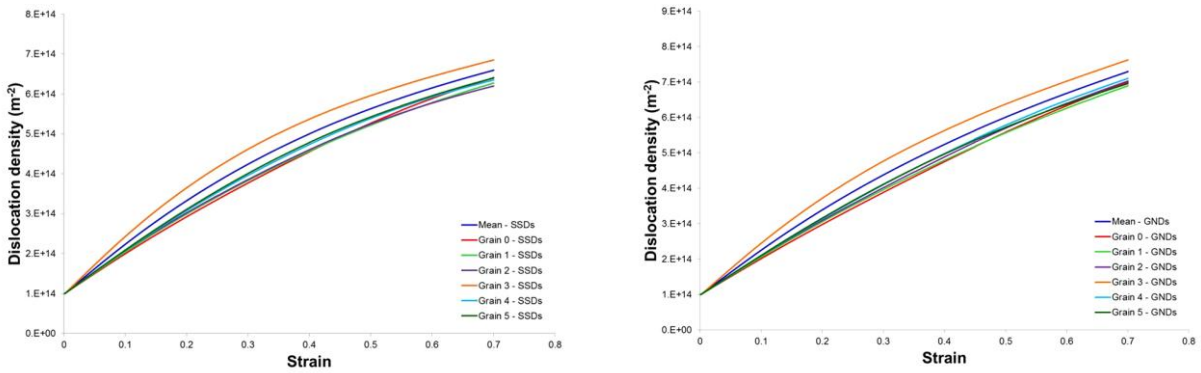

(a) SSDs (a) SSDs+GNDs

Figure 3.36: *(a) Dislocation density evolution as a function of strain for six tantalum grains.*

For both hardening models, grain 3 exhibits the highest dislocation density during the total material deformation. Differences may appear for other grains. In chapter 5, these type of numerical results will be used to simulate recrystallization processes. In this context, the above differences can result in a difference in the nucleation site positions and, as a consequence, in differences on the predicted recrystallization kinetics.

The intra granular scale analysis can be performed as well, looking at the mean dislocation density as a function of the distance to the closest grain boundary. This is done in Figure 3.37 for different deformation levels, and with distances expressed in cm.

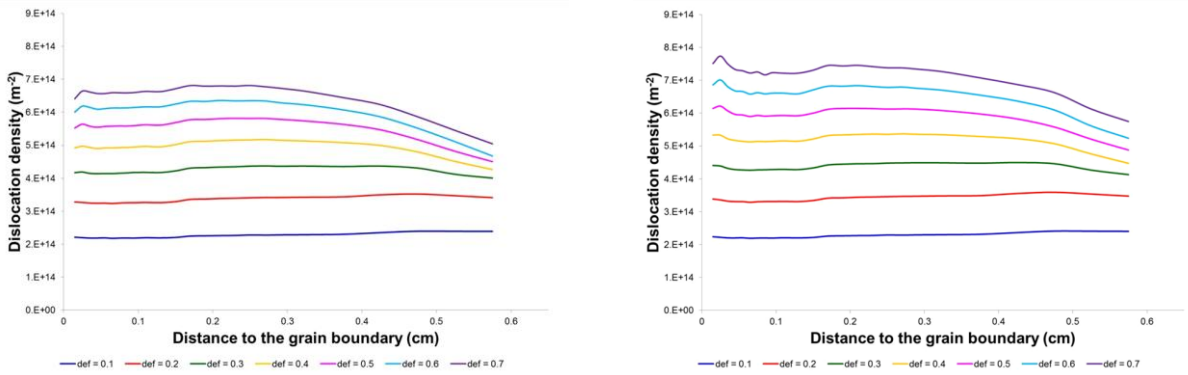

SSDs SSDs+GNDs

Figure 3.37: *Dislocation density distribution as a function of the distance to the closest grain boundary for ε=0.1, ε=0.2, ε=0.3, ε=0.4, ε=0.5, ε=0.6 and ε=0.7.*

For distances between 0.2 cm and 0.4 cm, the dislocation density is higher than for distance around 0.1 cm. In the SSDs model, the dislocation density in this area is actually even higher than near the grain boundary. This is a consequence of a geometrical effect in the oligocrystal, which can be understood from Figure 3.38. A high density dislocation area is observed far from the grain boundaries, represented by yellow and green zones, due to strong local curvatures. Note that in Figure 3.38, the oligocrystal is viewed from behind, when compared to the views given previously (e.g. Fig. 3.34).

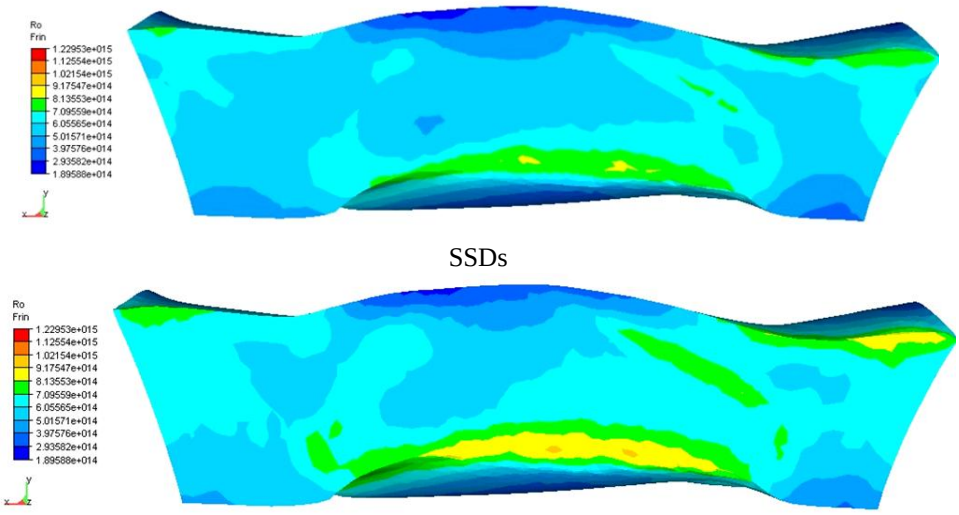

Figure3.38: *Dislocation density distribution for ε_{ZZ} = 0.5 (view from behind).*

This behaviour is therefore particular to the large grains oligocrystals: it is not expected to happen in standard polycrystals, at least not in uniaxial compression.

From Figure 3.37, SSD results would indicate a preferential nucleation of recrystallization between 0.2 and 0.4 cm from the closest grain boundary. On the contrary, when introducing GNDs, grain boundaries remain the preferential sites.

In order to understand in more details the dislocation density distribution for each grain, the spread, or dispersion of values is displayed in Figure 3.39.

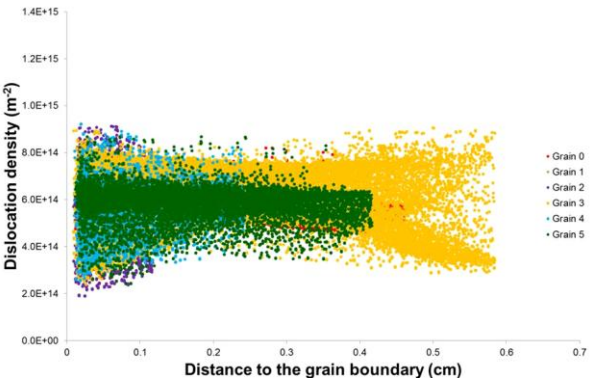

All grains – SSDs

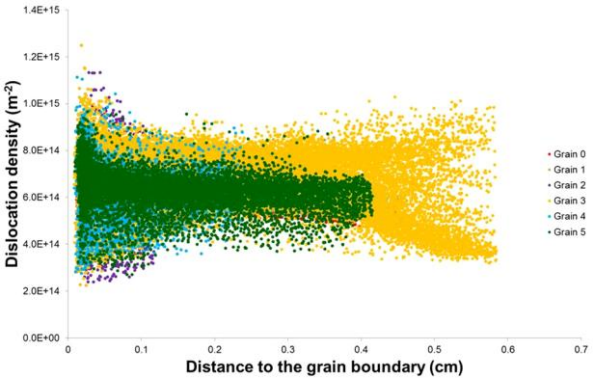

All grains - GNDs + SSDs

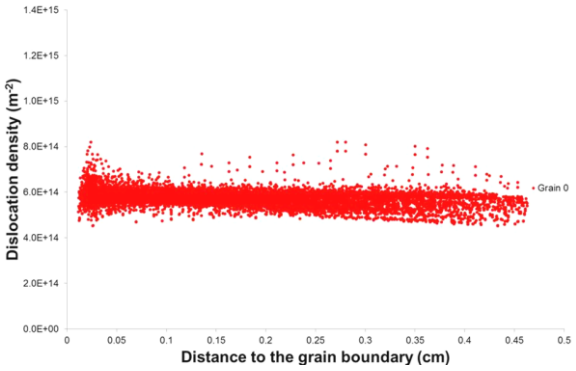

Grain 0 – SSDs

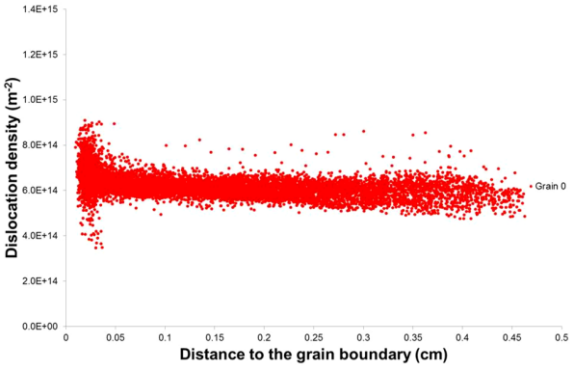

Grain 0 - GNDs + SSDs

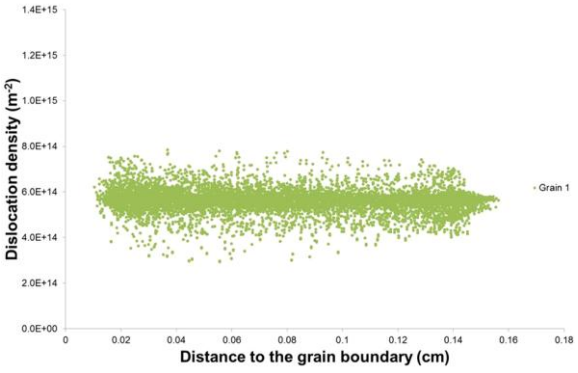

Grain 1 – SSDs

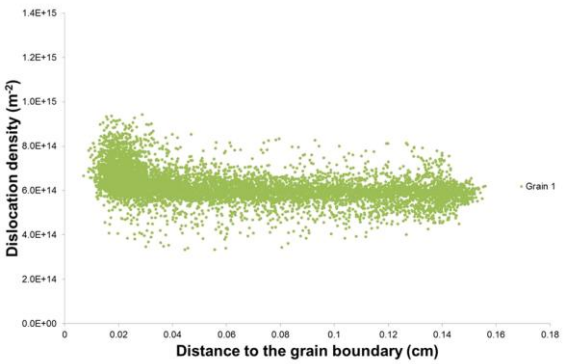

Grain 1 - GNDs + SSDs

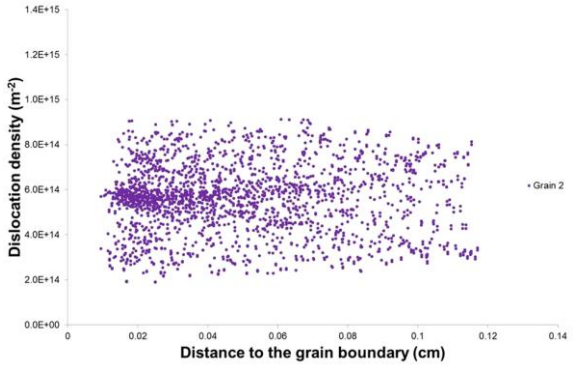

Grain 2 – SSDs

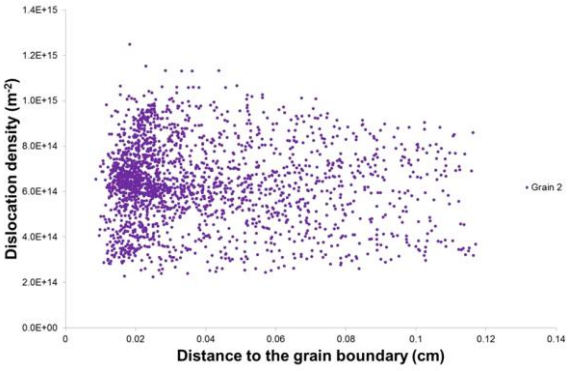

Grain 2 - GNDs + SSDs

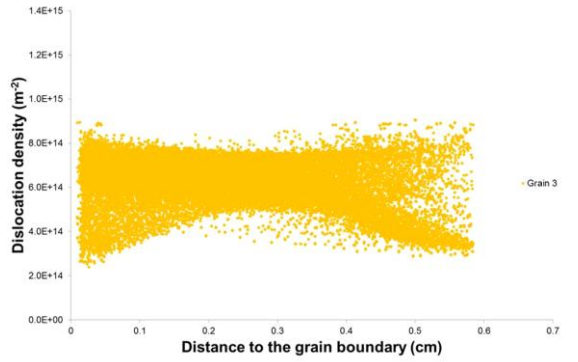

Grain 3 – SSDs

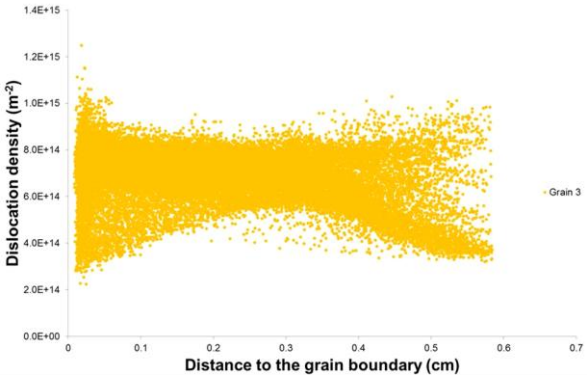

Grain 3 - GNDs + SSDs

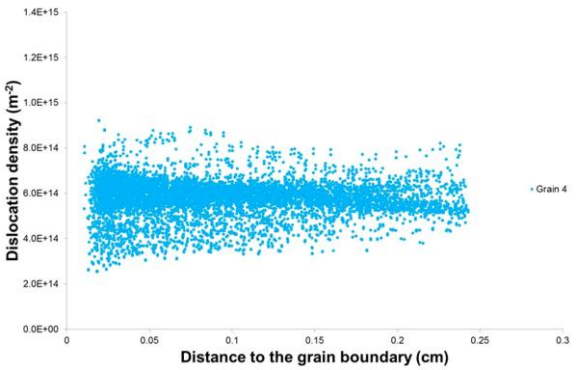

Grain 4 – SSDs

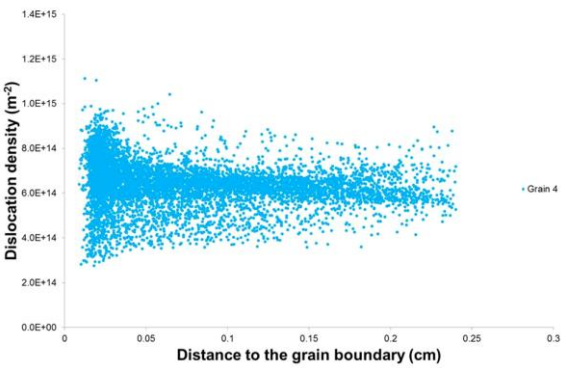

Grain 4 - GNDs + SSDs

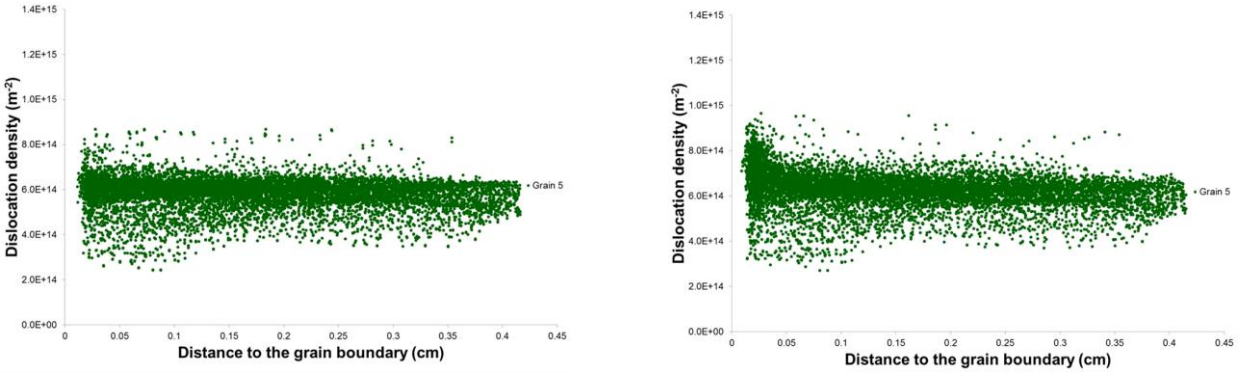

Grain 5 – SSDs Grain 5 - GNDs + SSDs

Figure 3.39: *Dislocation density distribution at ε_{ZZ} = 0.5 for the whole oligocrystal and for all six individual grains.*

Comparing the dislocation density dispersion obtained with both models, we observe that, for all grains, the dispersion near the grain boundary is more important when the GND density is taken into account.

Also, it is interesting to observe that each grain behaves differently. For example, grain 0, 1, 4 and 5 present a narrower distribution. On the other hand, grain 2 is very heterogeneous. Finally, grain 3, with its five neighbouring grains, has an intermediate behaviour. In some regions, the dislocation density is relatively homogeneous (similar to grains 0, 1, 4 and 5), and in others it is much more heterogeneous. The dislocation density profiles at interfaces between neighbouring grains (Figure 3.40) vary also, indicating more or less compatible deformations between the neighbours.

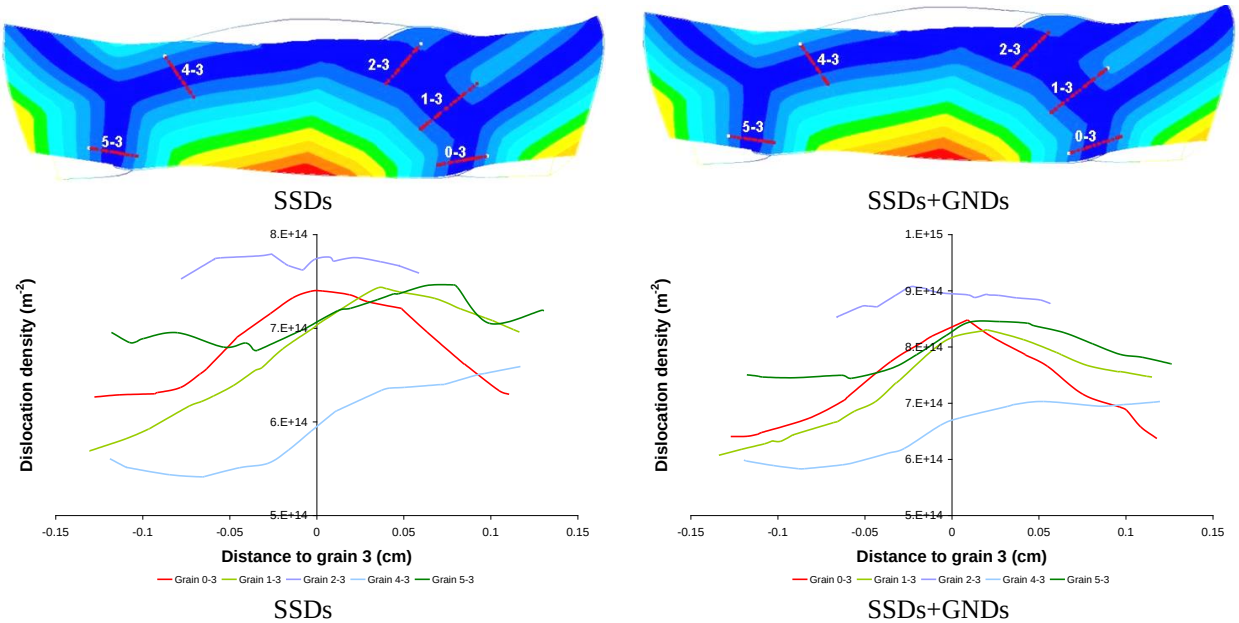

SSDs SSDs+GNDs

SSDs SSDs+GNDs

Figure 3.40: *Dislocation density distribution for ε_{ZZ} = 0.5 for the neighbouring zones of grain 3.*

Coming back to criteria for the nucleation of new grains, not only a critical dislocation density is necessary, but there is also a role played by dislocation density gradients (grain boundary motion and driving forces are discussed in details in chapters 4 and 5).

Dislocation energy is calculated using Equation 3.11. Figure 3.41 presents the norm of dislocation energy gradient distribution for ε_{ZZ} = 0.5, and Figure 3.42 presents the intra granular dislocation energy gradient distribution.

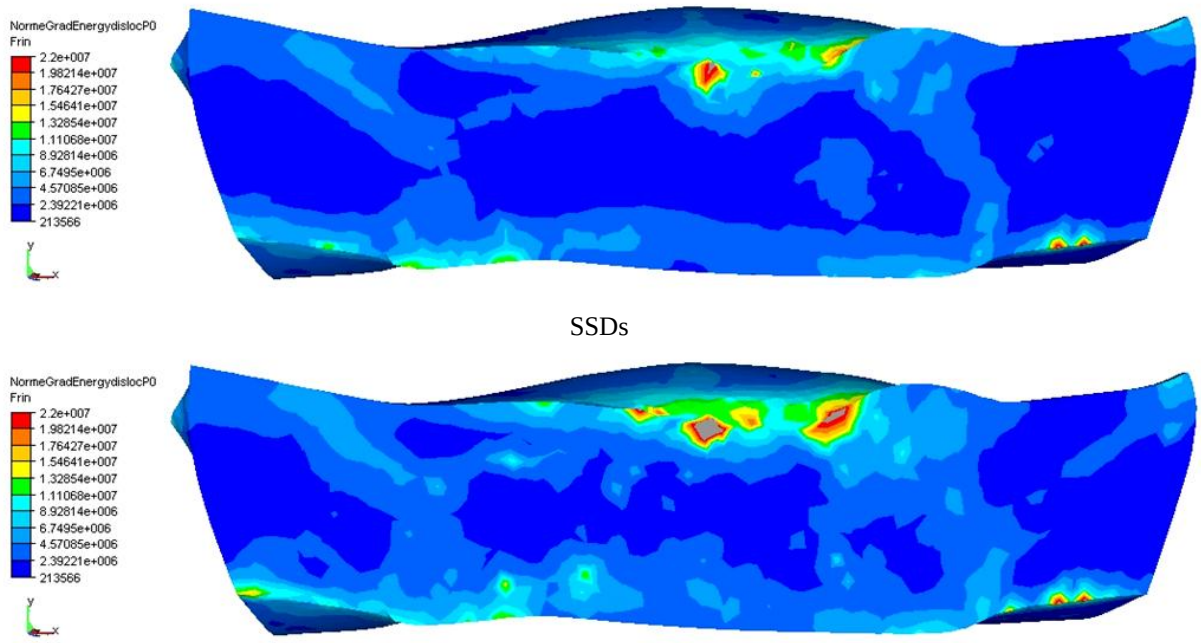

Figure 3.41: *Norm of dislocation energy gradient distribution for ε_{ZZ} = 0.5.*

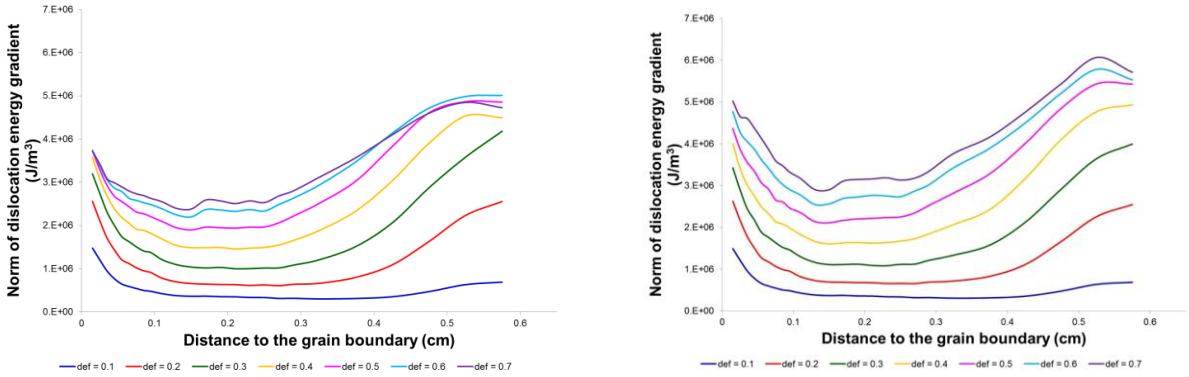

Figure 3.42: *Norm of dislocation energy gradient as a function of the distance to the closest grain boundary for ε=0.1, ε=0.2, ε=0.3, ε=0.4, ε=0.5, ε=0.6 and ε=0.7.*

Dislocation energy gradients, especially near the grain boundaries, are slightly increased with the SSD+GND hardening model, however profiles look similar. Two areas of high gradients are near the grain boundaries, and around 0.4 cm from them. The second one is related to the geometrical effects already discussed for Fig. 3.38.

3.3.3 Deformation distribution

As already noticed in the 304L plane strain test case, the hardening model does not influence much the spatial distribution of strains in the sample (Fig. 3.43).

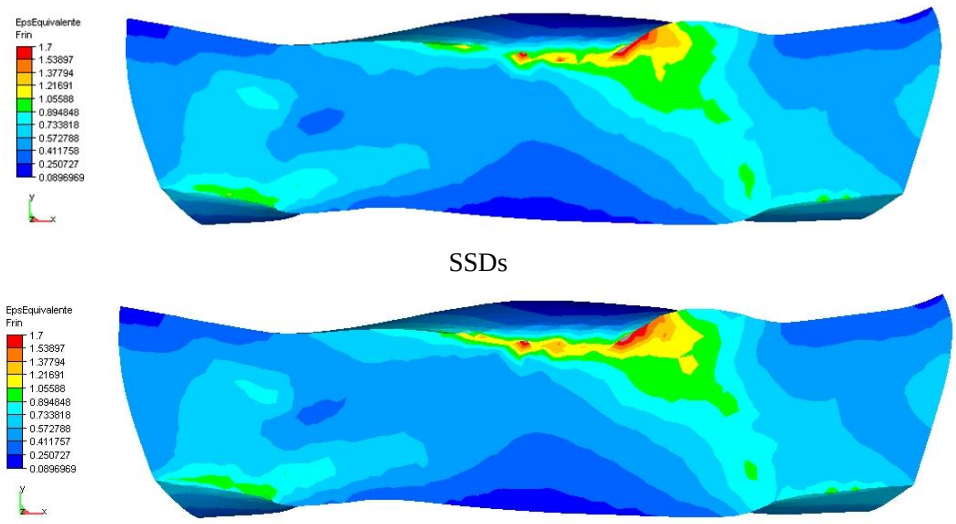

Figure 3.43: *strain distribution in the oligocrystal for* $\varepsilon_{ZZ} = 0.5$.

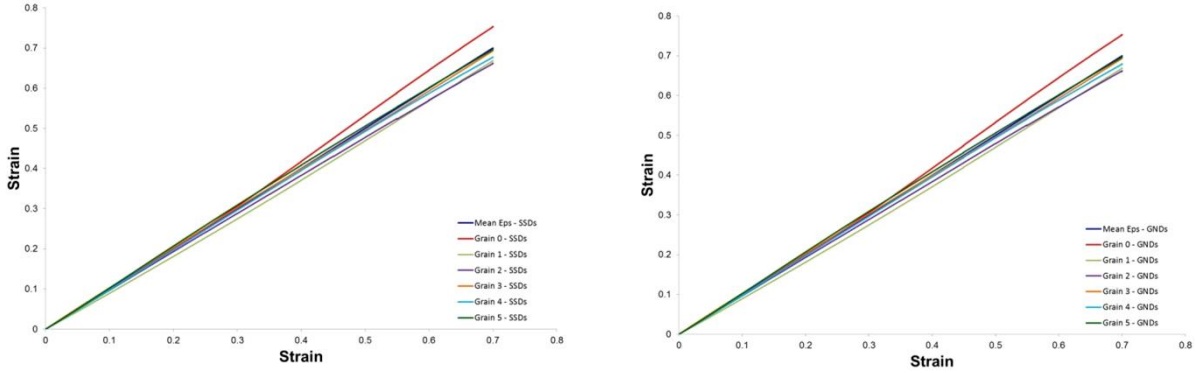

Figure 3.44: *(a) Strain evolution as a function of the macroscopic strain for the six tantalum grains.*

The grain-by-grain evolution of strain given in Figure 3.44 exhibits that grain 0 is the one that eventually deforms the most. The initial Taylor factor is not the highest (M = 3.351 – Table 3.9), but crystal reorientation with plastic deformation is responsible for the progressive increase of strain. The connection between Taylor factor and amount of strain is quite systematic, with however some neighbourhood effects which can influence the strain distribution (e.g. grain 5 which is the 2nd most deformed, but with a Taylor factor which is not the 2nd).

Analysing the intragranular strain distribution (Figure 3.45), it is observed that both hardening models present almost the same curves.

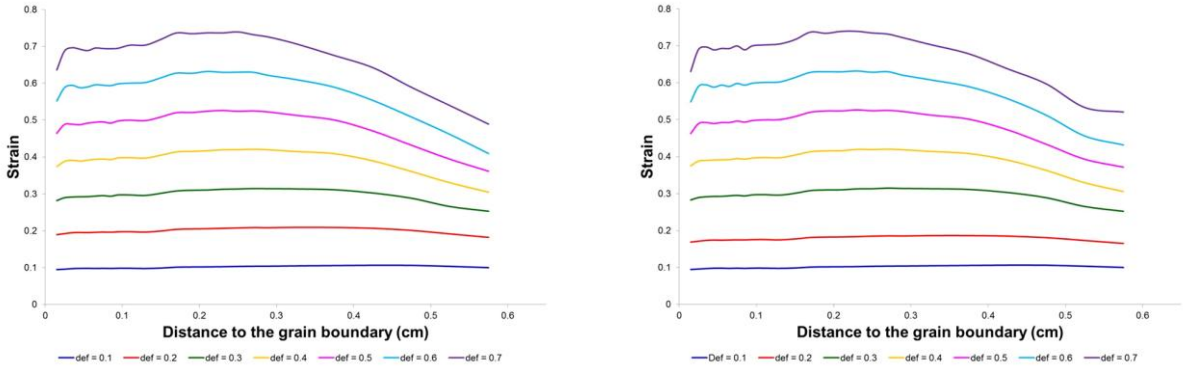

SSDs SSDs+GNDs

Figure 3.45: *Strain evolution in function of the distance to the grain boundary for ε=0.1, ε=0.2, ε=0.3, ε=0.4, ε=0.5, ε=0.6 and ε=0.7.*

The strain dispersion within individual grains of the oligocrystal (Figure 3.46) shows once again contrasted behaviours, with a distinction between grains 0, 1, 4 and 5 (homogeneous), and grains 2 and 3 (more heterogeneous). With the SSD+GND model, strain dispersion near the grain boundaries is increased.

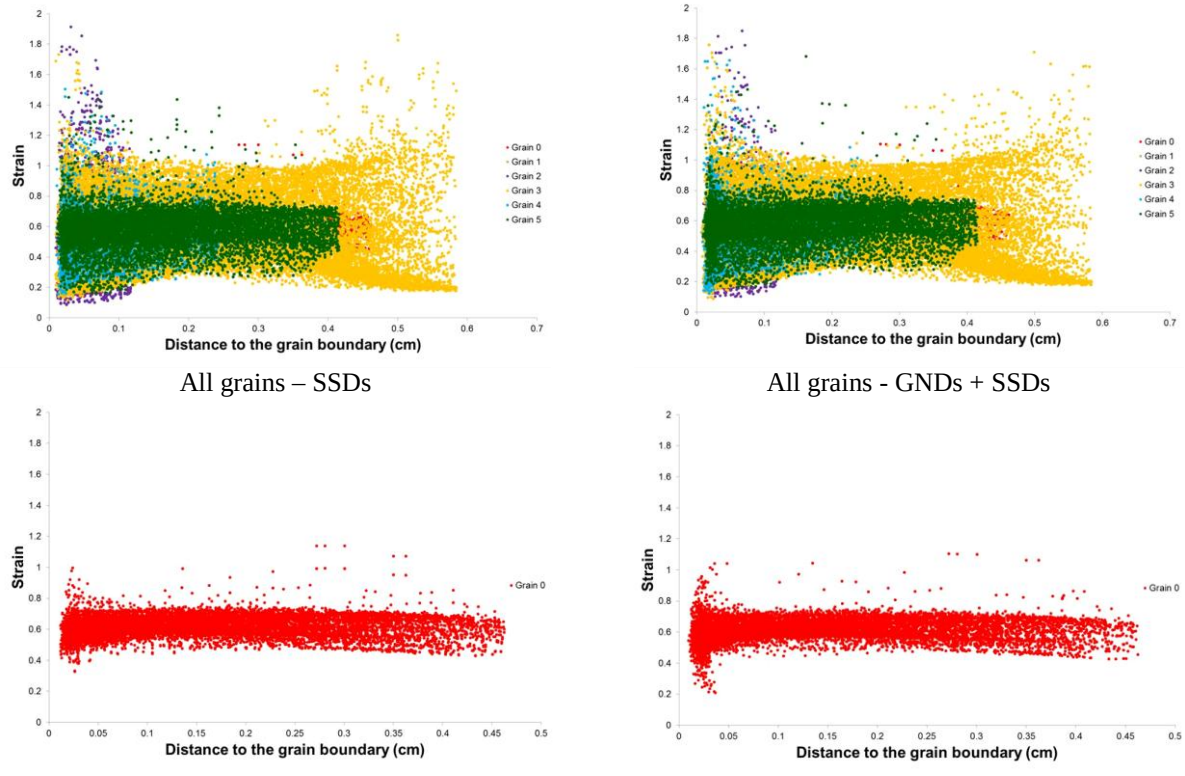

All grains – SSDs All grains - GNDs + SSDs

Grain 0 – SSDs Grain 0 - GNDs + SSDs

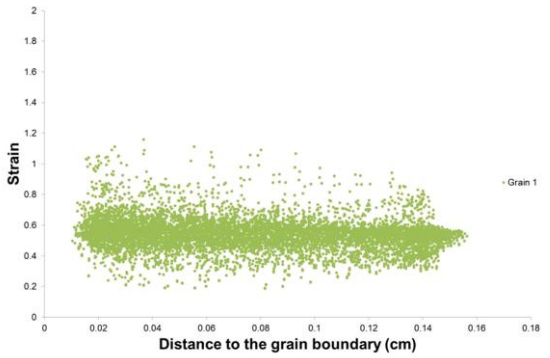

Grain 1 – SSDs

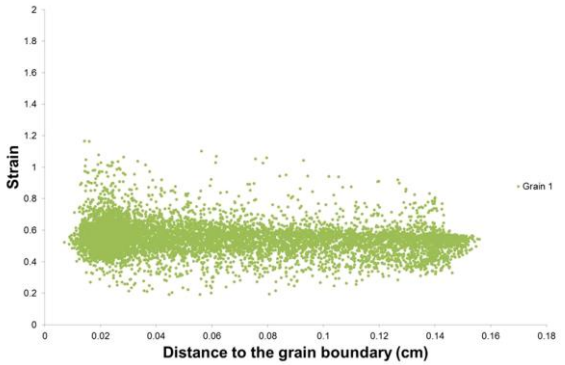

Grain 1 - GNDs + SSDs

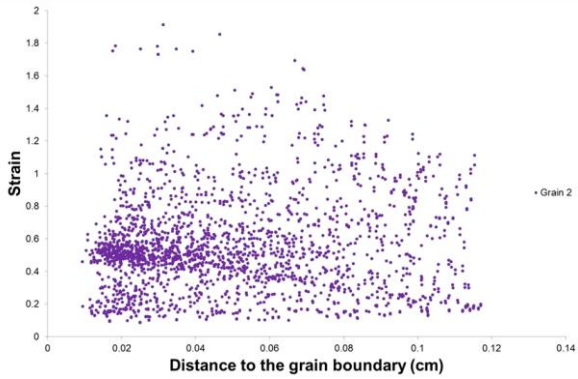

Grain 2 – SSDs

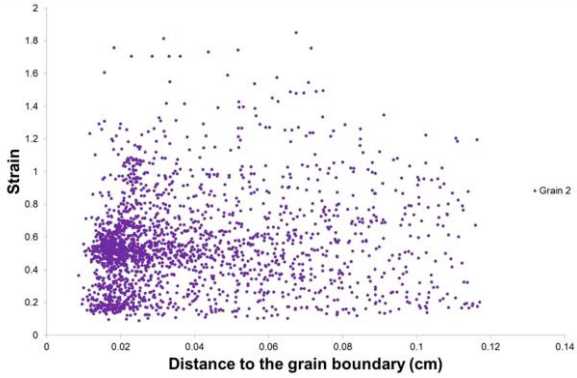

Grain 2 - GNDs + SSDs

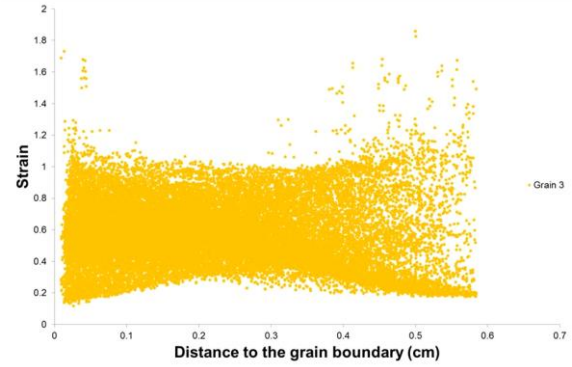

Grain 3 – SSDs

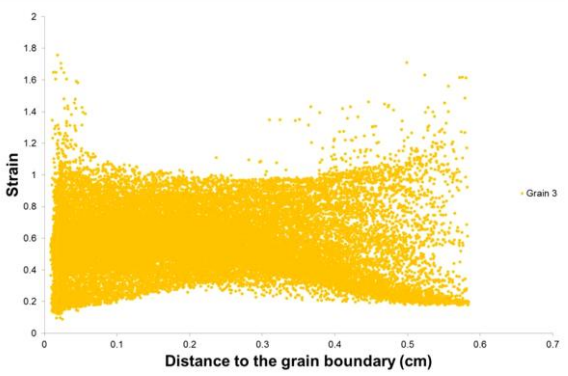

Grain 3 - GNDs + SSDs

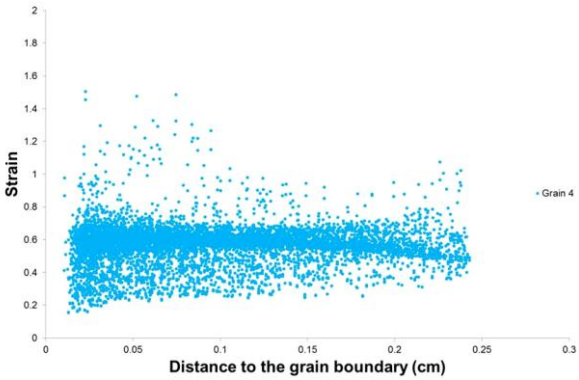

Grain 4 – SSDs

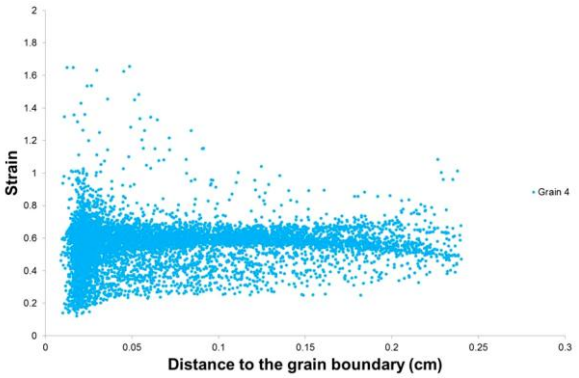

Grain 4 - GNDs + SSDs

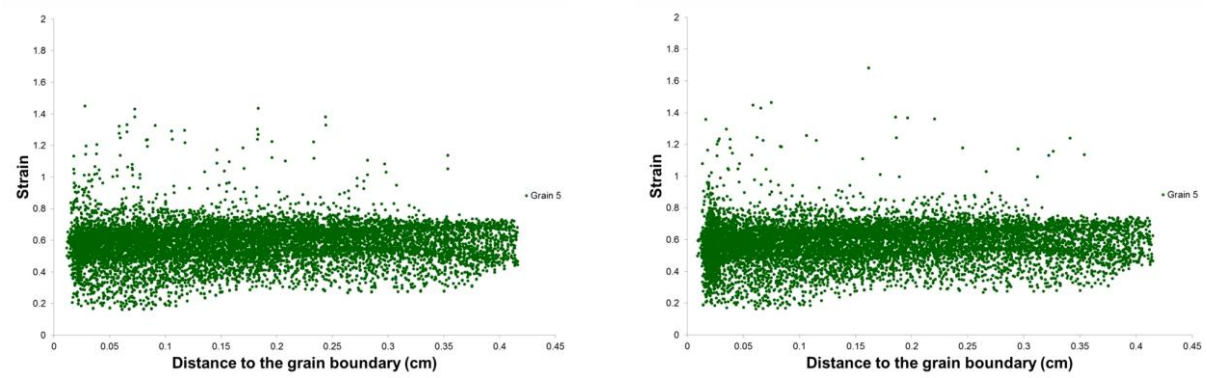

Grain 5 – SSDs Grain 5 - GNDs + SSDs

Figure 3.46: *Strain dispersion for ε_{ZZ} = 0.5 for the whole oligocrystal and for all six individual grain.*

3.3.4 Texture analysis

In this section, predicted crystallographic textures are analysed and compared to experimental results in Figure 3.47. The numerical textures are gathered from all finite elements on the surface of the mesh. Experimentally, however, textures are measured from local scans within the different grains. This explains a general trend in having more dispersed crystallographic orientations from the model.

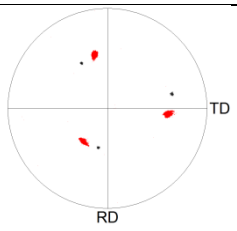	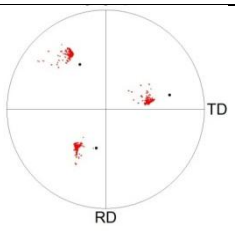	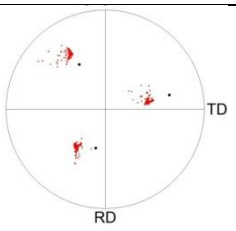
Experimental	**SSDs**	**SSDs+GNDs**
Grain 0		
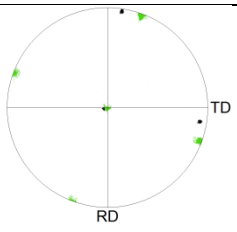	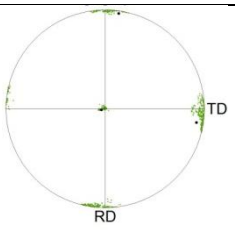	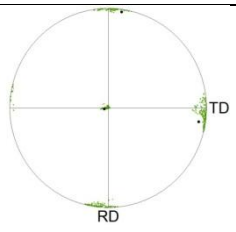
Experimental	**SSDs**	**SSDs+GNDs**
Grain 1		
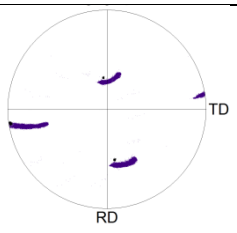	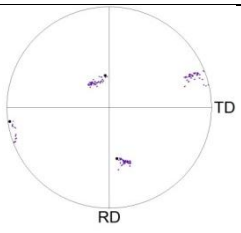	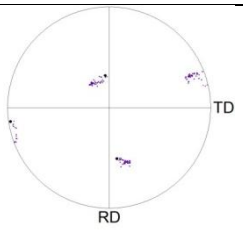
Experimental	**SSDs**	**SSDs+GNDs**
Grain 2		

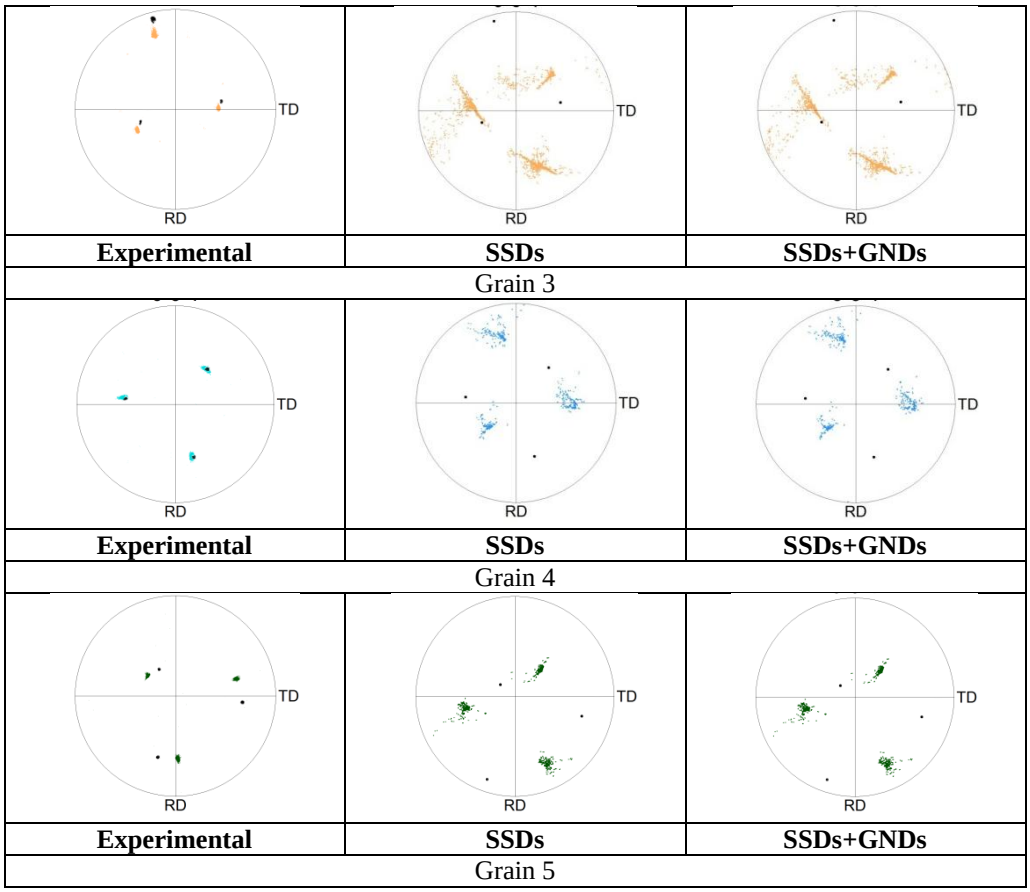

Figure 3.47: *Comparison between experimental and numerical pole figures. The black dots correspond to the initial crystallographic orientation and the coloured dots represent the crystallographic orientation for* $\varepsilon_{ZZ}=0.5$ *for direction (001).*

Numerical predictions do not exactly match the experimental results, at least for some grains. In [Resk, 2010], the texture prediction of an Al (FCC) polycrystal was successfully predicted, using the same model. In the Ta case, the bcc structure differs. Also, it was noticed earlier that some geometrical evolutions of the oligocrystal were not well predicted. Additional measurements, covering the whole surface of the oligocrystal, should help in understanding better the origins of the discrepancies. For example, grain 2 is very well predicted by the model, including the crystallographic fragmentation of the grain, and it is also the smallest grain in size, which means that experimental and numerical surfaces are probably the closest.

One way of analysing intragranular texture evolutions is to look at the rotation angle from the initial state (Figure 3.48). Experimentally, the fragmentation of grain 2 is significant, and this is reflected by the wider dispersion of rotation angles, as compared to the other grains. When the distributions of rotation angles are narrow, it indicates a “global” crystallographic rotation, with no significant fragmentation.

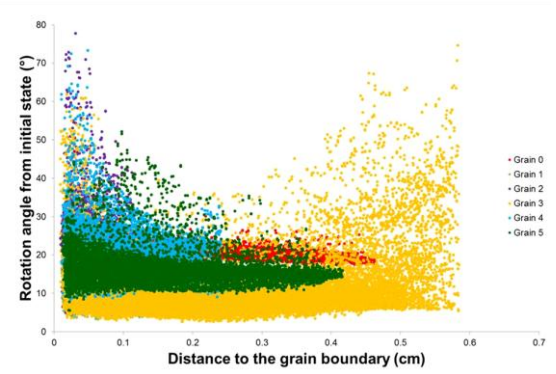

All grains – SSDs

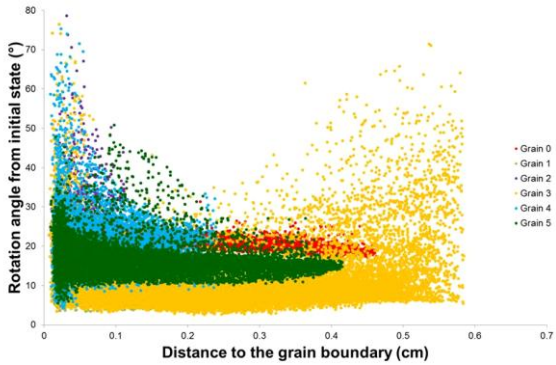

All grains - GNDs + SSDs

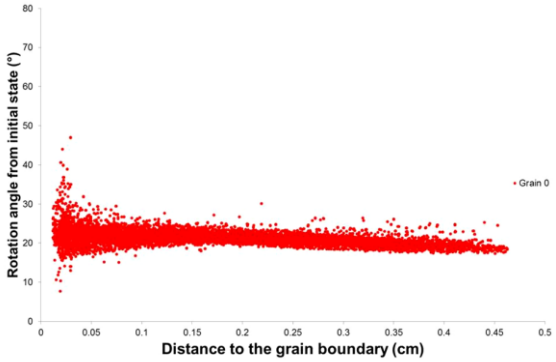

Grain 0 – SSDs

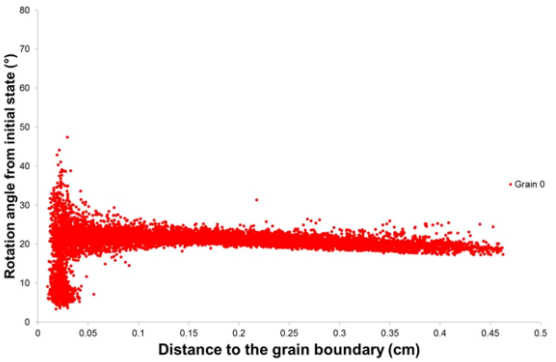

Grain 0 - GNDs + SSDs

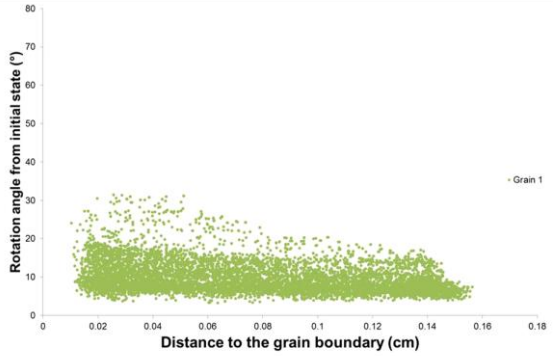

Grain 1 – SSDs

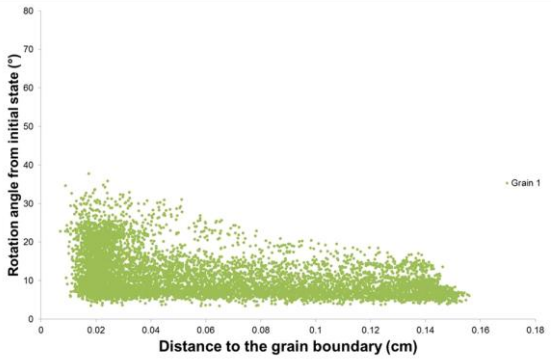

Grain 1 - GNDs + SSDs

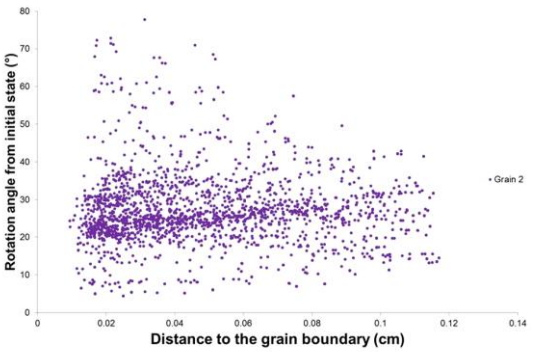

Grain 2 – SSDs

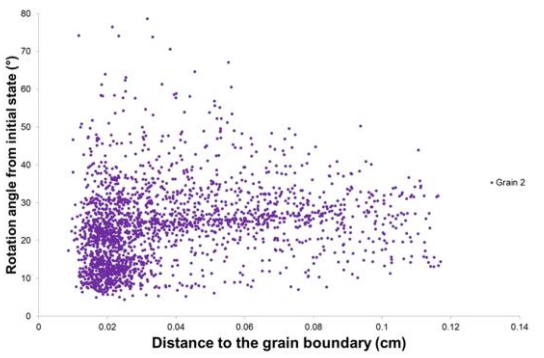

Grain 2 - GNDs + SSDs

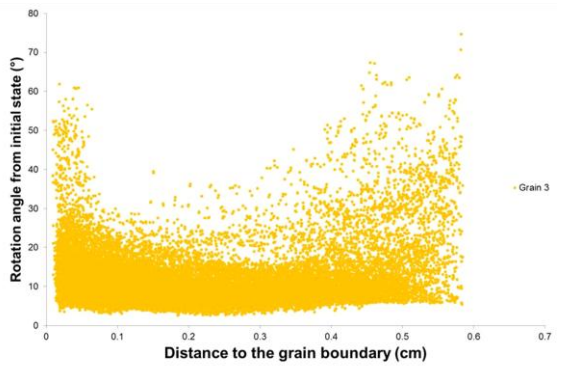

Grain 3 – SSDs

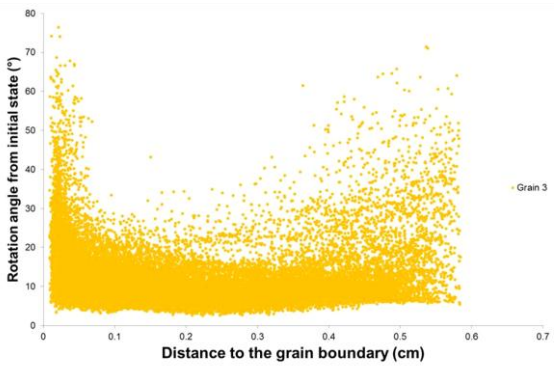

Grain 3 - GNDs + SSDs

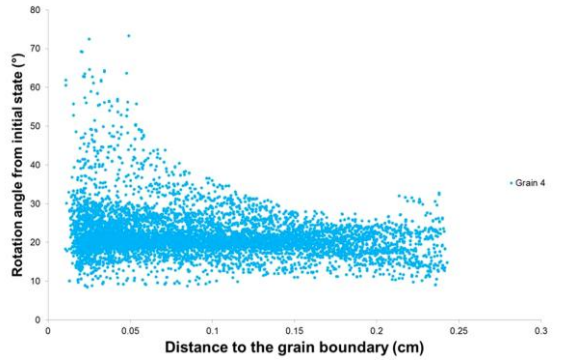

Grain 4 – SSDs

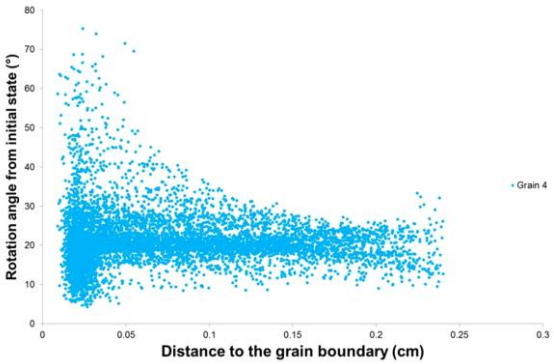

Grain 4 - GNDs + SSDs

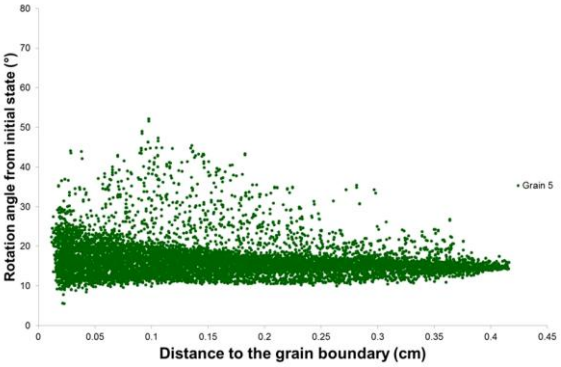

Grain 5 – SSDs

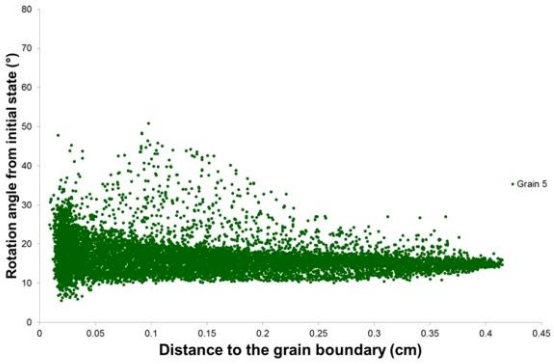

Grain 5 - GNDs + SSDs

Figure 3.48: *rotation angle from initial state at* $\varepsilon_{ZZ} = 0.5$ *for the whole olygocrystal and for all six individual grains.*

It is interesting to highlight that the increased dispersion of grain 2 is not only observed for the rotation angle from the initial state, but also for the dislocation density and the local strain. This makes him a good candidate for early initiation of recrystallization.

4 Conclusion

In this chapter, numerical microstructures induced by plastic deformation are investigated. The Crystal Plasticity Finite Element (CPFEM) model used is this chapter is explained in details in chapter 1. Two different hardening models are studied: the first one computes the total dislocation density, and the second one distinguishes two different dislocation types – statistically stored dislocations (SSD) and geometrically necessary dislocations (GND). Test cases are performed based on (i) a plane strain compression of a 304L steel at 1000°C and $\dot{\varepsilon} = 0.01\,\mathrm{s}^{-1}$, and (ii) a uniaxial compression of a 6-grains oligocrystal of Ta, at room temperature, with $\dot{\varepsilon} = 0.01\,\mathrm{s}^{-1}$.

Considering the first test case, both hardening models can correctly predict the stress-strain experimental behaviour. The dislocation density distribution calculated with the SSD hardening model is more homogeneous than that obtained with the SSD+GND model. In the latter case, the dislocation density is larger near the grain boundaries. Even though the dislocation distribution is different, for both models, the dislocation density dispersion is larger near the grain boundaries. It is in this area that the highest dislocation density values are found. As a consequence, the norm of the dislocation energy gradient is also larger near the grain boundaries.

When the local strain distribution is analysed, both hardening models present similar results. The strain intragranular distribution is rather homogeneous, with however, once again, an increased dispersion near the grain boundaries. Based on these results, nucleation of new grains during a recrystallization process should take place near the grain boundaries, as most often observed in experiments.

For the second test case (tantalum oligocrystal), the prediction of final macroscopic shape is well predicted for four grains, out of six. Once again, the dislocation density distribution shows a concentration near the grain boundaries, especially when using the SSD+GND hardening model. Other maxima of dislocation density (and its gradient) are found away from the grain boundaries, as a consequence of macroscopic geometrical effects.

The predicted material texture of the oligocrystal at $\varepsilon_{ZZ} = 0.5$ tends to overestimate the spread of crystallographic orientations, and sometimes does not predict well the mean orientation. However, it is noticed that when the numerical and experimental areas are very close to each other (as the case for grain 2), both the mean orientation and the grain fragmentation are well predicted. Based on three different criteria on the dislocation densities and their gradients, the distribution of local strain, and the grain fragmentation, one grain of the polycrystal – grain 2 – is a good candidate for early recrystallization, if the olygocrystal is to be subjected to a heat treatment.

The numerical results obtained is this chapter will be used in chapter 5 in order to predict the location of nucleation sites, and the kinetics of static recrystallization.

Résumé en Français

Dans ce chapitre, la déformation plastique de microstructures digitales, générées grâce aux outils numériques présentés dans le chapitre précédent à partir de données expérimentales, est étudiée en utilisant le formalisme de plasticité cristalline introduit dans le premier chapitre. Différents cas tests sont considérés (description différenciée ou non des SSDs et GNDs) pour différents essais : le premier correspond à un essai de compression plane sur un polycristal d'acier 304L $\left(T = 1000^{o}C, \dot{\bar{\varepsilon}} = 0.01s^{-1}\right)$ tandis que le deuxième correspond à un essai de compression simple à froid d'un oligocristal de tantale composé de six grains avec une vitesse de déformation égale à 0.01 s^{-1}. Concernant l'acier 304L, il est mis en évidence, entre autres, que les deux lois d'écrouissage permettent de prédire correctement son comportement et que les résultats sont similaires en terme de distribution de déformation. La distribution de densité de dislocations obtenue est cependant plus hétérogène lorsque les deux types de dislocation sont considérés avec principalement une plus forte dispersion au niveau des joints de grains.

Concernant l'oligocristal de tantale, une confrontation directe entre les formes des grains obtenues après essai et les formes prédites numériquement est réalisée. La distribution de densité de dislocations est également plus élevée dans les zones plus proches des joints de grains, ce phénomène étant, comme pour le 304L, exacerbé lorsque la distinction entre SSDs et GNDs est faite. L'aspect prédiction de texture est également abordé.

Chapter 4

Grain Boundary Migration - Grain Growth Modelling

Contents

1 Introduction 121
2 Context and Equations 121
2.1 Full Field modelling of grain growth assuming isotropic grain boundary energy and mobility 121
2.2 The equations 123
2.2.1 Mobility 123
2.2.2 The grain boundary energy 124
3 Finite element model in a level set framework 127
3.1 Velocity field expression 127
3.2 Numerical treatment for multi-junctions 128
3.3 Container level set functions 129
3.4 Grain growth algorithm 130
4 Results 130
4.1 Academic Test - Circular grain case 130
4.2 Academic test - 3 grains case 132
4.3 Von Neumann-Mullins case 133
4.4 2D polycrystal grain growth 136
4.5 Influence of the microstructure generation method on grain growth prediction 139
5 Assessment of simplified 2D grain growth models from numerical experiments based on a level set framework 141
5.1 Grain size distributions 142
5.2 Burke and Turnbull study 147
5.3 Hillert/Abbruzzese model study 150
6 Conclusion 154

1 Introduction

Grain growth phenomena in polycrystalline metals occur during and after full recrystallization, and have the effect of increasing the average grain size at the expense of smaller ones that will tend to disappear. Even if this phenomenon of capillarity is always present, it is generally neglected during primary recrystallization comparatively to the predominant driving force induced by the inhomogeneous spatial distribution of dislocations stored energies. Grain growth is however known to be of primary importance when dealing with long annealing treatments, where capillarity effects become predominant. It then largely dictates the final grain size of the material.

In chapter 5 it will be shown that, depending on the spatial position of new grains (nuclei), capillarity effects may have a significant impact during recrystallization on the evolving microstructures and on the recrystallization kinetics. Understanding and modelling capillarity forces and their interactions with other driving forces appears therefore to be an important challenge, besides the better understanding of pure grain growth itself.

In this chapter, after a brief overview of the state of art concerning full field modelling of grain growth, a new full field grain growth model is proposed, in the context of isotropic grain boundary energy and mobility. The model is based on a finite element formulation combined with a level set framework. It is initially tested with some academic cases presenting known results. In a second part, polycrystalline grain growth is simulated and the assessment of two 2D mean field grain growth models is done based on the full field simulation results. The two mean field grain growth models discussed in this chapter are: the Burke and Turnbull model and the Abbruzzese/Hillert model. The mean field models, which were developed based on theoretical assumptions, are not easily verified experimentally. Since the full field method presented in this chapter allows the control of the initial microstructure and of the material properties, the verification of the mean field models under different conditions can be done in details. Also, based on the results obtained using a full field model, mean field models can be corrected or improved. All the simulations presented in this chapter are 2D simulations and for all systems solved (convective and/or diffusive equations), a stabilized P1 solver as SUPG or RFB method was used.

In the next chapter, the proposed full field method will be extended to a primary recrystallization model, and applied to 2D and 3D static recrystallization cases.

As in chapter 2, all the distributions or mean values discussed in this chapter concerning grain features were evaluated as number-weighted.

2 Context and Equations

2.1 Full Field modelling of grain growth assuming isotropic grain boundary energy and mobility

For the last three decades, under simplified conditions of isotropic grain boundary energy and mobility, several grain growth modelling methods at the mesoscopic scale have been developed [Miodownik, 2002]. The improvement of the physical understanding of grain growth phenomena associated to an explosion of numerical resources, explain the improvement in the field of grain growth modelling.

The most famous and still widely used grain growth modelling technique is the probabilistic Monte-Carlo method (MC). This method is based on two main points: first, the use of a pixilated or voxelated description of the granular microstructure and, secondly, the construction of probabilistic evolution rules [Rollet, 2001]. In the case of grain growth

modelling, a Hamiltonian energy minimization, defined by summing the interfacial energies, is used as an evolution rule. The interfaces are represented by the faces of the elementary cells, favouring the modelling of the topological evolutions. This is the first main advantage of this method. Moreover, it is noticeable that the use of regular grids associated with a simple evolution law, results in a negligible numerical cost for any simulation [Hassold, 1993]. However, the simple nature of this approach is also synonymous of defects. Indeed, the absence of time scale complicates any comparison with experimental data [Rollet, 1997]. Moreover, this method is only statistically representative, which means that a large number of simulations, having a great number of cells could be necessary to ensure a good statistics of the phenomenon. This is even more important when the material presents a heterogeneous microstructure.

The cellular automaton (CA) approach is another probabilistic method. Several physical rules are used to locally determine the cell propagation in relation to the neighboring cells and all the cells can be updated at the same time solving the first MC negative aspect. However, as in the MC approach, the stochastic nature can lead to the same problem of representativity.

In a finite element context, three main methods are developed nowadays: the Vertex method (VM), the Phase Field method (PF) and the Level-Set method (LS). Only the VM method presents an explicit grain boundary description. Surface elements of the considered mesh are used to describe the grain boundaries. This approach allows a simple representation of the initial microstructure in a finite element mesh and the microstructure evolution is modeled by calculating the new position of the nodes belonging to the grain boundaries. A velocity field normal to the grain boundary is used to calculate the new nodes position [Nagai, 1990]. However, the main weakness of this approach is that topological events are controlled by mesh adaptation rules. As a consequence, the management of topological events (like grains disappearance) is not straightforward. Even though a set of well calibrated changing mesh rules exists in 2D, its extension in 3D is very complex and expensive [Weygand, 2001], [Siha, 2010], [Barrales, 2008].

In both PF [Chen, 1995] and LS [Zhao, 1996] methods, the grains boundaries are implicitly described. For the PF method, this representation is obtained from a continuous approximation of the Heaviside function at the interface (hence the notion of fuzzy or diffuse interfaces). For the LS method, as explained in chapter 2, the zero isovalue of a distance function represents the grain boundary. As a consequence, these two approaches can automatically handle topological changes. For the PF method, each granular orientation is used as an order parameter field and the grain free energy is expressed as a Landau development of the structural order parameters. The grain boundary energy is introduced as the gradient of structural order parameters and the interfaces are described by an isovalue (arbitrary within the diffuse zone) of the order parameter fields. An important number of publications have illustrated the potential of this approach in modeling the grain growth phenomenon in 2D [Chen, 2002] and, more recently, in 3D [Moelans, 2009]. The main difficulties of this approach remain:

- the construction of the free energy density expression (using a Landau development) which must reflect as closely as possible the material physical properties and microstructure;
- the abrupt phase functions transition within the interfaces can be synonymous of intensive and expensive calculations, especially in 3D (degree of interpolation, mesh refinement …);

Finally, grain growth can also be modelled using a level set description of interfaces in the context of uniform grids [Elsey, 2009] or finite elements (FE) [Bernacki, 2011], [Fabiano, 2013]. As for the PF approach, in the LS method, topological changes are treated automatically. From a purely mathematical point of view, a grain disappears when the corresponding level set function becomes negative over the entire domain. The level set technique was used in

[Elsey, 2009] to model 2-D and 3-D isotropic grain growth in the context of uniform grids with a finite-difference formulation. In this work grain growth simulations are performed using level set techniques combined with a finite element formulation, not only to avoid all the disadvantages presented by the other methods, but also, as it will be illustrated in the next chapter, to be able to extend these developments to a primary recrystallization model, and to couple them to the CPFEM calculations developed within the same formalism [Logé, 2008], [Bernacki, 2009].

2.2 The equations

The mechanism of boundary migration depends on several parameters including the boundary structure which, in a given material, is a function of the misorientation between two neighbouring grains, and of the boundary plane. It also depends on the experimental conditions, in particular the heat treatment temperature. Finally, the grain boundary migration is strongly influenced by point defects such as solutes and vacancies.

It is usually assumed that grain boundary displacement can be approximated by [Humphreys, 2004], [Bernacki, 2009], [Kugler, 2004]:

$$\vec{v} = M(\Delta E - \gamma\kappa)\vec{n}\,, \tag{4.1}$$

where M is the grain boundary mobility; ΔE is the material internal energy gradient, which depends on the dislocation density; γ is the grain boundary energy, κ is the grain boundary mean curvature and $\vec{n}$ is the outward unit normal to the grain boundary. The grain boundary driving force can therefore be divided into two parts: the first one is related to the internal material energy field ($\Delta E\vec{n}$), and the second one is related to the grain boundary capillarity effects ($-\gamma\kappa\vec{n}$). In pure grain growth, a homogeneous dislocation density may be assumed, with ΔE=0, and therefore only the capillarity term is taken into account.

It will be considered that grain boundary mobility and energy are uniform throughout the microstructure, however a brief recall of the meaning of these physical parameters is done below.

2.2.1 Mobility

Low angle grain boundaries migrate through climb and glide of dislocations. As a consequence, many aspects of low angle grain boundary migration may be interpreted in terms of the theory of dislocations. In general, low angle boundary mobilities are lower than those of high angle boundaries. In the case of high angle grain boundaries, the basic process for boundary migration is the atoms transfer to and from neighbouring grains. The activation energy for boundary migration was found to be a function of misorientation up to, approximately, 14°, above which it remained constant.

As the transfer of atoms together with dislocations climb and glide are temperature dependent, we can also say that the mobility of grain boundaries is temperature dependent. Actually, it is usually found that the grain boundary mobility evolution as a function of temperature obeys an Arrhenius type relationship of the form [Humphreys, 2004], [Bernacki, 2009], [Kugler, 2004]:

$$M = m_0(T)\exp\left(-\frac{Q_b}{RT}\right), \tag{4.2}$$

where Q_b the boundary diffusion activation energy. Figure 4.1 illustrates the mobility dependence on temperature and misorientation in Al-0.05%Si [Humphreys, 2004].

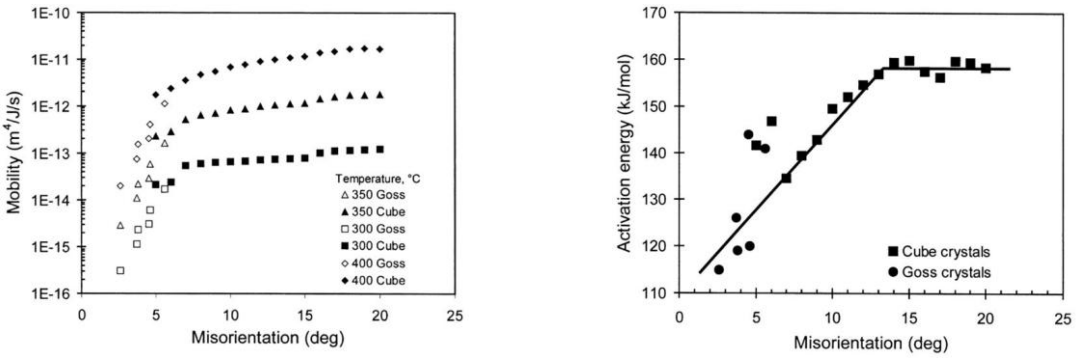

(a) (b)

Figure 4.1: *(a) The effect of misorientation and temperature on boundary mobility in Al-0.05%Si as a function of misorientation, measured from subgrain growth in crystals of Goss and Cube orientation [Huang, 2000]. (b) The effect of misorientation on activation energies for low angle boundary migration in Al-0.05%Si measured from subgrain growth in single crystals [Humphreys, 2004].*

In the context of this PhD work, the misorientation impact on the mobility is not considered and the value of the mobility at high misorientation is used uniformly. In the case of 304L steel, El Wahabi [El Wahabi, 2003] reports Q_b = 280 kJ.mol^{-1} and $m_0(T)$ = 0.156. Table 4.1 summarizes the 304L steel mobility values for temperatures ranging between 1000°C and 1200°C.

Table 4.1: *304L Steel grain boundary mobility in function of temperature and in isotropic mobility context.*

Temperature (°C)	**Mobility (m^4/J.s)**
1000	5.08 10^{-13}
1050	1.37 10^{-12}
1100	3.48 10^{-12}
1150	8.25 10^{-12}
1200	1.84 10^{-11}

All grain growth simulations in this chapter were performed using an Arrhenius interpolation of the data coming from table 4.1.

2.2.2 The grain boundary energy

Low angle boundary energy

Grain boundary energy also depends on the misorientation. Low angle grain boundaries can be represented by an array of dislocations. In this case, each dislocation accommodates the mismatch between the two lattices on either side of the boundary. For small values of misorientation between two neighbouring grains, the dislocation spacing is large and the grain boundary energy is approximately proportional to the density of dislocations in the boundary. The free energy of a low angle grain boundary can be calculated from the Read-Shockley theory, resulting in the following equation [Shockley, 1949], [Humphreys, 2004], [Bernacki, 2009]:

$$\gamma = \frac{\gamma_m}{\theta_m}\theta\left(1 - \ln\left(\frac{\theta}{\theta_m}\right)\right), \tag{4.3}$$

where θ is the grain boundary misorientation, γ_m and θ_m are, respectively, the grain boundary energy and the misorientation for a high-angle boundary. According to Equation 4.3, the grain boundary energy γ increases with the misorientation θ, as shown in Figure 4.2 for various metals.

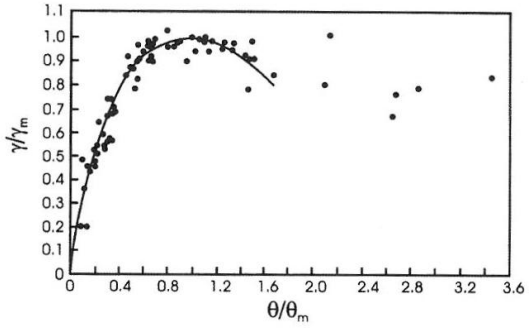

Figure 4.2: *The measured (symbols) and calculated (solid line) energy of low angle tilt boundaries as a function of misorientation, for various metals [Shockley, 1949].*

High angle boundary energy

For low angle boundaries, the Read-Shockley model has been well established. However, for misorientations higher than 15°, measurements of grain boundary energy reveal no further change with increasing rotation angle. In this case, the dislocation spacing is so small that the dislocation cores overlap and it is then impossible to physically identify the individual dislocations. As a consequence the dislocation model fails and the grain boundary energy is almost independent of misorientation.

However, not all high angle boundaries have an open disordered structure as presented in the general introduction. There are some special high angle grain boundaries which have significantly lower grain boundary energy. These boundaries only occur at particular misorientations and boundary planes which allow the two adjoining lattices to fit together with relatively little distortion of the interatomic bonds. One example of special grain boundary is the twin boundary. A twin boundary is a symmetry plane between two areas of the crystal. In the case of F.C.C. crystal, planes {111} are close packed with a stacking sequence …ABCABCABC… A change in this stacking sequence that divides the crystal in two parts, one being the reflection of the other, …ABCA**B**ACBA… is a twin boundary.

One may classify twin boundaries as either coherent or partially coherent. Figure 4.3.a illustrates a complete coherent twin boundary, which is obtained without any deformation of the lattices since a perfect lattice is automatically obtained. If the twin boundary rotates off the symmetry plane (figure 4.3.b) we obtain a partially or non coherent twin boundary. The energy of a twin boundary is therefore very sensitive to the orientation of the boundary plane.

(a) (b)

Figure 4.3: *(a) a coherent twin boundary and (b) a partially coherent twin boundary [Verhoeven, 1975].*

Figure 4.4 describes measured grain boundary energies for several symmetric tilt boundaries in aluminium. When the two grains are related by a rotation about (100) axis (figure 4.4.a), we observe that the grain boundary energy is relatively constant for high angle grain boundaries. So, the high angle grain boundaries in this case have a relatively disordered structure characteristic of random boundaries. However, when two grains are related by a rotation about a (110) axis (figure 4.4.b), several high angle orientations which have significantly lower grain boundary energy than the random boundaries are observed. The misorientation equal to 70.5° corresponds to a F.C.C. coherent twin boundary.

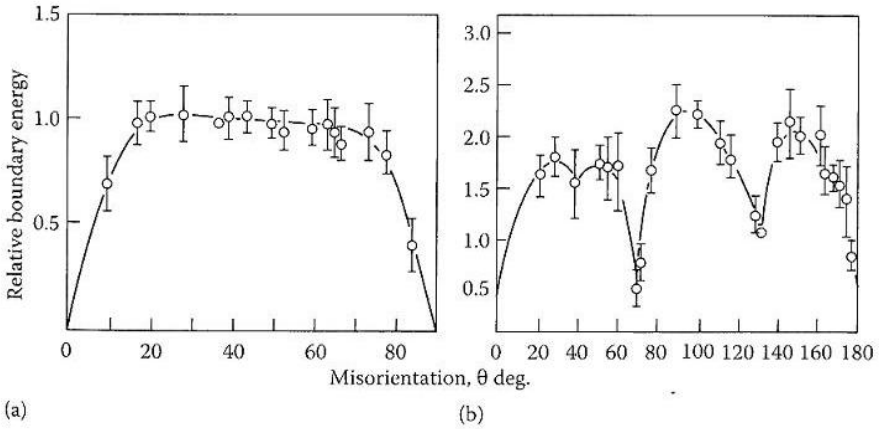

Figure 4.4: *Measured grain boundary energies for symmetric tilt boundaries in Al (a) when the rotation axis is parallel to (100) and (b) when the rotation axis is parallel to (110) [Hasson, 1971].*

Finally, if heterogeneity of the energy boundary is directly responsible of local fluctuations of the grain growth kinetics (see Equation 4.1), another impact of the energy boundary, less visible, concerns the equilibrium position of the multiple junctions. The triple junction angles are determined based on the grain boundary energies by [Humphreys, 2004], [Garcke, 1991]:

$$\frac{\sin\alpha_1}{\gamma_{23}} = \frac{\sin\alpha_2}{\gamma_{13}} = \frac{\sin\alpha_3}{\gamma_{12}}, \tag{4.4}$$

where γ_{ij} represents the energy boundary between grain G_i and G_j and α_i the angle formed by the grain G_i at the triple junction. Based on the relationship 4.4, if the boundary energy is homogeneous, the triple junction angles are then equal to 120°.

3 Finite element model in a level set framework

In order to properly model the grain growth phenomenon, we must, initially, generate a digital microstructure that is representative of the material of interest. We come back here to the 304L steel discussed previously. The grain size distribution is determined based on optical microscope image analysis. The corresponding digital microstructure is generated using a Voronoï-Laguerre method (chapter 2, paragraph 2). The grains are implicitly identified using level set functions and the mesh is adapted around the grain boundaries. All numerical tools used were already described in details in chapter 2.

3.1 Velocity field expression

The model presented here is an extension of the recrystallization model proposed by [Loge, 2008], [Bernacki, 2009]. This extension includes the capillarity term of the grain boundary kinetics Equation 4.1 into the recrystallization model, as was briefly described in [Bernacki, 2011]. In recrystallization regime, the grain boundary velocity between two neighbouring grains (G_i and G_j) is defined as the addition of a primary recrystallization term (PR) with a grain growth term (GG):

$$\begin{aligned}&\vec{v}_{ij}(x,t)=\vec{v}_{PR_{ij}}(x,t)+\vec{v}_{GG_i}(x,t),\\&\vec{v}_{PR_{ij}}(x,t)=M(e_j(x,t)-e_i(x,t))\vec{n}_i(x,t),\quad \vec{v}_{GG_i}(x,t)=-M\gamma\kappa_i(x,t)\vec{n}_i(x,t).\end{aligned} \tag{4.5}$$

In this chapter, only grain growth is taken into account, so $\vec{v}_{PR_{ij}}=\vec{0}$ and $\vec{v}_{ij}=\vec{v}_{GG_i}$. The GG term depends on the grains curvature which can be computed from the level set description of the granular structure. Indeed, by considering ϕ_i the level set function of grain G_i, we have:

$$\kappa_i(x,t)=-\nabla.\left(\frac{\nabla\phi_i(x,t)}{\|\nabla\phi_i(x,t)\|}\right). \tag{4.6}$$

Knowing that in our FE formalism, a linear approximation (P1) for the level set functions is used and that a P1 description of the curvature is necessary (since velocity interpolation must be P1), the direct use of Equation 4.6 to calculate $\vec{v}_{GG_i}$ is not recommended. Indeed, such approach will imply a two-step P0-P1 interpolation and therefore a very poor accuracy. Another difficulty in the grain curvature calculation is related to its non regular behaviour in polygonal grains. At the multiple junctions, the curvature has extremely high values (theoretically infinite), making any attempt to solve the convective problem very difficult. So, to avoid the direct grain curvature calculation (Equation 4.6), the following grain curvature equation was considered and solved in a weak sense:

$$\kappa_i(x,t)-\varepsilon\Delta\kappa_i(x,t)=-\nabla\left(\frac{\nabla\phi_i(x,t)}{\|\nabla\phi_i(x,t)\|}\right), \tag{4.7}$$

with $\varepsilon\Delta\kappa$ a diffusive term allowing the regularization of the grain curvature calculation. This equation also allows avoiding the two-step P0-P1 interpolation thanks to the integration of its weak form. Even though this technique is effective when considering a circular grain

shrinking study (paragraph 4.1), it has not improved the grain curvature calculation in multiple junctions in the case of polyhedral structures (paragraph 4.2). So, an alternative approach, considering the level set functions metric properties is used. If level set functions remain, near the grain interfaces, distance functions, then, for $1 \le i \le N_G$ (N_G being the number of grains):

$$\kappa_i(x,t) \underset{\|\nabla\phi_i\|=1}{=} -\Delta\phi_i(x,t) \text{ and } \vec{n}_i(x,t).\nabla\phi_i(x,t) = -\|\nabla\phi_i(x,t)\|^2 \underset{\|\nabla\phi_i\|=1}{=} -1, \tag{4.8}$$

so:

$$\vec{v}_{GG_i}(x,t).\nabla\phi_i(x,t) = -M\gamma\kappa_i(x,t)\vec{n}_i(x,t)\nabla\phi_i(x,t) = -M\gamma\Delta\phi_i(x,t). \tag{4.9}$$

Therefore, the convection term of the grain boundary motion problem becomes a simple diffusion term. In [Merriman, 1994], [Elsey, 2009], the same approach was used in a finite-difference method context. Finally, the problem solved in order to model the pure grain growth process boils down to a diffusion problem:

$$\begin{cases} \dfrac{\partial\phi_i(x)}{\partial t} - \gamma M\Delta\phi_i(x) = 0 \\ \phi_i(t=0,x) = \phi_i^0(x) \end{cases}, \forall i \in \{1,...,N_G\}. \tag{4.10}$$

The system is solved for all N_G grains present in the domain Ω. Solving the weak form of Equation 4.10 avoids the resolution of a difficult curvature-dependent convection problem. The assumption that the capillarity effects can be described by a level set diffusion equation is true if and only if the level set functions satisfy a distance function property near the boundaries. So, to ensure this condition, a re-initialization treatment must be done at each time step [Osher, 1988].

Also the diffusion of the level set function can generate some kinematic incompatibilities: vacuums regions or level set overlapping [Merriman, 1994]. To avoid this kind of problem, a treatment at multiple junctions is performed [Bernacki, 2011]. This treatment is presented in details in the following paragraph.

3.2 Numerical treatment for multi-junctions

Compatibility problems, as vacuum or overlapping regions, can occur when the diffusion approach is used [Merriman, 1994]. To avoid this problem, a multiple junction treatment is performed at each time step, after solving Equation 4.10. This method consists in removing all incompatibilities by modifying all level set functions according to:

$$\begin{aligned} &\tilde{\phi}_i(x,t) = \frac{1}{2}\left(\phi_i(x,t) - \max_{j\neq i}(\phi_j(x,t))\right), \\ &\forall i \in \{1,...,N_G\}. \end{aligned} \tag{4.11}$$

In other words, this method calculates the bisector between the debonding level set functions (red dashed lines in Figure 4.5) and replace the zero isovalue of these level set functions to the bisector position. Figure 4.5 illustrates the method.

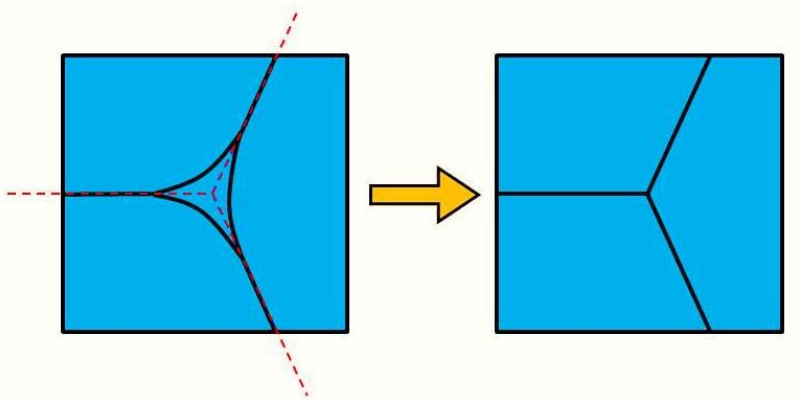

Figure 4.5: *Scheme of how the numerical treatment of multiple junctions works: calculation of the bisector between the debonding level set functions (red dashed lines) and replace the zero isovalue of these level set functions to the bisector position.*

However, this method presents the disadvantage of being valid only in case of homogeneous grain boundary energy, i.e. when the triple junction equilibrium angles are equal to 120° (according to Eq. 4.4).

Also, it is important to highlight that this treatment is performed only in a thin layer around the zero isovalues, and always before the re-initialisation treatment (since it modifies the distance functions metric properties).

3.3 Container level set functions

All the presented procedures (diffusion of level set functions, re-initialisation technique and numerical treatment at multiple junctions) are solved for each level set function existing in the domain. So, the principal weakness for the grain growth algorithm remains the numerical cost, particularly in 3D. A first waste of computational resources can be identified in the fact that we work with one-level set per grain. Even for the recrystallization modelling (which will be detailed in chapter 5), a global velocity depending on local properties can be defined without the knowledge of individual grains topology. Finally when modelling recrystallization or grain growth phenomena, knowing the individual level set function of each grain is not necessary to perform numerical simulation. In order to limit the number of required level-set functions needed in our simulations, we use a classical technique of graph colouring [Kubale, 2004]. The idea is to colour the vertices of a graph such that no two adjacent vertices share the same colour with a minimal number of colours. The most famous result from the graph colouring field of research is the four colour theorem [Kubale, 2004]. Here we use the algorithm implemented by Hitti [Hitti, 2012]. The idea developed by Hitti is to use a simple graph coloring algorithm on the Delaunay (or weighted Delaunay) triangulation used on level set functions calculation (see chapter 2). Several non-neighbouring grains are grouped in only one level set function (called container level set function). As a consequence, the whole microstructure can be represented by a few level set functions corresponding to a set of strictly disjoint grains. Figure 4.6a illustrates a 2D equiaxial polycrystal made of 2000 grains represented using only five level set functions (each colour representing one container level set function). Figure 4.6b illustrates a 3D polycrystal of 440 grains represented using only 15 container level set functions.

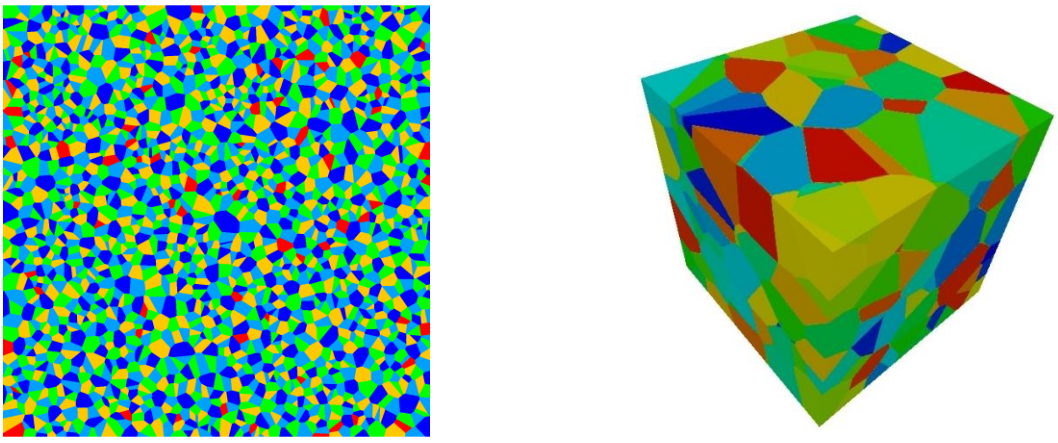

(a) (b)

Figure 4.6: *(a) A 2000-grain 2D equiaxial polycrystal described using five level set functions and (b) a 440-grain 3D equiaxial polycrystal described using 15 level set functions.*

The above technique however presents the limitation that when two grains belonging to the same container level set function start touching each other, they coalesce. In [Elsey, 2009], a method is proposed to avoid this problem: when two different grains belonging to the same container level set function get closer than a critical distance, one of the two grains is removed from the container level set function, and placed in another one. However, if the proposed methodology can be used in the context of regular grids where the connected components (the individual grains) of each container level set function can be easily extracted, the problem becomes much more complex for unstructured FE meshes. Therefore, in this work, in order to delay the onset of grains coalescence, a constraint is introduced in the graph colouring such that only the n^{th} ($n = 2, 3, 4\ldots$) nearest neighbour can belong to the same level set function. The simulation is then stopped as soon as two grains begin to coalesce. The choice of n value depends on how long we want to simulate the phenomenon before coalescence appears.

3.4 Grain growth algorithm

Using all the numerical tools presented above, we propose the following grain growth algorithm:

GG1 – Resolution of Equation 4.10 for all active container level set functions.
GG2 – Numerical treatment (Equation 4.11) for all active container level set functions.
GG3 – Re-initialization step for all activate container level set functions.
GG4 – Deactivation of all container level set functions that are negative all over the domain (meaning that all grains of the container level set function have disappeared).
GG5 – Re-meshing operation.

4 Results

4.1 Academic Test - Circular grain case

In order to verify the grain growth algorithm proposed in paragraph 3, one first simple test case is performed. The interest is to compare a pure diffusive approach (paragraph 3) with a convective approach associated with the reinitialization procedure [Coupez, 2007], [Bernacki, 2009]

$$\begin{cases} \dfrac{\partial \phi_i(x)}{\partial t} + \vec{v}\nabla\phi_i(x) + \lambda s\left(\left\|\nabla\phi\right\| - 1\right) = s \\ \phi_i(t=0,x) = \phi_i^0(x) \end{cases}, \forall i \in \{1,...,N_G\}, \tag{4.12}$$

where s is a function of ϕ and λ a coefficient defined thanks to the mesh size and the time step. We refer the reader to [Coupez, 2007] for a more precise description of the method and its extension (regular truncation of ϕ). In the convective approach (Eq. 4.12), the grain curvature is calculated using the resolution of the weak form of Equation 4.7 in our context of P1 interpolation. To compare these two approaches, we consider a test case defined by a grain embedded in another large grain. The domain size is 1 mm x 1 mm and an *a priori* remeshing technique is used to adapt the mesh around the grain boundary (see chapter 2). Both grain boundary mobility and energy are considered isotropic and equal to one. In the test case, the grain shrinks while remaining a circle, and the GG kinetics could be summarized as a simple differential equation on the circle radius:

$$\dot{r}(t) = \kappa(t) = -\frac{1}{r(t)} \Rightarrow r(t) = \sqrt{r(0)^2 - 2t}. \tag{4.13}$$

The initial grain radius is set to 0.25 mm. In a first stage, both methods are tested under the same mesh and time step conditions. In this case, the mesh size outside the adapted zone is equal to 0.01 mm. Within the adapted zone, the mesh size in the direction perpendicular to the boundary is equal to 2 µm, and remains equal to 0.01 mm in the tangential direction. The time step is set to 0.1ms. Remeshing operations are performed at each time step with the same parameters. Figure 4.7 compares the grain shrinking kinetics of both approaches with the analytical solution.

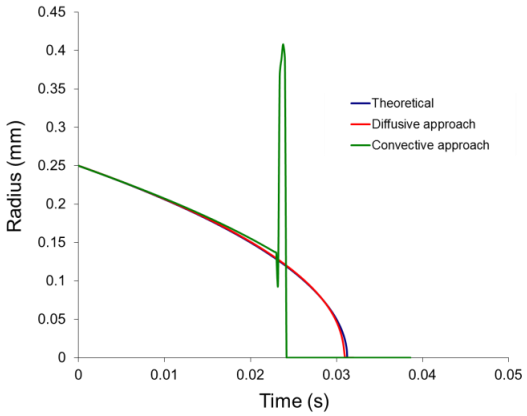

Figure 4.7: *Comparison between numerical and theoretical results for the shrinking of a circular grain with a mesh size equal to 0.01 mm outside the remeshed zone and 0.002 mm on the anisotropic adapted zone (in the normal direction to the interface)*

Graph from figure 4.7 illustrates that, for the mesh and time step conditions tested in this case, the convective approach is not stable and the simulation of a shrinking circular grain is not possible. On the other hand, when using the diffusive approach, the grain shrinking simulation was possible. So, a second test of the convective approach, using a finer mesh and a smaller time step is performed. In this case, the mesh size outside the adapted area and within the adapted area in the tangential direction remains equal to 0.01 mm, whereas the

mesh size near the interface in the normal direction is fixed to 0.8 μm. The time step is reduced to 50 μs. Figure 4.8 presents the comparison between the convective and diffusive approaches.

For this simple case presenting a regular grain curvature, both approaches ensure a good description of the grain shrinking kinetics. For both cases, the L2 error (Equation 2.9 applied to the equivalent radius) is smaller than 1%

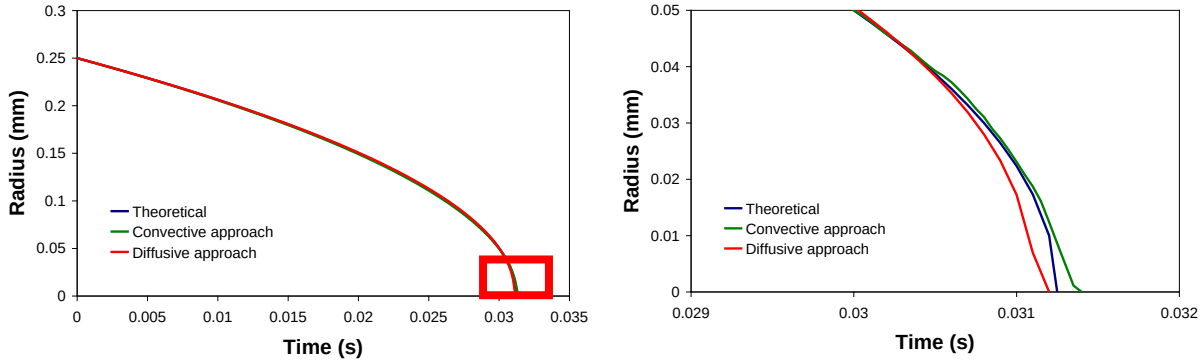

(a) (b)

Figure 4.8: *Comparison between numerical and theoretical result for the shrinking of a circular grain: (a) complete evolution in function of time; (b) zoom of grain shrinking end. The number of mesh elements at the simulation beginning is equal to 27900 for the diffusive approach and 44000 for the convective approach.*

For the diffusive approach, the computation time is about 40 minutes (1 CPU, 2.3 GHz, 2 Go) while for the convective approach, the computation time is equal to 1 hour and 10 minutes (1CPU, 2.3 GHz, 2 Go).

These results show that for a simple grain growth case, when the grain curvature is regular all over the domain, both diffusive and convective approaches can describe with good accuracy the grain shrinking kinetics. However, with the convective approach a finer mesh around the boundaries (for this case, 2.5 times smaller) and a smaller time step (for this case, 2 times smaller) is needed in order to obtain the same accuracy as the diffusive method. Finally, since a finer mesh and a smaller time step is needed, the calculation time for the convective approach is higher than for the diffusive approach.

4.2 Academic test - 3 grains case

In this part, two different tests were performed, both with 3 polygonal grains. In both cases the grain boundary mobility and energy are isotropic and uniform, equal to one. The first test represents a triple junction in the equilibrium state (angles between the grain boundaries are equal to 120°) in the middle of a 1mm x 1 mm domain. As the triple junction is already in the equilibrium state, the triple junction should not deform or move during the simulation. An *a priori* anisotropic remeshing technique is used. The number of mesh elements present in the domain is equal to 110000. The time step of the simulation is equal to 2.5 ms. Figure 4.9 illustrates the configuration of this test.

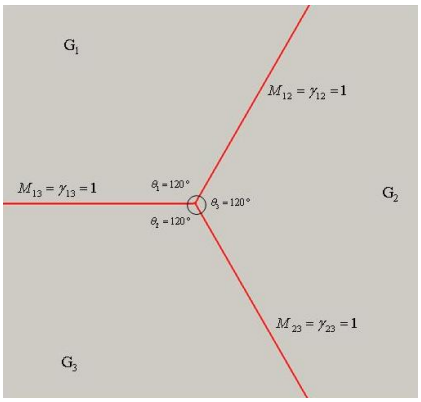

Figure 4.9: *Initial configuration of the triple junction test - triple junction in equilibrium conditions respecting the 120° equilibrium angle.*

It was not possible with the considered mesh adaptation and time step to model this triple grain configuration using a convective approach either by direct (Equation 4.6) or indirect (Equation 4.7) calculation of the grain curvature. On the other hand, the diffusive approach allows the verification that the equilibrium state from figure 4.9 does not evolve during the simulation (simulation was performed until t = 1.75 s). So the diffusive approach leads to the equilibrium angle of 120° at the triple junctions.

The second test case is the « T » configuration. In [Garcke, 1991], Garcke has proved the existence of an exact solution for the grains configuration when pure grain growth takes place. In this case we use an *a posteriori* mesh adaptation and the number of mesh elements is equal to 32800. Figure 4.10a illustrates the initial configuration and figure 4.10b represents the obtained result.

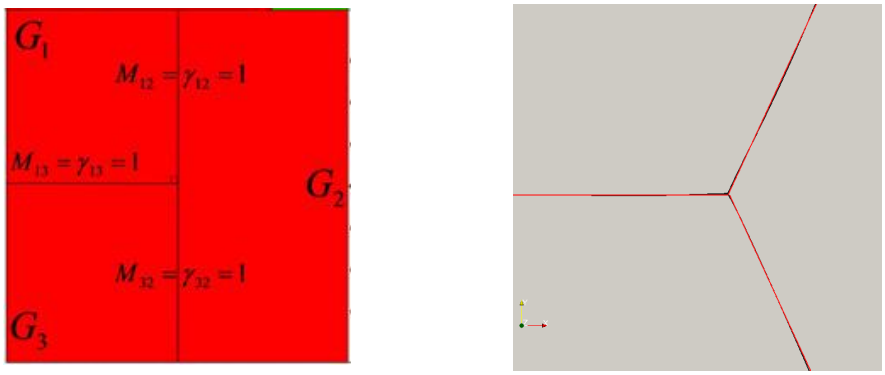

(a) (b)

Figure 4.10: *Garcke case: (a) initial configuration, (b) equilibrium configuration (black line) compared with the theoretical result (red line) for t = 47 ms – zoom of triple junction.*

Red line in figure 4.10b represents the theoretical result while the black line is the numerical result obtained at t = 47 ms (time step is equal to 1 ms). The L2 error concerning the final positions of the interfaces is smaller than 1%.

These two tests illustrate that the diffusive algorithm associated with an anisotropic mesh adaptation allows an accurate simulation of pure grain growth phenomena, even with a non regular grain curvature.

4.3 Von Neumann-Mullins cases

From Equation 4.4 we note that in a two dimensional grain structure, when the grain boundary energy is isotropic, the only stable arrangement which can fulfil the boundary

tension equilibrium requirements is an array of regular hexagons. This is true because regular hexagons angles are equal to 120° (figure 4.11) which is the equilibrium angle for grains triple junctions. Any other topological arrangement will inevitably lead to grain growth. From figure 4.11 we observe that for grains with a number of sides different from 6, in order to maintain the 120° angles at the vertices, the sides of the grains must become curved. Grain boundary migration then tends to occur in order to reduce the boundary area, and the boundaries migrate towards their centre of curvature. Any grain with more than six sides will tend to grow because its boundaries are concave. Similarly, any grain with less than six sides will tend to shrink since its boundaries are convex.

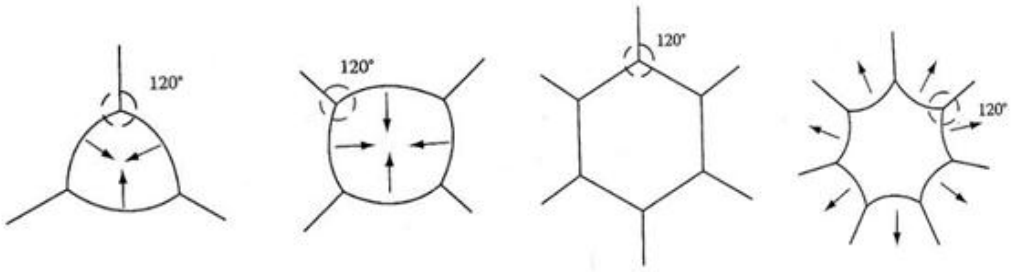

Figure 4.11: *2D grain boundary configurations. The arrows indicate the directions boundaries will migrate during grain growth [Porter, 2008].*

Based on this idea, von Neumann [vonNeumann, 1952] and Mullins [Mullins, 1956] proposed that the growth of a 2D grain of area A and N sides is given by the following relation:

$$\frac{dA}{dt} = (N-6)C. \tag{4.14}$$

where C is a constant that depends on the material parameters. In order to verify if the grain growth algorithm obeys this model, we simulate the grain growth of five different regular polygons: a square, a pentagon, a hexagon, a heptagon and an octagon. In all cases the grain boundary mobility and energy are considered isotropic and uniform (equal to one). Also, an adapted mesh around the boundaries is used and the simulation time step is fixed to 0.1 ms. The adapted mesh is generated using an *a posteriori* remeshing technique. The number of mesh elements depends on the polygon. For example, for the hexagon, the initial number of mesh elements existing in the domain is equal to 50,000. A remeshing operation is performed at each time increment. Figure 4.12 illustrates the different shape evolutions throughout the simulations (with S_r the surface ratio), and the graph in figure 4.13 shows the corresponding grain growth kinetics.

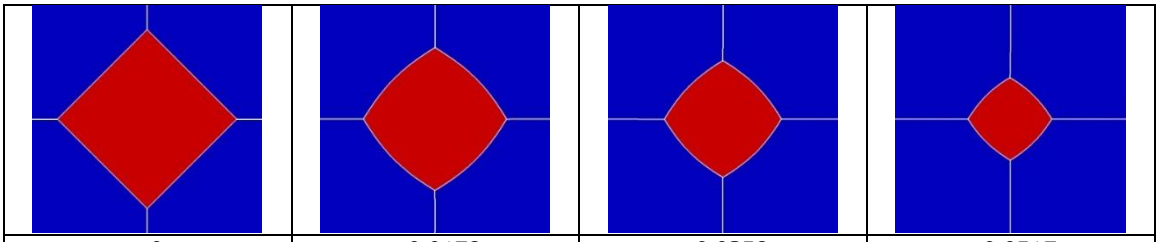

t = 0 s	t = 0.0178 s	t = 0.0358 s	t = 0.0517 s
S_r = 1.0	S_r = 0.75	S_r = 0.5	S_r = 0.25

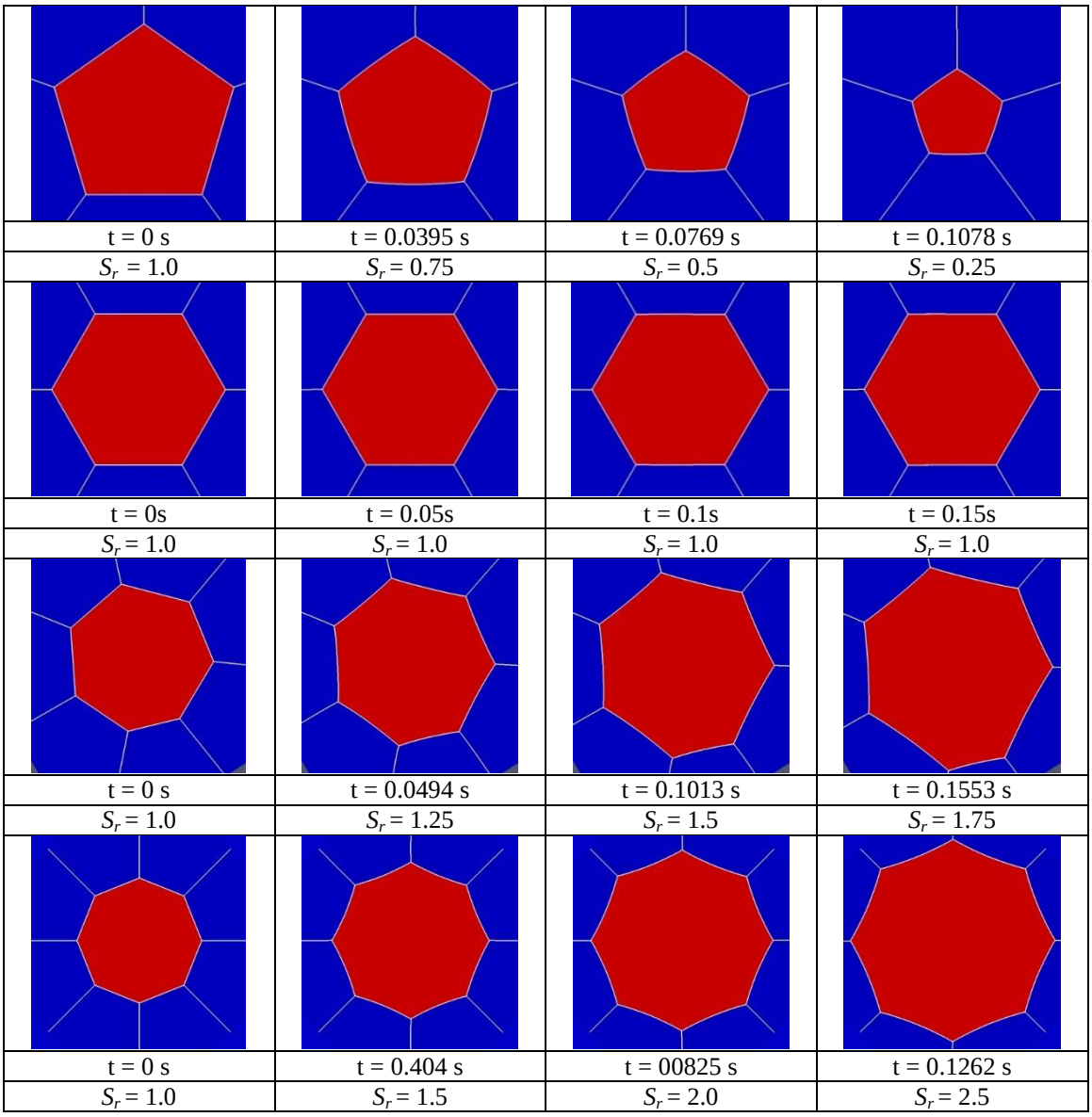

t = 0 s	t = 0.0395 s	t = 0.0769 s	t = 0.1078 s
S_r = 1.0	S_r = 0.75	S_r = 0.5	S_r = 0.25
t = 0s	t = 0.05s	t = 0.1s	t = 0.15s
S_r = 1.0	S_r = 1.0	S_r = 1.0	S_r = 1.0
t = 0 s	t = 0.0494 s	t = 0.1013 s	t = 0.1553 s
S_r = 1.0	S_r = 1.25	S_r = 1.5	S_r = 1.75
t = 0 s	t = 0.404 s	t = 00825 s	t = 0.1262 s
S_r = 1.0	S_r = 1.5	S_r = 2.0	S_r = 2.5

Figure 4.12: *Polygonal grains evolution in function of time: square, pentagon, hexagon, heptagon and octagon-shape grains.*

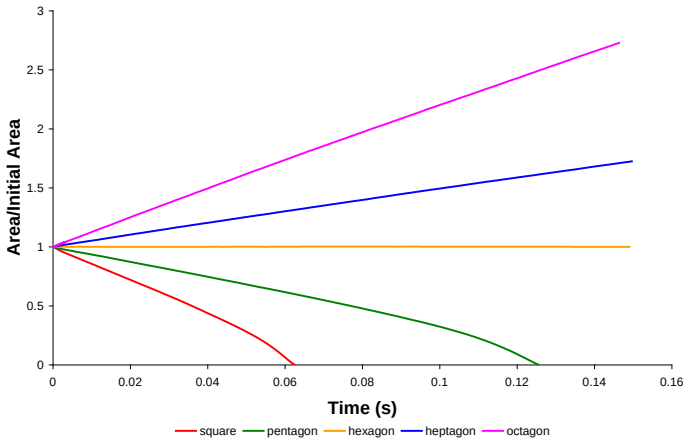

Figure 4.13: *Normalized area evolution for all five different polygons studied: square, pentagon, hexagon, heptagon and octagon.*

From Figure 4.12, we observe the change in the grain boundaries shapes in order to conform to the 120° equilibrium angle at the vertices. Consequently the grains with a number of sides smaller than 6 shrink, a grain with 6 sides remain unchanged and grains with more than 6 sides grow, following the von Neumann-Mullins theory. Finally, analysing the graph in figure 4.13, we observe that the area mainly evolves linearly with time. The non linearity in the end of the simulation for grains which disappear, i.e. with 4 and 5 sides, is a consequence of numerical accuracy issues when the ratio "grain size/ finite element mesh size near the grain boundaries" becomes too low. Indeed, while the mesh evolves spatially with time it does maintain constant parameters concerning the mesh size. When the ratio becomes low, the grain interfaces become poorly described and the numerical simulation accuracy drops. One way to avoid this problem is to decrease the mesh size near the grain boundaries (at least in the normal direction) during the simulation. Now, to verify if the kinetic behaviour of the grains obeys Equation 4.14, we analysed the linear part of all curves, and calculated the alpha value from Equation 4.15.

$$\frac{dA}{dt} = \alpha C \tag{4.15}$$

The graph in Figure 4.14 compares the numerical results obtained from the simulations with the theoretical results from which $\alpha = N - 6$ (Eq. 4.14).

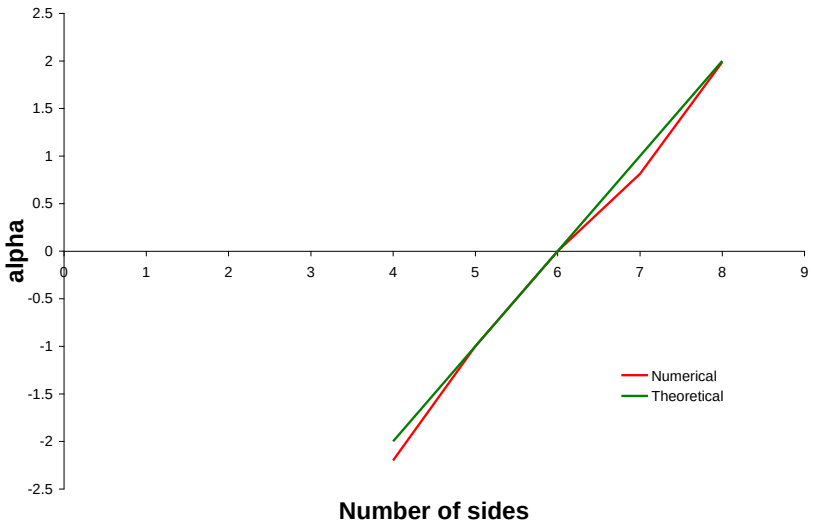

Figure 4.14: *Comparison between the von Neumann Mullins model and the numerical results of polygonal grains: square, pentagon, hexagon, heptagon and octagon-shape grains.*

The L2 error between the two curves is less than 7% for all considered shapes, which represents a clear agreement with the von Neumann-Mullins model, and therefore a good validation of the numerical approach.

4.4 304L - 2D polycrystal grain growth

After testing academic configurations with well-known theoretical results, a polycrystal grain growth simulation is performed. The digital microstructure is generated using the Laguerre-Voronoï technique (chapter 2, paragraph 2) based on an experimental 304L steel grain size distribution. The heat treatment is performed at 1050°C. Grain boundary energy and mobility are isotropic and uniform equal to 0.6 J/m² and 1.37×10^{-12} $m^4 J^{-1} s^{-1}$, respectively.

The size of the square domain is set to 4 mm x 4 mm and approximately one thousand grains are generated. An *a posteriori* remeshing adaptation is used and the number of mesh elements existing initially in the domain is equal to 1450000. The time step is set to 120 seconds. Figure 4.15 illustrates the resulting microstructure evolution as a function of time.

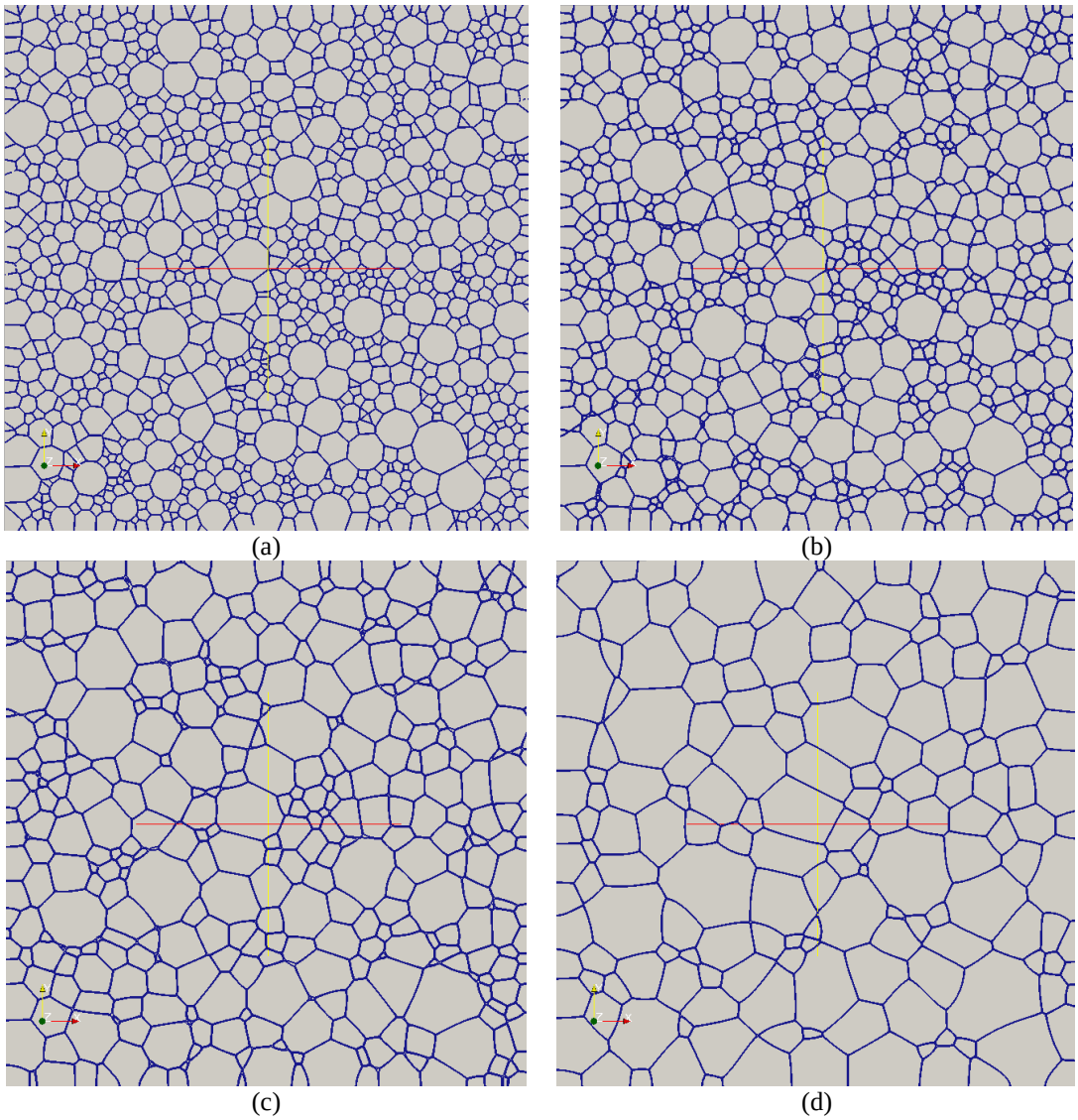

Figure 4.15: *Grain growth of 304L steel at 1050°C after: (a) t = 0; (b) t= 20 min; (c) t = 1h 40 min; (d) t = 5 h.*

Again, the grains with more than 6 sides grow while those with less than 6 sides shrink, in agreement with the von Neumann Mullins theory.

Figure 4.16 describes the number of grains and the mean grain surface evolution as a function of time.

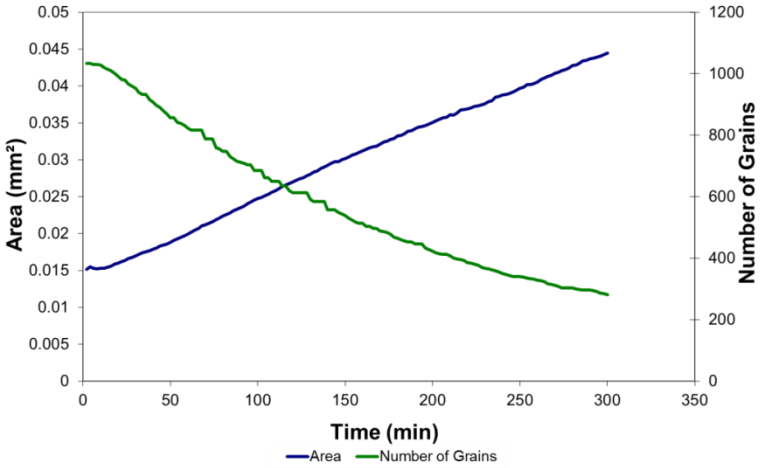

Figure 4.16: *Evolution of number of grains (green line) and mean area (blue line) in function of time.*

The mean surface per grain evolves quasi linearly with time, while the evolution of the number of grains is proportional to $1/t$. A more detailed study of grain growth kinetics, with comparisons with the Burke and Turnbull model [Burke, 1952] and with the Hillert/Abbruzzese model [Hillert, 1965], [Lücke, 1992], [Lücke, 1998] and [Abbruzzese, 1992] is presented in paragraph 5.

A selection of four individual grains is done in order to analyse the normalized area evolution (normalized by the initial grain surface) and the number of sides evolution with time (figure 4.17). The area evolution with time is clearly not linear, and the type of evolution is related to the interaction with neighbours. However, the number of sides of each grain does dictate the tendency to grow, shrink, or remain stable, in agreement with the von Neumann Mullins theory.

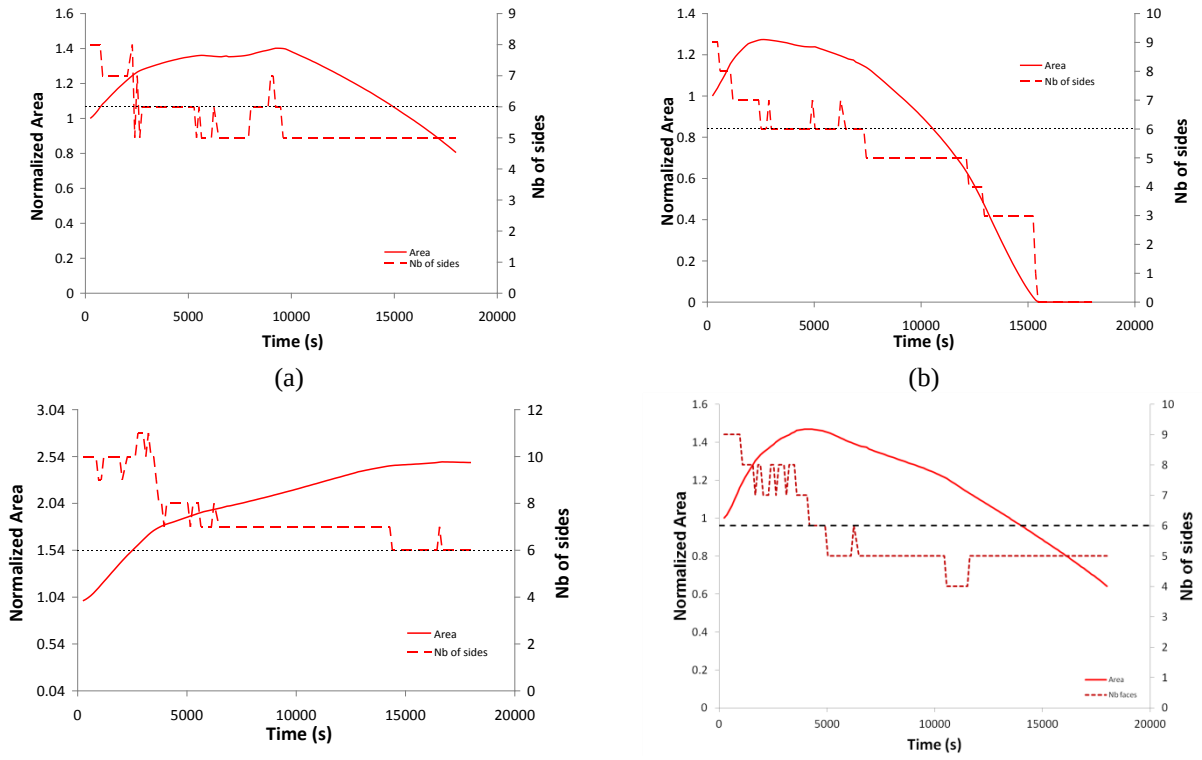

Figure 4.17: *Evolution of grain normalized area (full red lines) and number of sider (dashed red lines) in function of time.*

In figure 4.17c, we clearly see the connexion between the grain growth rate and the number of sides. At the beginning the grain grows fast since the number of sides is around 10. At t = 4500 s, the number of sides decreases to 8, and the grain area evolution becomes slower. In the end the number of sides becomes equal to 6 and, once again, the grain growth rate decreases, becoming negligible. The same kind of analysis can be done with figures 4.17a, 4.17b and 4.17d and all of them will show the same type of connexion between the two monitored quantities.

This first pure grain growth simulation of a 304L polycrystal illustrates the capability of the proposed formalism. We now come back to the issues already discussed in chapter 2 concerning the impact of the method used to generate digital microstructures. In chapter 2, the geometrical aspects of polycrystalline aggregates were analysed for two different generation methods (Voronoï, and Laguerre-Voronoï). In what follows, a similar analysis is done regarding the grain growth prediction. Section 5 will then be dedicated to the impact of the grain size distribution, and comparisons with grain growth mean field models predictions.

4.5 Influence of the microstructure generation method on grain growth prediction

As it was discussed in chapter 2, the Voronoï method is the most widely used technique to generate a digital microstructure. The Voronoï approach allows to define the mean grain size by setting the number of grains (i.e. the number of Voronoï sites) in a given volume. However, using this method it is not possible to obey a given grain size distribution. On the other hand, with the Laguerre-Voronoï technique (also discussed in details in chapter 2), a given grain size distribution can be obeyed. In [Xu, 2009], Xu highlighted divergences between statistical properties classically observed in equiaxed polycrystals and those obtained using the Voronoï method. However the influence of the grain size distribution on the grain growth kinetics and the importance of obeying an experimental grain size distribution are not well discussed in the literature. So, in this section, a comparison between the grain growth kinetics of two digital microstructures with the same mean grain size but generated with different methods (Voronoï and Laguerre-Voronoï) is performed. The digital Laguerre-Voronoï microstructure was already used in the previous paragraph (304L grain size distribution, square domain of 4 mm x 4 mm, 1033 grains). In the digital Voronoï microstructure, the mean grain size of the 304L microstructure is set (67.4μm) using 1120 grains randomly generated in the 4 mm x 4 mm square domain. For both cases the grain boundary mobility and energy are isotropic and uniform (T=1050°C), equal to 0.6 J/m² and 1.37 10^{-12} $m^4J^{-1}s^{-1}$, respectively. Figure 4.18 illustrates the two digital microstructures (a similar comparison has already been done in a 12 mm x 12 mm square domain from figures 2.9 and 2.13 in chapter 2) and figure 4.19 presents the grain size and the number of sides distribution for both of them.

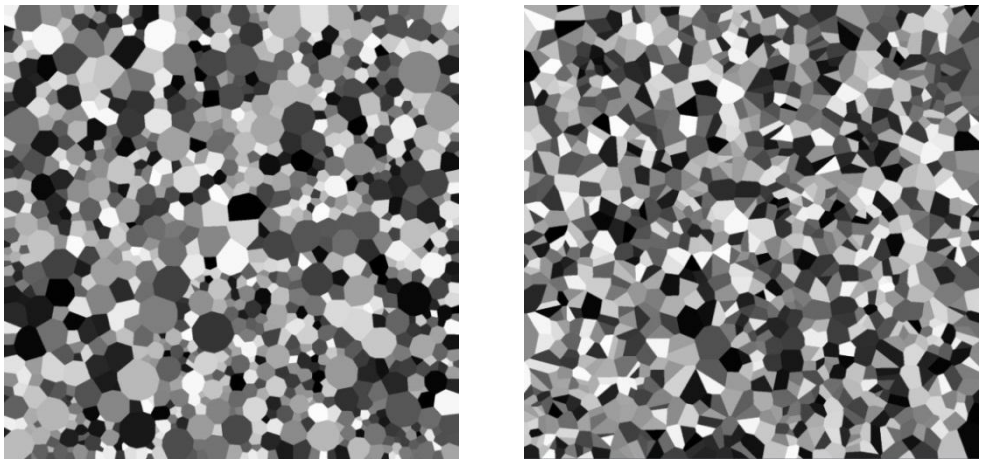

(a) (b)

Figure 4.18: *304L Polycrystal in a 4 mm x 4 mm square domain generated using a (a) Laguerre-Voronoï method (1033 grains) and (b) Voronoï method (1120 grains)*

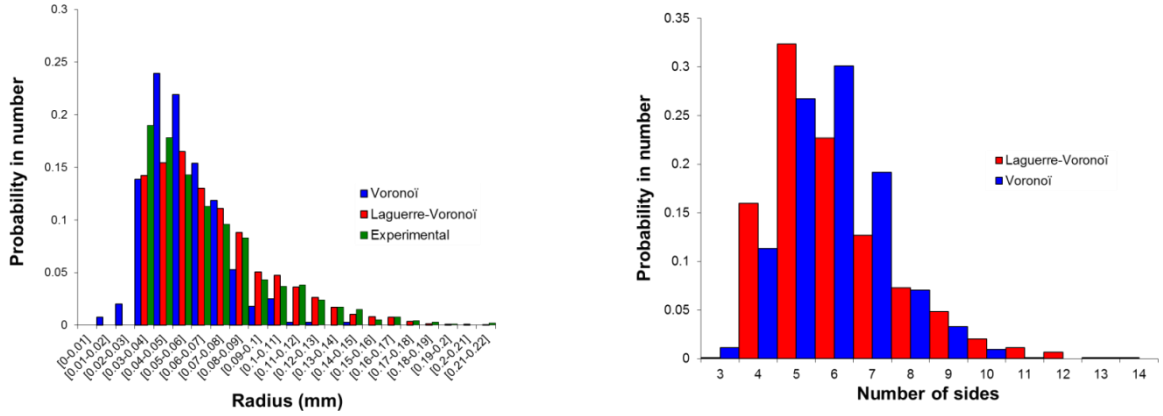

(a) (b)

Figure 4.19: *Comparison of (a) grain size distribution and (b) number of sides' distribution for both digital microstructures, one generated with the Voronoï method and the other generated using a Laguerre-Voronoï method.*

Comparing Laguerre-Voronoï and Voronoï grain size distributions, we observe, as already discussed in chapter 2, that Laguerre-Voronoï is a log normal distribution while Voronoï is a Gaussian distribution. Considering the number of sides distribution, even though both microstructures present a mean number of sides around 6 (5.95 for Voronoï and 5.97 for Laguerre-Voronoï), their distributions are different. Once again, the number of sides distribution is closer to a Gaussian shape for the Voronoï case, and closer to a log-normal shape for the Laguerre-Voronoï case. In Table 4.2, we observe that even though both grain structures present a majority of grains with less than 6 sides, this proportion in almost 10% higher for the Laguerre-Voronoï structure. The proportion of grains with more than 6 sides is almost the same for both microstructures, but the Laguerre-Voronoï distribution presents larger grains, with more sides. Finally, the Voronoï microstructure shows a higher proportion of grains with 6 sides.

Table 4.2: *Proportion of grain with less than 6 sides, exactly 6 sides and more than 6 sides for the Laguerre-Voronoï and Voronoï grain structure of 304L generated in a 4mm x 4mm square domain.*

	Laguerre-Voronoï	Voronoï
n < 6	48.4 %	39.2%
n = 6	22.7 %	30.1%
n > 6	28.9 %	30.7%

Analysing the graph of the normalized average grain surface evolution with time (Figure 4.20), we observe that the Laguerre-Voronoï grain growth is faster than the Voronoï one. This behaviour is related to the grain size distribution. The Laguerre-Voronoï distribution is more spread and as a consequence, the difference between the equivalent radii of neighbouring grains is, in average, larger for the Laguerre-Voronoï distribution. This behaviour is also observed in Figure 4.18. For the Laguerre-Voronoï microstructure (Figure 4.18a) a few bigger grains are surrounded by small grains. In these areas the local curvatures will be increased and the grain growth kinetics will be faster. For the Voronoï microstructure, since the grain size difference between neighbouring grains is smaller, the local curvatures are not as high.

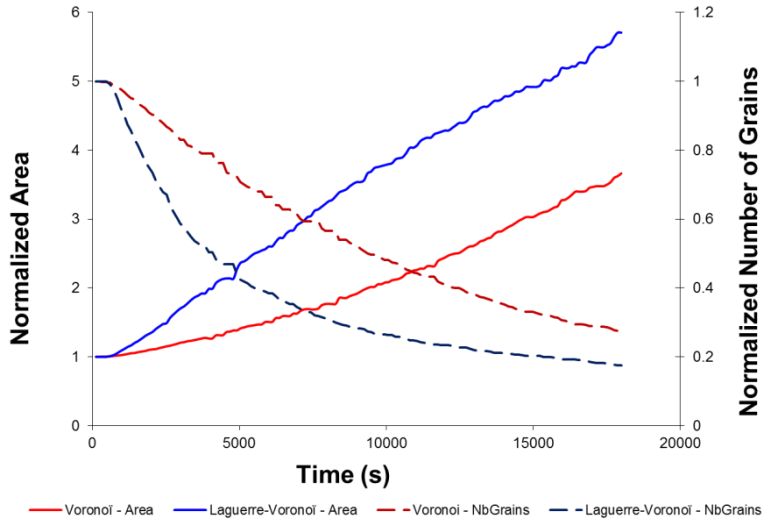

Figure 4.20: *Comparison for 304L in a 4mm x 4mm square domain of the normalized number of grains evolution during pure grain growth regime for the Laguerre-Voronoï method (blue dashed line) with the one for the Voronoï method (red dashed line); comparison of the normalized mean grain area evolution for the Laguerre-Voronoï methods (blue full line) with the one for the Voronoï method (red full line).*

It is confirmed in this chapter that taking into account the neighbourhood effects is of fundamental importance in determining the kinetics of grain growth. Generating a digital microstructure using a Voronoï method cannot ensure a good prediction of experimental grain growth when dealing with log-normal grain size distributions. On the contrary the Laguerre-Voronoï method is appropriate.

In the next section a more detailed study of the influence of the grain size distribution on grain growth kinetics is performed.

5 Assessment of simplified 2D grain growth models from numerical experiments based on a level set framework

The study presented in this paragraph has two main purposes. The first one is to test, in 2D, two mean field grain growth models existing in the literature - Burke and Turnbull [Burke, 1952] and Hillert/Abbruzzese [Hillert, 1965], [Lücke, 1992], [Lücke, 1998], [Abbruzzese, 1992] – under simplified conditions of isotropic grain boundary energy and mobility, constant temperature, and absence of precipitates, using the results obtained with our full field modelling method for different initial grain size distributions. These models were developed based on theoretical assumptions and they are not easily verified

experimentally. So, the idea is to use the full field simulations results, thus verifying if and when the mean field model predictions are acceptable. The second main purpose of this section is to study whether or not a full field model is needed under these simple conditions.

In [Kamachali, 2012], the authors present a similar study using a phase field framework combined with a finite difference modelling technique. Kamachali discusses both statistical and topological perspectives of ideal grain growth using the results of 3D simulations. The paper shows that, despite a few discrepancies with the mean field theory (Burke and Turnbull model and Hillert model) the parabolic kinetics of grain growth remains valid for the entire process. The simulation reaches a steady state and the grain size distribution in this steady state agrees with the Hillert distribution [Hillert, 1965]. The volumetric growth rate obtained compares well with the mean field assumptions. However, the paper analyses only one initial grain size distribution, putting aside the influence of the initial grain size distribution on the grain growth kinetics. In this section, the influence of the initial grain size distribution is studied by considering seven different cases in 2D configurations.

5.1 Grain size distributions

To check the validity of different grain growth models, we now study seven different grain size distributions. These seven grain size distributions were described in details in chapter 2. Table 4.3 sums up their principal features.

Table 4.3: *Characteristics of grain size distributions and error concerning the digital generation of the seven microstructures*

	Mean Radius - μ (µm)	Standard Deviation - σ (µm)	σ/μ	Initial number of grains	Domain Size (mm)	Error (%)
Log1	61.7	7.2	0.12	9728	11 x 11	2.9
Log2	63.7	14.1	0.22	10517	12 x 12	7.1
Log3	67.4	23.5	0.35	10464	13 x 13	2.0
Log4	71.4	31.6	0.44	9999	14 x 14	1.8
Log5	75.3	38.4	0.51	8583	14 x 14	4.9
304L	67.4	31.0	0.45	9211	13 x 13	5.3
Bimodal	62.8	24.3	0.37	9933	12 x 12	8.3

In all cases, the number of grains is around 10000, which ensures a good statistics during the simulation.

Figure 4.21 recalls the comparison between the targeted microstructures and those built numerically (see Figures 2.14 and 2.11b). In this figure, the x-axis corresponds to the normalized radius $(R/<R>)$, where $<R>$ corresponds to the mean grain size. Table 4.3 presents the L2 errors between the theoretical and the obtained numerical distributions.

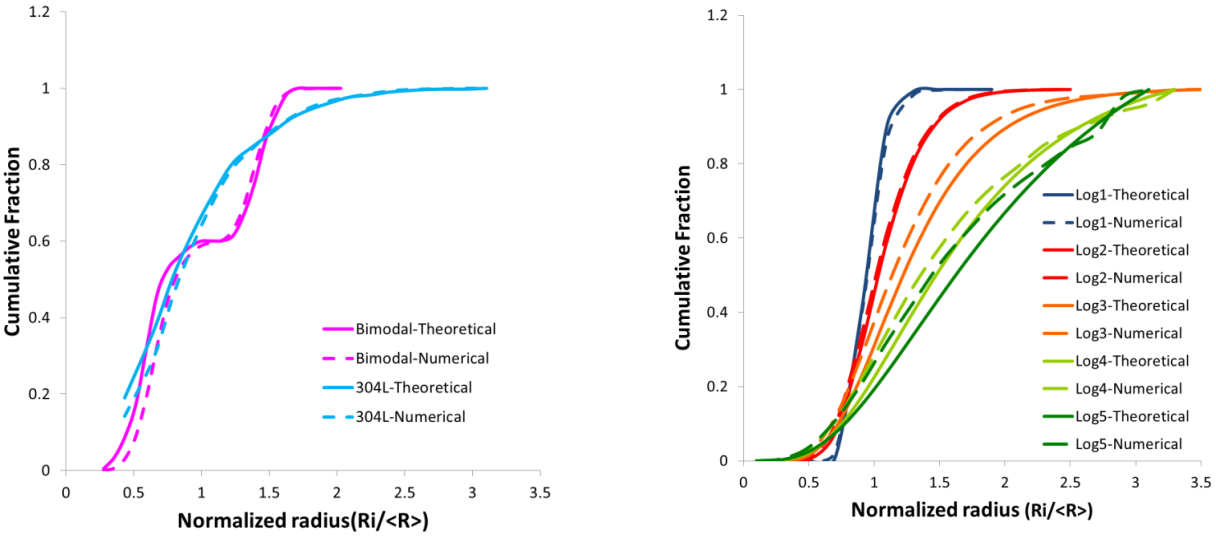

(a) (b)

Figure 4.21: *Numerical initial grain size distributions compared with the targeted one: (a) Bimodal and 304L distribution; (b) Log1, Log2, Log3, Log4 and Log5 distributions.*

For all simulations presented here and referring to the 304L steel properties, the time step is 120 seconds, the thermal treatment is applied 5h and the temperature is constant and equal to 1050°C (M = 1.37 10^{-12} m^4/(J.s) and γ = 0.6 J/m^2). The finite elements meshes are adapted thanks to the *a posteriori* method in a square domain of 13 mm x 13 mm, leading to an average of 3,200,000 mesh elements for the initial microstructures. The computation time is around 24 hours using 128 cpu for all calculations.

A graph colouring technique (paragraph 3.4) is used for limiting the number of level set functions required to describe the whole microstructure. In other words, one level set function will describe several non-neighbouring grains instead of describing only one grain. So, instead of dealing with N_G level set functions in the domain, we will have N_C container level set functions, knowing that N_C is significantly smaller than N_G. In order to delay the onset of grains coalescence, we impose that only the 4^{th} nearest neighbour can belong to the same level set function. Therefore, using this coloration technique, the whole aggregate (around 10000 for the considered microstructures) can be fully described using only around 30 container level set functions. Figure 4.22 illustrates the grain growth simulation of the 304L grain structure.

(a)

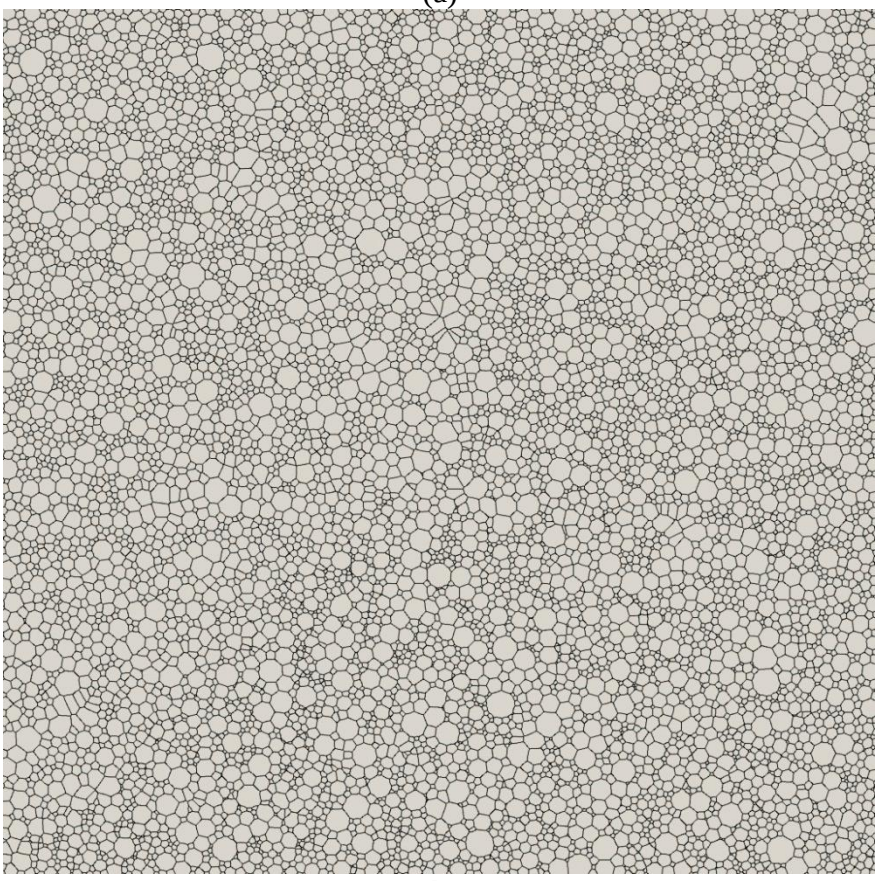

(b)

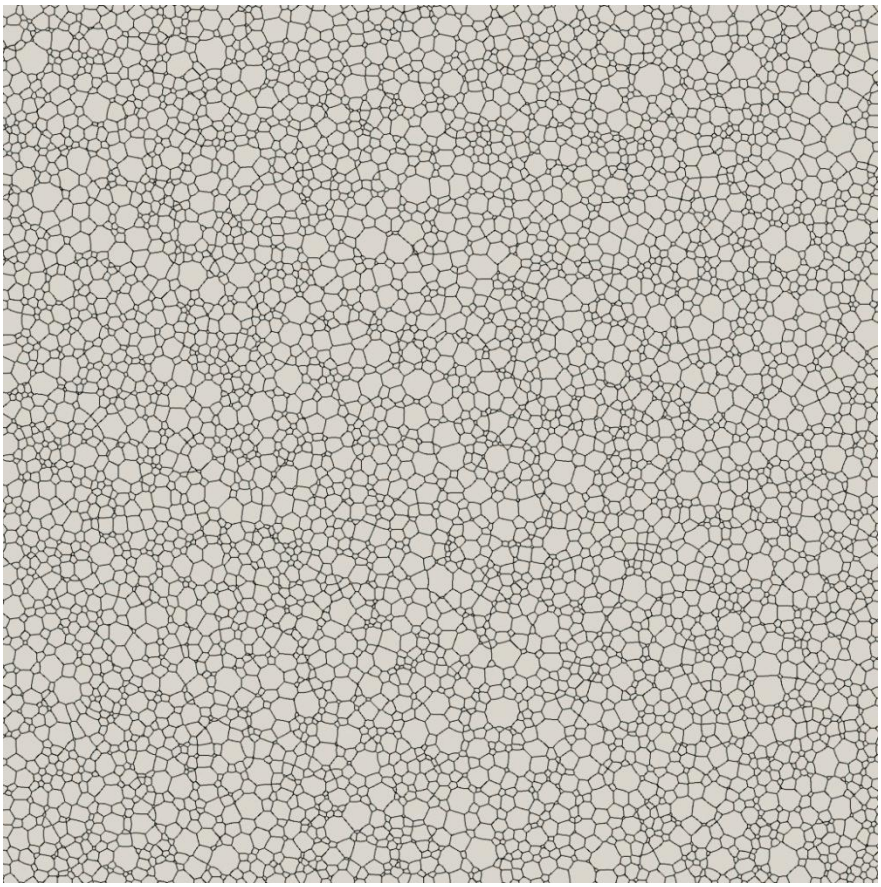

(c)

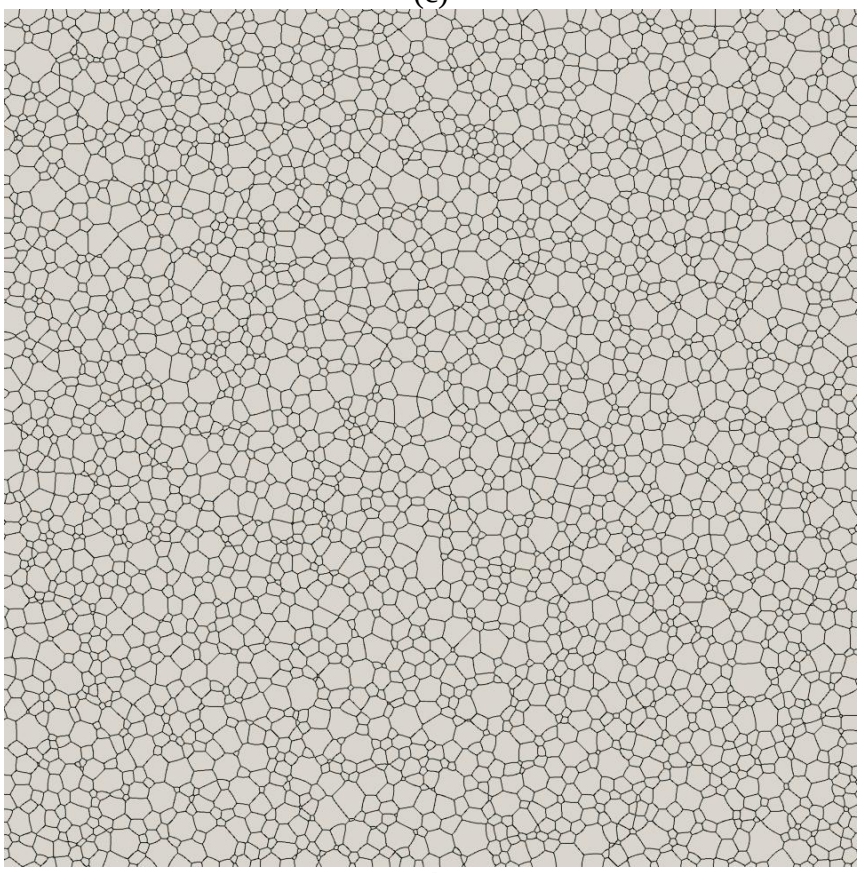

(d)

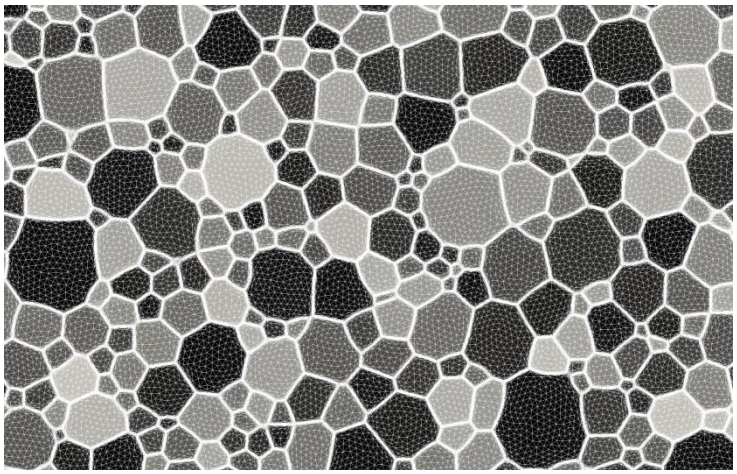

(e)

Figure 4.22: *304L steel grain growth at 1050°C : (a) to (d) grain interfaces after, respectively, 0 min, 20min, 1h40min and 5h; and (e) zoom on a few grains after 1h30min where an anisotropic FE mesh appears in white. Grey levels of the grains relate to the container level-set functions.*

All the studied distributions – except for the Bimodal distribution (which will be discussed later) – reach at some point a quasi stationary steady state. The final grain size distributions calculated from the six distributions are compared with Hillert [Hillert, 1965] and Rayleigh distributions. The Rayleigh distribution was originally derived in the 2D grain growth context by Louat [Louat, 1974] and corrected by Mullins in [Mullins, 1998]. Table 4.4 presents the equations for these theoretical stationary distributions in 2D.

Table 4.4: *Hillert and Rayleigh distribution equations.*

Hillert distribution	$P_H\left(\frac{R}{<R>}\right) = \frac{2^3 e^2 \left(\frac{R}{<R>}\right)}{\left(2-\left(\frac{R}{<R>}\right)\right)^4} \exp\left[-\frac{4}{2-\left(\frac{R}{<R>}\right)}\right]$
Rayleigh distribution	$P_R\left(\frac{R}{<R>}\right) = \frac{\pi\left(\frac{R}{<R>}\right)}{2} \exp\left[-\frac{\pi\left(\frac{R}{<R>}\right)^2}{4}\right]$

The Hillert distribution has a non-analytic cut off at $(R/<R>) = 2$ while the Rayleigh distribution presents an infinite tail. In Figure 4.23 the obtained numerical quasi-stationary distributions are in good agreement with the Rayleigh distribution, which is coherent with Mullins work (the Bimodal distribution did not reached a quasi-stationary state so the corresponding results will be discussed later).

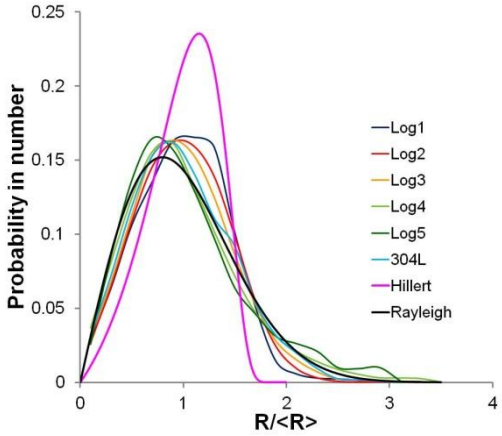

Figure 4.23: *Quasi-stationary state and comparison with Hillert and Rayleigh predictions.*

According to [Mullins, 1998], the reason for the discrepancy between the Hillert theoretical distribution and the experimental and/or numerical results comes from topological reasons: in 2D, the Hillert distribution is reached only if the average number of sides relates linearly to the grain size. The relationship between the number of sides and the grain size in the results presented in Figure 4.23 should therefore be the subject of future work.

5.2 Burke and Turnbull study

The first mean field model tested is the Burke and Turnbull model [Burke, 1952]. This model is based on three main hypotheses:

- the driving force for the phenomenon is proportional to the grain boundary mean curvature $(1/R)$, where R is the equivalent radius. So the grain boundary migrates toward the centre of its curvature, which in turns reduces the interfacial area as well as its associated energy;
- the mobility and grain boundary energy are isotropic and uniform. As a consequence the angles in the triple junction are equal to 120°C;
- the heat treatment temperature is constant.

These hypotheses lead to the following grain growth kinetics equation in 2D:

$$< R > ^2 - < R >_0^2 = \frac{1}{2} M \gamma t \,, \tag{4.16}$$

where $< R >$ (resp. $< R >_0$) corresponds to the average grain radius (resp. at t = 0s). With this equation, neither the topological nor the neighbouring effects are taken into account; the grain growth kinetics is characterized only by the average grain size.

To check the consistency between the full field simulation results and this model, the curves $\log\left(< R >^2 - < R >_0^2\right) = f\left(\log(t)\right)$ have been plotted in Figure 4.24 for each initial distribution described in Table 1, except for the Bimodal distribution, which will be treated separately. For these distributions, Equation 4.17 is generalized according to:

$$< R > ^2 - < R >_0^2 = \alpha M \gamma t^n \,. \tag{4.17}$$

From Equation 4.17, the validity of the Burke and Turnbull model can be verified if the slope of $\log\left(< R >^2 - < R >_0^2\right) = f\left(\log(t)\right)$, *n*, is equal to 1 and if the fitted curve leads to an α value around 0.5. Computed curves and their linear fits are given in Figure 4.24 and lead to the α and *n* parameters summarized in Table 4.5.

Table 4.5: *Burke and Turnbull model analysis thanks to full field simulations results for different grain size distributions.*

Distribution	Slope (*n*)	α	Number of grains in the end	σ/μ
Log1	2.48	$1.21\ 10^{-7}$	4078	0.12
Log2	1.59	$1.08\ 10^{-3}$	3747	0.22
Log3	1.19	0.08	2889	0.35
Log4	1.02	0.38	2782	0.44
Log5	0.89	2.30	2743	0.51
304L	1.04	0.42	3271	0.45

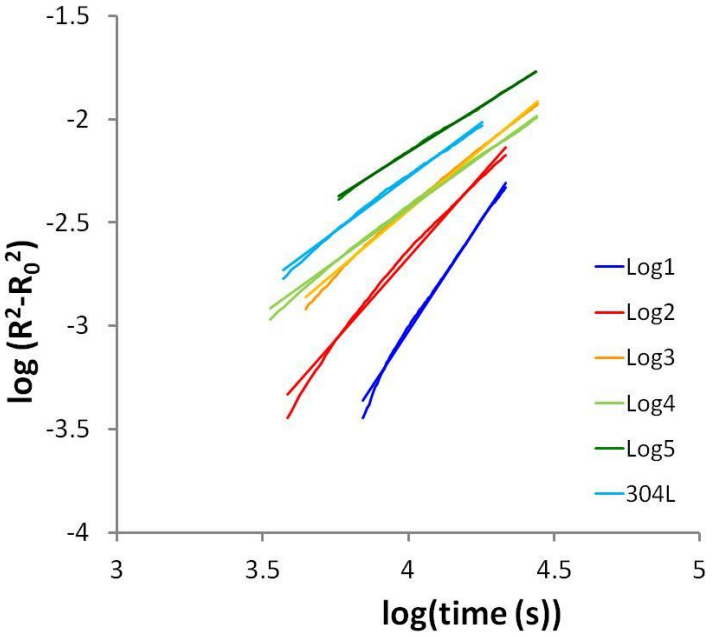

Figure 4.24: *Computed evolutions of grain structures starting with different initial grain size distributions, using the full field model. Linear approximations are used for comparison with the Burke and Turnbull model.*

As illustrated in Table 4.5 and Figure 4.24, *n* and α are highly dependent on the initial grain size distribution. Only the Log4 and 304L distributions lead to the values of *n* and α expected by the Burke and Turnbull model. Both distributions are log-normal with a value of $\sigma/\mu \cong 0.45$ (see Table 4.3). For the other distributions, it can be noticed in Figure 4.25 that *n* values decrease with the increase of σ/μ, while α values increase with σ/μ. These evolutions can be approximated by the following simple relationships:

$$\ln\alpha = 11.15\ln\left(\frac{\sigma}{\mu}\right) + 8.62, \tag{4.18}$$

$$n = -1.08.\ln\left(\frac{\sigma}{\mu}\right) + 0.1. \tag{4.19}$$

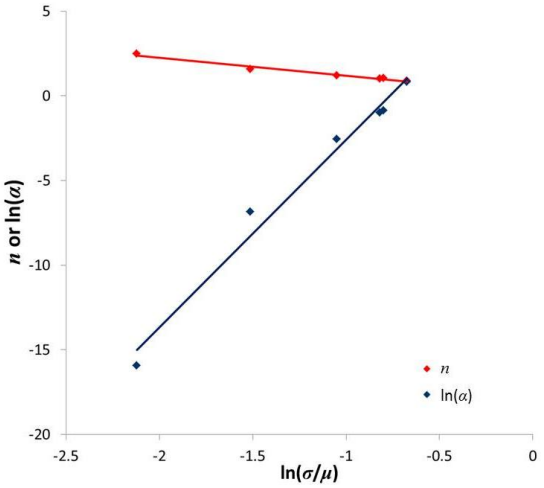

Figure 4.25: *Relationship between α and n fitted parameters and σ/μ of the initial grain size distributions (given in Table 4.3)*

For a log-normal distribution, α presents an power law dependence on σ/μ and n a logarithmic dependence. Equations 4.18 and 4.19 confirm that grain growth kinetics significantly depends on grain structure and neighbourhood effects.

Figure 4.26 shows that the Bimodal kinetics can be divided in two linear parts – 'A' between t = 0s and t = 4400s and 'B', between t = 4400s and t = 18000s. In an attempt to understand this behaviour, the grain size distribution at t = 0s, t = 4400s and t = 10800s (figure 4.27) are analysed.

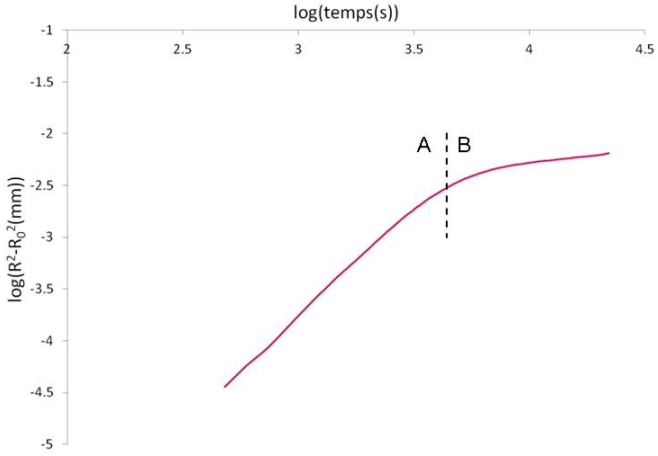

Figure 4.26: *Burke and Turnbull model study for Bimodal grain structure.*

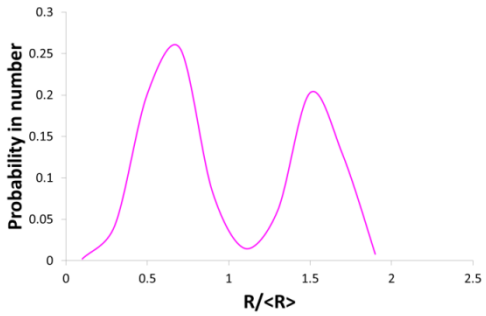

(a)

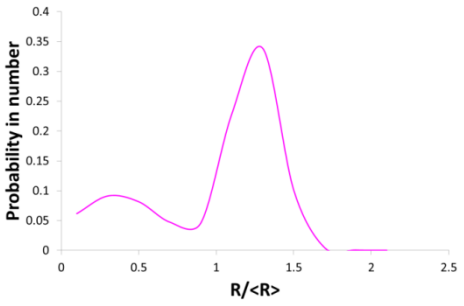

(b)

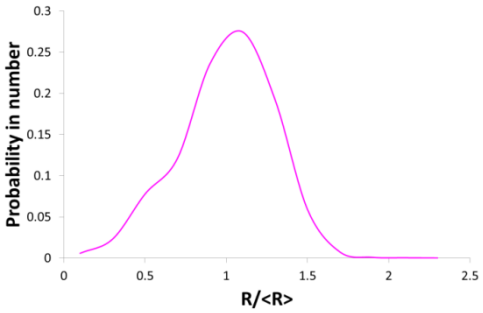

(c)

Figure 4.27: *Grain size distribution at (a) t=240s, (b) t=4400s and (c) t=10800s for the Bimodal grain structure.*

Figure 4.27 shows that for t = 0 s, we have two different grains populations. The number of grains belonging to the smaller radius family is bigger than the one belonging to the larger radius family. Knowing that the average grain curvature is equal to the inverse of the equivalent radius, grains having a smaller radius will have a bigger curvature and, as a consequence, will be quickly consumed. At t = 4400 s, the grain size distribution has changed, and starts switching to a single peak distribution. The average grain curvature decreases, and the grain growth kinetics consequently becomes slower. Finally, t = 10800 s, a single peak distribution is reached. One can conclude that the slope change in the kinetics of grain growth coincides with the quasi disappearance of the smallest grains population, i.e. with the switching from a bimodal distribution to a single peak distribution.

It is therefore concluded that the Burke and Turnbull model is *not* valid for most of the investigated grain size distributions. The model only behaves well for lognormal grain size distributions, with a σ/μ value close to 0.45.

5.3 Hillert/Abbruzzese model study

In a second part, both Hillert [Hillert, 1965] and Abbruzzese [Lücke, 1992], [Lücke, 1998], [Abbruzzese, 1992] mean field models were studied. Both models are derived from von Neumann-Mullins [von Neumann, 1952], [Mullins, 1956] model. Even though the development of the model proposed by Hillert is different from the one proposed by Abbruzzese, both authors finally propose the same grain growth model equation (Equation 4.20). In the development of the Abbruzzese model, the authors use the "Special Linear Relationship" (SLR) $\bar{n}_i = 3.\left(1+\frac{R_i}{< R >}\right)$ [Abbruzzese, 1992] discussed in chapter 2. In this work, both models are analysed as one. The central equation is:

$$V_i = \beta M \gamma \left(\frac{1}{< R >} - \frac{1}{R_i}\right), \tag{4.20}$$

where the grain structure is assumed to be described by a discrete set of grain families (each family being labelled with a subscript i), V_i corresponds to the average grain boundary velocity of the grain family i, $< R >$ corresponds to the average grain size and β is a constant generally assumed to be 0.5 in 2D, and 1 in 3D, even though other values can be found in the literature. For example, in [Kamachali, 2012], Kamachali found a value of 1.25 in 3D, using a phase field framework combined with a finite-difference modelling technique. In [Rios,

2008], Rios and Glicksman calculated a 3D value of 0.81, using the average *N*-hedra method (ANH) [Glicksman, 2005].

In this model, the neighbouring effects are taken into account by the addition of the term $1/< R >$. This term represents the mean curvature of all the grains belonging to the domain. Also, in the Hillert/Abbruzzese model, the grain growth behaviour of a histogram with several grain families is analysed. As a consequence, the interaction between the different families is also taken into account (in the Burke and Turnbull model this interaction is ignored). Figure 4.28 illustrates the interaction between the different families.

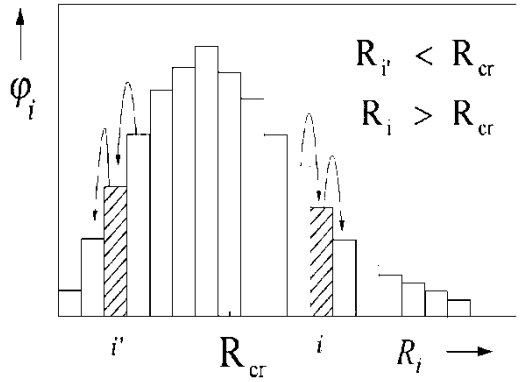

Figure 4.28: *Grain size distribution: probability (φi) vs. radius (Ri). Examples for the grain size flux during grain growth are indicated for the cases $R_{i'} < R_{cr}$ and $R_i > R_{cr}$) [Lücke, 1998].*

To check the consistency between the full field simulation and the Hillert/Abbruzzese model, we compared the grain size distributions obtained with the full field model and the mean field model described by Equation 4.20, and implemented within a more general model described in [Bernard, 2011]. Three different time steps (t = 2 min, t = 76 min and t = 150 min) were analysed. Figure 4.29 illustrates the comparison and table 4.6 numerically quantifies the comparisons for the seven grain size distributions.

Table 4.6: *Error between histograms obtained with full field model and Hillert/Abbruzzese mean field model.*

	Error L2 (%)		
	t = 2 min	t = 76 min	t = 150 min
Log1	10.7	4.6	3.9
Log2	4.5	4.6	6.3
Log3	1.9	4.0	6.0
Log4	1.6	4.5	7.6
Log5	1.9	2.4	3.4
304L	1.9	5.5	5.5
Bimodal	4.9	6.8	10.3

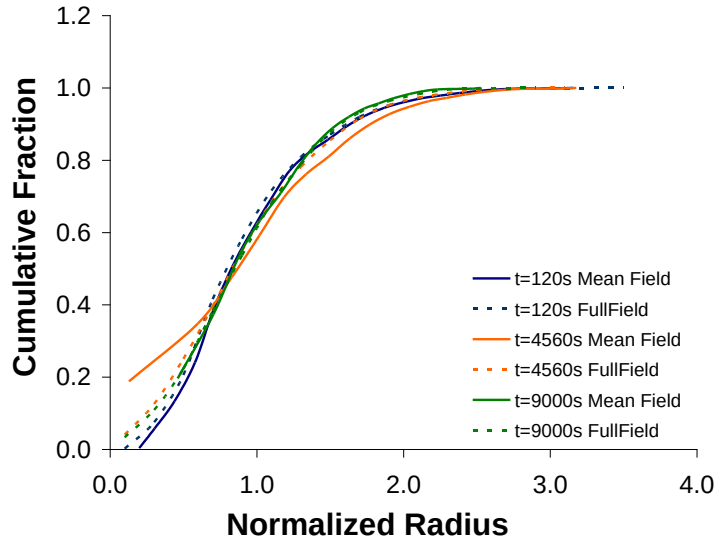

304L

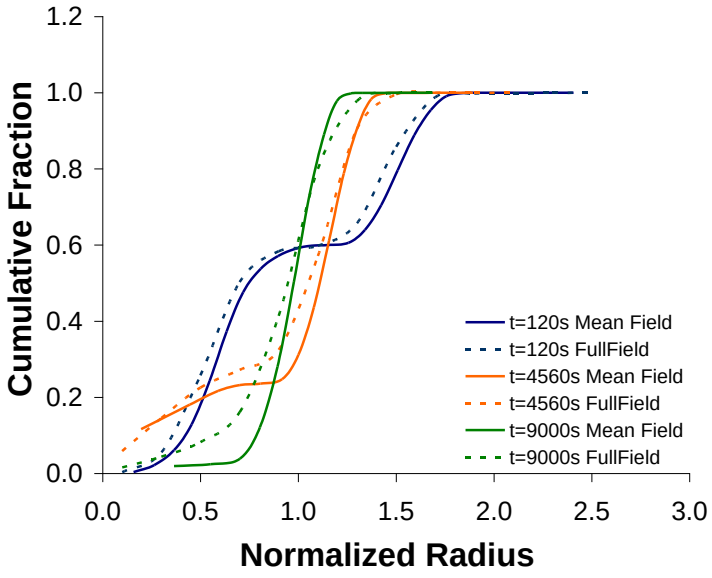

Bimodal

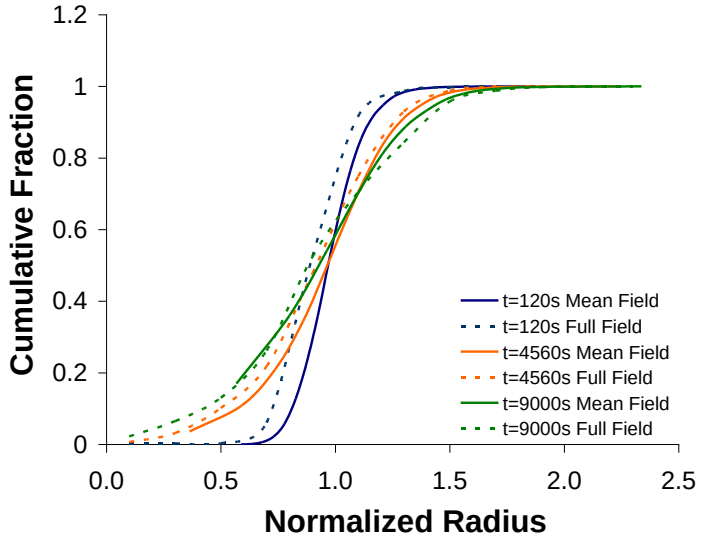

Log1

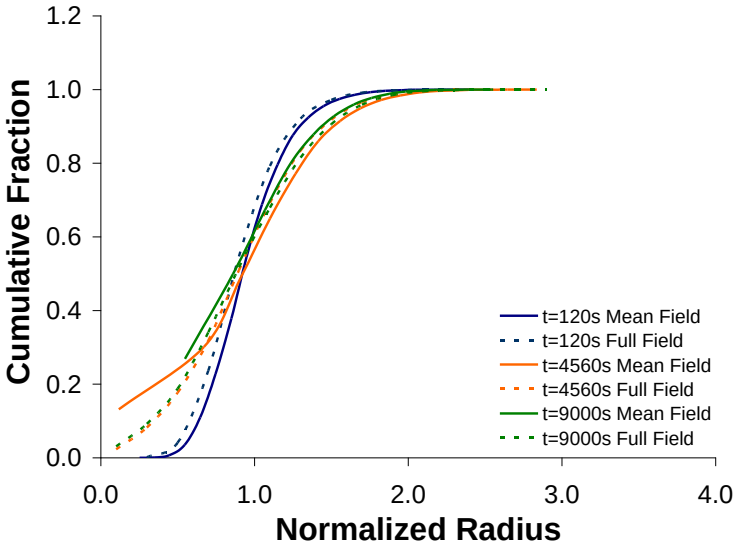

Log2

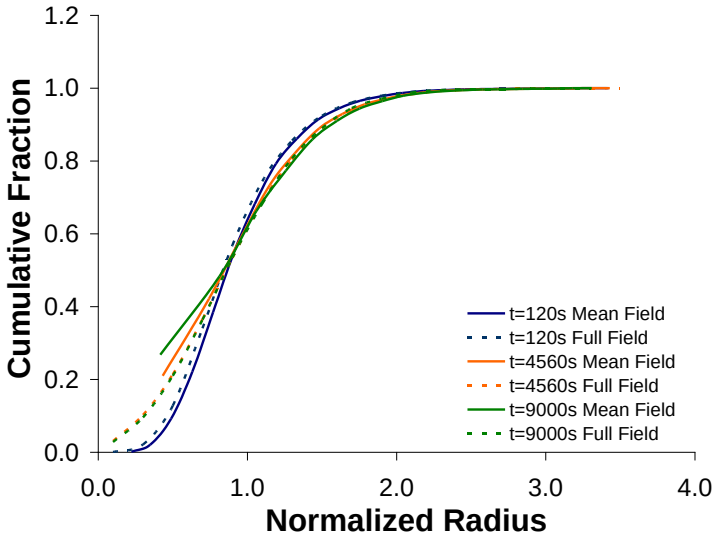

Log3

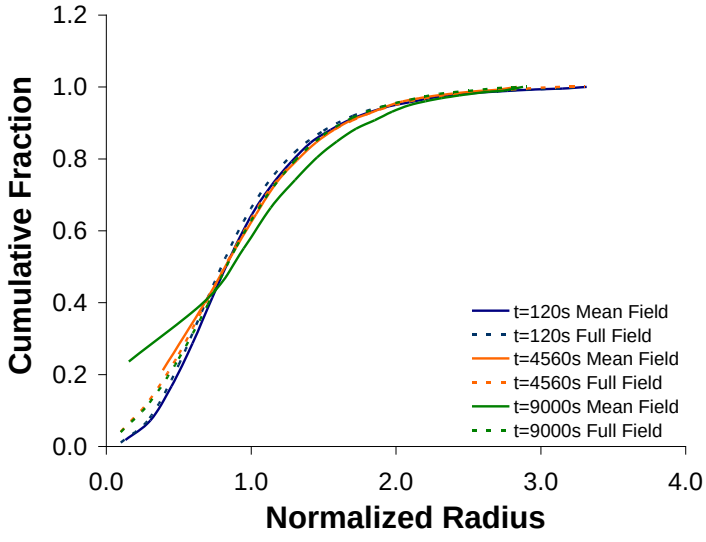

Log4

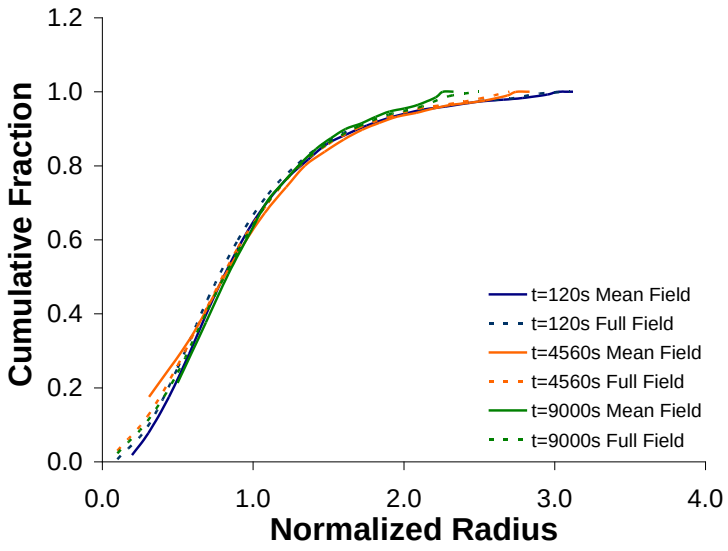

Log5

Figure 4.29: *Comparison between full field results and Hillert/Abbruzzese mean field results for all grains structures studied: 304L, Bimodal, Log1, Log2, Log3, Log4, and Log5.*

From Table 4.6 it can be concluded that the Hillert/Abbruzzese mean field model is in good agreement with the computations. For all considered grain size distributions, the error between the grain size cumulative histograms obtained with the two different approaches is smaller than 11%, even for the Bimodal distribution. A closer look at the distributions illustrated in Figure 4.29, shows that errors increase in the lowest grain sizes range. A hypothesis was initially made to explain this localization. The idea was to relate this error to volume conservation issues discussed in [Bernard, 2011]: volume changes of the shrinking grains are computed by redistributing the total volume changes of growing grains. Consequently, the rates of volume change for small grain sizes are slightly modified from the values strictly deriving from Equation 4.20. Comparing the results obtained using the mean field model discussed in [Bernard, 2011] and the direct use of Equation 4.20, we observe that the effect of this volume conservation treatment is more important for a small number of representative grains (around 50). In fact, when using 40 representative grain families (as in the comparisons presented in Figure 4.29), the direct use of Equation 4.20 gives better results than the use of the model presented in [Bernard, 2011]. However, for a number of representative grains around 200, both methods present the same results, and the volume conservation treatment does not affect the results anymore.

Therefore, in the simple considered configurations, i.e. when grain boundary mobility and energy are isotropic throughout the polycrystal, and no Zener pinning forces are taken into account (absence of second phase particles), the Hillert/Abbruzzese mean field models describe quite accurately the grain growth phenomenon for any initial grain size distribution.

6 Conclusion

In this chapter a finite element model was proposed in order to simulate the grain growth phenomenon. Grain boundaries are implicitly represented using level set functions. Two different methods to simulate grain boundary motion are tested: a convective approach and a diffusive approach. Even though both approaches are appropriate to simulate grain growth with regular grain curvature (for example, a circular grain immerged in an infinite medium), the diffusive approach was the only method able to simulate polyhedral grain growth with no regular grain curvature.

It was also shown that the diffusive approach associated with a multiple junction treatment and isotropic boundary energy leads to the expected 120° equilibrium angle at triple junctions. Finally, the simulation results of different polyhedra (square, pentagon, hexagon, heptagon and octagon) growth rates is shown to agree well with the von Neumann-Mullins theory.

A comparison between the grain growth kinetics of two different digital microstructures, one based on setting the mean grain size (Voronoï approach), and the other based on obeying a grain size distribution (Laguerre-Voronoï), has been performed for an isotherm thermal treatment. The kinetics were shown to be significantly different: the Laguerre-Voronoï one is faster than the Voronoï. This result highlights the importance of the size distribution on global grain growth kinetics.

Finally, in this chapter we discussed the validity of two grain growth models (Burke and Turnbull, Hillert/Abbruzzese) using full field modelling results. Seven initial grain size distributions have been considered in order to test these mean field methods.

The Burke and Turnbull model, which does not take into account the topology or the neighbourhood effects, is valid only for two distributions and both of them are lognormal and present a standard deviation value roughly equal to 0.45 of the mean grain size. Coincidentally, one of these two distributions is the one based on experimental 304L data. Also, this kind of distribution is classically observed in polycrystalline metals. On the other hand the Hillert/ Abbruzzese model is valid for all tested distributions, even for the bimodal one. Consequently, if the development of full field models is justified for the description of grain growth in complex conditions, their use appears disproportionate in the simple configurations investigated here, where the Hillert/ Abbruzzese approach is sufficient.

This assessment test was not performed in 3D because of lack of time. 3D simulations with a representative number of grains (around 10000 grains) are time and computational resources consuming. During this Ph.D. thesis we did not have the time to perform all these simulations. Comparisons between 3D grain growth simulations and mean field models will be done in the near future.

In chapter 5, the grain growth model introduced in this chapter is extended to a recrystallization model. The influence of capillarity effects is investigated. The coupling between the recrystallization – grain growth model with the crystal plasticity model is then detailed. The chapter ends with an analysis of nucleation criteria in recrystallization.

Résumé en français

Un modèle de croissance de grain à l'échelle mésoscopique basé sur une formulation éléments finis dans un cadre level-set est proposé dans ce chapitre. Dans une première partie, deux approches pour simuler la capillarité des joints de grains sont testées: une approche convective et une approche diffusive. L'approche diffusive développée est finalement retenue par sa capacité à simuler précisément la croissance de grains initialement polyédriques en respectant les angles d'équilibre de 120° aux joints multiples imposés physiquement par l'hypothèse d'isotropie de l'énergie d'interface.

Finalement, grâce au formalisme développé, un travail d'analyse de modèles de croissance des grains à champ moyen existant dans la littérature est réalisé. Deux modèles particuliers ont été étudiés : celui de Burke et Turnbull et celui de Hillert/Abbruzzese. En comparant ces modèles avec les résultats obtenus par notre approche en champ complet, il est mis en évidence que le modèle simple de Burke et Turnbull, qui ne prend pas en compte les caractéristiques topologiques de la microstructure, n'est pas approprié pour décrire la croissance de grains pour tout type de distribution initiale de taille de grains. Pour le modèle de Hillert/Abbruzzese, nous prouvons que le modèle est valide pour toutes les distributions

analysées. Dans le chapitre 5, le modèle de croissance de grains présenté dans ce chapitre est couplé à un modèle de recristallisation statique.

Chapter 5

Grain Boundary Migration - Static Recrystallization

Contents

1 Introduction 158
1.1 Static recrystallization 158
1.1.1 Nucleation mechanisms 159
1.1.2 Nuclei growth 162
1.2 The Johnson-Mehl-Avrami-Kolmogorov (JMAK) model 163
1.3 304L steel static recrystallization 164
1.4.1 Strain level effect 164
1.4.2 Temperature and strain rate effect 164
1.4 Recrystallization simulations using a full field formulation 166
2 Finite element model on a level set framework 167
2.1 Velocity field expression 167
2.2 Recrystallization algorithm 168
3 Results 169
3.1 Academic Test - Circular grain case 169
3.2 Academic Test – 2 grains case 171
3.3 Polycrystalline 2D simulation 173
3.3.1 Random nucleation sites 173
3.3.2 Necklace-type nucleation sites 177
4 Coupling of crystal plasticity and static recrystallization 182
4.1 Critical dislocation density and nucleus radius 182
4.2 Number of nucleation sites 183
4.3 Coupling with crystal plasticity results 184
4.4 3D recrystallization kinetics results in site saturated nucleation context 187
5 Conclusion 191

1 Introduction

A driving force for grain boundary displacement arises when a boundary displacement leads to a reduction of the total energy. In recrystallization phenomena, two kinds of energy are responsible for the grain boundary motion: (1) an excess of energy due to grain boundary itself (grain boundary curvature) and (2) a free energy difference between the adjacent grains due to energy stored during deformation. In chapter 4, grain boundary migration due to the grain boundary curvature was presented and discussed in details. In this chapter, grain boundary motion based on both driving forces (recrystallization regime) is studied. A first study analysing the influence of the grain boundary curvature effects during the recrystallization process is presented, and the results show that the capillarity effects cannot be neglected in all cases, in contrast with what is often accepted in the literature. In fact, the importance of the grain boundary curvature effects on recrystallization kinetics depends on the nuclei spatial distribution throughout the material. These results highlight the importance of the developments performed in this work, for the improvement of the formalism developed in [Bernacki, 2009] and [Logé, 2008]. In a second part, the static recrystallization model is coupled to the crystal plasticity model discussed in chapter 1. An analysis of nucleation criteria for static recrystallization is presented, distinguishing the two crystal plasticity hardening laws discussed in chapters 1 and 3 (one model considering the total dislocation density and a second model considering two dislocation types, SSDs and GNDs).

1.1 Static recrystallization

The recrystallization process involves the formation of new strain-free grains in certain parts of the material and the subsequent growth of these to consume the deformed microstructure. The microstructure at any point is divided into recrystallized or non-recrystallized regions (Figure 5.1). The recrystallized fraction increases from 0 to 1 during the recrystallization process.

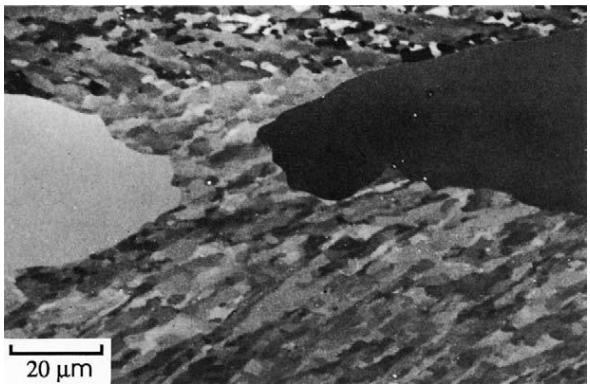

Figure 5.1: *An SEM channelling contrast micrograph of aluminium showing recrystallized grains growing into the recovered sub grain structure [Humphreys, 2004].*

It is convenient to divide the recrystallization process into two regimes: (i) nucleation which corresponds to the appearance of new grains and (ii) growth of these new grains, which replace the deformed material.

The extent of recrystallization is often described by the recrystallized fraction (X_v). However, it is also possible to follow the progress of recrystallization by measurement of various physical or mechanical properties, like the material hardening.

1.1.1 Nucleation mechanisms

Nucleation is the key concept in the understanding of microstructure recrystallization. The classical homogeneous nucleation theories associated with solidification or phase transformation do not hold true for recrystallization due to its low driving force and high grain boundary energies [Humphreys, 2004]. Dislocation free regions are not formed by thermal fluctuations, as in the solidification process. It is now well-known that a critical stored energy must be reached before the onset of recrystallization. Also, nuclei mostly originate at or near the pre-existing grain boundaries, since this is where the highest dislocation density is found.

Even though extensive investigation has been made, significant disagreements on the mechanisms of nucleation still exist. The mostly accepted mechanisms are summarized below.

Strain induced boundary migration (SIBM)

SIBM is the most common nucleation mechanism and it is also known as bulging or migration of pre-existing grains boundaries. This mechanism was originally proposed by Beck and Sperry [Beck, 1950] based on Al optical microscopy observations. This mechanism considers the migration of a pre-existing grain boundary toward the interior of a more highly deformed grain, leaving a dislocation free region behind the migrating grain boundary. Figure 5.2 illustrates this phenomenon. In this case, the nuclei have a similar orientation to the old grain, from which they have grown.

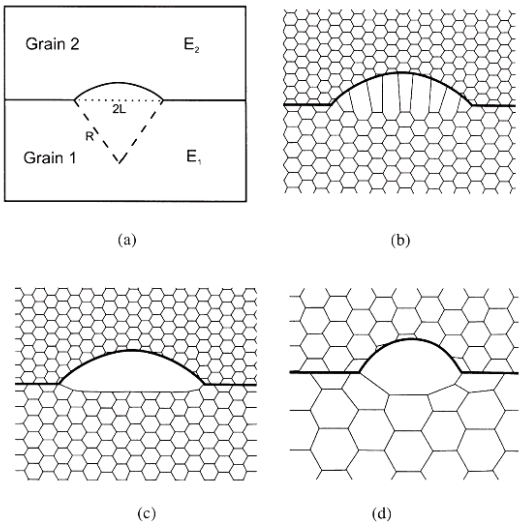

Figure 5.2: *(a) SIBM of a boundary separating a grain of low stored energy (E1) from one of a higher energy (E2), (b) dragging of the dislocation structure behind the migrating boundary, (c) the migrating boundary is free from the dislocation structure, (d) SIBM originating at a single large subgrain.*

The SIBM mechanism occurs when the process is energetically favourable. In other words, the decrease of stored energy due to the elimination of dislocations in the area behind the migrating grain boundary should be higher than the total grain boundary surface increase due to boundary bulging. The growth condition is given by:

$$L > \frac{2\gamma_b}{\Delta E}, \tag{5.1}$$

where γ_b is the grain boundary surface energy per unit of area, ΔE is the released energy associated with the decrease in defects, and 2L is the initial bulging boundary length (Figure 5.3.a). Therefore, a critical stored energy difference is necessary for the nucleation onset.

This mechanism is believed to be particularly important for strains up to 40%. Recent research has shown that the SIBM mechanism is also very important during recrystallization after high temperature deformation of steels. In this case, the material presents a deformed microstructure more homogeneous than when the material is deformed at low temperature [Theyssier, 1999], [Hutchinson, 1999]. Other types of nucleation also seem possible in association with existing grain boundaries. Beck and Sperry [Beck, 1950] also presented evidence for new recrystallized grains which did not share either of the parent grains' orientation. The same phenomenon has been observed in bicrystals of iron by Hutchinson [Hutchinson, 1989].

Nucleation by low angle boundary migration

This model has been presented independently by both Beck [Beck, 1949] and Cahn [Cahn, 1950] in the 1940s. The dislocation density around low angle boundaries maybe relatively high, promoting their migration. During the migration of the sub-boundaries, the dislocations are continuously absorbed increasing the low angle boundary orientation until it is finally transformed into a high angle boundary. The microstructural defects behind the moving subgrain boundaries are removed or rearranged hence decreasing the stored energy. In [Rios, 2005], the authors summarized the experimental evidences for this nucleation mechanism. In this paper the authors also exhibit that this mechanism usually occurs at high strains, largely spread subgrain size distribution, high annealing temperatures. Finally this mechanism occurs specially in low SFE (stacking fault energy) metals. Figure 5.3 illustrates the sub boundary migration nucleation mechanism.

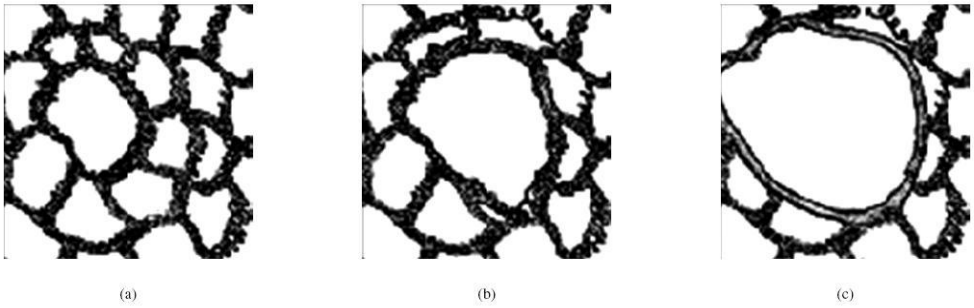

Figure 5.3: *The sequence shows the nucleation of a recrystallized grain starting from a subgrain: (a) initial substructure; (b) the larger (middle) subgrain growth over the other (smaller) ones and (c) an area free of defects associated to the large angle boundary that is being formed [Rios, 2005].*

Figure 5.4 presents an experimental analysis of a low angle boundary migration. In this case, the recrystallization of a Zr-2Hf alloy deformed by planar compression test at room temperature is studied.

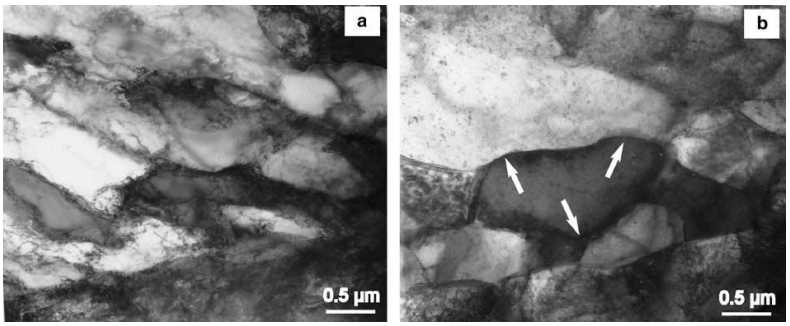

Figure 5.4: *HVEM bright field images of the same area (a) in the as-deformed condition (55% strain) and (b) after in situ annealing at 700 C for 5 min, revealing the rearrangement of dislocations into a subgrain structure and low angle boundary migration (white arrows) [Zhu, 2005].*

Nucleation by subgrains coalescence

The mechanism of subgrain coalescence is based upon the coalescence of two adjacent subgrains. This coalescence is equivalent to the rotation of the grains causing the crystal lattices to coincide, as illustrated in Figure 5.5.

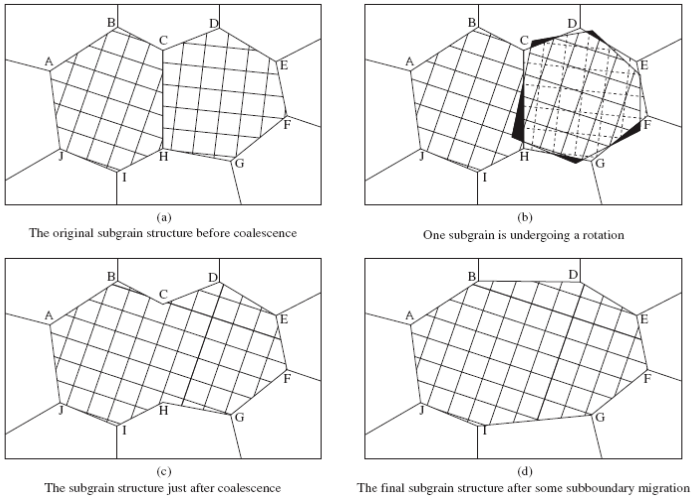

Figure 5.5: *Coalescence of two subgrains by "rotation" of one of them: (a) original structure prior to coalescence; (b) rotation of the CDEFGH grain; (c) subgrain structure subsequent to coalescence and (d) final structure after sub-boundaries migration.*

This mechanism seems to be associated with transition bands (which consists of a cluster of long narrow cells or subgrains with a cumulative misorientation from one side of the cluster to the other [Humphreys, 2004]), large spread in the distribution of subgrains angles, moderate strains, relatively low annealing temperature and metals with high SFE.

Figure 5.6 presents an experimental analysis of a low angle boundary migration. In this case, a Zr-2Hf alloy deformed by planar compression test at room temperature is used in order to study static recrystallization.

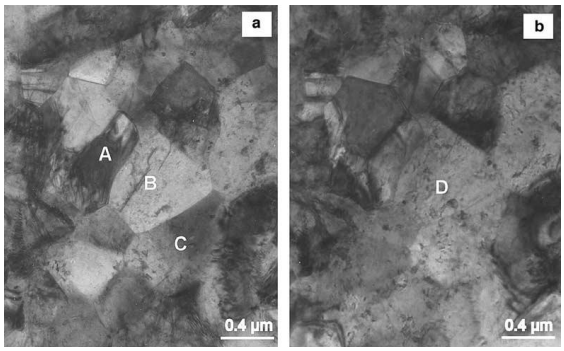

Figure 5.6: *HVEM bright field images of the same area after in situ annealing at 700 C for 5 min (a) and 30 min (b), revealing the coalescence of subgrains. Subgrains A, B and C form a larger subgrain D [Zhu, 2005].*

Table 5.1 sums up some conditions for which the different nucleation mechanisms occur.

Table 5.1: *Summary for nucleation mechanism.*

Strain induced grain boundary migration	Sub-boundary migration	Subgrain coalescence
• small strains (up to 40%) • hot working	• high strains • high temperatures • heterogeneous subgrain size distribution • low SFE metals and alloys	• moderate strains • relatively low temperatures • large spread in the distribution of subgrain misorientation • transition bands • high SFE metals and alloys

1.1.2 Nuclei growth

The expansion of new grains follows the grain boundary motion equations already discussed in chapter 4. It is generally accepted that the velocity of a high angle grain boundary can be approximated by [Humphreys, 2004], [Bernacki, 2009], [Kugler, 2004]:

$$\vec{v} = M\left(\Delta E - \gamma\kappa\right)\vec{n} \tag{5.2}$$

where M is the grain boundary mobility; ΔE is the material internal energy difference, which depends on the dislocation density; γ is the grain boundary energy; κ is the grain boundary mean curvature and $\vec{n}$ is the outward unit normal to the grain boundary. As already explained, the grain boundary driving force can be divided in two parts: the first one is related to the internal material energy gradient ($\Delta E\vec{n}$) and the second one is related to the grain boundary capillarity effects ($-\gamma\kappa\vec{n}$). Experimentally, the driving force of grain boundary motion, and therefore the boundary velocity, may not remain constant during recrystallization. In particular, the driving force may be lowered by concurrent recovery and both the driving force and the mobility may vary through the specimen. As a consequence, the grain boundary velocity, which is an important parameter in any recrystallization model, is a complex function of the material and the deformation and annealing conditions.

In this work, the material recovery is not considered during the recrystallization simulations. As a consequence, the internal energy stored by dislocations during the plastic deformation will not evolve during the recrystallization simulations.

1.3 The Johnson-Mahl-Avrami-Kolmogorov (JMAK) model

The first and still widely used model to describe the recrystallization process based on nucleation and growth of new grains was developed in the 30's by [Johnson, 1939], [Avrami, 1939], [Kolmogorov, 1937]. This model, also known as the Johnson-Mehl-Avrami-Kolmogorov (JMAK) model is largely discussed in the literature. For example, in [Cho, 2001], [Barraclough, 1979], [Towle, 1979], the authors use the JMAK approach to model 304L steel static recrystallization kinetics.

This model is based on three main hypotheses: (i) thermal treatment is performed in isothermal conditions; (ii) the material presents a homogeneous state after plastic deformation; (iii) nucleation sites are assumed to be randomly distributed.

When recrystallization begins, new grains nucleate with a nucleation rate $\dot{N}$ and grow with a growth rate $\dot{G}$. The resulting recrystallized fraction X_v is given by:

$$X_v(t) = 1 - \exp(-Bt^n), \tag{5.3}$$

where B is a constant depending on a shape factor f, $\dot{N}$ and $\dot{G}$ (Equation 5.4), and n is the JMAK or Avrami exponent.

$$B = \frac{f\dot{N}\dot{G}^3}{4}. \tag{5.4}$$

This JMAK model proposed above assumes that the rate of nucleation and growth remains constant during the recrystallization process. In [Avrami, 1939], the authors also considered the case in which the nucleation rate is not constant, but a decreasing function of time, $\dot{N}$ having a simple power law dependence on time. In this situation, the obtained n value is different from the case where $\dot{N}$ is constant. Also, the exact value of n depends on the form of $\dot{N}$ functions.

Two limiting cases are important: the first one in which $\dot{N}$ is constant with a three dimensional growth and the second one, where the nucleation rate decreases so rapidly that all nucleation events occur at the recrystallization start. This is termed site saturated nucleation. In this case, $\dot{N}$ is replaced by N (number of nuclei) in Equation 5.4. Once again the n value obtained in these conditions will be different from the n value obtained with constant $\dot{N}$.

Finally, if the grains are constrained either by the sample geometry or by some internal microstructural constraint, the nuclei will grow only in one or two dimensions. As a consequence, in these situations, the JMAK exponent will present different values summarized in Table 5.2.

Table 5.2: *Ideal JMAK exponents for different nucleation conditions.*

Growth dimensionality	Site saturated nucleation	Constant nucleation rate
3-D	3	4
2-D	2	3
1-D	1	2

In [Cahn, 1956], the author has extended the theory to include nucleation at random sites near the grain boundaries and found n ranging from 4 at the start of recrystallization to 1 at the end. However, no general analytical treatment of non-randomly distributed nucleation

sites is available. In this work, for all simulations, a site saturation nucleation condition is considered. This means that for all simulations, all nuclei are created at the same time, at the beginning of the simulation.

1.4 304L steel static recrystallization

The material studied in this chapter is 304L steel. In this section, a brief review of the 304L steel static recrystallization behaviour is presented. All experiments presented here were performed by Ke HUANG during his PhD Thesis [Huang, 2011]. Samples have been submitted to torsion tests (Appendix 3), and heat treated afterwards for different times. Recrystallized fractions have been measured using the EBSD technique (Appendix 4).

1.4.1 Strain level effect

Besides the processing conditions (temperature and strain rate, which will be discussed in the next subsection), the amount of applied deformation plays a role on the static recrystallization kinetics. When the material is deformed until higher strain levels, the amount of stored energy is higher. As a consequence, the static recrystallization kinetics will change. Figure 5.7 presents two different static recrystallization tests, both of them were performed at 1000°C with a strain rate equal to 0.01 s^{-1} but one sample was deformed until $\varepsilon = 0.3$ (blue line) and the other until $\varepsilon = 0.5$ (red line).

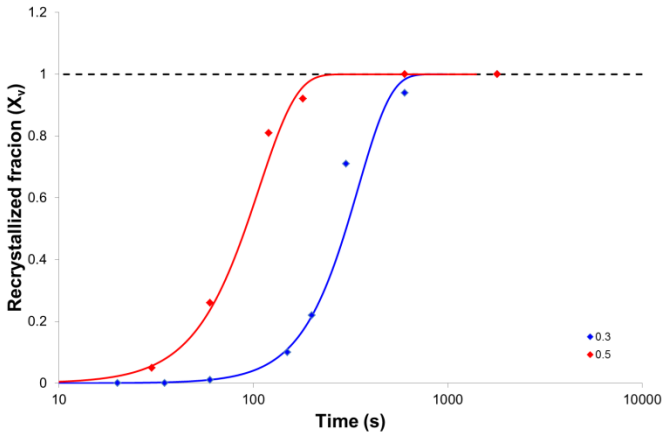

Figure 5.7: *Effect of applied strain on the static recrystallization kinetics in 304L steel deformed at 1000°C to $\varepsilon = 0.3$ and $\varepsilon = 0.5$ with a strain rate of $\dot{\varepsilon} = 0.01\ s^{-1}$.*

Comparing both kinetics curves, we observe that larger strain levels can decrease the incubation time needed to start the static recrystallization process and, at the same time, accelerate recrystallization kinetics.

Also, as it was discussed in paragraph 1.1.1, the type of nucleation mechanism is also a function of strain. If the nucleation type changes when the strain level increases, new spatial distributions of grains may impact the recrystallization kinetics as well.

1.4.2 Temperature and strain rate effects

At temperatures where thermally activated restoration processes such as dislocation climb occur during deformation, the microstructure will be dependent on the deformation temperature and strain rate in addition to the strain. After deformation at high temperatures the stored energy will be reduced and recrystallization will occur less readily than after

deformation to a similar strain at low temperature. On the other hand, since the grain boundary motion velocity depends on the grain boundary mobility (Equation 4.2 – chapter 4) and, as it was discussed is chapter 4, the mobility increases with temperature, one can conclude that the grain boundary motion also increases when increasing the heat treatment temperature. So, when deformation and static recrystallization are performed at higher temperatures, a competition between the material recovery, which decreases the internal energy, and the grain boundary mobility, which increases the grain boundary motion will take place.

In the case of 304L steel, from Figure 5.8 (both samples are deformed with $\dot{\varepsilon} = 0.1\ s^{-1}$ until $\varepsilon = 0.3$ for two different temperatures) we observe that when increasing the deformation and annealing temperature, the recrystallization kinetics becomes faster. So, in this case, the effect of the grain boundary mobility is more important than the material recovery.

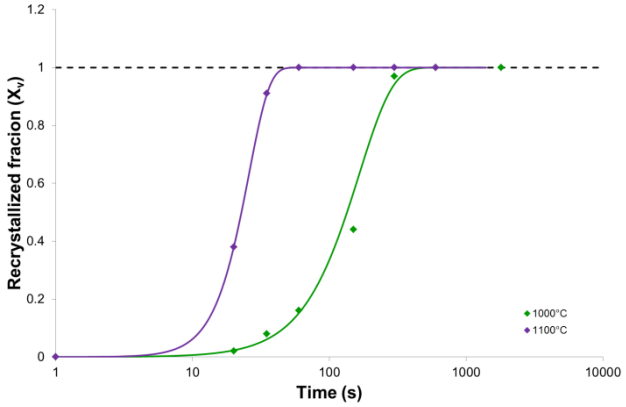

Figure 5.8: *Effect of temperature on the static recrystallization kinetics in 304L steel deformed at 1000°C and 1100°C to ε = 0.3 with a strain rate of $\dot{\varepsilon} = 0.1 s^{-1}$.*

Considering the strain rate effect, after deformation with lower strain rate, the stored energy and, as a consequence, the recrystallization driving force will be reduced. Figure 5.9 describes the recrystallization kinetics for two 304L steel samples, both of them deformed (ε = 0.3) and annealed at 1000°C, but with different strain rates.

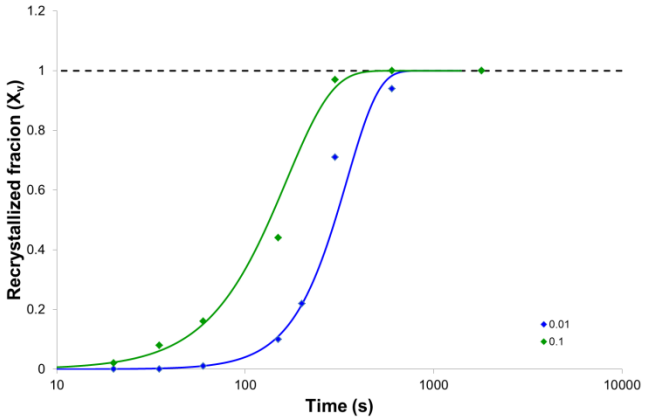

Figure 5.9: *Effect of strain rate on the static recrystallization kinetics in 304L steel deformed at 1000°C to ε = 0.3, strain rates of $\dot{\varepsilon} = 0.01\ s^{-1}$ and $\dot{\varepsilon} = 0.1\ s^{-1}$.*

The recrystallization kinetics is faster when the material is deformed with a higher strain rate, which agrees with the expectations [Humphreys, 2004]. In [Cho, 2001] and [McQueen, 1995], a similar analysis of 304L steel recrystallization behaviour is presented and the results agree with those reported above.

1.5 Recrystallization simulations using a full field formulation

All full field methods developed for grain growth modelling were described in details in chapter 4. In this chapter a brief recall of these methods with their applications in recrystallization simulations is presented.

The first method is the probabilistic Monte-Carlo method (MC). When used to model recrystallization phenomena, this method presented the following disadvantages:

- the linear relationship between the grain boundaries velocity and the stored energy cannot be verified when using the standard form of these approaches;
- the absence of time scale complicates any comparison with experimental data [Rollet, 1997];
- these method principles are only statistically representative, meaning that a large number of simulations need to be done in order to ensure the simulation validity.

The cellular automaton (CA) approach is another probabilistic method, which is usually used to model the primary recrystallization phenomenon [Raabe, 1999]. Several physical rules are used to locally determine the cell propagation in relation to the neighbouring cells, solving the first MC negative aspect. However, this method still presents a few negative points when modelling the recrystallization process:

- at present, there is not an effective CA method to manage new grains nucleation during recrystallization [Rollet, 1997].

In a finite element context, three main methods are developed nowadays: Vertex (VM) Phase Field (PF) and Level-Set (LS). Although the VM method was initially developed for the grain growth modelling [Nagai, 1990], this approach was recently extended to primary recrystallization modelling, taking into account an early nucleation phase [Piekos, 2008a; Piekos, 2008b]. As for the grain growth modelling, topological events are controlled by mesh adaptation rules. As a consequence, the management of topological events (like grains nucleation or grains disappearance) is not always easy. Nowadays, a VM technique taking into account a non-early nucleation phase does not exist.

For the PF method, despite recent developments [Takaki, 2008], modelling the nucleation phase during primary recrystallization, remains an open problem.

In LS methods [Zhao, 1996], [Osher, 1988], [Sussman, 1994], [Merriman, 1994], the grains boundaries are implicitly represented. This method has already been used to model 2D or 3D primary recrystallization, including the nucleation stage [Bernacki, 2008], [Bernacki, 2009], [Loge, 2008]. This method was first briefly described in [Bernacki, 2008] for very simple microstructures. It was then improved to deal with more realistic 2D and 3D microstructures and to make the link with stored energies induced by large plastic deformations [Bernacki, 2009], [Loge, 2008]. As it was already discussed in chapter 4, one of the prominent advantages of level set approaches is that topological changes are automatically taken into account. In the case of primary recrystallization, the introduction of new nuclei during the simulation can be easily done. A simple method to create a nucleation site is to build a new signed distance function at a desired time increment and at a given spatial position. The new distance function can be initialized as the distance to a sphere (3D) or to a circle (2D), centred around one node of the mesh. The signed distance functions of grains intersecting these new nuclei are accordingly modified.

In this chapter, a level set method associated with a finite element formulation is chosen to model recrystallization and grain growth phenomena not only to avoid all the limitations presented by the other methods, but also in order to make an efficient link with the crystal plasticity model discussed in chapters 1 and 3.

2 Finite element model and level set framework

In order to model the recrystallization phenomenon, we must, initially, generate a digital microstructure and a set of nuclei throughout the microstructure. The grains and nuclei are implicitly identified using level set functions and the mesh is adapted around the grain boundaries. All numerical tools are described in details in chapter 2.

2.1 Velocity field expression

The model presented here is an extension of the recrystallization model proposed by [Loge, 2008], [Bernacki, 2009]. This extension includes the capillarity term [Fabiano, 2013] of the grain boundary displacement (Equation 5.2) into the recrystallization model, and was briefly described in [Bernacki, 2011]. The impact of the capillarity term on static recrystallization modelling is one of the aspects which have not been discussed in depth, and for which the literature is relatively quiet.

Considering the global recrystallization model, the grain boundary velocity between two neighbouring grains (G_i and G_j) is defined as the addition of a primary recrystallization term (PR) and a grain growth term (GG):

$$\begin{aligned} &\vec{v}_{ij}(x,t) = \vec{v}_{PR_{ij}}(x,t) + \vec{v}_{GG_i}(x,t) \\ &\vec{v}_{PR_{ij}}(x,t) = M\left(e_j(x,t) - e_i(x,t)\right)\vec{n}_i(x,t), \quad \vec{v}_{GG_i}(x,t) = -M\gamma\kappa_i(x,t)\vec{n}_i(x,t). \end{aligned} \tag{5.5}$$

Until now, as described in chapter 4 by the Equation 4.12 and recalled here with the following Equation 5.6, interfaces motion during recrystallization was modelled using a set of convection-reinitialization equations [Bernacki, 2008], [Bernacki, 2009], [Loge, 2008], [Coupez, 2000]:

$$\begin{cases} \dfrac{\partial \phi_i(x,t)}{\partial t} - \vec{v}_{PR_{ij}}.\nabla\phi_i(x,t) + \lambda s_i\left(\left\|\nabla \phi i(x,t) - 1\right\|\right) = 0 \\ \phi_i(t=0,x) = \phi_i^0(x) \end{cases}, \quad \forall i \in \{1,...,N_G\} \tag{5.6}$$

where $\vec{v}_{PR_{ij}}(x,t)$ was null in chapter 4 and now defined by Equation 5.5. At any time t, the interface Γ_i of grain G_i is implicitly given by the equation $\phi_i(x,t) = 0$. The third term of Equation 5.6 is a reinitialization term necessary to keep the property of the distance function $\left(\|\nabla\phi\| = 1\right)$, which is crucial for the accuracy of the resolution. It is important to highlight that Equation 5.6 is solved, in our formalism, with one single velocity value at each mesh node and a given time t, in order to avoid kinematic incompatibilities due to the convection part of our formulation. Indeed, these incompatibilities would result from Equation 5.5, where $\vec{v}_{PR_{ij}}$ is built according to parameters which are specific to local features (grain G_i and its neighbours). In [Bernacki, 2008], the authors propose instead a velocity expression, denoted

$\vec{v}_{PR}(x,t)$, allowing to use a common global velocity for all grains of the microstructure. This velocity expression is given by:

$$\vec{v}_{PR}(x,t) = \sum_{i=1}^{N_G} \sum_{\substack{j=1 \\ j\neq 1}}^{N_G} \chi_{G_i}(x,t) M \exp(-\alpha |\phi_j(x,t)|)(e_i - e_j)\vec{n}_j(x,t), \tag{5.7}$$

where α is a positive parameter [Bernacki, 2008], $\vec{n}_j(x,t)$ the unit outside normal of grain G_j calculated as the opposite of the function ϕ_j gradient (with the considered sign convention of level-set generation), and $\chi_{G_i}(x,t)$ is the characteristic function of grain G_i. During this Ph.D. thesis, the capillarity term $\vec{v}_{GG_i}$ was introduced into the recrystallization formulation.

As it was discussed in details in chapter 4, the GG term depends on the grains curvature and is treated as a diffusion term in our formalism (see Eqs. 4.8 and 4.9).

Finally, the problem solved in order to model the recrystallization process taking into account the capillarity effects boils down to a convection-diffusion problem:

$$\begin{cases} \dfrac{\partial \phi_i(x,t)}{\partial t} + \vec{v}_{PR}(x,t).\nabla \phi_i(x,t) - \gamma M \Delta \phi_i(x,t) = 0 \\ \phi_i(x,t=0) = \phi_i^0(x) \end{cases}, \forall i \in \{1,...,N_G\}. \tag{5.8}$$

The system is solved for all N_G grains present in domain Ω. Of course, as for pure grain growth problems discussed in the previous chapter, the translation of the capillarity term into a diffusive term is only true if the level set functions satisfy a distance function property $(\|\nabla\phi\| = 1)$ near the boundaries. So, to ensure this condition, a re-initialization treatment must be done at each time step [Osher, 1988]. Moreover the treatment in multiple junctions, detailed in chapter 4 paragraph 3.2, is also performed at each time step.

Finally, a few simulations presented in this chapter were performed using the colouring techniques (chapter 4, paragraph 3.3). The use of this technique in the context of recrystallization is less systematic and more restrictive than for pure grain growth. This is due to the fact that the energy of each container level set function must be assumed homogeneous to be used in Equation 5.7. When this strategy is used, it implies that all the grains of a considered container level-set function have the same stored energy. It will specify for each described simulation if this hypothesis is verified.

2.2 Recrystallization algorithm

Using all the numerical tools presented above and considering the use of the container level-set functions, we propose the following recrystallization algorithm (at each time step):

RX1 – Calculation of $\vec{v}_{PR}(x,t)$ from Equation 5.7 (with a double summation over the container level-set functions).

RX2 – Resolution of system 5.8 for all active container level set functions.

RX3 – Numerical treatment (Equation 4.11, chapter 4) for all active container level set functions.

RX4 – Re-initialization step for all active container level set functions [Osher, 1988], [Coupez, 2000].

RX5 – Deactivation of all container level set functions that are negative all over the domain (meaning that all grains of the considered container level set functions have disappeared).

RX6 –Nucleation criteria: Probabilistic or deterministic rule to choose the new nucleation sites (ignoring the part of the domain that is already recrystallized). A nucleus is assumed circular in 2D (spherical in 3D) and centred around one node of the FE mesh. If at least one nucleation site is activated, the corresponding new signed distance functions are built and the container level-set functions of the existing grains, which have an intersection with these new grains, are modified accordingly. More precisely by denoting, at the considered time step, $\phi(x)$ a container level-set function and $\phi_n(x)$ the level-set function corresponding to the distance to the union of the new nuclei, the modified container level-set function $\phi_m(x)$ is obtained, at each integration point, thanks to the following equation:

$$\phi_m(x) = \min\left(\phi(x), -\phi_n(x)\right). \tag{5.9}$$

RX7 – Re-meshing operation.

Two main remarks:

- when each grain is considered separately (no container level-set functions), the same algorithm is used by replacing the term container level-set function by level-set function,
- the previous algorithm is in fact adapted in the more global context of non site saturated nucleation, which is not considered in the simulations presented in this chapter. Finally, when only site saturated nucleation is considered, the step RX6 can be ignored and the generation of the new grains is performed only at the beginning of the simulation.

3 Results

3.1 Academic Test - Circular grain case

Analysing the grain boundary motion equation (Equation 5.2) we observe that a competition between the two driving forces (driving force due to internal energy gradients, $M\Delta E\vec{n}$, and driving force due to grain boundary capillarity effects, $M\gamma\kappa\vec{n}$) can take place during the recrystallization process.

A first simple test case was performed in order to verify if the recrystallization algorithm correctly describes the grain boundary motion when the two driving forces are taken into account. To do so, we have considered a grain embedded in a media where the capillarity effect promotes the grain shrinking while the internal energy difference promotes the grain growth. The domain size is 1 mm x 1 mm and an *a priori* remeshing technique is used to adapt the mesh around the grain boundary. The initial grain radius is set to 0.2 mm and the grain is centred in the middle of the domain. The mesh size outside the adapted zone is 10 µm. In the adapted zone, the mesh size in the direction perpendicular to the grain interface is 2 µm, and 10 µm in the tangential direction. The number of elements at the simulation beginning is 40300. Both grain boundary mobility and energy are considered isotropic and equal to one. Finally, an internal energy difference between the circular grain and the domain is imposed. Six different values of internal energy difference are tested: 2, 3, 4, 5, 6 and 7 J/mm². Figure 5.10 illustrates the test scheme and table 5.3 sums up all tested

cases. In Figure 5.10 the black arrows represent the grain boundary motion due to internal energy difference, while the orange arrows represent the grain boundary motion due to the grain capillarity forces.

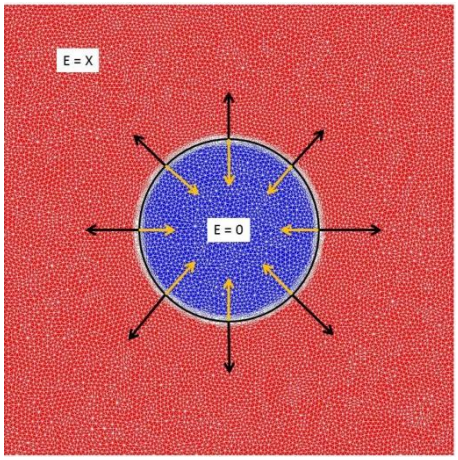

Figure 5.10: *Circular grain case scheme. The black arrows represent the grain boundary motion due to internal energy difference while the orange arrows represent the grain boundary motion due to the grain capillarity forces. White lines represent the mesh used.*

Table 5.3: *Internal energy difference values tested.*

	ΔEnergy (J/mm²)
Case 1	2
Case 2	3
Case 3	4
Case 4	5
Case 5	6
Case 6	7

Knowing that the initial grain radius is set to 0.2 mm, the initial grain curvature is equal to 5 mm^{-1}. As a consequence, for cases 1, 2 and 3 we expect that the circular grain will shrink with different shrinking rates. For test case 4, the grain will remain unchanged and, finally, for test cases 5 and 6, we expect the grain to grow, with different growing rates. As for the configuration of the shrinking of one circular grain by pure capillarity grain growth considered in the previous chapter, the problem could be summarized as a simple differential equation in time for the circle radius, but here without analytical solution. In order to compare the 2D-FE predictions with a theoretical radius value, the following first-order scheme, explicit in time, was used:

$$R^{t+\Delta t} = R^t + \Delta t\left(\Delta E - \frac{1}{R^t}\right), \tag{5.10}$$

where $R^{t+\Delta t}$ and R^t are, respectively, the grain radius at $t+\Delta t$ and t, ΔE is the internal energy difference and Δt is the time step. Figure 5.11 illustrates the kinetics curves for all the tested cases. Concerning the radius of the FE simulations, it was obtained, at each time step, as an average of the distance of positions of the grain interface to the centre of the domain (each position being separated by an angle of 45°).

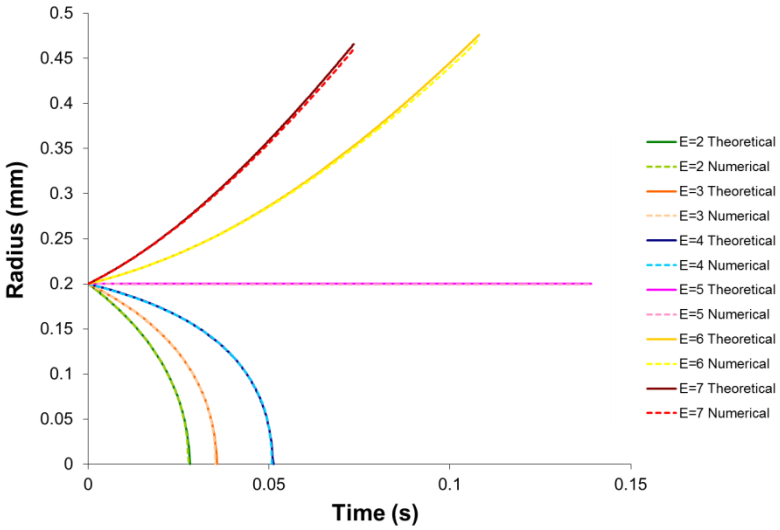

Figure 5.11: *Comparison between numerical and theoretical result for the static recrystallization of a circular grain embedded in an infinite medium.*

For all test cases, the model correctly simulates the behaviour of the circular grain. L2 errors on the radius prediction remain smaller than 2% (table 5.4).

Table 5.4: *L2 errors for the six circular grains test cases.*

	ΔEnergy (J/mm²)	L2 Error (%)
Case 1	2	1,6
Case 2	3	1,4
Case 3	4	0,9
Case 4	5	0,2
Case 5	6	0,8
Case 6	7	0,9

These results illustrate that the diffusive-convective approach developed here can represent with a very good accuracy the grain motion kinetics resulting from the competition between two driving forces: internal energy difference and grain boundary curvature.

3.2 Academic Test – 2 grains case

The second test case corresponds to a bicrystal recrystallization. Once again, the grain boundary mobility and energy are isotropic and equal to one. An energy difference is imposed between the two grains. The domain size is 1 mm x 1 mm and an *a priori* remeshing technique is used to adapt the mesh around the grain boundary with the same features as those described for the previous test case. The number of elements at the simulation beginning is 12,300. Figure 5.12 illustrates this second test case setup.

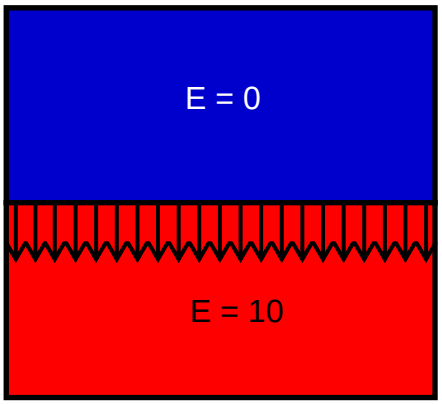

Figure 5.12: *Bicrystal test case: the black vectors correspond to the recrystallization velocity at the grain interface.*

The internal energy of the blue grain is null while the internal energy of the red grain is 10 J/mm². As a consequence, the grain boundary will move towards the red grain and the blue grain will grow while the red grain will shrink. Since the grain boundary is flat, the grain boundary curvature is equal to zero: only the internal energy difference will drive the grain boundary motion, and the grain boundary will remain flat. Figure 5.13 describes the grain boundary motion obtained by solving the system 5.6.

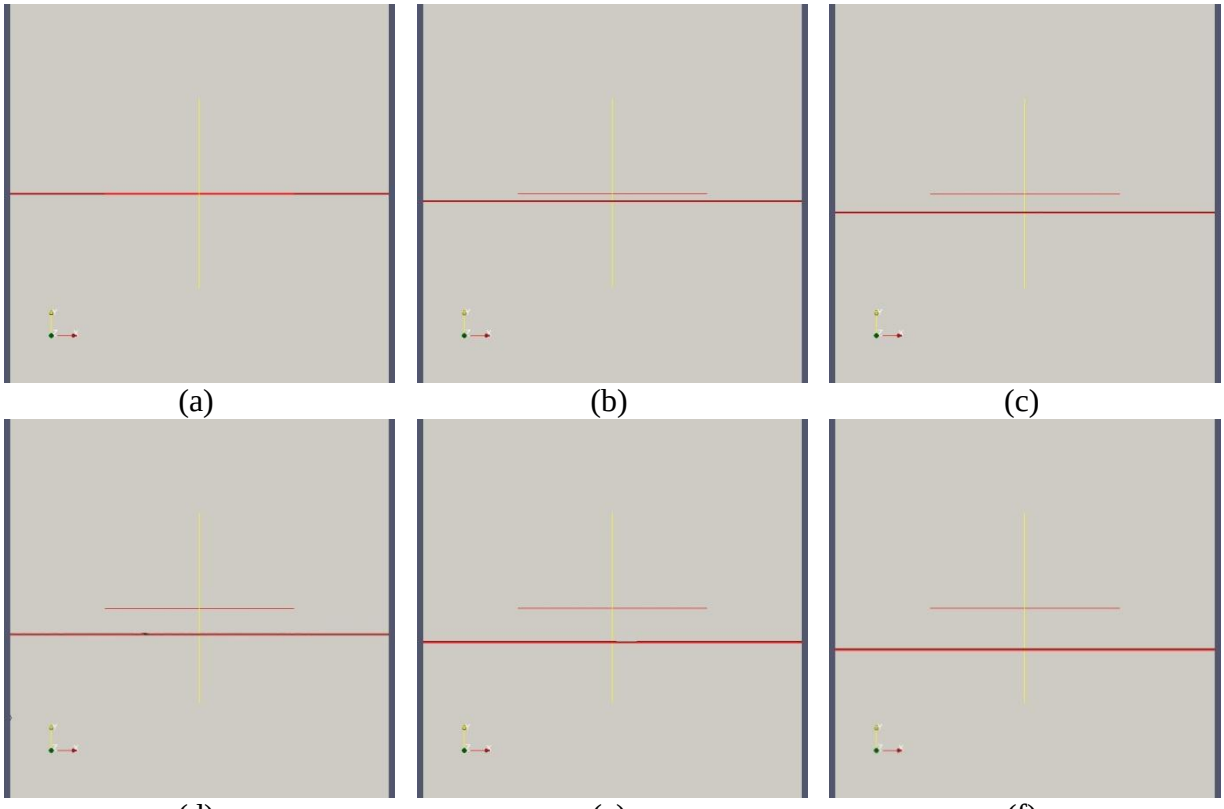

Figure 5.13: *Bicrystal test results. The black line represents the numerical result while the red line corresponds to the theoretical result. (a) t = 0 s ; (b) t = 2 ms ; (c) t = 4 ms ; (d) t = 6 ms ; (e) t = 8 ms and (f) t = 10 ms.*

Errors between the numerical and theoretical results are smaller than 3% for all cases (obtained by the comparison of the theoretical vertical position of the grain interface with an average of the vertical coordinates of ten positions of the simulated grain interface). One can conclude that the convective-diffusive approach associated with an anisotropic mesh adaptation allows here an accurate simulation of the static recrystallization phenomenon.

3.3 Polycrystalline 2D simulation

Usually, when modelling the recrystallization phenomena, the capillarity effects are not taken into account and only the internal energy difference is considered [Montheillet, 2009], [Bernacki, 2009]. So, the first interesting point to test with our modelling methodology is whether or not this assumption is valid. In other words, we want to estimate the impact of the capillarity term on the recrystallization kinetics and on the microstructure after total recrystallization. Simulations with random nucleation sites and with necklace-type nucleation are studied, and are restricted for the moment to 2D configurations. For all tested cases, grain boundary mobility and energy were considered isotropic throughout the domain and are equal to, respectively, 5.08 10^{-13} $m^4/(J.s)$ and 0.6 J/m^2. These values correspond to 304L steel data at 1000°C.

3.3.1 Random nucleation sites

In this first recrystallization test, 636 randomly distributed nuclei are generated in a polycrystal with 76 grains. The energy difference between the matrix and the nuclei is homogeneous throughout the domain and it is equal to 2.18 10^{-4} J/mm^2. In this case, the colouring technique was used separately for the initial unrecrystallized grains and for the initial nuclei. Indeed, as initial unrecrystallized grains are assumed to have the same stored energy, the graph colouring technique can be used without any difficulty. The same procedure is used for the initial nuclei (which share the same null energy). Finally, the initial "unrecrystallized grain - container level-set functions", modified thanks to Eq. (5.9) in order to take into account the presence of the nuclei, are concatenated with the "nuclei - container level-set functions" to generate the initial set of container level-set functions used for the simulation. It must be noticed that for the nuclei, the colouring technique is applied to the Delaunay triangulation of the sites formed by the centres of the nuclei, in contrast with the initial unrecrystallized grains where the Delaunay triangulation is performed with the Laguerre-Voronoï sites. Figure 5.14 illustrates a comparison of the microstructure evolution, as a function of time, between recrystallization simulations with and without capillarity effects. The graph in Figure 5.15 presents a kinetics comparison of these two cases and also the Avrami exponent analysis.

Time (s)	**ReX with capillarity effects**	**ReX without capillarity effects**
0	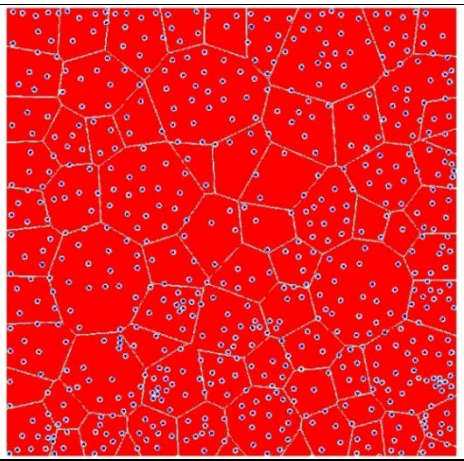	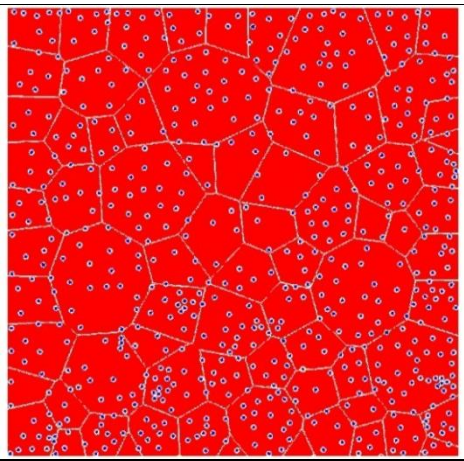
	Recrystallized fraction: 5%	Recrystallized fraction: 5%

50	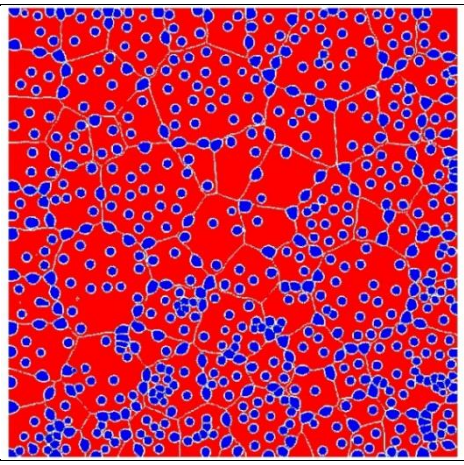	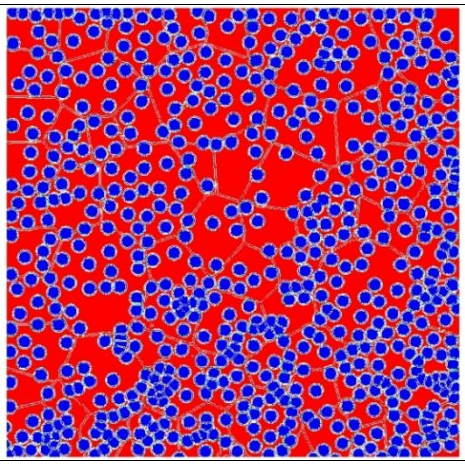
	Recrystallized fraction: 26%	Recrystallized fraction: 42%
100	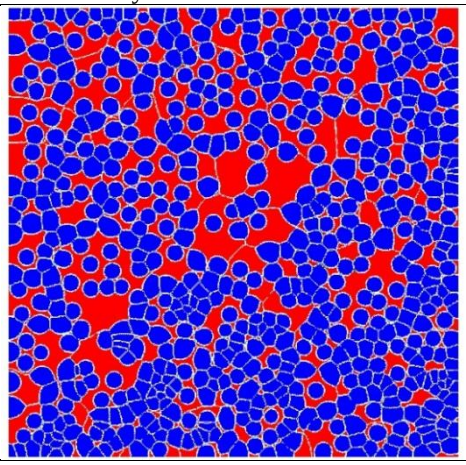	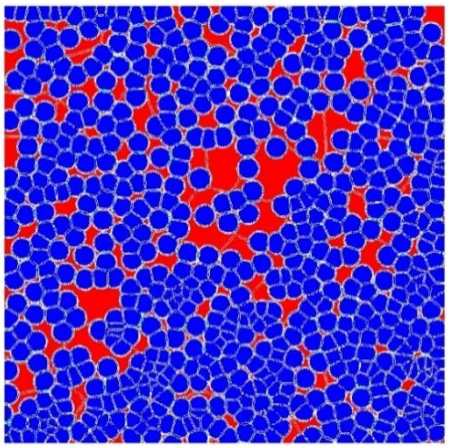
	Recrystallized fraction: 69%	Recrystallized fraction: 80%
250	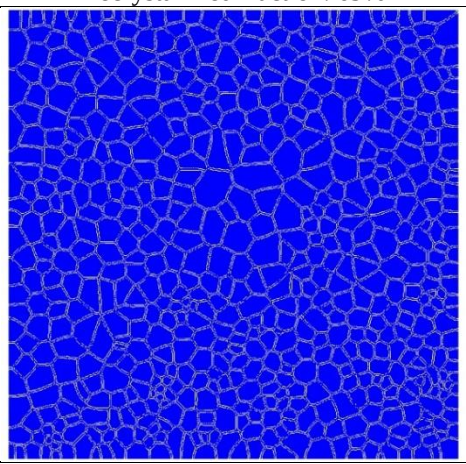	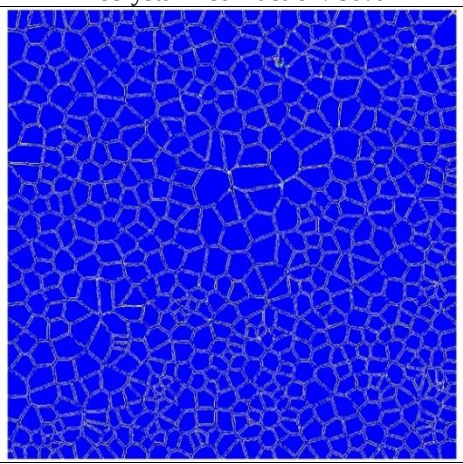
	Recrystallized fraction: 100%	Recrystallized fraction: 100%

Figure 5.14: *Microstructure evolution comparison, in function of time, between the recrystallization simulation with capillarity effects and without capillarity effects (304L, T= 1000°C)*

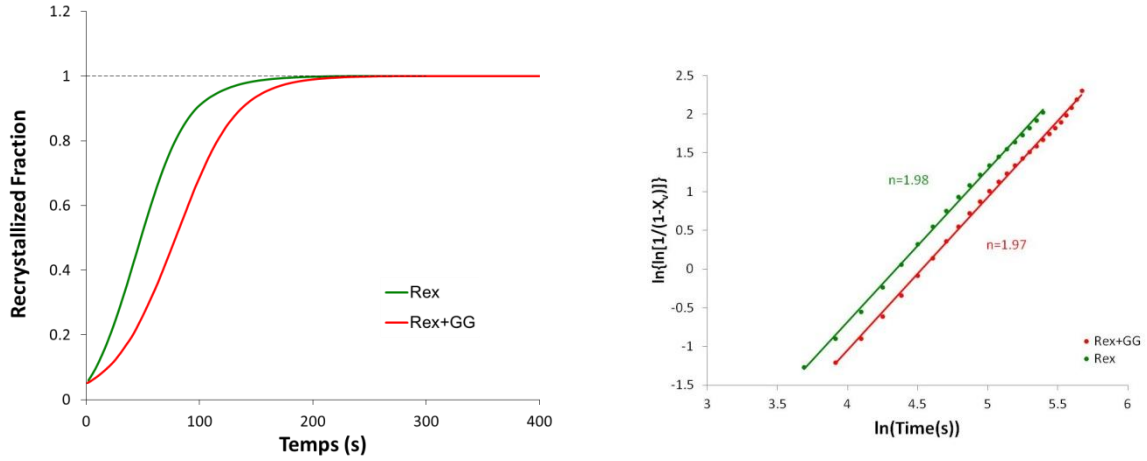

(a) (b)

Figure 5.15: *Recrystallization kinetics comparison between a case taking into account the capillarity effects (red line) and another case that do not take into account the capillarity effects (green line).*

Comparing the kinetics of both cases (Figure 5.15.a) we observe that, at the beginning of recrystallization, the kinetics of the simulation which does take into account the capillarity effects is slower than the one which does not. This is a consequence of the competition held between the two types of driving forces, as discussed in paragraph 3.1.

Analysing a zoom of the microstructure for t = 40 s (Figure 5.16), few differences can be observed between the two simulations.

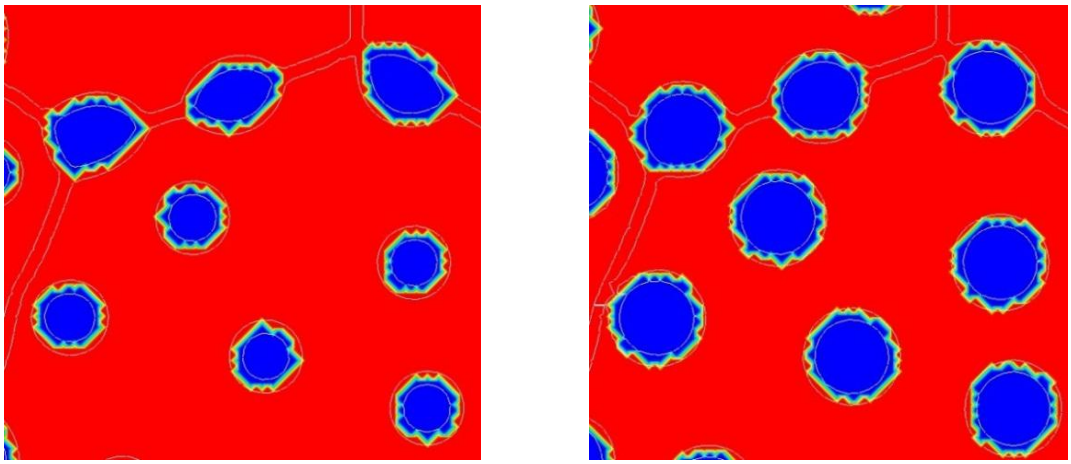

(a) (b)

Figure 5.16: *Zoom of the microstructure for t = 40s: (a) simulation with capillarity effects, (b) simulation without capillarity effects.*

Considering the nuclei within the grains in Fig. 5.16, we observe that capillarity effects reduce their size. As we discussed above, this difference is again a consequence of the competition between the two types of driving forces.

Looking now at the nuclei localized on the grain boundaries, we observe a difference between the two cases concerning their shape. Capillarity effects lead to nuclei which are no longer circular, but ovalized. This is a consequence of the equilibrium angle of 120° at a triple junction (Figure 5.17) [Bernacki, 2009], [Humphreys, 2004].

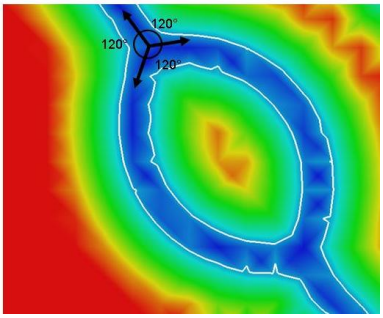

Figure 5.17: *A triple junction for a nucleus on a grain boundary - equilibrium contact angle of 120°.*

The competition between the two driving forces is more apparent for small nuclei as their curvature is high. When the nuclei become larger, the capillarity forces are reduced, but the rate at which recrystallization progresses remains different from the case where capillarity forces are ignored (see Fig. 5.15). In the end, however, both simulations reach 100% of recrystallization almost at the same time, due to an asymptotic behaviour which appears to be faster when including capillarity.

Analysing a zoom of the microstructure for t = 250s (Figure 5.18), we observe that generally the microstructures obtained in the two simulations are very similar. A difference comes from the existence of equilibrium angles at multiple junctions when introducing capillarity, but in the presence of stored energy forces, these equilibrium angles may not be satisfied completely during recrystallization (Fig. 5.14). At the end of recrystallization, we still find a few quadruple junctions, or grains with only 3 or 4 faces (Figure 5.18), but these features disappear progressively with increasing annealing time, which is not the case when only stored energy forces act on the microstructure.

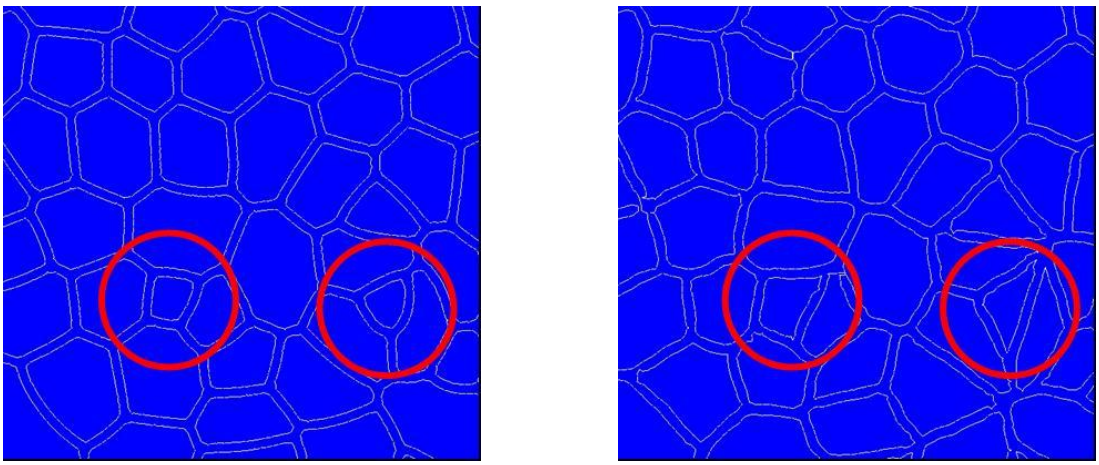

(a) (b)

Figure 5.18: *Zoom of the microstructure for t = 250s. (a) Simulation with capillarity effects, (b) simulation without capillarity effects.*

Concerning results of Fig 5.15(b), they are in agreement with the JMAK model (see Eq. 5.3) as the function $\ln\{\ln[1/(1-X_v)]\}$ is a linear function of $\ln(t)$ for both cases. Moreover the Avrami exponent obtained for both cases is very close of its theoretical value of 2 for this topological configuration (site saturated nucleation with a growth dimensionality equal to 2 as the nucleation is random, see Table 5.2).

As a conclusion, for randomly distributed nuclei, taking into account the grain curvature changes the shape of the recrystallization kinetics curve but does not change significantly the time needed to fully recrystallize the material. Ignoring capillarity effects lead to multiple

junctions which do not form 120° equilibrium angles, and the corresponding microstructures are therefore not very realistic.

3.3.2 Necklace-type nucleation sites

It is widely recognized that the nucleation sites in recrystallization are non-randomly distributed. They are often located in the grain boundaries areas. So, to verify the influence of the grain curvature on the recrystallization kinetics, 1236 nuclei distributed along the grain boundaries were generated in a polycrystal with 100 grains. Once again, the energy difference between the matrix and the nuclei is homogeneous throughout the domain and it is equal to 2.18 10^{-4} J/mm^2. The same strategy used in the previous test case concerning the unrecrystallized grains and nuclei colouring can be used. Figure 5.19 illustrates a comparison of the microstructure evolution, as a function of time, between the recrystallization simulation with capillarity effects and without capillarity effects. The graph in Figure 5.20.a presents a kinetics comparison of between the two cases, and Figure 5.20.b describes the Avrami exponents for both simulations.

Time (s)	**ReX with capillarity effects**	**ReX without capillarity effects**
0	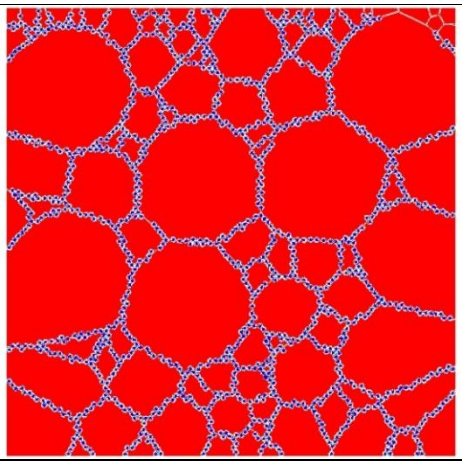	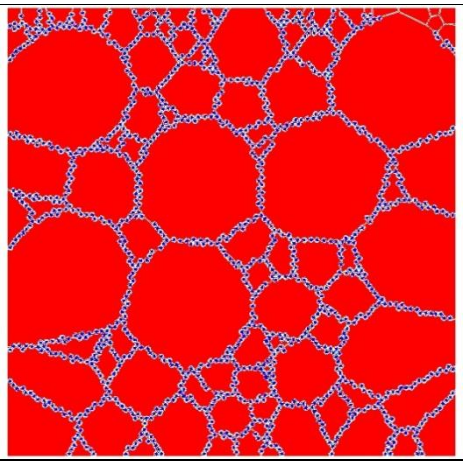
	Recrystallized fraction: 10%	Recrystallized fraction: 10%
50	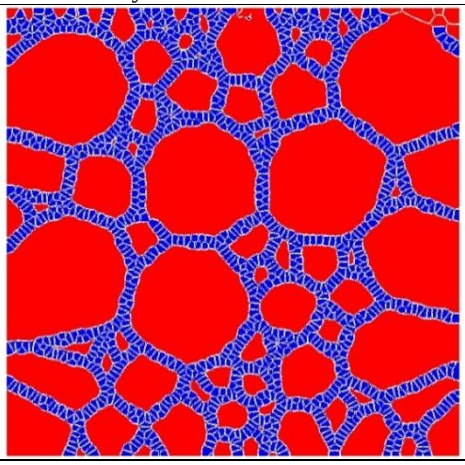	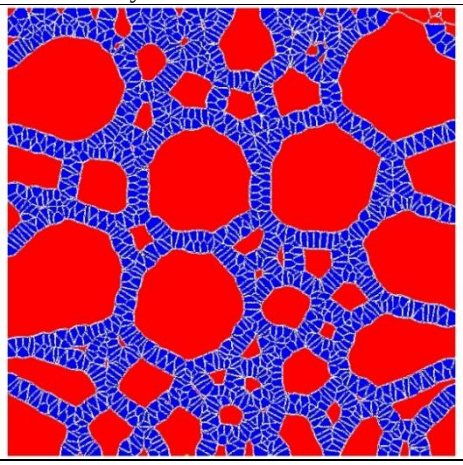
	Recrystallized fraction: 33%	Recrystallized fraction: 46%

150	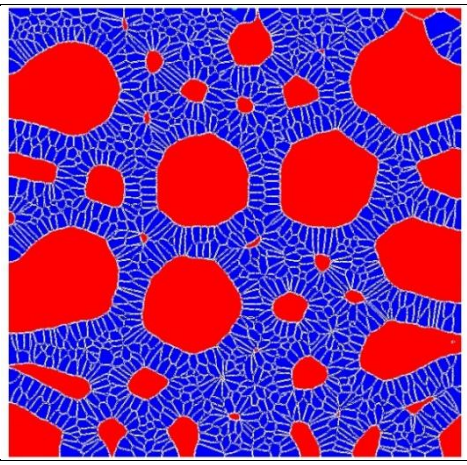	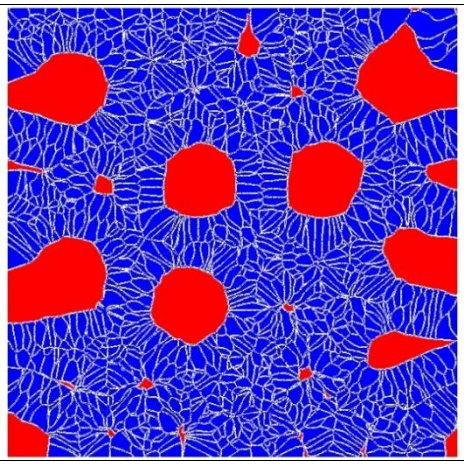
	Recrystallized fraction: 62%	Recrystallized fraction: 79%
400	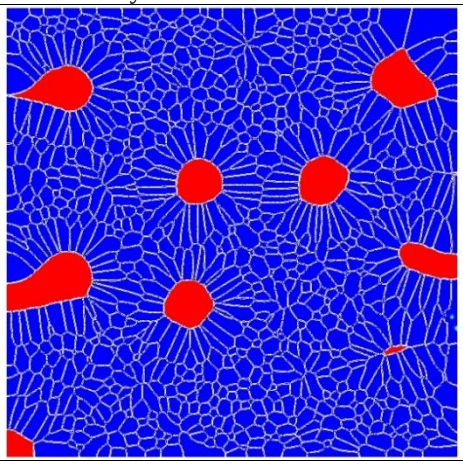	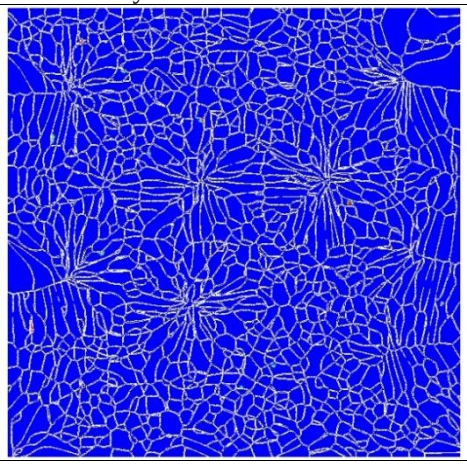
	Recrystallized fraction: 93%	Recrystallized fraction: 100%
650	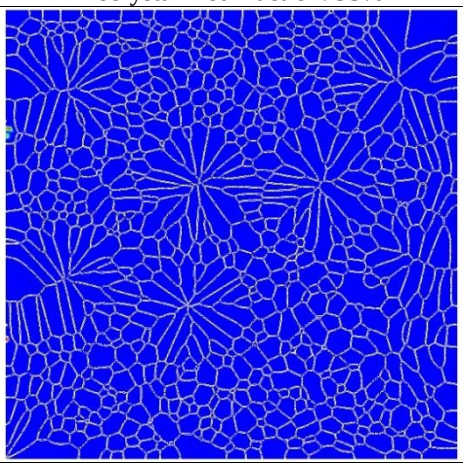	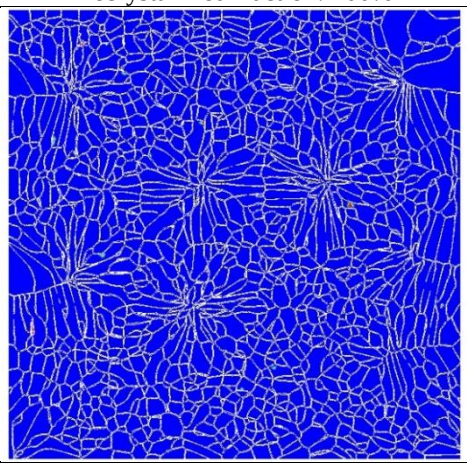
	Recrystallized fraction: 100%	Recrystallized fraction: 100%

Figure 5.19: *Microstructure evolution comparison, as a function of time, between the recrystallization simulation with and without capillarity effects.*

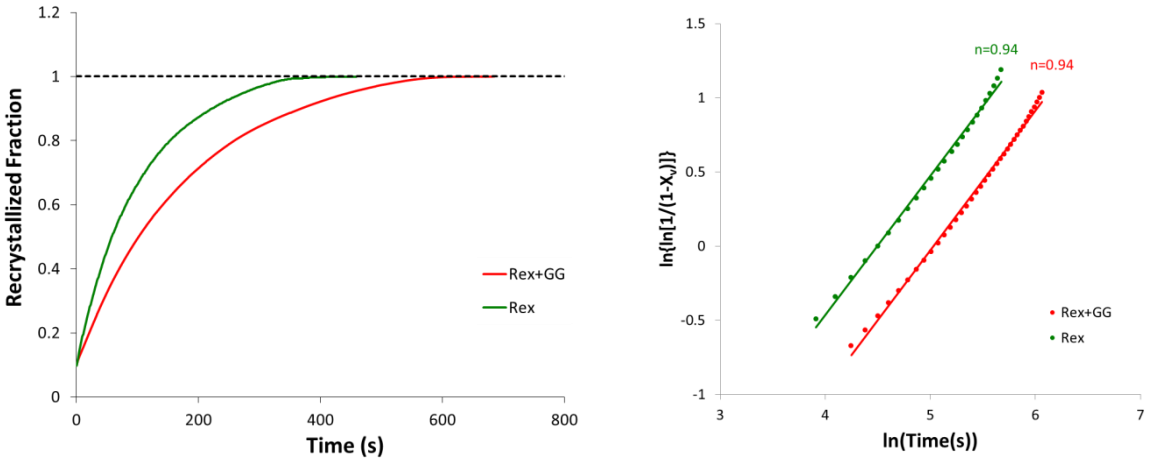

(a) (b)

Figure 5.20: *Recrystallization kinetics comparison between a case with capillarity effects (red line) and another case without the capillarity effects (green line).*

From Figures 5.19 and 5.20 we see that the effects of the grain curvature on the recrystallization kinetics and geometry are more important than in the first case (with randomly distributed nucleation sites). Here, when the capillarity effects are not taken into account, total recrystallization is reached after about 400 seconds. When the capillarity effects are introduced, total recrystallization is reached after 600 seconds. This is a consequence, once again, of the competition between the driving forces.

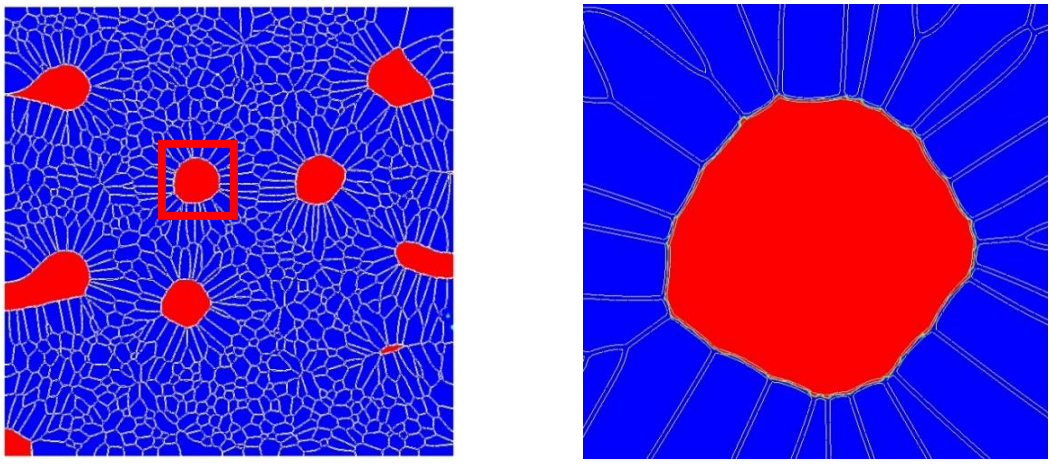

(a) (b)

Figure 5.21: *Microstructure after 400s when taking into account the capillarity effects: (a) general view and zoom of an area with unrecrystallized and recrystallized grains.*

In Figure 5.21, we observe that the local radii of recrystallized grains are small as a consequence of the initial position of the nuclei. Therefore, the capillarity effects cannot be neglected and they continue to be significant during all the recrystallization process.

Interestingly, as expected for this topological configuration (site saturated nucleation with a growth dimensionality equal to 1 due to the necklace-type configuration), both simulations present an Avrami exponent around 1 (see Fig. 5.20b). In comparison to the previous test case, the capillarity effects here seem to affect only the coefficient *B* of Eq. 5.3, but not the Avrami exponent.

Looking at microstructures in the fully recrystallized state (Figure 5.22), we observe again the issue on the triple junction equilibrium angle of 120°. This leads to very unrealistic shapes, as those highlighted with the red squares in Fig. 5.22b.

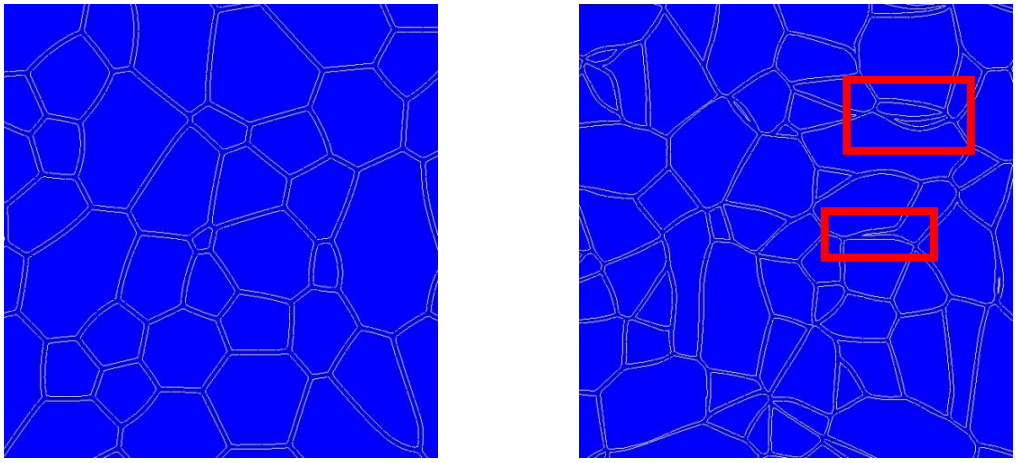

(a) (b)

Figure 5.22: *Zoom of the microstructure for 100% recrystallization fraction: (a) simulation with capillarity effects, (b) simulation without capillarity effects. The red squares highlight grains with unrealistic shape obtained when capillarity effects are not taken into account.*

As a conclusion, for necklace-type nucleation, taking into account the grain curvature affects both the recrystallization kinetics and the fully recrystallized microstructure. Neglecting capillarity effects not only results in non equilibrium angles at triple junctions, but also to very unrealistic grain shapes.

In order to study this competition between the grain curvature and the internal energy gradients in more details, we carried out five different tests. In all cases we have the same initial distribution as for the previous necklace-type configuration. The grain boundary mobility and grain boundary energy are the same for all cases. Stored energy is assumed to be constant in the recrystallized part (equal to 0 J/mm^2), and also in the unrecrystallized part. The internal energy value for the unrecrystallized part is changed from one test to another, as shown in Table 5.5.

Table 5.5: *Tests performed in order to study the competition between the internal energy gradient and the curvature effects in the recrystallization phenomenon for a necklace-type site saturated nucleation.*

	ΔEnergy (J/mm²)	γ (J/mm)	ΔEnergy/ γ (mm^{-1})
1	2.18 10^{-4}	6.0 10^{-7}	362.8
2	4.40 10^{-4}	6.0 10^{-7}	733.3
3	6.60 10^{-4}	6.0 10^{-7}	1100
4	8.80 10^{-4}	6.0 10^{-7}	1466.7
5	11.0 10^{-4}	6.0 10^{-7}	1833.3

For all cases we simulate the recrystallization with and without the capillarity effects. Figure 5.23 describes all the recrystallization kinetics curves obtained and Figure 5.24 presents the corresponding L2 “errors” (or difference) between the simulations with and without the capillarity effect.

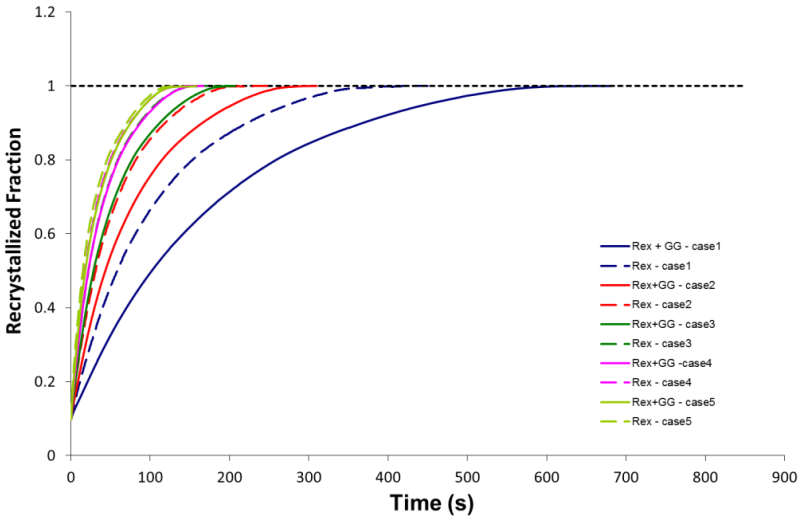

(a)

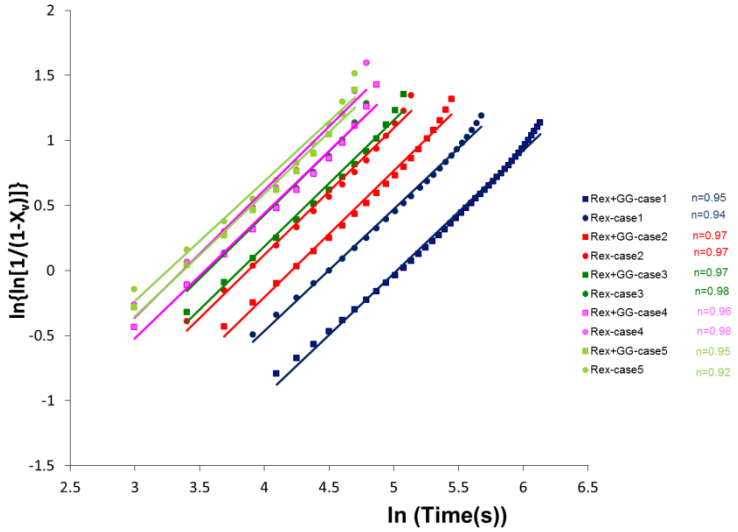

(b)

Figure 5.23: *(a) Recrystallization kinetics comparison between a case taking into account the capillarity effects (Rex+GG continuous lines) and another case that does not take into account the capillarity effects (Rex - dashed lines). (b) Avrami exponent analysis for all tested cases.*

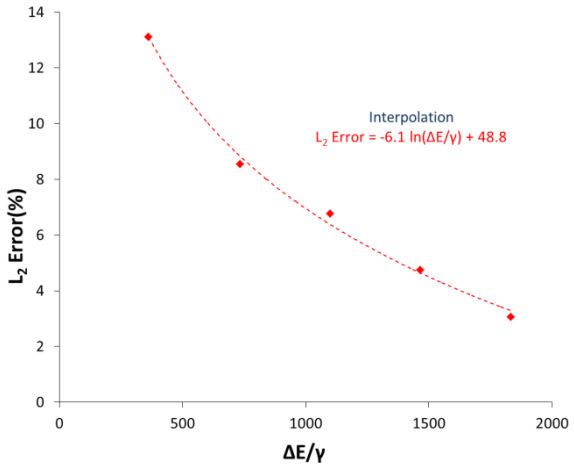

Figure 5.24: *Error between the recrystallization kinetics curves obtained with and without the capillarity effect for the 5 studied cases.*

In Figures 5.23.a and 5.24, it is interesting to observe that the impact of the grain curvature effects decreases when the ratio $\Delta E/\gamma$ increases and that the L2 error converges toward zero. Based on these results we can estimate how the capillarity forces will affect the recrystallization kinetics. Also, for any $\Delta E/\gamma$, we have confirmed that the capillarity effects changes only the coefficient *B* of Eq. 5.3, but not the Avrami exponent (Figure 5.23.b) in the considered necklace-type sites saturated nucleation.

The next step for the static recrystallization simulation consists in coupling the crystal plasticity simulation results to the recrystallization simulation. This is the topic of the next section.

4 Coupling crystal plasticity and static recrystallization

After analysing the influence of the capillarity effects on static recrystallization phenomena, the recrystallization algorithm is now coupled to the crystal plasticity model. A 100-grain digital microstructure is subjected to a plane strain compression up to $\varepsilon = 0.3$. For this deformation level, the appearance of new grains has not started. So, only static recrystallization is simulated. The calculated dislocation density distribution is used to define a set of potential nucleation sites. Then, the dislocation density average of each grain is computed in order to calculate the grain boundary motion rate (Equation 5.7). In the next sections, the definition of the nucleation sites is explained. Finally, the obtained numerical results are compared to the available experimental results.

4.1 Critical dislocation density and nucleus radius

Static recrystallization may occur when a deformed material is subsequently annealed. In [Kerisit, 2012], the critical dislocation density for static recrystallization is identified based on experimental tests. These experimental tests correspond to mechanical tests followed by an annealing treatment. However, a large number of tests, with different strain rates at different annealing temperatures need to be performed in order to correctly estimate the critical dislocation density needed to trigger recrystallization, after a given time.

In this current work, we use the same equations used as those found in the numerical model proposed in [Huang, 2011]. The framework of this model is the same as that of the dynamic recrystallization (DRX) mean field model, with however some modifications due to the different nature of static recrystallization (SRX) as compared to DRX.

For the DRX model, the critical dislocation density depends on deformation conditions (temperature and strain rate), and can be determined from the energy changes in relation to the formation of a nucleus on a pre-existing grain boundary. In [Sandstrom, 1975], the authors proposed a semi-quantitative approach by assuming that DRX is only possible when the rate of boundary migration of the potential nucleus is high in relation to the rate of reaccumulation of dislocations behind it. Following their model, [Roberts, 1978] further analysed the critical condition for DRX. Based on the results presented in [Roberts, 1978], the following Equation 5.11 is proposed, using parameters of the mean field model developed in [Huang, 2011], to calculate the critical dislocation density value for nucleation in dynamic recrystallization:

$$\rho_{cr}^{DRX} = \left(\frac{20.K_1.\gamma.\dot{\varepsilon}}{3.K_3.\tau} \right)^{\frac{1}{3}}, \tag{5.11}$$

where τ is the dislocation line energy and $K_3 = M\tau$. It is observed from Equation 5.11 that ρ_{cr}^{DRX} is indirectly influenced by temperature and strain rate through the parameters K_1 and K_3. As it was discussed in chapter 3 (Yoshie-Laasraoui-Jonas equation), K_1 is a material parameter representing the material hardening. Temperature variation of ρ_{cr}^{DRX} is mainly dictated by K_3 through the temperature dependence of M (Equation 4.2, chapter 4). The influence of strain rate is incorporated only by the variations of K_1. In general, Equation 5.11 expresses that the critical dislocation density increases with decreasing temperature and increasing strain rate, which is physically justified.

However, the critical dislocation density obtained using Equation 5.11 neglects the material recovery. So, in order to take it into account, ρ_{cr}^{DRX} is finally defined as a solution of the following equation:

$$\rho_{cr}^{DRX} = \left[\frac{-2\gamma\dot{\varepsilon}\dfrac{K_2}{K_3\tau}}{\ln\left(1-\dfrac{K_2}{K_1}\rho_{cr}^{DRX}\right)} \right]^{\frac{1}{2}}, \tag{5.12}$$

where K_2 is a material parameter representing the material recovery (as it was discussed in details in chapter 3 - Yoshie-Laasraoui-Jonas equation). The initial guess value of ρ_{cr}^{DRX} is obtained directly from Equation 5.11 and iterative calculation by Equation 5.12 leads to a converged value of ρ_{cr}^{DRX} which is then used in the model.

In the current work, the critical dislocation density for static recrystallization process, ρ_{cr}^{SRX} , is related to the ρ_{cr}^{DRX} using the following equation:

$$\rho_{cr}^{SRX} = \xi.\rho_{cr}^{DRX}, \tag{5.13}$$

where ξ is a constant chosen equal to 0.3 according to the analysis presented in [Huang, 2011].

A nucleus becomes viable when its radius reaches a critical value R_{cr}^{SRX} . This corresponds to the condition when the stored energy of the material is large enough to overcome the capillarity force of the nucleus, so we have:

$$\rho_{cr}^{SRX}.\tau = \frac{2\gamma}{R_{cr}^{SRX}} \text{ i.e. } R_{cr}^{SRX} = \frac{2\gamma}{\rho_{cr}^{SRX}.\tau}. \tag{5.14}$$

To overcome the problem that a nucleus may shrink soon after its creation, all the nuclei created in the REV have a radius bigger than R_{cr}^{SRX} , thereby ensuring that a created nucleus has the needed driving force to grow.

4.2 Number of nucleation sites

It is assumed that new grains appear in areas where the dislocation density is greater than a critical value ρ_{cr} . As a consequence, in the mean field theory, the nucleation of new

grains will happen in grains presenting a dislocation density value higher than the critical dislocation density. Since the nucleation rate is difficult to evaluate experimentally [Humphreys, 2004], it is presumed that a certain percentage per unit time of the potential nucleating sites actually nucleates. If nucleation happens in the bulk, the number of potential nucleating sites N_p will be proportional to the total volume of grains with a dislocation density higher than ρ_{cr}^{SRX}. If nucleation happens mainly at grain boundaries, the total surface of the same grains will be considered instead of the volume. In the general situation, the number of potential nucleation sites N_p is therefore written as

$$N_p = \sum_{\rho_i > \rho_{cr}} N_{pi} \propto \sum_{\rho_i > \rho_{cr}} R_i^q \,, \tag{5.15}$$

where q = 2 in case of necklace-type nucleation and q = 3 in case of bulk nucleation. R_i is the grain radius of the i^{th} grain family presenting a dislocation density value higher than the critical dislocation density. Based on experimental 304L analysis [Huang, 2011], we observe that, during static recrystallization, the 304L steel new grains appear near the grain boundaries, like a necklace-type nucleation. So, the value q = 2 is chosen. Equation 5.16 is then applied to each representative grain presenting a dislocation density value higher than the critical dislocation density in order to determine the number of nucleation sites:

$$N_{i,nucl} = K_g S_{cr} \frac{N_i r_i^q \left(\rho_i - \rho_{cr}\right)^{bg}}{\sum_{\rho_k > \rho_{cr}} N_k r_k^q \left(\rho_k - \rho_{cr}\right)^{bg}} \,. \tag{5.16}$$

where bg is a constant which is chosen to be 3, as found in [Montheillet, 2009], and $K_g = K_g(T, \dot{\varepsilon})$ a probability constant depending on the processing conditions, S_{cr} the total surface area of grains with $\rho > \rho_{cr}$, and N_k the number of grains composing the k^{th} family of grains. All nuclei are assumed to start with the same initial radius R_{cr}^{SRX}. The K_g value used in this work was identified by [Huang, 2011].

4.3 Coupling with crystal plasticity results

Previous equations allow evaluating the critical dislocation density and the volume of new grains appearing during the static recrystallization process. The next step is then to couple the static recrystallization simulations to the crystal plasticity results. As it was discussed in chapter 3, in this work, two different hardening models have been studied: the first one considering the material total dislocation density, and a second one considering two dislocations types: statistically stored dislocations (SSD) and geometrically necessary dislocations (GND). In this paragraph, the analysis of nucleation sites is done for both hardening models and the influence of the results on the recrystallization kinetics is presented. For both cases the applied deformation is 0.3 and the annealing treatment temperature is 1000°C (still referring to 304L steel).

Initially, the critical dislocation density for the mean field model and the number of new grains are calculated. Using the parameters presented on table 5.6 (for confidentiality, the parameters are presented as letters) the critical dislocation density calculated using Equations 5.11, 5.12 and 5.13 is equal to 1.6 10^{14} m^{-2} and the number of grains to be generated, calculated using Equation 5.16, is 2060.

Table 5.6: *304L steel parameters.*

K_1 (m^{-2})	A
K_2	B
K_3	C
K_g	D
τ (J/m)	E
$\dot{\varepsilon}$ (ms^{-1})	1

It is important to highlight that the critical dislocation density calculated with Equations 5.11, 5.12 and 5.13 are valid for the mean field models. The value needs to be adapted to the mesoscopic scale, based on the crystal plasticity formulation. As it was discussed in details in chapter 3, it is possible to assume that the dislocation density, at any point of the grain is defined with the following equation:

$$\rho\left(\phi(x)/<R>,\varepsilon\right)=\beta\left(\phi(x)/<R>,\varepsilon\right)<\rho>\left(\varepsilon\right), \tag{5.17}$$

where $<\rho>(\varepsilon)$ is the mean dislocation density in the RVE and $\beta\left(\phi(x)/<R>,\varepsilon\right)$ a function of the deformation and of the distance to the closest grain boundary normalized by $<R>$, the polycrystal mean grain size. This function is described in Fig. 5.25 for ε = 0.3 with and without the introduction of GNDs.

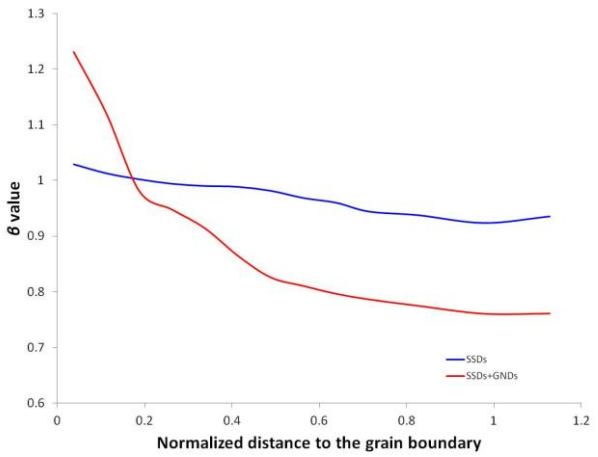

Figure 5.25: *304L steel β function as a function of the normalized distance to the grain boundary for ε = 0.3 at T = 1000°C.*

Knowing that for the 304L steel, nucleation takes place mainly near the grain boundaries, we can calculate the mesoscopic critical dislocation density using Equation 5.17 from the knowledge of the β function at the grain boundary. Based on Figure 5.26, we obtain $\beta_{SSD}(0,0.3)=1.03$ and $\beta_{SSD+GND}(0,0.3)=1.22$. Using Equation 5.17 and both β values, we find $\rho_{cr}^{SSD}(0.3)=1.65\,10^{14}\,\mathrm{m}^{-2}$ and $\rho_{cr}^{GND}(0.3)=1.95\,10^{14}\,\mathrm{m}^{-2}$. To choose the nucleation sites in the mesoscopic simulation, we choose only the nodes presenting a dislocation density higher than these values. Figure 5.26 presents the dislocation density dispersion for the two hardening models, together with the mean field critical dislocation density and the mesoscopic critical dislocation density.

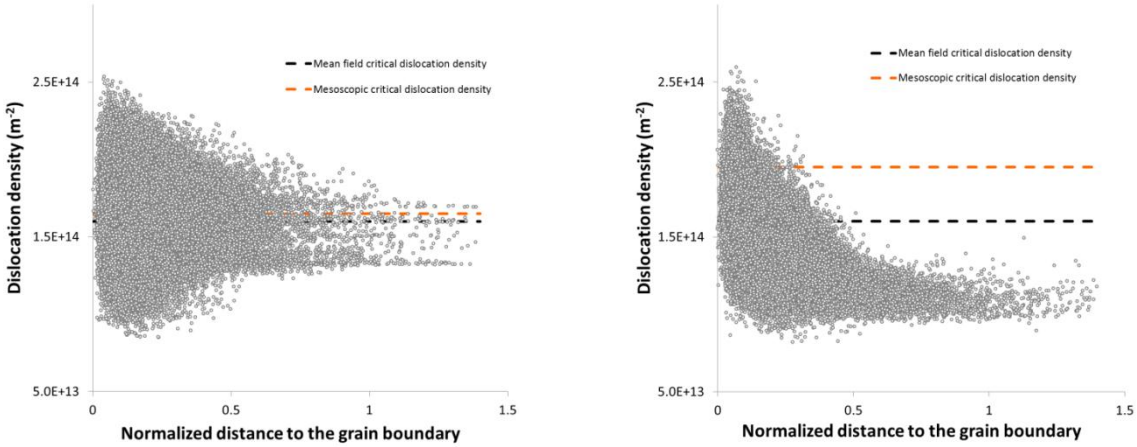

(a) SSD (b) SSD+GND

Figure 5.26: *Dislocation density dispersion compared to the mean field and mesoscale critical dislocation densities.*

The number and distribution of possible new nucleation sites based on the crystal plasticity simulations results are different for the two hardening models. Considering only the SSDs dislocations (Figure 5.26.a), the possible nucleation sites are found all over the material and not only near the grain boundary. Also, half of the material shows a dislocation density higher than the critical mesoscopic dislocation density. On the other hand, in Figure 5.26.b we observe that the possible nucleation sites are only concentrated near the grain boundaries as only this zone presents a dislocation density higher than the critical mesoscopic dislocation density.

For both cases, the number of nodes presenting a dislocation density higher than the mesoscopic critical dislocation density is larger than the 2060 nuclei expected in the RVE. So, two different criteria are set in order to choose the nucleation sites. The first one takes the dislocation density and the distance to the grain boundary into account and the second one considers only the dislocation density value. Table 5.7 sums up these criteria.

Table 5.7: *Nucleation test cases description.*

Case 1	- the first 2060 nodes with a normalized distance to the grain boundary smaller than 0.075; and with the highest dislocation density values.
Case 2	- the first 2060 nodes presenting the highest dislocation density values.

Figure 5.27 shows the first 2060 nodes taken into account for each case and for each hardening model. Each node corresponds to a new nucleus.

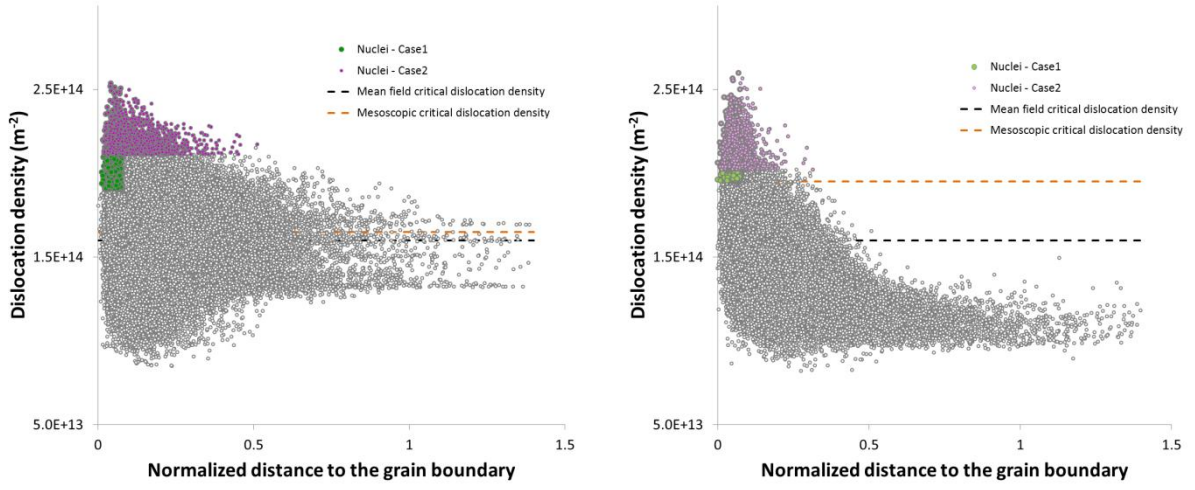

Figure 5.27: *Dislocation density dispersion graph with the description of the nucleation sites for two types of hardening models: (a) only SSDs and (b) both SSDs+GNDs.*

When only SSDs are taken into account, the new grains positions are quite different for both tested cases. For case 1, the new grains mean normalized distance to the grain boundary is equal to 0.057, while for case 2, the normalized distance becomes 0.131. When both SSDs and GNDs are taken into account, the new grains mean normalized distances are 0.055 and 0.075, respectively for cases 1 and 2. They are therefore closer to each other. In the next paragraph, the influence of the choice of nucleation sites on the recrystallization kinetics is studied.

4.4 3D recrystallization kinetics results in site saturated nucleation conditions

The static recrystallization simulation was performed for the two test cases defined in the previous section and for both hardening models. In these simulations, all the new grains are represented initially using the same level set function. As a consequence, only the recrystallization front is simulated (not the individual nuclei). Figures 5.28 and 5.29 present the recrystallization evolution when only SSDs are taken into account and Figures 5.30 and 5.31 present the recrystallization evolution when both SSDs and GNDs are taken into account.

X_v	Internal Energy	Recrystallization front
0%	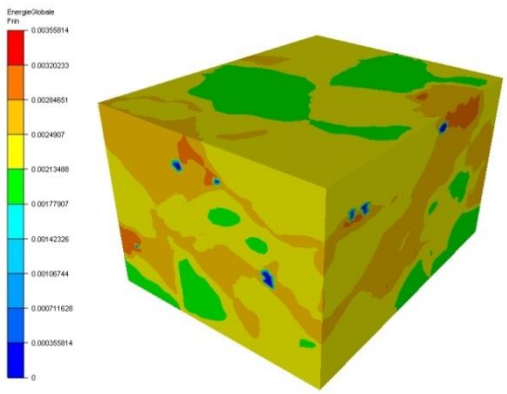	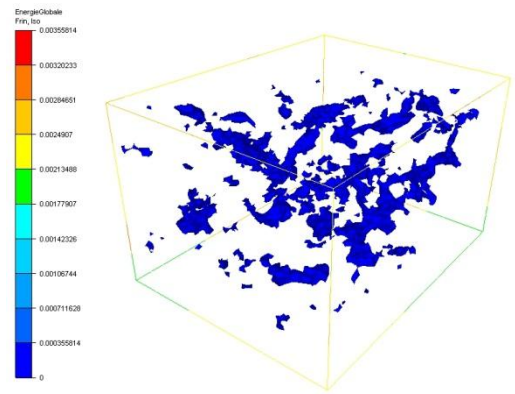

50%	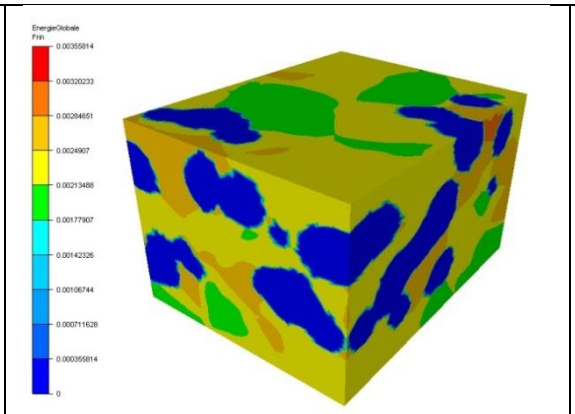	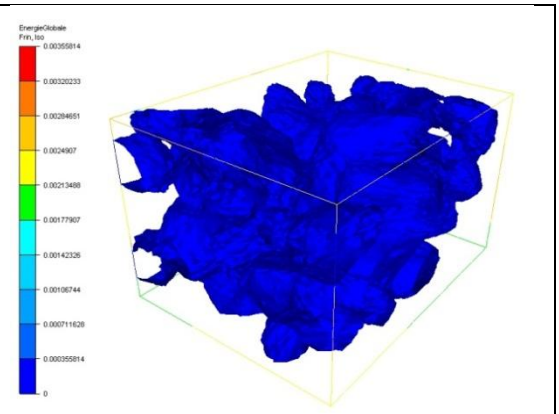
75%	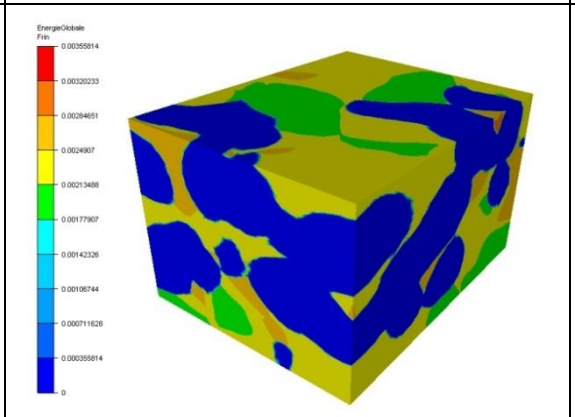	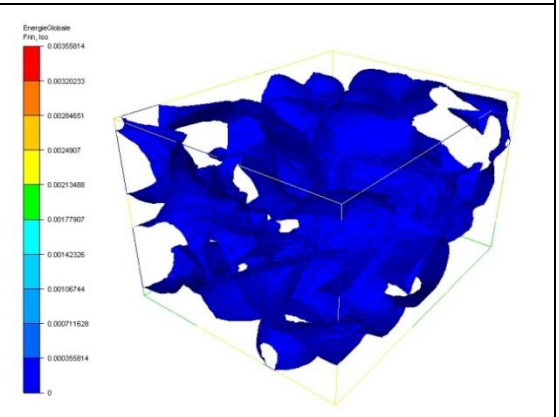

Figure 5.28: *3D recrystallization simulation based on the crystal plasticity simulation results considering only SSDs and for Case 1 concerning the nuclei positions.*

X_v	Internal Energy	Recrystallization front
0%	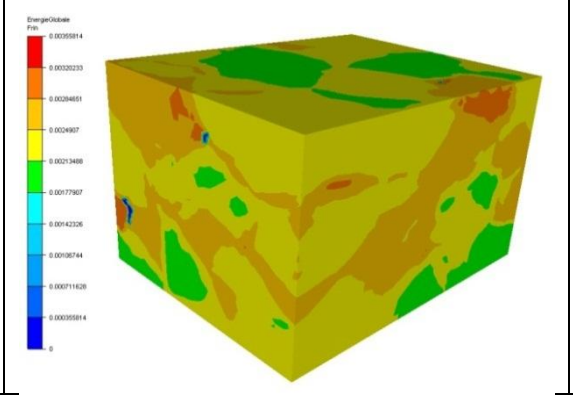	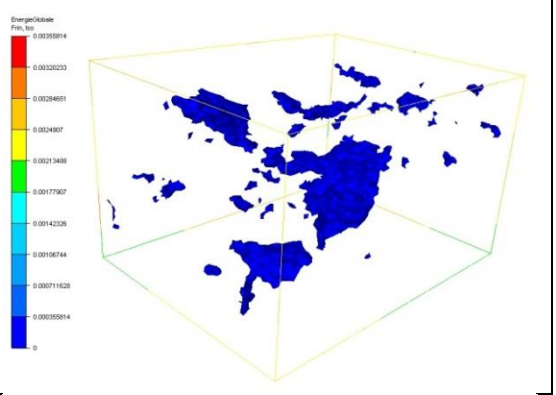
50%	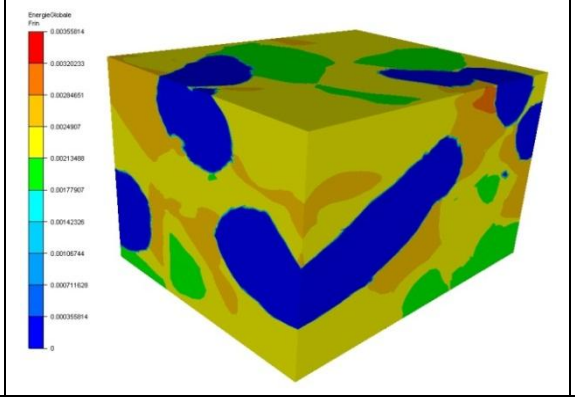	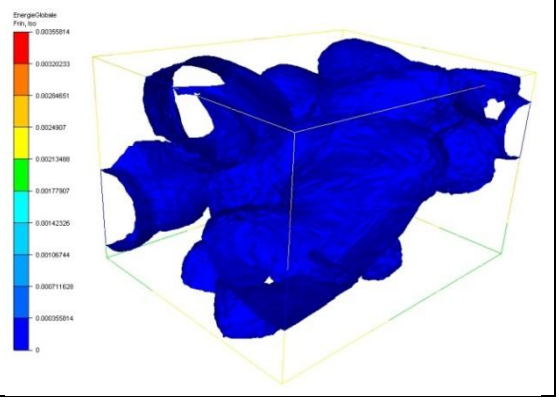

75%	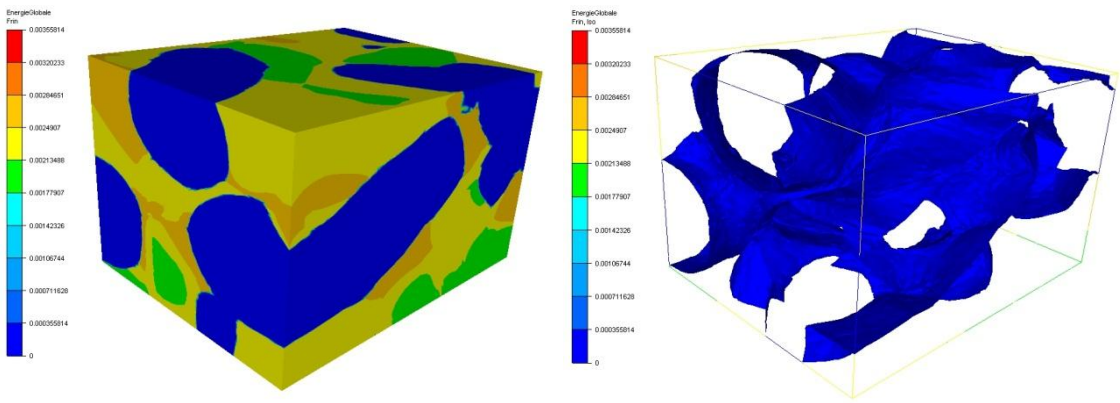

Figure 5.29: *3D recrystallization simulation based on the crystal plasticity simulation results considering only SSDs and for Case 2 concerning the nuclei positions.*

X_v	Internal Energy	Recrystallization front
0%	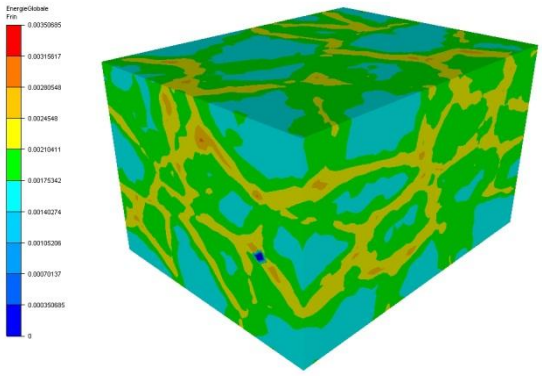	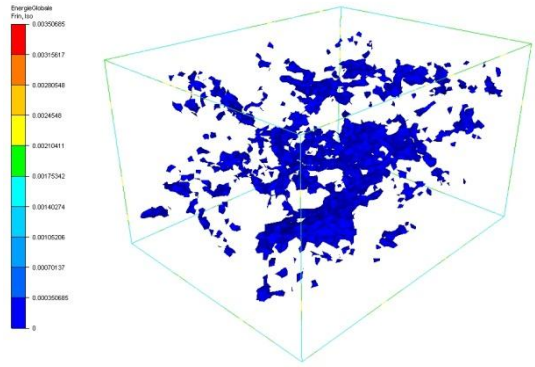
50%	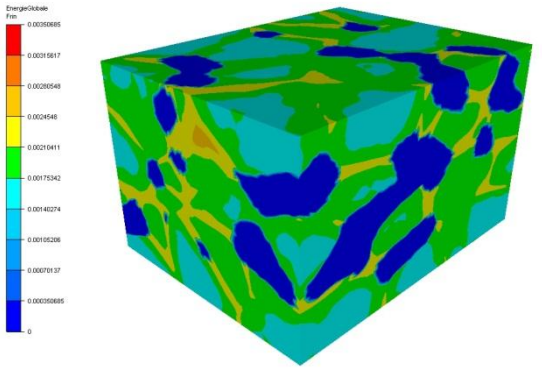	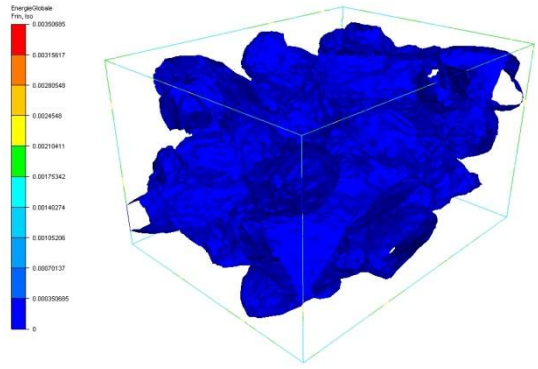
75%	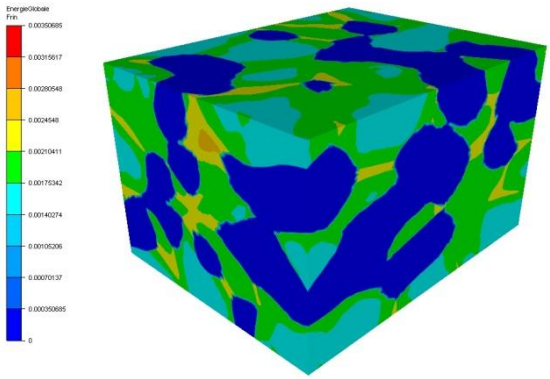	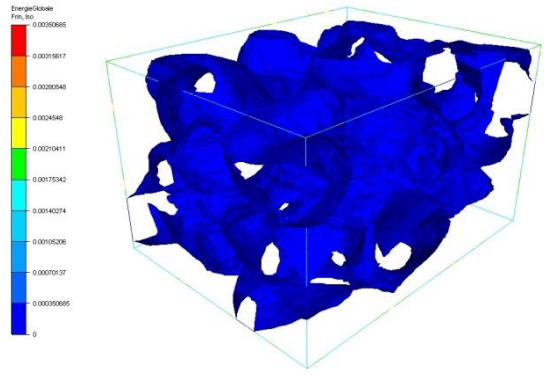

Figure 5.30: *3D recrystallization simulation based on the crystal plasticity simulation results considering both SSDs+GNDs and for Case 1 concerning the nuclei positions.*

X_v	Internal Energy	Recrystallization front
0%	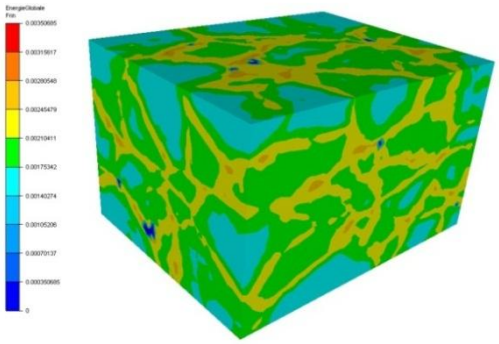	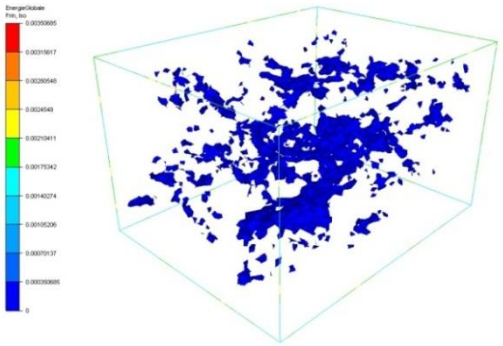
50%	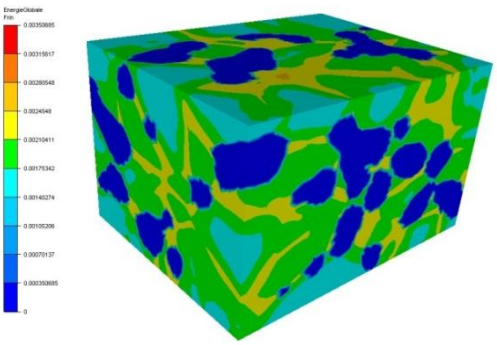	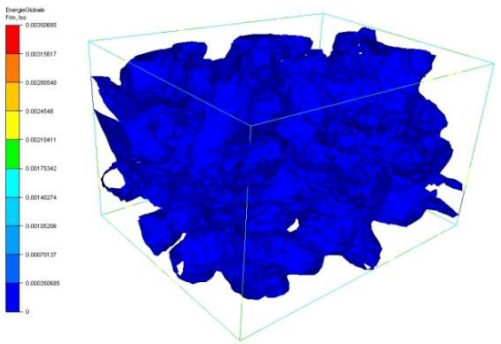
75%	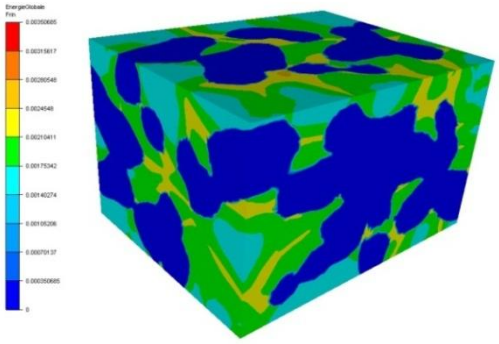	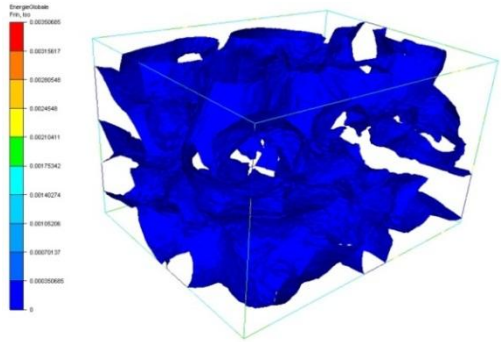

Figure 5.31: *3D recrystallization simulation based on the crystal plasticity simulation results considering both SSDs+GNDs and for Case 2 concerning the nuclei positions.*

The recrystallization kinetics summarizing the above figures are compared to the experimental data in Figure 5.32.

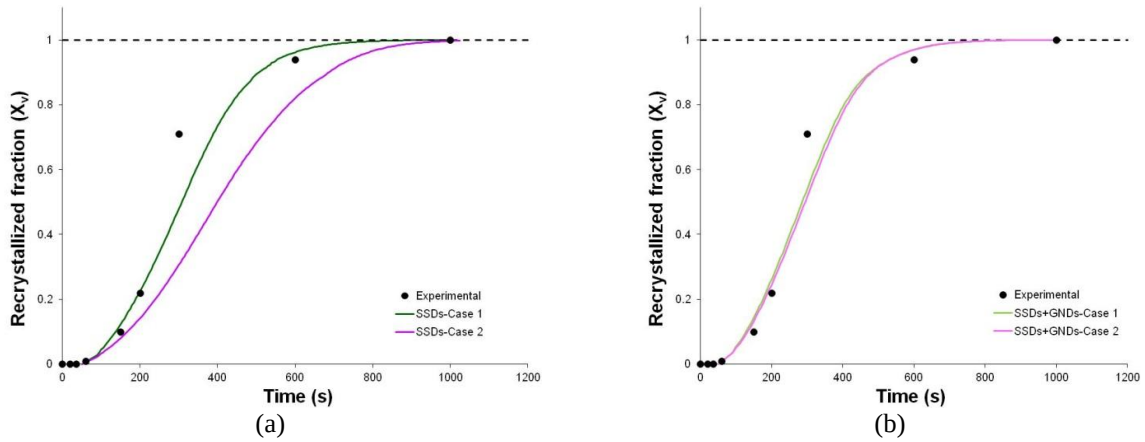

(a) (b)

Figure 5.32: *Recrystallization kinetics simulation results compared to the experimental results when (a) only SSDs are taken into account and when (b) both SSDs + GNDs are taken into account.*

In Figure 5.32.a, when considering only SSDs, we observe that the recrystallization kinetics is not the same for case 1 and case 2. Comparing both cases with the experimental data, we observe that only case 1 correctly predicts the experimental static recrystallization kinetics. For case 2, the recrystallization kinetics is slower than the experimental data. From Figures 5.27.a, 5.28 and 5.29 we observe that the nucleation sites distribution is different for cases 1 and 2. While for case 1 all nuclei are localized near the grain boundaries; for case 2, the nuclei are more spread inside the grain. So, these results show, once again, that the recrystallization kinetics is strongly dependent on the spatial distribution of nuclei. Based on these results, one can conclude that, when only SSDs are taken into account, not only the dislocation density but also the distance to the closest grain boundary must be taken into account in order to define a nucleation model allowing to predict correctly the recrystallization kinetics.

In Figure 5.32.b, considering the SSDs+GNDs hardening model, we observe that both cases results correctly reproduce the experimental recrystallization kinetics. Analysing Figures 5.27.b, 5.30 and 5.31 we observe that for both cases, the nucleation sites are localized near the grain boundaries. One can conclude that, when a static recrystallization model is based on crystal plasticity calculations considering both SSDs and GNDs, a simple dislocation density criterion is sufficient to correctly predict the nucleation sites positions, and the corresponding recrystallization kinetics.

As seen in Figure 5.27, the mesoscale critical dislocation density calculated from crystal plasticity simulations considering only the SSDs is much smaller than the nucleation sites dislocation density. When considering both SSDs and GNDs, the mesoscale critical dislocation density this time corresponds to the minimum value found in the selected nucleation sites. It can therefore be reasonably concluded that taking into account both dislocation densities is important to correctly predict nucleation in static recrystallization.

In the above simulations, only the recrystallization front is followed and, as a consequence, only the recrystallization kinetics is studied. In order to study the final grain size distribution after the recrystallization process, several level set functions are needed to represent the evolution of the individual grains. The study of the grain size distribution after the recrystallization process is left for future work. It would also be interesting to perform similar analyses for different deformation levels in order to validate the current conclusions.

5 Conclusion

In this chapter, a finite element model was proposed in order to simulate the static recrystallization phenomenon. Grain boundaries are implicitly represented using level set functions. A convective-diffusive approach is used to simulate the grain boundary motion taking two driving forces into account: (1) an excess of energy due to grain boundary itself (grain boundary curvature) and (2) a free energy difference between the adjacent grains due to energy stored during deformation. The convective part of the model represents the grain boundary motion due to the free internal energy gradients and the diffusive part represents the grain boundary motion due to the grain boundary curvature. Two academic test cases with well-known results have been presented in order to illustrate the capability of the proposed convective-diffusive approach to finely model the considered phenomena.

In a second part, the effect of introducing capillarity forces in site saturated nucleation conditions is studied. Considering randomly distributed nucleation sites, it is observed that taking into account the grain curvature impacts the shape of the recrystallization kinetics curve (even though the JMAK exponent are the same for both simulations) but do not change significantly the time needed to fully recrystallize the material. However, the microstructure

obtained when ignoring the capillarity effects fails to impose the 120° equilibrium angle at the triple junctions. As a consequence, the microstructures contain grains with unrealistic and/or unstable shapes. In necklace-type nucleation conditions, taking into account the grain curvature driving force affects both the recrystallization kinetics and the microstructure, but the Avrami exponent of the JMAK model is, this time, not affected.

From a global perspective, it is demonstrated that the influence of the grain curvature decreases when increasing the ratio between the magnitude of the internal energy gradients, and the boundary energy.

In a third part, the static recrystallization model is coupled to the crystal plasticity simulation results from chapter 3. A nucleation criterion is borrowed from that introduced in the mean field model developed in [Huang, 2011]. The influence of the dislocation density distributions obtained with two hardening models is evaluated based on the capacity to determine nucleation sites. The corresponding static recrystallization kinetics are compared to experimental data obtained in previous work [Huang, 2011]. It is concluded that considering a hardening model which introduces geometrically necessary dislocations is important to correctly predict nucleation in static recrystallization, as well as the recrystallization kinetics.

In order to study the final grain size distributions after the recrystallization process, several level set functions are needed in order to represent the evolution of the individual grains. This is left to future work. Other extensions of the present work include the modelling of dynamic recrystallization.

Résumé en français

Dans ce chapitre, un modèle de recristallisation à l'échelle mésoscopique basé sur une formulation éléments finis dans un cadre level-set est proposé. Les deux forces motrices du phénomène de recristallisation sont prises en compte. Une approche convective-diffusive est utilisée afin de modéliser le déplacement des joints de grains. La partie convective correspond à la migration des joints de grains liée aux gradients d'énergie stockée sous la forme de dislocations tandis que la partie diffusive, développée dans le chapitre précédent, correspond à celle liée à la capillarité des joints de grains. Plusieurs cas tests académiques sont présentés afin de valider l'algorithme proposé.

Ensuite, l'influence de la prise en compte des effets capillaires est étudiée à partir de la simulation de la recristallisation statique de microstructures présentant différentes distributions de germes en site saturé. Il est par exemple illustré que pour une distribution aléatoire des germes, la prise en compte des effets capillaires a peu d'influence sur le temps total de recristallisation mais modifie de manière significative les paramètres du modèle JMAK. Pour une distribution en collier, les effets capillaires influencent alors le temps total de recristallisation et l'exposant d'Avrami du modèle JMAK.

Finalement, l'algorithme de recristallisation statique est couplé aux résultats des simulations de plasticité cristalline (chapitre 3). La recristallisation d'un échantillon déformé de 304L jusqu'à 0.3 à 1000°C est étudiée et les prédictions numériques sont confrontées aux résultats expérimentaux. L'influence du type de modèle d'écrouissage utilisé dans le modèle de plasticité cristalline sur la cinétique de recristallisation statique est discutée principalement pour les critères de germination qui en découlent.

Conclusions and future work

The full field modeling of metallurgical phenomena which occur during thermal and mechanical processes is nowadays of prime importance in order to provide correct predictions of crystallographic orientations (textures) and grain size distributions. Indeed, metallurgical transformations are complex phenomena and, generally, their experimental study is not easily done. The numerical work performed in this PhD thesis, dedicated to the development of a new full field FE formalism for recrystallization and grain growth, can be summarized in three main parts: (i) the generation and the immersion of statistical digital microstructures in a finite element context (chapter 2); (ii) the crystal plasticity modeling (chapters 1 and 3) and (iii) the grain boundary motion modeling (chapters 4 and 5).

Considering the digital microstructures statistical generation, two different generation methods were presented: Voronoï and Laguerre-Voronoï. Based on the results discussed in this document, we can conclude that the use of a Laguerre-Voronoï method allows the generation of a microstructure that obeys the experimental grain size distribution with a very small L2 error, even for a digital microstructure generated with a reasonable number of grains. Moreover, it was also proved that the well-known and widely used Voronoï method does not allow to obey a given grain size distribution. Even though the mean grain size is well defined, the error between the numerical and the experimental grain size distribution can be very large, even for a microstructure with a high number of grains. These observations were verified for 2D and 3D microstructures. In a second part, a topological and morphological study of seven different digital microstructures, generated using a Laguerre-Voronoï method, was also presented. The ability of this approach to generate, in 2D, equiaxed microstructures and to obey the well-known SLR (special linear relationship) of Abbruzzese [Abbruzzese, 1992a] was described. Future work will consist in extending this study to 3D Laguerre-Voronoï digital microstructures.

The process of plastic deformation of FCC metals was briefly reviewed so as to underline the resulting intergranular and intragranular heterogeneities, from crystal plasticity simulations. The crystal plasticity finite element model used in this work was presented and analysed. Considering the material hardening, physically-based models were emphasized, focusing on the use of one or several dislocations densities as primary variables. The account of size effects was discussed, distinguishing between statistically stored dislocations (SSDs), and geometrically necessary dislocations (GNDs). A simple model (Yoshie-Laasraoui-Jonas [Laasraoui, 2009]) was adopted to estimate the SSD density evolution with plastic deformation, while the Busso model [Busso, 2000] was chosen to evaluate the contribution of the GND density.

Two different mechanical tests were used to validate the crystal plasticity model: a channel-die hot compression test of a 304L steel for a 100-grains polycrystal, and a simple uniaxial compression test of a tantalum 6-grains oligocrystal. For both mechanical tests, the two investigated hardening laws were compared. Considering the first test case (304L polycrystal), the hardening models correctly predict the stress-strain experimental behaviour. The dislocation density distribution calculated with the first hardening law (only considering the total dislocation density) is more homogeneous than the dislocation density distribution computed with the model which takes into account both SSDs and GNDs. Even though the dislocation distribution is different, for both cases the dislocation density dispersion is increased near the grain boundaries, where the highest and lowest dislocation density values are found. When the strain distribution is analysed, we observe that both models present similar results. The strain intragranular distribution as a function of the distance to the closest grain boundary is rather homogeneous. Once again, the strain dispersion is more important near the grain boundaries. Based on these results, nucleation of new grains during the

recrystallization process is expected to take place near the grain boundaries, as experimental results show.

For the second test case (tantalum oligocrystal), we observe that the oligocrystal shape induced by plastic deformation is correctly predicted for four grains, out of six. Once again, the dislocation density distribution exhibits concentration near the grain boundaries. When comparing the two investigated hardening models, dislocation density near the grain boundaries is higher when both SSDs and GNDs are taken into account. The material texture changes for $\varepsilon_{zz} = 0.5$ predicted with the crystal plasticity model overestimate the experimental results, but this can be partly attributed to the difficulty in comparing similar areas. In one grain where numerical and experimental areas are expected to be close to each other, the texture changes are well predicted, including the extent of grain fragmentation. The fragmentation is observed not only for the crystallographic orientations, but also for dislocation density and strain.

Finally, considering grain boundary migration, two phenomena were studied. The first one is the grain growth phenomenon where the decrease of the interfacial energy is the driving force of the grain boundary migration. An improvement of the level-set formalism developed at CEMEF for primary recrystallization modelling [Bernacki, 2009], [Logé, 2008], was proposed in order to take into account the capillarity effects. The ability, in the considered isotropic mobility and interface energy context, of the proposed diffusive approach to simulate very accurately academic test cases, to deal with complex 2D configurations and to be connected with primary recrystallization simulations was illustrated.

This numerical development was used to discuss the impact of an initial grain size distribution on the grain growth phenomenon in a single phase material. Based on full field simulations, the validity of two grain growth mean field models was discussed. It was illustrated that, in general, the simple model of Burke and Turnbull is not predictive, contrary to the Hillert/ Abbruzzese model. The latter approach was shown to be predictive for all considered grain size distributions, even for the more complex ones. Consequently, if the development of full field models is justified for the description of grain growth in complex conditions, their use appears disproportionate in the simple configurations investigated here, where the Hillert/ Abbruzzese approach is sufficient. By lack of time, the same assessment was not performed in 3D but such a study represents a short-term extension of this work.

As explained above, the diffusion formulation accounting for capillarity effects was added to the pre-existing primary recrystallization algorithm developed in [Bernacki, 2009], [Logé, 2008]. Once again, this new model was validated for academic and complex test cases. With these developments, it was mainly highlighted that the classical hypothesis which consists in neglecting the capillarity term when stored energy gradients and nucleation of new grains are present, can be very harmful concerning the predictions of the grain shapes, but also for statistical results such as the grain size distribution or the recrystallized fraction. This result is amplified when necklace-type site saturated nucleation is considered. It was also proved that the influence of the capillarity effects decreases with the increase of the stored energy gradient/boundary energy ratio.

The static recrystallization model has been finally coupled to the crystal plasticity simulation results. A nucleation criterion is borrowed from that introduced in the mean field model developed in [Huang, 2011]. The influence of the dislocation density distributions obtained with two hardening models is evaluated based on the capacity to determine nucleation sites. The corresponding static recrystallization kinetics are compared to experimental data. It is concluded that considering a hardening model which introduces geometrically necessary dislocations is important to correctly predict nucleation in static recrystallization, as well as the recrystallization kinetics.

Finally, if the developments performed in this work have allowed focusing on different fine metallurgical questions, they have also permitted to build a robust and precise FE framework concerning the modelling of recrystallization. Besides the improvement of the numerical cost, which is still a limitation of the proposed methodology for 3D simulations with a large number of grains, current other developments concerning these numerical tools are dedicated to Zener pinning phenomenon, anisotropy of mobility and boundary energy, twinning appearance and disappearance/impact of the twins in the recrystallization kinetics, and dynamic recrystallization modelling.

References

[Abbruzzese, 1992a] G. Abbruzzese, I. Heckelmann, K. Lücke. Statistical theory of two-dimensional grain growth - I. The topological foundation. Acta Metallurgica et Materialia, 40, pp. 519-32, 1992.

[Abbruzzese, 1992b] G. Abbruzzese, I. Heckelmann, K. Lücke. Statistical theory of two-dimensional grain growth - II. Kinetics of Grain Growth. Acta Metallurgica et Materialia, 40, pp. 533-42, 1992.

[Abrivard, 2009] G. Abrivard. A coupled crystal plasticity – phase field formulation to describe microstructural evolution in polycrystalline aggregates during recrystallization. PhD thesis, Ecole Nationale Supérieure des Mines de Paris, 2009.

[Abu Al-Rub, 2006] R.K. Abu Al-Rub, G.Z. Voyiadjis. A physically based gradient plasticity theory. International Journal of Plasticity, 22, pp. 654-684, 2006.

[Acharya, 2000] A. Acharya, J.L. Bassani. Lattice incompatibility and a gradient theory of crystal. Journal of the Mechanics and Physics of Solids 48, pp. 1565-1595, 2000.

[Acharya, 2001] Acharya A. A model of crystal plasticity based on the theory of continuously distributed dislocations. Journal of the Mechanics and Physics of Solids, 49, pp. 761-784, 2001.

[Acharya, 2004] A. Acharya. Constitutive analysis of finite deformation field dislocation mechanics. Journal of the Mechanics and Physics of Solids, 52, pp. 301-316, 2004.

[Agnoli, 2012] A. Agnoli, M. Bernacki, R. Logé, J.-M. Franchet, J. Laigo, N. Bozzolo, Understanding and modeling of grain boundary pinning in Inconel 718, Proceedings of the 12th International Symposium on Superalloys, Champion, Pennsylvania, USA, 2012.

[Almeida, 2000] R.C. Almeida, R.A. Feijoo, A.C. Galeao, C. Padra, R.S. Silva. Adaptive finite element computational fluid dynamics using an anisotropic error estimator. Computer Methods in Applied Mechanics and Engineering, 182, pp. 379-400, 2000.

[Al-Rub, 2006] R.K.A. Al-Rub, G.Z. Voyiadjis. A physically based gradient plasticity theory. International Journal of Plasticity, 22, pp. 654–684, 2006.

[Arsenlis, 1999] Arsenlis A., Parks D. M. Crystallographic aspects of geometrically-necessary and statistically-stored dislocation density. Acta Materialia, 47, pp. 1597-1611, 1999.

[Arsenlis, 2004] A. Arsenlis, D.M. Parks, R. Becker, V.V. Bulatova. On the evolution of crystallographic dislocation density in non-homogeneously deforming crystals. Journal of the Mechanics and Physics of Solid, 52, pp. 1213 – 1246, 2004.

[Ashby, 1970] M.F. Ashby. The deformation of plastically non-homogeneous materials. Philosophical Magazine, 21, pp 399-424, 1970.

[Ashby, 2009] M.F. Ashby. Engineering Materials and Processes Desk Reference. Elsevier, U.S.A., 2009

[ASM, 1982] ASM, Material and process engineering bookshelf: selection of stainless steels, ASM, Ohio, 1982.

[Aurenhammer, 1987] F. Aurenhammer, Power diagrams: properties, algorithms and applications, SIAM Journal on Computing, 16, pp. 78-96, 1987.

[Avrami, 1939] M. Avrami. Kinetics of Phase Change. I General Theory. Journal of chemical physics, 12, pp.1103-1112, 1939.

[Barbe, 2001a] F. Barbe, L. Decker, D. Jeulin, G. Cailletaud. Intergranular and intragranular behaviour of polycrystalline aggregates. Part 1: FE model. International Journal of Plasticity, 17, pp. 513-536, 2001.

[Barbe, 2001b] F. Barbe, S. Forest, G. Cailletaud. Intergranular and intragranular behaviour of polycrystalline aggregates. Part 2: Results. International Journal of Plasticity, pp. 537-563, 2001.

[Barraclough, 1979] D.R. Barraclough, C.M. Sellars. Static recrystallization and restauration after hot deformation of type 304 stainless steel. Metal Science 13, pp. 257-267, 1979.

[Barrales, 2008] L.A. Barrales Mora, G. Gottstein, L.S. Shvindlerman. Three dimensional grain growth : Analytical approaches and computer simulations. Acta Materialia, 56, pp. 5915–5926, 2008.

[Bassani, 2001] J.L Bassani. Incompatibility and a simple gradient theory of plasticity. Journal of the Mechanics and Physics of Solids, 49, pp. 1983-1996, 2001.

[Beaudoin, 1995] A.J. Beaudoin, P.R. Dawson, K.K. Mathur, U.F. Kocks. A hybrid finite element formulation for polycrystal plasticity with consideration of macrostructural and microstructural linking. International Journal of Plasticity, 11, 501-521, 1995.

[Beaudoin, 2000] A.J. Beaudoin, A. Acharya, S.R. Chen, D.A. Korzekw, M.G. Stout. Consideration of grain-size effect and kinetics in the plastic deformation of metal polycrystals. Acta Materialia, 48, pp. 3409-3423, 2000.

[Beck, 1949] P.A. Beck. The formation of recrystallization nuclei. Journal of Applied Physics, 20, pp. 633-634, 1949.

[Beck, 1950] P.A. Beck, P.R. Sperry. Strain induced boundary migration in high purity aluminium. Journal of Applied Physics, 21, pp. 150-152, 1950.

[Beck, 1954] P.A. Beck. Annealing of cold worked metals. Advanced Physics 3, pp. 245-324, 1954.

[Benabbou, 2010] A. Benabbou, H. Borouchaki, P. Laug, and J. Lu, Numerical modelling of nanostructured materials, Finite Elements in Analysis and Design, 46, pp. 165-180, 2010.

[Bernacki, 2008] M. Bernacki, Y. Chastel, T. Coupez, R.E. Loge. Level set framework for the numerical modelling of primary recrystallization in polycrystalline materials. Scripta Materialia, 58, pp. 1129-32, 2008.

[Bernacki, 2009] M. Bernacki, H. Resk, T. Coupez, R.E. Logé. Finite element model of primary recrystallization in polycrystalline aggregates using a level set framework. Modelling and Simulation in Materials Science and Engineering, 17, no. 064006, 2009.

[Bernacki, 2011] M. Bernacki, R. Loge, T. Coupez. Level set framework for finite-element modelling of recrystallization and grain growth in polycrystalline materials. Scripta Materialia, 64, pp. 525-528, 2011.

[Bernard, 2011] P. Bernard, S. Bag, K. Huang, R.E. Logé. A two site mean field model of discontinuous dynamic recrystallization. Materials Science and Engineering A, 528, pp. 7357-7367, 2011.

[Berveiller, 1979] M. Berveiller, A. Zaoui. An extension of the self consistent scheme to plastically flowing polycrystals. Journal of the Mechanics and Physics of Solids, 23, pp. 325-344, 1979.

[Bever, 1957] M.B. Bever. Creep and recovery. ASM, 14, Cleveland, 1957.

[Bilby, 1957] B.A. Bilby, L.R.T. Gardner, A.N. Stroh. Continuous distributions of dislocations and the theory of plasticity. IXe Congrès International de Mécanique Appliquée, III. Bruxelles, Berlgique, pp. 35-44, 1957.

[Brenner, 2009] R. Brenner, R.A. Lebensohn, O. Castelnau. Elastic anisotropy and yield surface estimates of polycrystals. International Journal of Solids and Structures, 46, pp. 3018-3026, 2009.

[Brezzi, 1991] F. Brezzi, M. Fortin. Mixed and hybrid finite elements methods, volume Springer Series in Computational Mathematics 15. Springer-Verlag, New York, 1991.

[Buchheit, 2005] T.E. Buchheit, G.W. Wellman, C.C. Battaile. Investigating the limits of polycrystal plasticity modelling. International Journal of Plasticity, 21, pp.221-249, 2005.

[Burgers, 1939] J.M. Burgers. Some considerations on the field of stress connected with dislocation in a regular crystal lattice I. Proceedings on the Koninklijke Nederlandse Akad. Wetenschappen, 42, pp. 293-325, 1939.

[Burke, 1952] J.E. Burke, D. Turnbull. Recrystallisation and grains growth. Progress in Metal Physics, 3, pp. 220-292, 1952.

[Busso, 1996] E.P. Busso, F.A. McClintock. A dislocation mechanics-based crystallographic model of a B2-type intermetallic alloy. International. Journal of Plasticity, 12, pp. 1-28, 1996.

[Busso, 2000] E.P. Busso, F.T. Meissonnier, N.P. O'Dowd. Gradient-dependent deformation of two-phase single crystals. Journal of the Mechanics and Physics of Solids, 48, pp. 2333-2361, 2000.

[Cahn, 1950] R.W. Cahn. A new theory of recrystallization nuclei. Proceedings of the Physical Society. Ser.AI, 63, pp. 323-336, 1950.

[Chen, 1995] L.Q. Chen. A novel computer simulation technique for modeling grain growth. Scripta Metallurgica et Materialia, 32, pp. 115-120, 1995.

[Chen, 1998] J.Y. Chen, Y. Huang, K.C. Hwang. Mode I and mode II plane-stress near-tip fields for cracks in materials with strain-gradient effects. 3rd International Conference on Fracture and Strength of Solids, Honk Kong. 145/149, pp. 19-28, 1998.

[Chen, 2002] L.Q. Chen. Phase-Field models for microstructure evolution. Annual Review of Materials Research, 32, pp. 113-140, 2002.

[Cheong, 2005] K.S. Cheong, E.P. Busso, A. Arsenlis. A study of microstructural length scale effects on the behavior of FCC polycrystals using strain gradient concepts. International Journal of Plasticity, 21, pp. 1797-1814, 2005.

[Cho, 2001] S.H. Cho, Y.C. Yoo. Static recrystallization kinetics of 304 stainless steel. Journal of Materials Science, 36, pp. 4267-4272, 2001.

[Chockalingam, 2013] K. Chockalingal, M.R. Tonks, J.D. Hales, D.R. Gaston, P.C. Millett, L. Zhang. Crystal plasticity with Jacobian-Free Newton-Krylov. Computational Mechanics, 51, pp. 617-627, 2013.

[Coupez, 1997] T. Coupez, S. Marie. From a direct solver to a parallel iterative solver in 3d forming simulation. International Journal of Supercomputer Applications, 11, pp. 205-211, 1997.

[Coupez, 2000] T. Coupez, H. Digonnet, and R. Ducloux, Parallel meshing and remeshing, Applied Mathematical Modelling, 25, pp. 153-175, 2000.

[Coupez, 2007] T. Coupez. Convection of local level set function for moving surfaces and interfaces in moving flow 9th Int. Conf. on Numerical Methods in Industrial Forming Processes Proc., Porto, Portugal, pp. 61-66, 2007.

[Dehghan-Manshadi, 2008] A. Dehghan-Manshadi, M.R. Barnett, P.D. Hodgson. Hot deformation and recrystallization of austenitic stainless steel: Part I. Dynamic recrystallization. Metallurgical and Materials Transactions A, 39, pp. 1359-1370, 2008.

[del Valle, 2006] J.A. del Valle, O.A. Ruano. Influence of the grain size on the strain rate sensitivity in an Mg–Al–Zn alloy at moderate temperatures. Scripta Materialia, 55, pp. 775-778, 2006.

[Delannay, 2006] L. Delannay, P.J. Jacques, S.R. Kalindindi. Finite element modelling of crystal plasticity with grains shaped as truncated octahedrons. Intenational Journal of Plasticity, 22, pp. 1879-1898, 2006.

[Diard, 2005] O. Diard, S. Leclercq, G. Rousselier, G. Cailletaud. Evaluation of finite element based analysis of 3D multicrystalline aggregates plasticity. International Journal of Palsticity, 21, pp. 691-722, 2005.

[Digonnet, 2007] H. Digonnet, L. Silva, and T. Coupez. Cimlib: a fully parallel application for numerical simulations based on components assembly. Materials Processing and Design; Modeling, Simulation and Applications; NUMIFORM '07; Proceedings of the 9th International Conference on Numerical Methods in Industrial, 2007, pp. 269-274.

[Doherty, 1997] R.D. Doherty, D.A. Hughes, F.J. Humphreys, J.J. Jonas, D. Juul Jensen, M.E. Kassner, W.E. King, T.R. McNelley, H.J. McQueen, A.D. Rollett. Current issues in recrystallization: a review. Materials Science and Engineering A, 238, pp. 219-274, 1997.

[El Wahabi, 2003] M. El Wahabi, J.M. Cabrera, J.M. Prado. Hot working of two AISI 304 steels: a comparative study. Materials Science and Engineering A, 343, pp. 116-125, 2003.

[Elsey, 2009] M. Elsey, S. Esedoglu, P. Smereka, Diffusion generated motion for grain growth in two and three dimensions, Journal of Computational Physics, 228, pp. 8015-8033, 2009.

[Elsey, 2013] M. Elsey, S. Esedoglu, P. Smereka. Simulations of anisotropic grain growth: Efficient algorithms and misorientation distributions. Acta Materialia, 61, pp.2033-2043, 2013.

[Erieau, 2004] P. Erieau, C. Rey. Modeling of deformation and rotation bands and of deformation induced grain boundaries in IF steel aggregate during large plane strain compression. International Journal of Plasticity, 20, pp. 1763-1788, 2004.

[Eshelby, 1957] J. Eshelby. The determination of the elastic field of an ellipsoidal inclusion and related problems. In Proceedings – Royal society of London A. Mathematical and physical sciences, 241, pp. 376-396, 1957.

[Estrin, 1998a] Y. Estrin. Dislocation theory based constitutive modelling: foundations and applications. Journal of Materials Processing Technology, 80-81, pp. 33-39, 1998.

[Estrin, 1998b] Y. Estrin, L.S. Toth, A. Molinari, Y. Bréchet. A dislocation-based model for all hardening stages in large strain deformation. Acta Materialia, 46, pp. 5509-5522, 1998.

[Evers, 2002] L.P. Evers, D.M. Parks, W.A.M. Brekelmans, M.G.D. Geers. Crystal plasticity model with enhanced hardening by geometrically necessary dislocation accumulation. Journal of the Mechanics and Physics of Solids, 50, pp. 2403-2424, 2002.

[Evers, 2004] L.P. Evers, W.A.M. Brekelmans, M.G.D. Geers. Scale dependent crystal plasticity framework with dislocation density and grain boundary effects. International Journal of Solids and Structures, 41, pp. 5209-5230, 2004.

[Fabiano, 2013] A.L. Fabiano, R. Logé, M. Bernacki, Assessment of simplified 2D grain growth models from numerical experiments based on a level set framework. Submitted Modelling and Simulation in materials Science and Engineering, 2013.

[Fan, 2004] Z. Fan, Y. Wu, X. Zhao, and Y. Lu, Simulation of polycrystalline structure with Voronoi diagram in Laguerre geometry based on random closed packing of spheres, Computational Materials Science, 29, pp. 301-308, 2004.

[Fields, 1957] D.S.Fields. W.A.Backofen. Determination of strain hardening characteristics by torsion testing. Proc.Am.Soc.Test. Mater., 57, pp.1259-1272, 1957.

[Finney, 1978] J.L.Finney. Volume occupation, environment, and accessibility in proteins. Environment and molecular area of rnase-s. Journal of Molecular Biology, 119, pp. 415-430, 1978.

[Frankel, 1926] J.Frankel. Zur theorie der elastizitätsgrenze und der festigkeit kristallinischer körper. Zeitschrift fur Physik, 37, pp. 572-609, 1926.

[Frénois, 2001] S. Frénois. Modélisation polycristalline du comportement mécanique du tantale. Application à la mise en forme par hydroformage. PhD Thesis, Ecole Centrale de Paris, 2001.

[Frey, 1999] P.J. Frey, P.L. George. Maillages: applications aux éléments finis. HERMES Science Publications, 1999.

[Frost, 1982] H.J. Frost, M.F. Ashby. Deformation mechanism maps. Pergamon Press, 1982.

[Garcke, 1991] H. Garcke, B. Nestler, B. Stoth. A multi phase field concept: numerical simulations of moving phase boundaries and multiple junctions. Mathematics Subject Classification, 1991.

[Gavard, 2001] L. Gavard. Recristallisation dynamique d'aciers inoxydables austénitiques de haute purete. PhD Thesis, Ecole Nationale Supérieure des Mines de Saint-Etienne, 2001.

[George, 1998] P.L. George, H. Bourouchaki, Delaunay triangulation and meshing - application to finite element. HERMES, Paris, 1998.

[Gerken, 2008, a] J.M. Gerken, P.R. Dawson. A crystal plasticity model that incorporates stresses and strains due to slip gradients. Journal of the Mechanics and Physics of Solids, 56, pp.1651-1672, 2008.

[Gerken, 2008, b] J.M. Gerken, P.R. Dawson. A finite element formulation to solve a non-local constitutive model with stresses and strains due to slip gradient. Computer Methods in Applied Mechanics and Engineering, 197, pp. 1343-1361, 2008.

[Glicksman, 2005] M.E. Glicksman. Analysis of 3-D network structures. Philosophical Magazine, 85, pp. 3-31, 2005.

[Gruau, 2005] C. Gruau, T. Coupez, Tetrahedral unstructured and anisotropic mesh generation with adaptation to natural and multidomain metric. Computer Methods in applied Mechanics and Engineering, 194, pp. 4951-4976, 2005.

[Gurtin, 2000] M.E. Gurtin. On the plasticity of single crystals: free energy, microforces, plastic-strain gradients. Journal of the Mechanics and Physics of Solids, 48, pp. 989-1036, 2000.

[Gurtin, 2002] M.E. Gurtin. A gradient theory of single-crystal viscoplasticity that accounts for geometrically necessary dislocations. Journal of the Mechanics and Physics of Solids, 50, pp. 5-32, 2002.

[Gurtin, 2008] M.E. Gurtin. A finite-deformation, gradient theory of single-crystal plasticity with free energy dependent on densities of geometrically necessary dislocations. International Journal of Plasticity, 24, pp. 702-725, 2008.

[Hall, 1951] E.O. Hall. The deformation and ageing of mild steel III. Discussion of results. Proc. Phys. Soc. Sect. B 64, pp. 747-753, 1951.

[Hassold, 1993] G.N. Hassold, E.A. Holm. A fast serial algorithm for the finite temperature quenched Potts model. Journal of Computational Physics, 7, pp. 97-107, 1993.

[Hasson, 1971] G.C. Hasson, C. Goux. Interfacial energies of tilt boundaries in aluminum. Experimental and theoretical determination. Scripta Metallurgica, 5, pp. 889-894, 1971

[Hill, 1965] R. Hill. Continuum micro-mechanics of elastoplastic polycrystals. Journal of the Mechanics and Physics of Solids, 13, pp. 89-101, 1965.

[Hillert, 1965] M. Hillert. On the theory of normal and abnormal grain growth. Acta Metallurgica et Materialia, 13, pp. 227-38, 1965.

[Hitti, 2011] K. Hitti. Direct numerical simulation of complex Representative Volume Elements (RVEs): Generation, Resolution and Homogenization. PhD. Thesis - Ecole Nationale Supérieure des Mines de Paris, 2011.

[Hitti, 2012] K. Hitti, P. Laure, T. Coupez, L. Silva, M. Bernacki. Precise generation of complex statistical Representative Volume Elements (RVEs) in a finite element context. Computational Materials Science, 6, pp. 224-238, 2012.

[Honeff, 1981] H. Honeff, H. Mecking. Analysis of the deformation texture at different rolling conditions. Proceedings of the 6th International Conference on Textures of Materials. The Iron and Steel Institute of Japan, pp. 347-355, 1981.

[Hoon Kim, 2013] J. Hoon Kim, M. G. Lee, D. Kim, F. Barlat. Numerical procedures for predicting localization in sheet metals using crystal plasticity. Computational Materials Science, 72, pp. 107-115, 2013.

[Huang, 2000] Y. Huang, F.J. Humphreys, and M. Ferry, The annealing behaviour of deformed cube-oriented aluminium single crystals, Acta Materialia, 48, pp. 2543-2556, 2000.

[Huang, 2011] K. Huang. Towards the modeling of recrystallization phenomena in multi-pass conditions - Applications to 304L steel. PhD Thesis - Ecole Nationale Supérieure des Mines de Paris, 2011.

[Humphreys, 2004] F.J. Humphreys, M. Hatherly. Recrystallization and related annealing phenomena. Elsevier, Amsterdam, 2004.

[Hutchinson, 1976] J.W. Hutchinson. Bounds and self-consistent estimates for creep of polycrystalline material. In Proceeding - Royal society of London A, 348, pp. 101-127, 1976.

[Hutchinson, 1977] J. W. Hutchinson. Creep and plasticity of hexagonal polycrystals as related to single crystal slip. Metallurgical Transactions A, 8, pp. 1465-1469, 1977.

[Hutchinson, 1989] W.B. Hutchinson, Recrystallization textures in iron resulting from nucleation at grain boundaries. Acta Materialia, 37, pp. 1047-1056, 1989.

[Hutchinson, 1999] W.B. Hutchinson, H. Magnusson, J.M. Feppon. Proc. 4th Int. Conf. on Recrystallization, eds Sakai and Suzuki, JIM, 49, 1999.

[Iadicola, 2012] M.A. Iadicola , L. Hu, A.D. Rollett, T. Foecke. Crystal plasticity analysis of constitutive behaviour of 5754 aluminum sheet deformed along bi-linear strain paths. International Journal of Solids and Structures, 49, pp. 3507-3516, 2012.

[Imai, 1985] H. Imai, M. Iri, and K. Murota, Voronoi diagram in the Laguerre geometry and its applications, SIAM Journal on Computing, 14, pp. 93-105, 1985.

[Jaouen, 1998] O. Jaouen. Modélisation tridimensionnelle par éléments finis pour l'analyse thermomécanique du refroidissement des pièces coulées. PhD Thesis, Ecole Nationale Supérieure des Mines de Paris, 1998.

[Jenkins, 2008] K. Jenkins, M. Lindenmo. Precipitates in electrical steels. Journal of Magnetism and Magnetic Materials, 320, pp. 2423-2429, 2008.

[Johnson, 1939] W.A. Johnson, R.F. Mehl. Reaction kinetics in processes of nucleation and growth. Transactions of the American Institute of Mining & Metallurgical Engineers, 135, pp. 416-478, 1939.

[Jonas, 2009] J.J. Jonas, X. Quelennec, L. Jiang, E. Martin. The Avrami kinetics of dynamic recrystallization. Acta Materialia, 57, pp. 2748-2756, 2009.

[Kamachali, 2012] R.D. Kamachali, I. Steinbach. 3D phase field simulation of grain growth: Topological analysis versus mean field approximations. Acta Materialia, 60, pp. 2719-2728, 2012.

[Kazaryan, 2002] A. Kazaryan, Y. Wang, S.A. Dregia, B.R. Patton. Grain growth in anisotropic systems: comparison of effects of energy and mobility. Acta Materialia, 20, pp. 2491-2502, 2002.

[Kerisit, 2012] C. Kerisit. Analyse des mécanismes de recristallisation statique du tantale déformé à froid pour une modélisation en champ moyen, PhD Thesis, Ecole Nationale Supérieure de Mines de Paris, 2012.

[Knipling, 2011] K.E. Knipling, D.N. Seidman, D.C. Dunand. Ambient- and high-temperature mechanical properties of isochronally aged Al–0.06Sc, Al–0.06Zr and Al–0.06Sc–0.06Zr (at.%) alloys. Acta Materialia, 59, pp. 943-954, 2011.

[Kocks, 1976] U.F. Kocks. Laws for work-hardening and low temperature creep. Journal of engineering materials and technology, 98, pp. 76-85, 1976.

[Kocks, 1982] U.F. Kocks, H. Chandra. Slip geometry in partially constrained deformation. Acta Metallurgica, 30, pp. 695-709, 1982.

[Kolmogorov, 1937] A. Kolmogorov. A statistical theory for the recrystallization of metals. Izv. Akad. nauk. USSR-Ser-Matemat, 3 pp. 355, 1937.

[Kröner, 1971] E. Kröner. Continuum theory of dislocations and self-stresses. College of Engineering, University of Florida, Gainsville, Fl, 1971.

[Kubale, 2004] M. Kubale, Graph Colorings. American Mathematical Society, Providence, Rhode Island, 2004.

[Kugler, 2004] G. Kugler, R. Turk. Modelling the dynamic recrystallization under multi-stage hot deformation. Acta Materialia, 52, pp. 4659-68, 2004.

[Laasraoui, 1991] A. Laasraoui, J.J. Jonas. Prediction of steel flow stresses at high-temperature and strain rates. Metallurgical Transactions A - Physical Metallurgy and Materials Science, 22, pp. 1545-1588, 1991.

[Lavergne, 2013] F. Lavergne, R. Brenner, K. Sabi, Effects of grain size distribution and stress heterogeneity on yield stress of polycrystals: A numerical approach, Computational Materials Science, 77, pp. 387-398, 2013.

[Lebensohn, 1993] R. Lebensohn, C. Tomé. A self-consistent anisotropic approach for the simulation of plastic deformation and texture development of polycrystals: application to zirconium alloys. Acta Metallurgica et Materialia, 41, pp. 2611-2624, 1993.

[Lebensohn, 2001] R. Lebensohn. N-site modeling of a 3D viscoplastic polycrystal using Fast Fourier transform. Acta Materialia 49, pp. 2723-2737, 2001.

[Lebensohn, 2008] R. Lebensohn, R. Brenner, O. Castelnau, A. Rollet. Orientation image-based micromechanical modelling of subgrain texture evolution in polycrystalline copper. Acta Materialia, 56, pp. 3914-3926, 2008.

[Lee, 1967] E.H. Lee, D.T. Liu. Finite-strain elastic-plastic theory with application to plane wave analysis. Journal of Applied Physics, 38, pp. 19-27, 1967.

[Lee, 1969] E.H. Lee. Elastic-plastic deformation at finite strains. Journal of Applied Mechanics, 36, pp. 1-6, 1969.

[Lee, 2011] S.B. Lee, R.A. Lebensohn, A.D. Rollett. Modeling the viscoplastic micromechanical response of two-phase materials using Fast Fourier Transforms. International Journal of Plasticity, 27, pp. 707-727, 2011.

[Liang, 2009] H. Liang, F.P.E. Dunne. GND accumulation in bi-crystal deformation: Crystal plasticity analysis and comparison with experiments. International Journal of Mechanical Sciences, 51, pp. 326-333, 2009.

[Loge, 2008] R. Loge, M. Bernacki, H. Resk, L. Delannay, H. Digonnet, Y. Chastel, T. Coupez, Linking plastic deformation to recrystallization in metals using digital microstructures, Philosophical Magazine, 88, pp. 3691-3712, 2008.

[Louat, 1974] N.P. Louat. On the theory of normal grain growth. Acta Metallurgica, 22, pp. 721-724, 1974.

[Lücke, 1992] K. Lücke, I. Heckelmann, G. Abbruzzese. Statistical theory of two-dimensional grain growth – II. Kinetics of grain growth. Acta Metallurgica et Materialia, 40, pp. 533-42, 1992.

[Lücke, 1998] K. Lücke, R. Brandt, G. Abbruzzese. Normal and abnormal grain growth as transient phenomena. Interface Science, 6, pp. 67-76, 1998.

[Ma, 2006] A. Ma, F. Roters, D. Raabe. A dislocation density based constitutive model for crystal plasticity FEM including geometrically necessary dislocations. Acta Materialia, 54, pp. 2169-2179, 2006.

[Mallick, 2009] A. Mallick, S. Vedantam, L. Lu. Grain size dependent tensile behavior of Mg–3%Al alloy at elevated temperatures. Materials Science and Engineering A, 515, pp. 14-18, 2009.

[Mallory, 1983] F.F. Mallory, B.N. Boots. Spatial distribution of lemming mats in the Canadian high arctic. Canadian Journal of Zoology, 61, pp. 99-107, 1983.

[Marin, 1998a] E. Marin, P. Dawson. Elastoplastic finite element analyses of metal deformations using polycrystal constitutive models. Computer Methods in Applied Mechanics and Engineering, 165, pp. 23-41, 1998.

[Marin, 1998b] E. Marin, P. Dawson. On modelling the elasto-viscoplastic response of metals using polycrystal plasticity. Computer Methods in Applied Mechanics and Engineering, 165, pp. 1-21, 1998.

[Mataya, 1990] M.C. Mataya, E.L. Brown, M.P. Riendeau. Effect of hot working on structure strength of type 304L austenitic stainless steel. Metallurgical Transactions A, 21, pp. 1969-1987, 1990.

[McQueen, 1995] H.J. McQueen, S. Yue, N.D. Ryan, E. Fry. Hot working characteristics of steels in austenitic state. Journal of Materials Processing Technology, 53, pp. 293-310, 1995.

[Merriman, 1994] B. Merryman, J.K. Bence, S. Osher. Motion of multiple junctions: A level set approach. Journal of Computational Physics, 112, pp. 334-63, 1994.

[Mesri, 2008] Y. Mesri, W. Zerguine, H. Digonnet, L. Silva, T. Coupez. Dynamic parallel adaption for three dimensional unstructured meshes: Application to interface tracking. Proceedings of the 17th International Meshing Roundtable, pp. 195-212, 2008.

[Miodownik, 2002] M.A. Miodownik. A review of microstructural computer models used to simulate grain growth and recrystallisation in aluminium alloys. Journal of Light Materials, 2, pp. 125-135, 2002.

[Mirzadeh, 2013] H. Mizardeh, M.H. Parsa, D. Ohadi. Hot deformation behavior of austenitic stainless steel for a wide range of initial grain size. Materials Science and Engineering A, 569, pp. 54-60, 2013.

[Moelans, 2009] N. Moelans, F. Wendler, B. Nestler. Comparative study of two phase-field models for grain growth. Computational Materials Science, 46, pp. 479-490, 2009.

[Molinari, 1987] A. Molinari, G.R. Canova, S. Ahzi. A self consistent approach of the large deformation polycrystal viscoplasticity. Acta Metallurgica, 35, pp. 2983-2994, 1987.

[Montheillet, 2009] F.Montheillet, O.Lurdos, G. Damamme, A grain scale approach for modeling steady-state discontinuous dynamic recrystallization. Acta Materialia, 57, pp. 1602-1612, 2009.

[Mullins, 1956] W.W. Mullins. Two-dimensional motion of idealized grain boundaries. Journal of Applied Physics, 27, pp. 900-904, 1956.

[Mullins, 1988] W.W. Mullins. On idealized two dimensional grain growth. Scripta Metallurgica, 22, pp. 1441-1444, 1988.

[Nagai, 1990] T. Nagai, S. Ohta, K. Kawasaki, T. Okuzono. Computer simulation of cellular pattern growth in two and three dimensions. Phase Transition, 28, pp. 177-211, 1990.

[Nes, 1995] E. Nes. Recovery revisited. Acta Metallurgica and Materialia, 43, pp. 2189-2207, 1995.

[Nix, 1998] W.D. Nix, H. Gao. Indentation size effects in crystalline materials: a law for strain gradient plasticity. Journal of the Mechanics and Physics of Solids, 46, pp. 411-425, 1998.

[Nye, 1953] J. Nye. Some geometrical relations in dislocated crystal. Acta Metallurgica, 1, pp 153-162, 1953.

[Ohno, 2007] N. Ohno, D. Okumura. Higher-order stress and grain size effects due to self-energy of geometrically necessary dislocations. Journal of the Mechanics and Physics of Solids, 55, pp. 1879-1898, 2007.

[Orowan, 1934] E.Orowan. Zur kristallplastizitat III. uber den mechanismus der gleitvorgagnes. Zeitschrift fur Physik, 89, pp. 634-659, 1934.

[Osher, 1988] S. Osher, J. Sethian. Fronts propagating with curvature-dependent speed - algorithms based on Hamilton-Jacobi formulations. Journal of Computational Physics, 79, pp. 12-49, 1988.

[Papadopoulos, 1996] I.V. Papadopoulos, V.P. Panoskaltsis. Invariant formulation of a gradient dependent multiaxial high-cycle fatigue criterion. Engineering Fracture Mechanics, 55, pp. 513-528, 1996.

[Peeters, 2001] B. Peeters, E. Hoferlin, P. Van Houtte, E. Aernoudt. Assessment of crystal plasticity based calculation of the lattice spin of polycrystalline metals for FE implementation. International Journal of Plasticity, 17, pp. 819-836, 2001.

[Petch, 1953] N.J. Petch. Cleavage strength of polycrystals. Journal Iron Steel Institute, 174, pp. 25-28, 1953.

[Piekos, 2008a] K. Piekos, J. Tarasiuk, K. Wierzbanowski, B. Bacroix. Stochastic vertex model of recrystallisation. Computational Materials Science, 42, pp. 36-42, 2008.

[Piekos, 2008b] K. Piekos, J. Tarasiuk, K. Wierzbanowski, B. Bacroix. Generalized vertex model of recrystallization - Application to polycrystalline copper. Computational Materials Science, 42, pp. 584-594, 2008.

[Polanyi, 1934] M. Polanyi. Gitterstorung die einem kristall plastisch machen konnte. Zeitschrift fur Physik, 89, pp. 660-664, 1934.

[Porter, 2008] D.A. Porter, K.E. Easterling, M.Y. Sherif. Phase transformations in Metals and Alloys, 3rd edition, CRC Press, 2008.

[Quey, 2011] R. Quey, P.R. Dawson, F.Barbe, Large scale 3D random polycrystals for finite element method: Generation, meshing and remeshing. Computer Methods in Applied Mechanics and Engineering, vol. 200, pp. 1729-1745, 2011.

[Raabe, 1999] D. Raabe. Introduction of a scalable 3D cellular automaton with a probabilistic switching rule for the discrete mesoscale simulation of recrystallization phenomena. Philosophical Magazine A, 79, pp. 2339-2358, 1999.

[Raghavan, 2009] S. Raghavan, Satyam S. Sahay. Modeling the topological features during grain growth by cellular automaton. Computational Materials Science, 46, pp.92-99, 2009.

[Resk, 2009] H. Resk, L. Delannay, M. Bernacki, T. Coupez, R.E. Logé. Adaptive mesh refinement and automatic remeshing in crystal plasticity finite element simulations. Modelling and Simulation in Materials Science and Engineering, 17, no. 075012, 2009.

[Resk, 2010] H. Resk. Modélisation par Éléments Finis des hétérogénéités à l'échelle granulaire au sein d'agrégats polycristallins, PhD Thesis, Ecole Nationale Supérieure des Mines de Paris, 2010.

[Rios, 2005] P.R. Rios, F.Siciliano, H.R.Z. Sandim, R.L. Plaut, A.F. Padilha. Nucleation and growth during recrystallization. Materials Research, 8, pp. 225-238, 2005.

[Rios, 2008] P.R. Rios, M.E. Glicksman. Polyhedral model for self similar grain growth. Acta Materialia, 56, pp. 1165-1171, 2008.

[Roberts, 1978] W. Roberts, B. Ahlblom. A nucleation criterion for dynamic recrystallization during hot working. Acta Metallurgica, 26, pp. 801-813, 1978.

[Rollet, 1997] A.D. Rollett. Overview of modeling and simulation of recrystallization. Progress in Materials Science, 42, pp. 79-99, 1997.

[Rollet, 2001] A.D. Rollet, D. Raabe. A hybrid model for mesoscopic simulation of recrystallization. Computational Materials Science, 21, pp. 69-78, 2001.

[Rollet, 2004] A.D. Rollett et al. Modelling polycrystalline microstructures in 3D. Proc. Conf. Numiform, Columbus. pp. 71-77, 2004.

[Roters, 2000] F. Roters, D. Raabe, G. Gottstein. Work hardening in heterogeneous alloys - A microstructural approach base don three internal state variables. Acta Materialia, 48, pp. 4181-4189, 2000.

[Roucoules, 1994] C. Roucoules, P.D. Hodgson, S. Yue, J.J. Jonas. Softening and microstructural change following the dynamic recrystallization of austenite. Metallurgical and Materials Transactions A, 25, pp. 389-400, 1994.

[Sandstrom, 1975] R.Sandstrom, R.Lagneborg. A controlling factor for dynamic recrystallization. Scripta Metallurgica. 9, pp. 59-65, 1975.

[Sarma, 1996] G. Sarma, P.Dawson. Effects of interactions among crystals on the inhomogeneous deformation of polycrystals. Acta Metallurgica et Materialia, 44, pp. 1937-1953, 1996.

[Sethian, 1996] J.A. Sethian. Level set methods. Cambridge University Press, 1996.

[Shabana, 2008] A. Shabana. Computational continuum mechanics. Cambridge University Press, New York, 2008.

[Shewmon, 1969] P.G. Shewmon. Transformations in Metals. McGraw-Hill, New York, 1969.

[Shockley, 1949] W. Shockley, W.T. Read. Quantitative predictions from dislocation models of crystal grain boundaries. Physical Review, 75, pp. 692, 1949.

[Siha, 2010] M. Siha, D. Weygand. A generalized vertex dynamics model for grain growth in three dimensions. Modelling Simulation of Materials Science and Engineering, 18, no 015010, 2010.

[Simo, 1998] J.C. Simo, T.J. Hughes. Computational inelasticity. Springer-Verlag, New York, 1998.

[Smith, 1948] C.S. Smith. Introduction to Grains, Phases, and Interfaces - an interpretation of microstructure. Trans. AIME, 175, pp. 15-51, 1948.

[Smith, 1952] C.S. Smith. Metal Interfaces, Seminar Report, Cleveland, Ohio. American Society for Metals, pp. 65, 1952.

[Sussman, 1994] M. Sussman, P. Smereka, S. Osher. A level-set approach for computing solutions to incompressible 2-phase flow. Journal of Computational Physics, 114, pp. 146-159, 1994.

[Suwa, 2008] Y. Suwa, Y. Saito, H. Onodera. Phase-field simulation of recrystallization based on the unified subgrain growth theory. Computational Materials Science, vol. 44 pp. 286-295, 2008.

[Takaki, 2008] T. Takaki, Y. Higa A. Yamanaka, and Y. Tomita. Phase-field model during static recrystallization based on crystal-plasticity theory. Journal of Computer-Aided Materials Design, 14, pp.75-84, 2008.

[Takaki, 2010] T.Takaki, Y.Tomita. Static recrystallization simulations starting from predicted deformation microstructure by coupling multi-phase-field method and finite element method based on crystal plasticity. International Journal of Mechanical Sciences, 52, pp. 320-328, 2010.

[Taylor, 1934] G.I. Taylor. The mechanism of plastic deformation of crystals Part I – Theoretical. Proc. Roy. Soc. London, A 145, pp. 362-387, 1934.

[Taylor, 1938] G.I. Taylor. Plastic Strain in metals. Journal of the Institute of Metals, 62, pp. 307-324, 1938.

[Theyssier, 1999] M.C. Theyssier, J.H. Driver. Recrystallization nucleation mechanism along boundaries in hot deformed aluminium bicrystals. Materials Science and Engineering A, 272, pp. 73-82, 1999.

[Titchener, 1958] A.L. Titchener, M.B. Bever. Progress in metal physics 7, pp. 247-338, Pergamon Press, London, 1958.

[Towle, 1979] D.J. Towle, T. Gladman. Recrystallization of austenitic stainless steels after hot rolling. Metal Science 13, pp. 246-256, 1979.

[Trivedi, 2004] P. Trivedi, D.P. Field, H. Weiland. Alloying effects on dislocation substructure evolution of aluminium alloys. International Journal of Plasticity, 20, pp. 459-476, 2004.

[Tucker, 2012] J.C. Tucker, L.H. Chan, G.S. Rohrer, M.A. Groeber, A.D. Rollet. Comparison of grain size distributions in Ni-based superalloy in three and two dimensions using the Saltykov method, Scripta Materialia, 66, pp. 554-557, 2012.

[Underwood, 1970] E.E. Underwood. Quantitative Stereology, Addison Wesley Publishing Company, 1970.

[Upmanyu, 2002] M. Upmanyu, G.N. Hassold, A. Kazaryan, E.A. Holm, Y. Wang, B. Patton, D.J. Srolovitz. Boundary mobility and energy anisotropy effects on microstructural evolution during grain growth. Interface Science, 10, pp. 201-216, 2002.

[Van Houtte, 2002] P. Van Houtte, L. Delannay, S.R. Kalidindi. Comparison of two grain interaction models for polycrystal plasticity and deformation texture prediction. International Journal of Plasticity, 18, pp. 359-377, 2002.

[Van Houtte, 2005] P. Van Houtte, S. Li, M. Seefeldt, L. Delannay. Deformation texture prediction: from the Taylor model to the advanced Lamel model. International Journal of Plasticity, 21, pp. 589-624, 2005.

[Vanherpe, 2011] L. Vanherpe, N. Moelans, B. Blanpain, S. Vandewalle. Bounding box framework for efficient phase field simulation of grain growth in anisotropic systems. Computational Materials Science, 50, pp. 2221-2231, 2011.

[Verhoeven, 1975] J.D. Verhoeven. Fundamentals of Physical Metallurgy, 1975.

[Von Neumann, 1952] J. Von Neumann. Metals Interfaces. ASM, Cleveland, Ohio, 1952.

[Weygand, 2001] D. Weygand, Y. Bréchet, J. Lépinoux. A vertex simulation of grain growth in 2D and 3D. Advanced Engineering Material 3, pp. 67-71, 2001.

[Xu, 2009] T. Xu, M. Li, Topological and statistical properties of a considered Voronoï tessellation, Philosophical Magazine, 89, pp. 349-374, 2009.

[Yu, 2005] C.Y. Yu, P.W. Kao, C.P. Chang. Transition of tensile deformation behaviors in ultrafine-grained aluminum. Acta Materialia, 53, pp. 4019-4028, 2005.

[Zhao, 1996] H.K. Zhao, T. Chan, B. Marriman, S. Oscher. A variational level set approach to multiphase motion. Journal of Computational Physics, 127, pp. 179-195, 1996.

[Zhu, 2005] K.Y. Zhu, D. Chaubet, B. Bacroix, F. Brisset. A study of recovery and primary recrystallization mechanisms in Zr-2Hf alloy. Acta Materialia, 53, pp. 5131-5140, 2005.

Appendix 1: Saltykov method

Considering that the grains are represented by their equivalent spheres, the Saltykov method is dedicated to the question of how to work backward from a grain size distribution (bar-plots) of two-dimensional sections of a material to a three-dimensional grain size distribution (discrete) of it. The problem is further complicated by the fact that for any positive value *d*, all the spheres with a diameter superior to *d* can contribute to the circles of diameter *d* obtained in a section of the considered 3D particle.

Now, considering the following notations in the discretization of the enunciated problem:

- Δ is defined as the ratio of the maximum diameter, $D_{max} = 2R_{max}$, to the total number of grains families considered, *m*. Then, the diameter of the 3D-particles belonging to the j^{th} group is equal to $j\Delta$ with $D_{max} = m\Delta$.
- $N_A(i)$, $\forall i \in \{1,...,m\}$, is defined as the number, per unit area, of 2D-grains with a diameter between $(i-1)\Delta$ and $i\Delta$. $\mathbf{N}_A$ denotes the corresponding vector.
- $N_V(j)$, $\forall j \in \{1,...,m\}$, is defined as the number of 3D-grains, per unit volume, with a diameter equal to $j\Delta$,. $\mathbf{N}_V$ denotes the corresponding vector.
- $N_A(i,j)$, $\forall (i,j) \in \{1,\cdots,j\} \times \{1,\cdots,m\}$, is the contribution of the 3D-grains from 3D-class *j* to the 2D-class *i*.

The number of grains in 2D-class *i* can be written as:

$$N_A(i) = \sum_{j=1}^{m} N_A(i,j). \tag{A.1}$$

Now, with the notations of the Figure A.1 which describes a 3D-grain of radius $r_j = j\frac{\Delta}{2}$: this grain will contribute to the 2D class i $(i \in \{1,...,j\})$ if this grain is intercepted between h_{i-1} and h_i with $h_k = \sqrt{r_j^2 - r_k^2} \forall k \in \{1,..,j\}$.

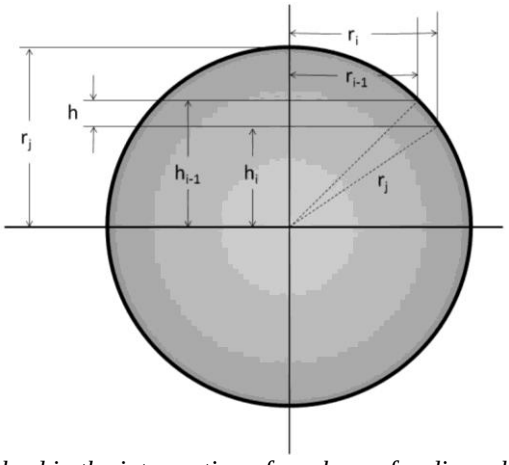

Figure A.1: Geometry involved in the intersection of a sphere of radius r_j by a plane within the slice h.

Thus, the contribution of grains from 3D-class *j* to the 2D-class *i* is given by:

$$N_A(i,j) = 2N_V(j)(h_{i-1} - h_i), \tag{A.2}$$

where the factor 2 is a consequence of considering both grain hemispheres. Then,

$$N_A(i,j) = 2N_V(j)\left(\sqrt{r_j^2 - r_{i-1}^2} - \sqrt{r_j^2 - r_i^2}\right) = 2N_V(j)\left(\sqrt{j^2 - (i-1)^2} - \sqrt{j^2 - i^2}\right) = N_V(j)\Delta k_{ij} \tag{A.3}$$

with the convention $k_{ij} = \sqrt{j^2 - (i-1)^2} - \sqrt{j^2 - i^2}$, $\forall (i,j) \in \{1,...,j\} \times \{1,...,m\}$.

It is interesting to highlight that k_{ij} coefficients depend only on the families size index *i* and *j*. By combining Eqs.(A.1) and (A.3), the upper triangular matrix, $\mathbf{K}$, composed by the k_{ij} coefficients allows to exhibit a 2D grain size distribution (bar-plots) based on the real 3D grain size distribution (discrete):

$$N_A(i) = \sum_{j=1}^{m} N_A(i,j) = \Delta \sum_{j=1}^{m} k_{ij} N_V(j) = \Delta(\mathbf{K}.\mathbf{N}_V)_i$$
$$\text{i.e. } \mathbf{N}_A = \Delta \mathbf{K}.\mathbf{N}_V \tag{A.5}$$

As $\mathbf{K}$ is an invertible matrix, indeed,

$$\det(\mathbf{K}) = \prod_{i=1}^{m} k_{ii} = \prod_{i=1}^{m} \sqrt{2i-1} = \sqrt{\frac{(2m)!}{2^m m!}} > 0 \tag{A.6}$$

the purpose of this annex, i.e. to be able to build a three-dimensional grain size distribution (discrete) thanks to a grain size distribution (bar-plots) of a two-dimensional section, is obtained by an inversion of Eq A.5:

$$\mathbf{N}_V = \frac{1}{\Delta} \mathbf{K}^{-1} \mathbf{N}_A. \tag{A.7}$$

The Table A.1 illustrates the values of the matrix $\mathbf{K}^{-1}$ for $m = 15$. If the use of the Saltykov methodology is based, of course, on an important number of hypotheses as the choice of *m*, the representativeness of the 2D section used to generate the 3D distribution and the approximation of the grain shape by spherical particles, it remains however a very useful tool to build a first approximation of a 3D distribution thanks to 2D data.

Table A.1: Coefficients of the Saltykov matrix $\mathbf{K}^{-1}$ *for m=15*

1.00	-1.55e-1	-3.57e-2	-1.3e-2	-6.07e-3	-3.28e-3	-1.97e-3	-1.27e-3	-8.69e-4	-6.19e-4	-4.57e-4	-3.46e-4	-2.69e-4	-2.13e-4	-1.72e-4
	5.77e-1	-1.53e-1	-4.19e-2	-1.72e-2	-8.73e-3	-5.04e-3	-3.18e-3	-2.13e-3	-1.50e-3	-1.10e-3	-8.30e-4	-6.41e-4	-5.06e-4	-4.06e-4
		4.47e-1	-1.38e-1	-4.07e-2	-1.77e-2	-9.42e-3	-5.65e-3	-3.67e-3	-2.53e-3	-1.82e-3	-1.36e-3	-1.04e-3	-8.15e-4	-6.51e-4
			3.78e-1	-1.26e-1	-3.86e-2	-1.74e-2	-9.52e-3	-5.85e-3	-3.89e-3	-2.73e-3	-1.99e-3	-1.51e-3	-1.17e-3	-9.25e-4
				3.33e-1	-1.16e-1	-3.65e-2	-1.68e-2	-9.40e-3	-5.88e-3	-3.97e-3	-2.82e-3	-2.09e-3	-1.59e-3	-1.25e-3
					3.02e-1	-1.08e-1	-3.46e-2	-1.62e-2	-9.19e-3	-5.83e-3	-3.98e-3	-2.86e-3	-2.14e-3	-1.64e-3
						2.77e-1	-1.02e-1	-3.29e-2	-1.56e-2	-8.96e-3	-5.74e-3	-3.95e-3	-2.86e-3	-2.16e-3
							2.58e-1	-9.60e-2	-3.15e-2	-1.51e-2	-8.71e-3	-5.63e-3	-3.90e-3	-2.85e-3
								2.43e-1	-9.13e-2	-3.01e-2	-1.46e-2	-8.47e-3	-5.51e-3	-3.85e-3
									2.29e-1	-8.72e-2	-2.90e-2	-1.41e-2	-8.25e-3	-5.39e-3
										2.18e-1	-8.36e-2	-2.79e-2	-1.36e-2	-8.03e-3
											2.09e-1	-8.04e-2	-2.70e-2	-1.32e-2
												2.00e-1	-7.76e-2	-2.61e-2
													1.92e-1	-7.50e-2
														1.86e-1

Appendix 2: 304L crystallographic orientation of grains

The grains crystallographic orientation in a polycrystalline sample can be defined in different ways. The most common orientation representation is based on the three Euler angles and is expressed as $g = g(\varphi_1, \Phi, \varphi_2)$ (symbol "g" is traditionally used for denoting the orientation). The three angles correspond to the successive rotations according to a specific sequence (Bunge, Roe, symmetric). In this work, the Bunge convention is used to represent the grains crystallographic orientations.

	φ_1 (°)	Φ(°)	φ_2(°)
1	84.1	18.6	298.8
2	215.1	33.9	136.0
3	139.4	47.2	249.9
4	170.1	32.4	227.7
5	354.1	38.3	42.4
6	73.9	33.4	271.2
7	196.3	22.4	191.7
8	127.5	40.6	244.1
9	238.0	44.2	134.9
10	298.6	35.1	96.0
11	191.9	25.3	158.5
12	238.4	44.3	135.0
13	305.1	50.0	33.3
14	127.0	40.8	244.4
15	37.3	26.6	1.2
16	128.9	51.4	210.5
17	19.8	36.5	337.5
18	163.5	26.0	176.2
19	174.2	16.6	160.5
20	4.3	32.4	22.0
21	257.2	47.7	138.4
22	92.4	40.5	292.7
23	251.8	8.6	81.3
24	203.8	40.6	165.4
25	136.8	13.9	267.4
26	77.7	41.6	298.2
27	170.1	25.9	178.8
28	126.9	41.0	244.3
29	310.9	7.3	23.4
30	336.5	39.6	2.0
31	85.2	18.4	298.2
32	128.7	51.0	211.1
33	202.4	24.5	201.8
34	103.6	44.1	233.7
35	3.0	38.4	327.6
36	159.2	10.3	226.4
37	261.6	23.6	98.3
38	118.4	38.2	253.1
39	335.9	11.8	355.6
40	28.5	24.3	305.9
41	354.9	38.2	41.9
42	35.5	26.7	2.1
43	7.8	41.6	327.3
44	211.2	30.9	118.6
45	321.3	44.2	3.6
46	55.9	17.0	312.8
47	126.8	41.1	243.8
48	251.0	22.5	84.3
49	138.0	34.7	233.5
50	182.9	14.0	219.8
51	19.7	36.9	337.3
52	240.2	19.9	161.3
53	122.6	36.8	219.8
54	121.7	21.5	227.6
55	150.0	41.1	335.4
56	289.3	8.4	61.6
57	174.3	5.2	189.0
58	270.6	16.6	120.4
59	295.3	39.8	77.4
60	54.7	53.5	312.1
61	119.6	17.4	219.2
62	239.0	46.0	118.9
63	239.2	33.3	124.8
64	357.6	24.1	336.6
65	0.0	17.7	32.5
66	137.4	33.4	222.9
67	48.3	58.7	315.0
68	98.1	18.7	235.3
69	195.3	48.2	142.8
70	113.9	19.9	253.4
71	26.4	19.0	353.5
72	108.2	30.5	230.2
73	136.9	54.1	210.6
74	233.1	53.9	135.7
75	202.8	26.2	119.4
76	37.0	37.6	331.4
77	265.4	12.2	136.8
78	295.1	37.8	26.7
79	34.6	26.4	350.9
80	292.2	51.5	39.9
81	226.1	11.0	138.5
82	97.0	2.8	297.0
83	286.3	49.8	40.5
84	231.0	53.3	146.2
85	247.5	33.4	113.5
86	58.8	14.6	340.2
87	317.6	43.5	43.7
88	350.8	28.2	32.3
89	122.5	21.7	226.2
90	320.1	48.4	53.7
91	90.3	30.3	232.4
92	47.5	43.8	343.6
93	294.1	12.3	37.8
94	157.4	11.5	196.1
95	120.3	38.0	207.8
96	135.7	33.8	225.9
97	141.2	43.1	221.5
98	290.5	40.0	110.5
99	223.3	38.9	174.8
100	238.7	26.5	130.8

Appendix 3: Torsion test

In the torsion test, the samples are submitted to a rotating load, as illustrated in Figure A.2. The experimental results presented in this report were obtained using samples presenting a cylindrical shape.

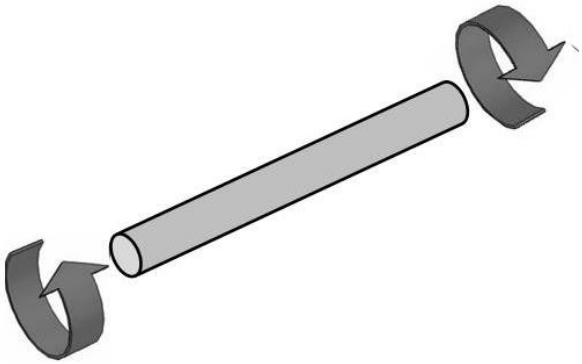

Figure A.2: Torsion test scheme.

Using torsion tests we are able to reach large strains before plastic instability occurs. In addition to this, the samples do not undergo significant shape change as they are deformed as long as the gage section is restrained to a fixed length. On the other hand, the interpretation of torsion test data is more complex than that used for axial –testing methods due to the fact that the strain and strain rate vary linearly with the sample radius.

In torsion tests, the stress-strain curves are derived from the torque-time data recorded automatically by the torsion test system. Assuming that the deformation along the rotation axes is homogeneous, the equivalent strain is calculated as:

$$\bar{\varepsilon}(R) = \int_0^t \frac{2}{\sqrt{3}} \frac{\pi \dot{N} R}{L} dt = \frac{2}{\sqrt{3}} \frac{\pi N R}{L}, \tag{A.8}$$

where N is the number of laps, $\dot{N}$ is the rotation speed (Rad/s), L is the gauge length (mm) and R is the gauge radius (mm).

The equivalent tensile stress $(\bar{\sigma}(R))$ is obtained using the Fields and Backofen [Fields, 1957] analysis:

$$\bar{\sigma}(R) = \frac{\sqrt{3}T(R)}{2\pi R^3}\left(\tilde{n} + \tilde{m} + 3\right), \tag{A.9}$$

where T is the torque (N.m), $\tilde{m}$ is the slope of the straight line $\ln T = f\left(\ln\left(\dot{N}\right)\right)$, for a given number of laps N, $\tilde{n}$ is the slope of the straight line $\ln T = f\left(\ln\left(N\right)\right)$, for a given rotation speed $\dot{N}$. In other words, $\tilde{m}$ and $\tilde{n}$ correspond respectively to:

$$\tilde{m} = \left(\frac{\partial \ln T}{\partial \ln \dot{N}}\right)_N \text{ and } \tilde{n} = \left(\frac{\partial \ln T}{\partial \ln N}\right)_{\dot{N}}. \tag{A.10}$$

It is interesting to notice the hypotheses of the Fields and Backofen [Fields, 1957] analysis:

- the materials are homogeneous and isotropic (material hardening is represented by an isotropic hardening law). In other words, the sample cylindrical shape does not change during deformation;
- plastic deformation is homogeneous throughout the sample;
- the deformation is uniform along the specimen (no flow localization);
- the cross sections are straight and move as a rigid body motion with speed ω.

Appendix 4: EBSD test

Electron backscattered diffraction (EBSD) is based on the acquisition of diffraction patterns from bulk samples in the scanning electron microscope (SEM). The EBSD acquisition hardware comprises a sensitive CCD camera and an image processing system for pattern averaging and background subtraction. Figure A.3 presents a schematic diagram illustrating the main components of an EBSD system.

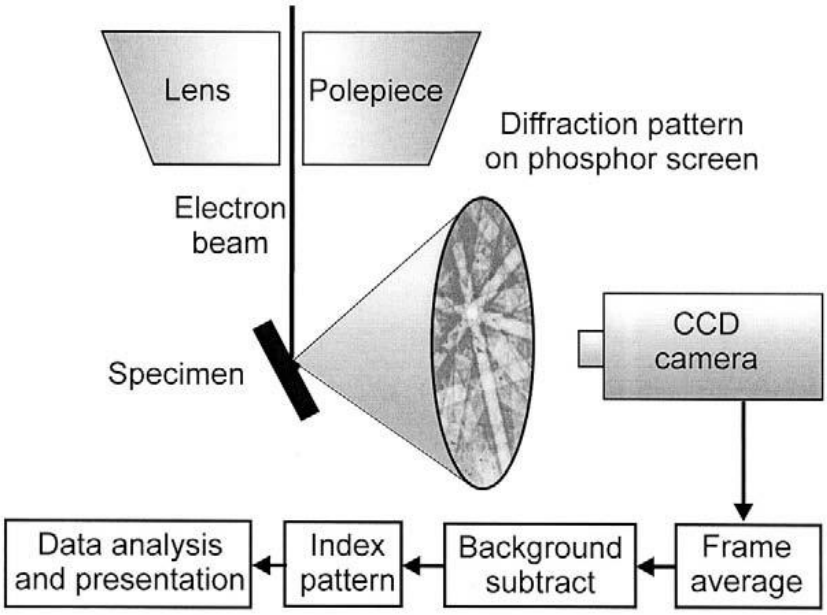

Figure A.3: Schematic diagram of a typical EBSD installation in an SEM [Humphreys, 2004].

The EBSD acquisition software (TSL OIM data collection 5) is used to control the data acquisition, to solve the diffraction patterns and to store the data. In order to analyse, manipulate and display all the stored data, the TSL OIM Analysis version 5.0 software is used in this work.

EBSD is carried out on a specimen which is tilted between 60° and 70° from the horizontal and a series of data points are obtained by scanning the electron beam across the sample.

Modélisation de la plasticité cristalline et de la migration des joints de grains de l'acier 304L à l'échelle mésoscopique

RESUME : Les propriétés des matériaux métalliques sont très liées à leurs caractéristiques microstructurales. Par exemple il est bien connu que la taille de grains joue sur la limite élastique du matériau ainsi que sur ses capacités d'écrouissage. Ainsi, la compréhension et la modélisation de l'évolution de la microstructure d'un métal pendant un traitement thermomécanique est d'une importance primordiale afin de prédire finement son comportement ainsi que ses propriétés finales. Dans le cadre de cette thèse, nous nous sommes concentrés sur la modélisation, à l'échelle d'un agrégat polycristallin, de la plasticité cristalline, de la recristallisation statique et de la croissance des grains dans un contexte de mobilité et d'énergie d'interface isotrope. Un modèle à champ complet dans un cadre éléments finis (EF) est proposé. Les grains sont représentés grâce à un formalisme level-set. L'étude EF développée peut être divisée en trois grandes parties: la génération statistique de microstructures digitales, la modélisation de la plasticité cristalline et la modélisation de la migration des joins de grains en régime de recristallisation statique. Concernant la génération statistique des microstructures digitales, une étude comparative entre deux méthodes de génération (Voronoï et Laguerre-Voronoï) a été réalisée. La capacité de la deuxième approche à respecter une microstructure basée sur des données expérimentales est mise en valeur en 2D et en 3D. Dans une deuxième étape, la plasticité cristalline des matériaux métalliques est étudiée. Deux modèles d'écrouissage ont été implémentés et validés : un premier modèle considérant uniquement les densités de dislocations totales, et un deuxième modèle différenciant les dislocations statistiquement stockées (SSDs) des dislocations géométriquement nécessaires (GNDs). Afin de valider l'implémentation de ces deux modèles issus de la littérature deux cas ont été étudiés : le premier correspond à l'étude à chaud d'un essai de compression plane d'un acier 304L, et le deuxième correspond à l'étude d'un essai à froid de compression simple d'un oligocristal de tantale composé de 6 grains. Les résultats numériques obtenus sont comparés avec les données expérimentales des deux essais. La migration des joints de grains est étudiée dans le contexte des régimes de recristallisation statique et de croissance de grains. Par rapport aux travaux pre-existants dans un cadre level-set, l'accent est mis sur la prise en compte des forces capillaires. La croissance des grains pure est en effet développée dans le formalisme éléments finis/level set considéré, et des validations à partir de résultats analytiques connus sont présentées. De plus, un travail d'analyse de modèles de croissance des grains à champ moyen existant dans la littérature est réalisé. Deux modèles en particuliers sont étudiés : celui de Burke et Turnbull et celui de Hillert/Abbruzzese. En comparant ces modèles avec les résultats obtenus par l'approche en champ complet développée, il est mis en évidence que le modèle simple de Burke et Turnbull n'est pas approprié pour décrire la croissance de grains pour tout type de distribution initiale de taille de grains. La recristallisation statique est ensuite abordée, avec une prise en compte des deux forces motrices liées (i) aux gradients d'énergies stockées sous la forme de dislocations, et (ii) aux effets capillaires. L'influence des effets de capillarité apparaît comme fortement liée à la distribution spatiale des nouveaux germes. Finalement, les résultats des simulations réalisées en plasticité cristalline sont utilisés comme données d'entrée du modèle de recristallisation statique développé. La comparaison des prédictions obtenues comparativement aux résultats expérimentaux sur 304L permet d'illustrer la pertinence d'une approche de type SSD/GND afin de prédire les sites de germination potentiels.

Mots clés : Modélisation à champ complet, plasticité cristalline, recristallisation, croissance des grains.

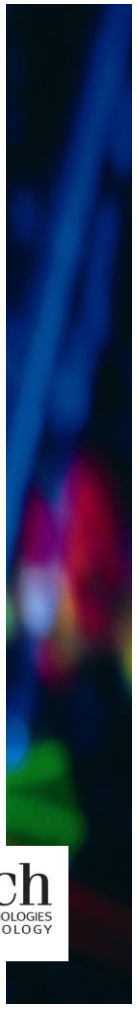

MINES ParisTech

ParisTech
INSTITUT DES SCIENCES ET TECHNOLOGIES
PARIS INSTITUTE OF TECHNOLOGY

Modelling of crystal plasticity and grain boundary motion of 304L steel at the mesoscopic scale

ABSTRACT: Mechanical and functional properties of metals are strongly related to their microstructures, which are themselves inherited from thermal and mechanical processing. For example, the material grain size distribution plays an important role on the material yield limit and work hardening. The understanding of these microstructure evolutions during thermo-mechanical processes is of prime importance for a better prediction and control of the material mechanical properties. During this Ph.D., we have worked on the modelling of crystal plasticity, static recrystallization and grain growth at the mesoscopic scale in the context of isotropic mobility and interface energy. The full field model developed is based on a finite element formulation combined with a level set framework used to describe the granular structure. This Ph.D. thesis is divided in three main parts: statistical generation of digital microstructures, crystal plasticity modelling and grain boundary migration modelling. In what concerns the digital microstructures statistical generation, a comparative study between two methods (Voronoï and Laguerre-Voronoï) is presented. The ability of the second approach to respect a given grain size distribution is highlighted in 2D and 3D. Secondly, the metallic materials crystal plasticity is studied. Two hardening laws have been implemented and validated: the first one considering the total dislocation density and a second one that differentiates the statistically stored dislocations (SSD) from geometrically necessary dislocations (GNDs). Two different tests cases are used in order to validate the implementation of both hardening laws in the considered crystal plasticity model. The first one corresponds to a planar hot compression test (channel die test) on a 304L stainless steel whereas the second one corresponds to a simple cold compression test on a tantalum olygocrystal composed by six different grains. The obtained results are compared to experimental data for both cases. Grain boundary migration is studied for static recrystallization and grain growth phenomena. Compared to previous work in the considered level-set framework, the focus is on the consideration of capillary forces. Indeed pure grain growth is developed in the considered finite elements/level set formalism and this algorithm is validated using well-known analytical results. Moreover, the results of the developed full field grain growth model are compared in 2D with several well-known mean field grain growth models (Burke and Turbull model and Hillert/Abbruzzese model). The results obtained illustrate that only the Hillert/Abbruzzese model accurately describes grain growth kinetics for all initial grain size distributions. The validity of the Burke and Turnbull model is, on the contrary, restricted to specific distributions. Static recrystallization is then discussed considering both driving forces: (i) internal energy gradient and (ii) grain boundaries capillarity effects. The influence of capillary effects appears to be strongly related to the spatial distribution of the new grains. Finally, the crystal plasticity numerical results are used as input data of the developed static recrystallization full field model. The comparison of the numerical predictions obtained with 304L experimental results allows to illustrate the relevance of the SSDs/GNDs formalism used concerning the prediction of the nuclei potential position.

Keywords : Full field modelling, crystal plasticity, recrystallization, grain growth.

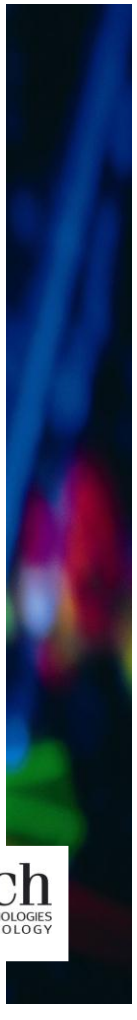

MINES ParisTech

ParisTech
INSTITUT DES SCIENCES ET TECHNOLOGIES
PARIS INSTITUTE OF TECHNOLOGY